

FRONTIERS IN ENERGY RESEARCH: RISING STARS

EDITED BY: Uwe Schröder, Simone Bastianoni, Andreas Borgschulte,
ZhaoYang Dong, Francois M. A. Marechal,
Fernando M. B. Marques, S. M. Muyeen, Ah-Hyung Alissa Park,
Shripad T. Revankar, Ellen B. Stechel, Michael Folsom Toney,
David Howe Wood and Sheng S. Zhang

PUBLISHED IN: Frontiers in Energy Research





frontiers

Frontiers eBook Copyright Statement

The copyright in the text of individual articles in this eBook is the property of their respective authors or their respective institutions or funders. The copyright in graphics and images within each article may be subject to copyright of other parties. In both cases this is subject to a license granted to Frontiers.

The compilation of articles constituting this eBook is the property of Frontiers.

Each article within this eBook, and the eBook itself, are published under the most recent version of the Creative Commons CC-BY licence.

The version current at the date of publication of this eBook is CC-BY 4.0. If the CC-BY licence is updated, the licence granted by Frontiers is automatically updated to the new version.

When exercising any right under the CC-BY licence, Frontiers must be attributed as the original publisher of the article or eBook, as applicable.

Authors have the responsibility of ensuring that any graphics or other materials which are the property of others may be included in the CC-BY licence, but this should be checked before relying on the CC-BY licence to reproduce those materials. Any copyright notices relating to those materials must be complied with.

Copyright and source acknowledgement notices may not be removed and must be displayed in any copy, derivative work or partial copy which includes the elements in question.

All copyright, and all rights therein, are protected by national and international copyright laws. The above represents a summary only. For further information please read Frontiers' Conditions for Website Use and Copyright Statement, and the applicable CC-BY licence.

ISSN 1664-8714

ISBN 978-2-88976-733-5

DOI 10.3389/978-2-88976-733-5

About Frontiers

Frontiers is more than just an open-access publisher of scholarly articles: it is a pioneering approach to the world of academia, radically improving the way scholarly research is managed. The grand vision of Frontiers is a world where all people have an equal opportunity to seek, share and generate knowledge. Frontiers provides immediate and permanent online open access to all its publications, but this alone is not enough to realize our grand goals.

Frontiers Journal Series

The Frontiers Journal Series is a multi-tier and interdisciplinary set of open-access, online journals, promising a paradigm shift from the current review, selection and dissemination processes in academic publishing. All Frontiers journals are driven by researchers for researchers; therefore, they constitute a service to the scholarly community. At the same time, the Frontiers Journal Series operates on a revolutionary invention, the tiered publishing system, initially addressing specific communities of scholars, and gradually climbing up to broader public understanding, thus serving the interests of the lay society, too.

Dedication to Quality

Each Frontiers article is a landmark of the highest quality, thanks to genuinely collaborative interactions between authors and review editors, who include some of the world's best academicians. Research must be certified by peers before entering a stream of knowledge that may eventually reach the public - and shape society; therefore, Frontiers only applies the most rigorous and unbiased reviews.

Frontiers revolutionizes research publishing by freely delivering the most outstanding research, evaluated with no bias from both the academic and social point of view. By applying the most advanced information technologies, Frontiers is catapulting scholarly publishing into a new generation.

What are Frontiers Research Topics?

Frontiers Research Topics are very popular trademarks of the Frontiers Journals Series: they are collections of at least ten articles, all centered on a particular subject. With their unique mix of varied contributions from Original Research to Review Articles, Frontiers Research Topics unify the most influential researchers, the latest key findings and historical advances in a hot research area! Find out more on how to host your own Frontiers Research Topic or contribute to one as an author by contacting the Frontiers Editorial Office: frontiersin.org/about/contact

FRONTIERS IN ENERGY RESEARCH: RISING STARS

Topic Editors:

Uwe Schröder, University of Greifswald, Germany

Simone Bastianoni, University of Siena, Italy

Andreas Borgschulte, Swiss Federal Laboratories for Materials Science and Technology, Switzerland

ZhaoYang Dong, Nanyang Technological University, Singapore

Francois M. A. Marechal, Swiss Federal Institute of Technology Lausanne, Switzerland

Fernando M. B. Marques, University of Aveiro, Portugal

S. M. Mueen, Qatar University, Qatar

Ah-Hyung Alissa Park, Columbia University, United States

Shripad T. Revankar, Purdue University, United States

Ellen B. Stechel, Arizona State University, United States

Michael Folsom Toney, University of Colorado Boulder, United States

David Howe Wood, University of Calgary, Canada

Sheng S. Zhang, United States Army Research Laboratory, United States

Citation: Schröder, U., Bastianoni, S., Borgschulte, A., Dong, Z., Marechal, F. M. A., Marques, F. M. B., Mueen, S. M., Park, A.-H. A., Revankar, S. T., Stechel, E. B., Toney, M. F., Wood, D. H., Zhang, S. S., eds. (2023). *Frontiers in Energy Research: Rising Stars*. Lausanne: Frontiers Media SA.
doi: 10.3389/978-2-88976-733-5

Table of Contents

- 04 Editorial: Frontiers in Energy Research: Rising Stars**
ZhaoYang Dong, Sheng S. Zhang, Shripad T. Revankar, Ah-Hyung A. Park, Andreas Borgschulte, Michael F. Toney and Uwe Schröder
- 06 New Hybrid Organic-Inorganic Thin Films by Molecular Layer Deposition for Rechargeable Batteries**
Jian Liu and Jiajun Wang
- 14 Exploring the Thermodynamic Limits of Enhanced H_2 Recovery With Inherent Carbon Removal From Low Value Aqueous Biomass Oxygenate Precursors**
Prince Ochonma, Claire Blaudeau, Rosalie Krasnoff and Greeshma Gadikota
- 30 Energetics of Li^+ Coordination with Asymmetric Anions in Ionic Liquids by Density Functional Theory**
Drace Penley, Stephen P. Vicchio, Rachel B. Getman and Burcu Gurkan
- 41 The Origins of Ion Conductivity in MOF-Ionic Liquids Hybrid Solid Electrolytes**
Roman Zettl and Ilie Hanzu
- 49 Surface Properties of $LaNi_5$ and $TiFe$ —Future Opportunities of Theoretical Research in Hydrides**
Zbigniew Łodziana
- 58 Degradation Comparison of Cyclic and Linear Siloxane Contamination on Solid Oxide Fuel Cells Ni-YSZ Anode**
Jiashen Tian and Ryan J. Milcarek
- 71 Biogas Upgradation Through CO_2 Conversion Into Acetic Acid via Microbial Electrosynthesis**
Moumita Roy, Sukrampal Yadav and Sunil A. Patil
- 80 Temperature-Dependent Crystallization Mechanisms of Methylammonium Lead Iodide Perovskite From Different Solvents**
Oleksandra Shargaieva, Hampus Näsström, Jinzhao Li, Daniel M. Töbrens and Eva L. Unger
- 91 Modeling and Simulation of Large-Scale Wind Power Base Output Considering the Clustering Characteristics and Correlation of Wind Farms**
Mingzhe Zhao, Yimin Wang, Xuebin Wang, Jianxia Chang, Yong Zhou and Tao Liu



Editorial: Frontiers in Energy Research: Rising Stars

ZhaoYang Dong¹, Sheng S. Zhang², Shripad T. Revankar³, Ah-Hyung A. Park⁴,
Andreas Borgschulte⁵, Michael F. Toney⁶ and Uwe Schröder^{7*}

¹Nanyang Technological University, Singapore, ²DEVCOM Army Research Laboratory, Adelphi, MD, United States, ³Purdue University, West Lafayette, IN, United States, ⁴Columbia University, New York City, NY, United States, ⁵Swiss Federal Laboratories for Materials Science and Technology, Dübendorf, Switzerland, ⁶Department of Chemical and Biological Engineering and Renewable and Sustainable Energy Institute, University of Colorado Boulder, Boulder, CO, United States, ⁷Institute of Biochemistry, University of Greifswald, Greifswald, Germany

Keywords: renewable energies, battery research, biomass, hydrogen, biogas, solid oxide fuel cells, wind energy, photovoltaics

Editorial on the Research Topic

Frontiers in Energy Research: Rising Stars

Science thrives on innovation and spirit of enquiry and thus encompasses change, renewal, and a constantly evolving body of thought. It is precise from this perspective that young scientists provide essential impetus for advancement in science and technology with creative new ideas, strategies, and methods.

In few scientific disciplines are these new impulses as important as in energy research: ensuring access to affordable, reliable, sustainable, clean, and modern energy for all (Sustainable Development Goal 7) is an immense challenge for humanity in the face of the consequences of global climate change and increasing geopolitical conflicts.

This Research Topic of articles, “*Frontiers in Energy Research: Rising Stars*,” provides a glimpse into the versatility of high-quality energy research, driven by internationally recognized researchers in their early stages of independent careers. These articles address key technologies for a path toward sustainable renewable energy practices with energy storage and hydrogen and biogas and biomass utilization.

Three articles under this Research Topic focus on electrochemical energy storage. Hereby, two research articles highlight ionic liquid electrolytes for high performance and safe operation of lithium ion batteries based on intrinsic conductivity, wide potential window, and negligible volatility of the ionic liquids. In one article, Penley et al. used the density functional theory to predict the solvation and coordination of lithium ions—crucial properties determining the solubility of lithium salts and the ability of lithium ions intercalating into the active electrode materials. By calculating the dissociation energies of lithium ions, the authors were able to predict the coordination of the lithium ions in the tailored ionic liquid electrolytes. In the other study, Zettl and Hanzu studied the ionic conductivity of a type of hybrid solid electrolytes consisting of a metal–organic framework and an ionic liquid. Such hybrid electrolytes may be considered a bridge between the classical liquid and solid electrolytes. In the third mini-review article, Liu and Wang examined the recent development in the molecular layer deposition technique for preparing the thin-film electrodes and electrolyte of rechargeable batteries. This is a highly interesting technique that allows to tailor thin-film battery materials by depositing hybrid organic–inorganic materials at a nanoscale level and with well-tunable and unique properties that conventional electrode materials lack.

Not only an efficient storage of electrical energy but also the storage of hydrogen is an important task and challenge, requiring a trade-off between storage density, energy expenditure, cyclic stability, and safety. Here, hydrogen storage in solid-state compounds can be considered a safe storage

OPEN ACCESS

Edited by:

Meisam Tabatabaei,
University of Malaysia Terengganu,
Malaysia

Reviewed by:

Sivakumar Nallusamy,
Sultan Qaboos University, Oman
Mortaza Aghbashlo,
University of Tehran, Iran

*Correspondence:

Uwe Schröder
uwe.schroeder@uni-greifswald.de

Specialty section:

This article was submitted to
Bioenergy and Biofuels,
a section of the journal
Frontiers in Energy Research

Received: 02 May 2022

Accepted: 17 May 2022

Published: 12 July 2022

Citation:

Dong Z, Zhang SS, Revankar ST,
Park A-HA, Borgschulte A, Toney MF
and Schröder U (2022) Editorial:
Frontiers in Energy Research:
Rising Stars.
Front. Energy Res. 10:934319.
doi: 10.3389/fenrg.2022.934319

method. Yet, research still has to identify the ultimate storage material. Parameters like the thermodynamics and kinetics of hydrogen adsorption and desorption and the resistance to contamination are only some aspects to be considered. In his research article, Zbigniew Łodziana applied surface energy calculations for LaNi_5 and TiFe as alloys relevant for hydrogen storage—highlighting, for example, the strong binding energies of CO , CO_2 , and H_2O at the alloy surfaces, thus blocking the active sites for dissociative hydrogen adsorption.

The major source of renewable hydrogen is probably the electrochemical water splitting. Yet, it can also be harnessed from biomass, for example, *via* steam reforming. This technology, however, requires “high-value” biomass—biomass with a low water contents—as feedstock. Worldwide, however, huge quantities of low-value biomass (e.g., aqueous waste streams) remain unexploited and require energy-extensive treatment to remove their carbon load before being discharged into the environment. Ochonma et al. studied the thermodynamic limits for an enhanced hydrogen production, combined with an inherent carbon removal from low-value aqueous biomass components. In their process, which takes place at considerably reduced temperatures and pressure as compared to conventional high-temperature reforming, the authors aimed to utilize the effect of coupling thermodynamically downhill carbon mineralization reactions for *in situ* CO_2 capture to enhance hydrogen evolution.

In addition to hydrogen, methane (in the form of biogas) is a promising energy carrier, which can be stored more easily than hydrogen and for which the existing natural gas infrastructure can be exploited. However, the high CO_2 contents of biogas (up to 50%) lower its calorific value. Hence, various biogas upgradation technologies are under intense investigation to increase the methane content to the desired level. In their article, Roy et al. used microbial electrosynthesis, a microbial electrochemical technology, for biogas upgrading. In this technology, microorganisms convert CO_2 (with the help of electric energy) to generate organic compounds. The authors could demonstrate a combined benefit of microbial electrosynthesis—an increase of the methane contents of the used biogas and a production of acetic acid in the liquid phase.

It is not only the carbon dioxide content that can be problematic for the energetic use of biogas but also impurities such as hydrogen sulfide and siloxanes. Thus, in solid oxide fuel cells (SOFCs), which can directly utilize biogas for electrochemical energy conversion, these impurities, even at low concentrations, can potentially damage the fuel cell's electrocatalyst. In their study, Tian and Milcarek studied the effect of cyclic and linear siloxane contaminations on the nickel-yttria-stabilized zirconia (Ni-YSZ) anode of a solid oxide fuel cell. By means of detailed electrochemical and postmortem analysis,

they showed cyclic siloxanes to possess the strongest degradation effects and identified silicon and silicon carbide as major siloxane decomposition products.

Two further research studies under this Research Topic address very different aspects of solar energy and wind power. Shargaieva et al. devoted their article to the crystallization mechanism of methylammonium lead iodide perovskite from different solvents. These perovskites are a novel type of semiconductors that show great potential for solution-processed optoelectronic devices including solar cells. Hereby, the performance of the respective device is intrinsically determined by the quality of the solution-processed halide perovskite thin films. The findings of this study allow a deeper understanding of the different roles that solvents play in the formation process of halide perovskite semiconductors, and they allow predicting optimum preparation conditions. In contrast to this materials science approach, the study by Zhao et al. addressed deficits in the prediction of large-scale wind power bases. Until now, the calculation of the power output of wind power bases assumes the wind power to be homogeneous for an entire region, neglecting heterogeneities and thus accepting large deviations in the simulation results of the wind power output. To obtain more accurate power output landscapes of large-scale wind power bases, the authors proposed a power output scene simulation method considering power station clustering and cluster correlation. They verified the validity and rationality of the new simulation method using physical data from the wind power base of the downstream Yalong River basin.

AUTHOR CONTRIBUTIONS

US wrote the first draft, and all other authors revised and added to it.

Conflict of Interest: The authors declare that the research was conducted in the absence of any commercial or financial relationships that could be construed as a potential conflict of interest.

Publisher's Note: All claims expressed in this article are solely those of the authors and do not necessarily represent those of their affiliated organizations, or those of the publisher, the editors, and the reviewers. Any product that may be evaluated in this article, or claim that may be made by its manufacturer, is not guaranteed or endorsed by the publisher.

Copyright © 2022 Dong, Zhang, Revankar, Park, Borgschulte, Toney and Schröder. This is an open-access article distributed under the terms of the Creative Commons Attribution License (CC BY). The use, distribution or reproduction in other forums is permitted, provided the original author(s) and the copyright owner(s) are credited and that the original publication in this journal is cited, in accordance with accepted academic practice. No use, distribution or reproduction is permitted which does not comply with these terms.



New Hybrid Organic-Inorganic Thin Films by Molecular Layer Deposition for Rechargeable Batteries

Jian Liu^{1*} and Jiajun Wang^{2*}

¹School of Engineering, Faculty of Applied Science, the University of British Columbia, Kelowna, BC, Canada, ²MIT Key Laboratory of Critical Materials Technology for New Energy Conversion and Storage, School of Chemistry and Chemical Engineering, Harbin Institute of Technology, Harbin, China

OPEN ACCESS

Edited by:

Sheng S. Zhang,
United States Army Research
Laboratory, United States

Reviewed by:

Xiulin Fan,
Zhejiang University, China
Wen Yang,
Beijing Institute of Technology, China

*Correspondence:

Jian Liu
Jian.liu@ubc.ca
Jiajun Wang
Jiajunhit@hit.edu.cn

Specialty section:

This article was submitted to
Electrochemical Energy Conversion
and Storage,
a section of the journal
Frontiers in Energy Research

Received: 09 February 2021

Accepted: 06 May 2021

Published: 21 May 2021

Citation:

Liu J and Wang J (2021) New Hybrid
Organic-Inorganic Thin Films by
Molecular Layer Deposition for
Rechargeable Batteries.
Front. Energy Res. 9:665884.
doi: 10.3389/fenrg.2021.665884

The design of multifunctional thin films holds the key to manipulate the surface and interface structure of the electrode and electrolyte in rechargeable batteries and achieve desirable performance for various applications. Molecular layer deposition (MLD) is an emerging thin-film technique with exclusive advantages of depositing hybrid organic-inorganic materials at a nanoscale level and with well tunable and unique properties that conventional thin films might not have. Herein, we provide a timely mini-review on the most recent progress in the surface chemistry and MLD process of novel hybrid organic-inorganic thin films and their applications as the anode, cathode, and solid electrolytes in lithium-ion batteries. Perspectives for future research in designing new MLD process and precursors, enriching MLD material library, and expanding their potential applications in other energy storage systems, are discussed at the end.

Keywords: molecular layer deposition, hybrid thin film, surface coating, lithium batteries, self-limiting growth

INTRODUCTION

Rechargeable batteries play an essential role in many applications nowadays, from portable devices and electric vehicles to miniaturized and intelligent systems, such as wearable devices, the Internet of things, micro-electromechanical system. The ever-increasing demand for high-performance batteries requires continuous materials innovation to address the limitation in current rechargeable batteries. In particular, many pressing issues in batteries, such as degradation, safety, gas evolution, etc., are closely associated with the structure and properties of the electrode and electrolyte interface (Xu et al., 2018; Banerjee et al., 2020; Rowden and Garcia-Araez, 2020). It is well recognized that being able to manipulate the interface, often at the nanoscale level, is a key to alleviate unwanted side reactions and improve the overall performance of batteries, particularly at extreme conditions, such as high temperatures, high voltages, fast charging, etc. (Chen et al., 2010; Zhao et al., 2021).

Over the past decades, atomic layer deposition (ALD) has been demonstrated as a promising thin film deposition technique to tailor the electrode-electrolyte interface in liquid and all-solid-state lithium-ion batteries (LIBs) (Knoops et al., 2012; Zhao et al., 2018b; Zhao et al., 2021). Distinguished from other techniques, ALD allows uniform and nanoscale coating of functional inorganic thin films (metal oxides, phosphates, fluorides, and nitrides) at the electrode-electrolyte interface in LIBs to suppress undesirable phenomena, such as detrimental surface and near-surface phase transition (Yan et al., 2018), electrode volume change (Xiao et al., 2011; Lotfabad et al., 2014), transitional metal dissolution (Scott et al., 2011), etc. Such success has stimulated the industrial pilot study of using a high-throughput continuous particle ALD process to achieve surface modification on large-scale

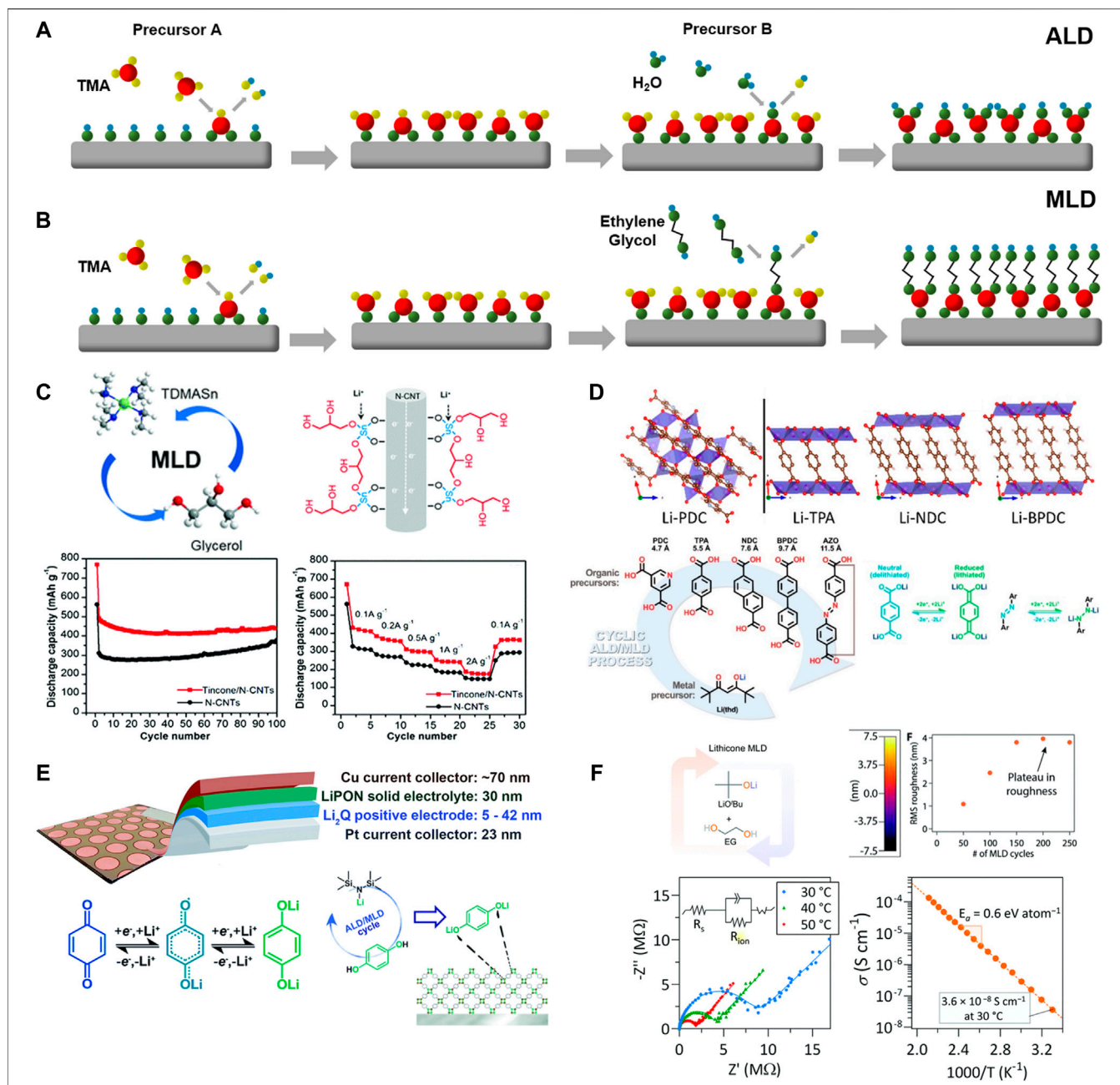


FIGURE 1 | Illustration of one cycle of (A) ALD-Al₂O₃ (trimethylaluminum (TMA)-H₂O) and (B) MLD-alucone (TMA-ethylene glycol) (reproduced from Zhao et al. (2021) with permission from The Royal Society of Chemistry); (C) electrochemical performance of MLD-tincone (TDMASn-glycerol) as the anode in LIBs (reproduced from Zhu et al. (2020) with permission from The Royal Society of Chemistry); (D) crystal structure of Li-PDC, Li-TPA, Li-NDC, and LiBPDC, with their corresponding organic precursors, and redox reactions mechanisms for Li-TPA and LiZAO (reprinted with permission from Multia et al. (2020) Copyright 2020 American Chemical Society); (E) configuration of an all ALD/MLD-made Li₂Q/LiPON/Cu cell, and Li-ion storage mechanism of Li₂Q as the cathode (reproduced from Nisula and Karppinen (2018) with permission from The Royal Society of Chemistry); (F) Nyquist plot, Arrhenius plot, and AFM roughness of lithicone by MLD (reproduced from Kazyak et al. (2020) with permission from The Royal Society of Chemistry).

battery materials (Weimer, 2019). Besides application in transitional LIBs, ALD has been recently demonstrated for fabricating three-dimensional (3D) microbatteries (Pearse et al., 2017; Liu et al., 2018; Pearse et al., 2018). 3D microbatteries allow significantly increased surface area of active materials in the limited footprint as planar thin-film

batteries and thus provide high energy and power densities (Figure 1A). However, manufacturing 3D microbatteries has been challenging due to the strict requirements on the uniformity and pinhole-free deposition of the anode, solid electrolyte, and cathode layers on high-surface-area substrates (Oudenhoven et al., 2011; Roberts et al., 2011; Liu et al., 2020),

and only become possible with the advances in new ALD process development for these electrode and electrolyte materials. Therefore, it is vital to design and develop novel functional thin films with unique properties because it will provide numerous opportunities for enabling better battery technologies.

While ALD can only deposit inorganic materials, molecular layer deposition (MLD) has emerged as a thin film technique that resembles the benefits of ALD in controlling film thickness, uniformity, conformity, and crystallinity, but is able to deposit hybrid organic-inorganic materials, namely “metalcone” (George et al., 2009; Lee et al., 2013). This is achieved by incorporating an organic fragment in the thin films by pairing metal precursors with organic reactants (**Figure 1B**), instead of water as in ALD (**Figure 1A**), during the sequential and self-limiting deposition process. One MLD cycle consists of four steps. During the first step of the MLD process, metalorganic precursor (such as trimethylaluminum-TMA) is introduced into the chamber and react with all surface functional groups (e.g., hydroxyl group) through ligand exchange. In the second step, the excessive precursor and any byproducts are entirely removed by inert gas purging. In the third step, an organic precursor (e.g., ethylene glycol-EG) is pulsed into the chamber to react with metalorganic ligands to convert the surface back to hydroxyl groups. Once the reaction is complete, the residual organic precursor and byproducts are pumped out using gas purging.

The incorporation of organic fragments technically opens unlimited possibilities for engineering the structure of metalcone at the molecular level and tailoring their mechanical, electrical, optical, and electrochemical properties for energy storage and conversion systems (Sundberg and Karppinen, 2014; Meng, 2017). For example, MLD alucone has been applied as a flexible surface coating layer on the various anode (Si, SnO₂, Li/Na/Zn metals) and cathode in rechargeable Li, Na, and Zn batteries (Piper et al., 2014; Zhao et al., 2018a; He and Liu, 2020), and been found to outperform its ALD Al₂O₃ counterpart in stabilizing the electrode-electrolyte interfaces owing to the added benefits from the organic fragment. For example, alucone coating, deposited by using trimethylaluminum (TMA) and glycerol (GL) at 140°C, was found to improve the cycling stability, rate, and Coulombic efficiency of nano-Si composite electrodes (Piper et al., 2014). Alucone was proven to be robust and resilient to accommodate the large volume change of Si and maintain an intimate network for fast ionic and electron conduction (Ma et al., 2015; Son et al., 2017), while conventional metal oxides are not suitable for large-volume-change materials due to mechanical failure at high stresses. Therefore, as a surface coating on the anode, the MLD films should have good uniformity and coverage on the electrode, good Li-ion conductivity upon lithiation, and excellent toughness and flexibility to tolerate repeated stress. The properties of MLD alucone might be tuned by precisely adjusting the organic reactants during the deposition process (Lee et al., 2013). For Li metal anode, alucone coating (10–25 cycles) showed improved stripping and plating performance, stabilized polarization curves, lowered internal resistance, and prolonged lifetime, compared with Al₂O₃-protected or bare Li metal (Zhao et al., 2018a; Chen et al., 2018). The highly cross-

linked structure in alucone coating with good mechanical properties and flexibility could effectively suppress dendrite formation, maintain continuous solid electrolyte interphase (SEI), and reduce the reactions and penetration of electrolyte with Li metal. MLD-alucone has also been applied as surface coating on P2-type Na_{0.66}Mn_{0.9}Mg_{0.1}O₂ (NMM) cathode in Na-ion batteries, in comparison with Al₂O₃ coating and no coating. The alucone coated NMM cathode exhibited a 96% capacity retention, compared to pristine (75%) and Al₂O₃-coated (71%) NMM, after 100 cycles between 2 and 4.5 V at 1°C (Kaliyappan et al., 2020). Besides the mechanical robustness, the more electronically conductive nature of the alucone thin film than alumina was essential to improved rate capability and benefited from the carbon linkers in the alucone film. Therefore, different from the surface coating on the anode, MLD film coating on the cathode should primarily consider electronic conductivity and uniformity while emphasizing mechanical properties. Consequently, we believe that MLD provides a new opportunity to innovate novel thin-film materials to catalyze energy storage and conversion research.

Despite the great promise, hybrid organic-inorganic materials and their MLD surface chemistry and process are minimal, unlike the rich ALD material library. Many possible MLD materials remain unexplored, probably due to challenges associated with the selection of MLD precursors and the development of the MLD process. Excitedly, several proof-of-concept MLD materials as the battery components, i.e., anode, cathode, and solid electrolytes, have been reported and demonstrated recently. As such, this mini-review is intended to provide a timely summary of the recent progress in MLD surface chemistry and process development for hybrid organic-inorganic materials, their applications and potentials in rechargeable batteries, and the intuitions learned so far to guide future multifunctional thin film design by MLD.

NEW MLD THIN FILMS DEMONSTRATED AS ACTIVE BATTERY MATERIALS

Early metalcone materials, i.e., titanicone (Van De Kerckhove et al., 2016), vanadicone (Van De Kerckhove et al., 2017), developed by MLD were electrochemically inactive toward Li-ion storage as the deposited state and required post-annealing to convert the metalcone into metal oxide-based materials to present Li-ion storage performance. However, the harsh post-annealing process caused the damage of the thin film uniformity and usually led to the formation of island structures (Kazyak et al., 2017), making them unsuitable for fabricating 3D microbatteries. As shown in previous ALD works (Pearse et al., 2018), the thin films need to be electrochemically functional so that they can be directly applied to fabricate 3D microbatteries. To satisfy 3D microbattery requirements, the MLD thin films should process high electrochemical activity toward Li-ion storage or transport, have high uniformity and conformity on high-aspect-ratio substrates, and relatively straightforward deposition process and receipts.

TABLE 1 | Summary of MLD receipts, growth behaviors, and applications of metalcone films.

Battery component	MLD film	Metal precursor	Organic reactant	Deposition T (°C)	GPC (Å)	Post annealing	Application	References
Anode	Tincone	TDMASn	GL	100	2.5	No	LIBs	Zhu et al. (2020)
	Li ₂ TP (or Li-TPA)	Li(thd)	TPA	200–240	3.0	No	LIBs	Nisula and Karppinen. (2016)
	Li ₂ TP-NH ₂	Li(thd)	TPA-NH ₂	200	3.6	No	LIBs	Heiska et al. (2020)
	Li-NDC	Li(thd)	NDC	220	2.3	No	LIBs	Multia et al. (2020)
	Li-BPDC	Li(thd)	BPDC	240	7.0	No	LIBs	Multia et al. (2020)
	Li-PDC	Li(thd)	PDC	220	2.5	No	LIBs	Multia et al. (2020)
	Li-AZO	Li(thd)	ZAO	270	7.0	No	LIBs	Multia et al. (2020)
	Titanicone	TDMAT	GL	80–160	0.9–0.2	Yes	LIBs	Van De Kerckhove et al. (2016)
	Magnesiancone	Mg(MeCp) ₂	EG or GL	100–250	2–3	Yes	N/A	Kint et al. (2020)
	Ti-based maleic acid	TiCl ₄	MA	140–280	1.42–0.16	No	N/A	Cao et al. (2019)
Cathode	Vanadicone	TEMAV	GL	80–180	1.2–1.5	Yes	LIBs	Van De Kerckhove et al. (2017)
	Li ₂ Q	LiHMDS	HQ	160	-	No	LIBs	Nisula and Karppinen. (2018)
	Manganicone	Mn(EtCp) ₂	EG	160	1	Yes	N/A	Bergsman et al. (2019)
	Mn-based hybrid film	Mn(thd)	TPA	200	1–2	Yes	N/A	Ahvenniemi and Karppinen. (2016)
	Co-based hybrid film	Co.(acac) ₃ or Co.(thd) ₂	TPA	200	1–2	Yes	N/A	Ahvenniemi and Karppinen. (2016)
Solid electrolyte	Lithicone	LiO ^t Bu	EG	135	2.6	Yes	LIBs	Kazyak et al. (2020)
	LPDO	LiO ^t Bu	PD	150–200	0.15–0.23	No	N/A	Wang et al. (2020)

TDMASn, tetrakis (dimethylamino) tin (IV); GL, glycerol; Li₂TP, lithium terephthalate; thd, 2,2,6,6-tetramethyl-3,5-heptanedione; TPA, terephthalic acid; TPA-NH₂-2, aminoterephthalic acid; PDC, pyridinedicarboxylic acid; NDC-2,6-naphthalenedicarboxylic acid; BPDC, 4,4'-biphenydicarboxylic acid; ZAO, 4,4'-azobenzenedicarboxylic acid; LiO^tBu, Lithium tert-butoxide; EG, ethylene glycol; TDMAT, tetrakisdimethylaminotitanium; Mg(MeCp)₂, TEMAV, tetrakisethylmethylaminovanadium; LiHMDS, lithium bis(trimethylsilyl)amide; HQ, hydroquinone; LPDO, lithium propane dioxide; PD, propanediol; Mn(EtCp)₂, bis(ethylcyclopentadienyl)manganese; maleic acid, MA. N/A, This new MLD material is presumably for LIB applications but not demonstrated yet.

Alloying-type anode materials (e.g., Sn, Si) are known for their high specific capacities and their obvious drawback of large volume change during the lithiation/de-lithiation process (Lao et al., 2017). The volume expansion could cause structural pulverization and rapid capacity decay, limiting their practical applications (Obrovac and Chevrier, 2014). Liu and co-workers recently reported the use of tincone, at the deposited state by MLD, as a stable and high-capacity anode in LIBs (Zhu et al., 2020). Tincone was deposited at 150°C by MLD using tetrakis(dimethylamino)tin(IV) (TDMASn) and GL as the precursors and exhibited a self-limiting growth behavior with a high growth per cycle (GPC) of 2.5 Å. The tincone on nitrogen-doped carbon nanotubes (tincone/NCNTs) delivered a reversible capacity of 490 mAh g⁻¹ for 100 cycles and excellent rate capability of 432.7, 368.7, 301.0, 242.1, and 173.2 mAh g⁻¹, at 0.1, 0.2, 0.5, 1.0, and 2.0 A g⁻¹, respectively (Figure 1C), which outperformed both pristine N-CNTs and ALD-deposited SnO₂/CNTs (Zhu et al., 2019a; Zhu et al., 2019b). It was found that the Sn ions in the unique tincone structure provided high Li-ion storage capacity and acted as redox-active sites, while the surrounding organic species served as a flexible matrix to accommodate the volume change of Sn during the cycling. This work not only provides a stable MLD anode for fabricating 3D microbatteries, but also points out a new route to address the long-standing problems in alloying-type anodes by engineering the material structure at the molecular level (such as Si-based metalcone).

Recently, Karppinen and co-workers made encouraging progress on MLD surface chemistry and process development for Li-containing organic-inorganic thin films (Li-dicarboxylates), and demonstration of these novel materials as

the anode [Li-TPA (Nisula and Karppinen, 2016), Li-PDC, Li-NDC, Li-BPDC, and Li-ZAO (Multia et al., 2020)] and the cathode (Li₂Q) (Nisula and Karppinen, 2018) in LIBs. For the first time, they reported the MLD recipes for these Li-dicarboxylates, by using lithium bis(trimethylsilyl)amide (LiHMDS) as the Li precursor, in combination with five organic linkers, terephthalic acid (TPA), pyridinedicarboxylic acid (PDC), 2,6-naphthalenedicarboxylic acid (NDC), 4,4'-biphenydicarboxylic acid (BPDC), and 4,4'-azobenzenedicarboxylic acid (AZO) (Figure 1D). Due to the different organic precursors employed, Li-TPA, Li-PDC, Li-NDC, Li-BPDC, and Li-ZAO exhibited a GPC of 3.0, 2.5, 2.3, 7.0, and 7.0 Å, respectively, (Table 1). Moreover, these MLD processes yielded highly crystalline and air-stable thin films at low deposition temperatures of 220–240°C. Furthermore, galvanostatic cycling experiments verified the electrochemical activity of these novel films toward Li-ion storage. The redox reaction mechanisms for Li-TPA and LZO are shown in Figure 1D. This series of MLD Li-dicarboxylates is an excellent example of engineering MLD material structures by adjusting the organic precursors and thus tailoring their electrochemical behaviors toward LIB applications. This strategy might be extended to other hybrid organic-inorganic materials by MLD.

In addition to the anode, cathode materials with hybrid organic-inorganic structures have been synthesized by MLD. Dilithium-1,4benzenediolate (Li₂Q) was successfully deposited at 160°C by MLD using LiHMDS and hydroquinone (HQ) as the precursors (Nisula and Karppinen, 2018). Compared with the known organic electrode materials (p-benzoquinone), MLD achieved *in-situ* incorporation of Li into the as-deposited Li₂Q

film and therefore, can be directly used as the cathode in full cells due to its lithiated state. The authors further fabricated a solid-state $\text{Li}_2\text{Q}/\text{LiPON}/\text{Cu}$ cell using Pt as the current collector, ALD-LiPON as the solid electrolyte (30 nm), and Li_2Q as the cathode (5–42 nm) (**Figure 1E**). Cyclic voltammetry (CV) testing revealed a pair of redox peaks at 3.38 V (oxidation) and 2.57 V (reduction) at 0.2 mV s^{-1} . Due to thin electrode design, the solid-state cell exhibited ultrahigh rate capabilities and could reach 50% of the full capacity in less than 0.25 s, with energy and power densities of 108 mWh cm^{-3} and 508 W cm^{-3} , respectively. Furthermore, a proof-of-concept all-ALD/MLD-made organic battery was fabricated by using Li_2Q cathode, LiPON solid electrolyte, and Li-TPA anode (Nisula and Karppinen, 2018), demonstrating the feasibility of ALD and/or MLD in the design of 3D microbatteries.

Solid electrolyte thin films have been limited to inorganic materials (Sheil and Chang, 2020) until very recently, Dasgupta et al. reported Li-ion conducting “lithicone” by MLD (Kazyak et al., 2020). The lithicone was deposited at 135°C by sequentially introducing lithium tert-butoxide (LiO^tBu) and EG (**Figure 1F**). Both precursors were chosen due to their sufficiently high vapor pressure, thermal stability and demonstrated self-limiting surface reactions. Lithicone possessed a stoichiometry of $\text{Li}_{1.5}\text{C}_2\text{O}_{1.8}$, with a bonding environment distinct from that of lithium carbonate. Most importantly, electrochemical impedance spectroscopy (EIS) measurements showed that lithicone, upon post-annealing at 350°C , exhibited an ionic conductivity of $3.6 \times 10^{-8} \text{ S cm}^{-1}$ at 30°C with an activation energy of 0.6 eV (**Figure 1F**). Chronoamperometry test revealed an electronic conductivity of the film 5–6 orders-of-magnitude lower than the ionic conductivity, making the lithicone suitable as an interlayer or bulk solid electrolyte in thin-film batteries. Although solid polymer electrolytes have been known for many years, this is the first time that organic-containing electrolyte was made in a layer-by-layer fashion by MLD and showed measurable ionic conductivity.

The above recent works positively proved the possibility and versatility of using the MLD technique to fabricate multifunctional hybrid organic-inorganic anode, cathode, and solid electrolyte with targeted applications in rechargeable batteries. Overall, it can be found that the use of organic precursors during the MLD processes adds extra, and sometimes surprising, functionalities into these novel thin-film materials to address existing challenges and open new opportunities.

OTHER NEW MLD THIN FILMS PROMISING FOR RECHARGEABLE BATTERIES

In addition to the aforementioned materials, several new MLD thin films have been developed recently with the potential for battery applications. This group of new MLD thin films includes magnesicone (Kint et al., 2020), manganicone (Ahvenniemi and Karppinen, 2016), lithium propane dioxide (Wang et al., 2020), Ti-based maleic acid (Cao et al., 2019), and Mn- and Co-based hybrid films (Ahvenniemi and Karppinen, 2016). The MLD receipts and growth behaviors of these MLD films are

summarized in **Table 1**. It can be found that these new MLD materials show high similarity to other hybrid films that have been validated in LIBs in terms of MLD surface chemistry and film structure, and therefore deserve to be evaluated in electrochemical cells in the future.

There are three main approaches for thoroughly assessing the potential of these new MLD hybrid films in rechargeable batteries. Firstly, these hybrid films, with or without post-annealing, might be directly applied as the anode, cathode, or solid electrolyte in LIBs, taking advantage of the electrochemical activity of metal ions. Secondly, the hybrid films could also be employed as surface coating layers to address liquid-solid and solid-solid interface issues in conventional liquid-based LIBs, solid-state LIBs, and next-generation batteries (e.g., Na, K, and Zn-ion). This surface-engineering approach has been widely demonstrated using alucone, a mature MLD material, in a broad range of applications, such as Si anode (Piper et al., 2014), Li metal (Zhao et al., 2018a), Na metal (Zhao et al., 2017), Zn metal (He and Liu, 2020), Na cathode (Kaliyappan et al., 2020), and many others (Zhao et al., 2021). Compared to *in-situ* formed SEI, the MLD coating, as an artificial SEI on the electrode, become ion and electron conductive upon contact with charge carriers (e.g., Li-ion, Na-ion), possess better mechanical stability and interfacial structure integrity over repeated cycling, and prevent further side reactions between the electrode and electrolyte. Comprehensive experiment and simulation work has been performed to understand the structure change and role of ALD- Al_2O_3 coating in LIBs, but not for MLD-alucone coating yet. Theoretical analysis using density functional theory, *ab initio* molecular dynamics simulations, and Green's function theory found that the alucone film was composed of Al-O complexes, and Li atoms bonded to these O atoms during the lithiation (Ma et al., 2015). Once the alucone film was irreversibly saturated with Li atoms, it became electronically conductive. Thirdly, MLD hybrid films (e.g., zincone, magnesicone) have been converted to corresponding highly porous metal oxide materials (e.g., ZnO, MgO) by removing the organic backbones *via* post-annealing (Perrotta et al., 2019a; Perrotta et al., 2019b; Kint et al., 2020). These porous metal oxide structures might be used reactive barrier layers or porous substrates for Li-ion composite solid electrolytes.

SUMMARY AND PERSPECTIVES

Herein, we discussed the most recent progress in the MLD surface chemistry, process development, and applications of metalcone thin films as active materials in rechargeable LIBs. Several hybrid organic-inorganic anode, cathode, and solid electrolytes have been synthesized by MLD and demonstrated promising electrochemical properties toward Li-ion storage or transport. Moreover, these novel materials have been integrated into all-solid-state thin-film batteries by combining MLD with ALD. Therefore, MLD has shown its great potential in engineering multifunctional thin films for 3D microbattery applications. Nevertheless, challenges remain in MLD and its further applications in energy storage devices and necessitates further

research into expanding MLD material library, exploiting their use for surface/interface modification in batteries, and developing new precursors and surface chemistries for MLD processes.

Develop New MLD Metalcone Materials

Despite recent progress in new MLD development, the number of available metalcone materials is still very limited. Further research needs to significantly develop new MLD surface chemistry and process for other metalcone thin films. This could be done by either switching metal-organic precursors that have been validated in ALD and/or adjusting organic reactants to manipulate the film properties. For example, Li-containing organic-inorganic materials might be extended to Na- and K-containing ones by changing the Li precursors (LiO^tBu and LiHMDS) to their Na- and K-counterparts (Østreng et al., 2014).

Exploit MLD Metalcones in Broad Energy Storage and Conversion Devices

The possibility of controlling metalcone structure at the molecular level creates tremendous opportunities for various energy storage and conversion systems. Further research might focus on exploring the use of multifunctional metalcones for surface modification purposes in liquid- and solid-state LIBs and other next-generation batteries to improve interfacial stability. Moreover, the metalcones could also be used as supports and over-coating on catalysts to increase their durability and catalytic activities (Gould et al., 2014).

New MLD Precursors and Surface Chemistry

New metal precursors with high vapor pressure and reactivity are urgently needed to enable the development of more MLD metalcones. For example, although lithicone has been developed, the used Li precursors (LiO^tBu) are certainly not ideal for the MLD process because they have low vapor pressure and require high sublimation temperatures. This

challenge becomes even severe in Na and K precursors (Østreng et al., 2014). A further advance in MLD would be benefited from the design of new precursor chemistry to satisfy self-limiting and complete growth reactions.

Overcome Shortcomings of MLD for Practical Applications

Many MLD thin films tend to be unstable in contact with water and oxygen and might experience immediate changes in the surface structure upon exposure to the ambient environment (Liang et al., 2009; Van De Kerckhove et al., 2018). It remains unknown how this surface change affects the properties of MLD coating on the electrode. The scalability of MLD is yet to be demonstrated using fluidized-bed or roll-to-roll equipment. In particular, the organic precursor is more “sticky” than water during the low-temperature deposition process and likely to require more purging time to remove physically absorbed precursors. There is little knowledge in scalable MLD and potential issues, which deserve further investigation.

AUTHOR CONTRIBUTIONS

JL and JW conceived the idea. JL wrote the manuscript, and JW revised it. All authors discussed the topics and contributed to the organization of this paper.

FUNDING

This work was supported by the Nature Sciences and Engineering Research Council of Canada (NSERC), Canada Foundation for Innovation (CFI), BC Knowledge Development Fund (BCKDF), and the University of British Columbia (UBC). JW's work was supported by the start-up fund and “Young Scientist Studio” of Harbin Institute of Technology, National Natural Science Foundation of China (No. U1932205, No. 22075063), Natural Science Funds of Heilongjiang Province (No. ZD2019B001).

REFERENCES

- Ahvenniemi, E., and Karppinen, M. (2016). ALD/MLD Processes for Mn and Co Based Hybrid Thin Films. *Dalton Trans.* 45 (26), 10730–10735. doi:10.1039/c6dt00851h
- Banerjee, A., Wang, X., Fang, C., Wu, E. A., and Meng, Y. S. (2020). Interfaces and Interphases in All-Solid-State Batteries with Inorganic Solid Electrolytes. *Chem. Rev.* 120 (14), 6878–6933. doi:10.1021/acs.chemrev.0c00101
- Bergsman, D. S., Baker, J. G., Closser, R. G., Macisaac, C., Lillethorup, M., Strickler, A. L., et al. (2019). Structurally Stable Manganese Alkoxide Films Grown by Hybrid Molecular Layer Deposition for Electrochemical Applications. *Adv. Funct. Mater.* 29 (43), 1904129. doi:10.1002/adfm.201904129
- Cao, Y.-Q., Zhang, W., Xu, L., Liu, C., Zhu, L., Wang, L.-G., et al. (2019). Growth Mechanism, Ambient Stability, and Charge Trapping Ability of Ti-Based Maleic Acid Hybrid Films by Molecular Layer Deposition. *Langmuir* 35 (8), 3020–3030. doi:10.1021/acs.langmuir.8b04137
- Chen, L., Huang, Z., Shahbazian-Yassar, R., Libera, J. A., Klavetter, K. C., Zavadil, K. R., et al. (2018). Directly Formed Alucone on Lithium Metal for High-Performance Li Batteries and Li-S Batteries with High Sulfur Mass Loading. *ACS Appl. Mater. Inter.* 10 (8), 7043–7051. doi:10.1021/acsami.7b15879
- Chen, Z., Qin, Y., Amine, K., and Sun, Y.-K. (2010). Role of Surface Coating on Cathode Materials for Lithium-Ion Batteries. *J. Mater. Chem.* 20 (36), 7606. doi:10.1039/c0jm00154f
- George, S. M., Yoon, B., and Dameron, A. A. (2009). Surface Chemistry for Molecular Layer Deposition of Organic and Hybrid Organic–Inorganic Polymers. *Acc. Chem. Res.* 42 (4), 498–508. doi:10.1021/ar800105q
- Gould, T. D., Izar, A., Weimer, A. W., Falconer, J. L., and Medlin, J. W. (2014). Stabilizing Ni Catalysts by Molecular Layer Deposition for Harsh, Dry Reforming Conditions. *ACS Catal.* 4 (8), 2714–2717. doi:10.1021/cs500809w
- He, H., and Liu, J. (2020). Suppressing Zn Dendrite Growth by Molecular Layer Deposition to Enable Long-Life and Deeply Rechargeable Aqueous Zn Anodes. *J. Mater. Chem. A* 8 (42), 22100–22110. doi:10.1039/d0ta07232j
- Heiska, J., Nisula, M., Rautama, E.-L., Karttunen, A. J., and Karppinen, M. (2020). Atomic/molecular Layer Deposition and Electrochemical Performance of Dilithium 2-aminoterephthalate. *Dalton Trans.* 49 (5), 1591–1599. doi:10.1039/c9dt04572d

- Kaliyappan, K., Or, T., Deng, Y. P., Hu, Y., Bai, Z., and Chen, Z. (2020). Constructing Safe and Durable High-Voltage P2 Layered Cathodes for Sodium Ion Batteries Enabled by Molecular Layer Deposition of Alucone. *Adv. Funct. Mater.* 30 (17), 1910251. doi:10.1002/adfm.201910251
- Kazyak, E., Chen, K.-H., Wood, K. N., Davis, A. L., Thompson, T., Bielinski, A. R., et al. (2017). Atomic Layer Deposition of the Solid Electrolyte Garnet Li₇La₃Zr₂O₁₂. *Chem. Mater.* 29 (8), 3785–3792. doi:10.1021/acs.chemmater.7b00944
- Kazyak, E., Shin, M., Lepage, W. S., Cho, T. H., and Dasgupta, N. P. (2020). Molecular Layer Deposition of Li-Ion Conducting “Lithicone” Solid Electrolytes. *Chem. Commun.* 56 (99), 15537–15540. doi:10.1039/d0cc06077a
- Kint, J., Mattelaer, F., Vandenbroucke, S. S. T., Muriqi, A., Minjauw, M. M., Nisula, M., et al. (2020). Molecular Layer Deposition of “Magnesicone”, a Magnesium-Based Hybrid Material. *Chem. Mater.* 32 (11), 4451–4466. doi:10.1021/acs.chemmater.9b05116
- Knoops, H. C. M., Donders, M. E., Van De Sanden, M. C. M., Notten, P. H. L., and Kessels, W. M. M. (2012). Atomic Layer Deposition for Nanostructured Li-Ion Batteries. *J. Vacuum Sci. Tech. A: Vacuum, Surf. Films* 30 (1), 010801. doi:10.1116/1.3660699
- Lao, M., Zhang, Y., Luo, W., Yan, Q., Sun, W., and Dou, S. X. (2017). Alloy-based Anode Materials toward Advanced Sodium-Ion Batteries. *Adv. Mater.* 29 (48), 1700622. doi:10.1002/adma.201700622
- Lee, B. H., Yoon, B., Abdulagatov, A. I., Hall, R. A., and George, S. M. (2013). Growth and Properties of Hybrid Organic-Inorganic Metalcone Films Using Molecular Layer Deposition Techniques. *Adv. Funct. Mater.* 23 (5), 532–546. doi:10.1002/adfm.201200370
- Liang, X., Yu, M., Li, J., Jiang, Y.-B., and Weimer, A. W. (2009). Ultra-thin Microporous-Mesoporous Metal Oxide Films Prepared by Molecular Layer Deposition (MLD). *Chem. Commun.* 14 (46), 7140. doi:10.1039/b911888h
- Liu, H., Zhang, G., Zheng, X., Chen, F., and Duan, H. (2020). Emerging Miniaturized Energy Storage Devices for Microsystem Applications: from Design to Integration. *Int. J. Extrem. Manuf.* 2 (4), 042001. doi:10.1088/2631-7990/abba12
- Liu, J., Zhu, H., and Shiraz, M. H. A. (2018). Toward 3D Solid-State Batteries via Atomic Layer Deposition Approach. *Front. Energ. Res.* 6. doi:10.3389/fenrg.2018.00010
- Lotfabad, E. M., Kalisvaart, P., Kohandehghan, A., Cui, K., Kupsta, M., Farbod, B., et al. (2014). Si Nanotubes ALD Coated with TiO₂, TiN or Al₂O₃ as High Performance Lithium Ion Battery Anodes. *J. Mater. Chem. A* 2 (8), 2504–2516. doi:10.1039/c3ta14302c
- Ma, Y., Martinez De La Hoz, J. M., Angarita, I., Berrio-Sanchez, J. M., Benitez, L., Seminario, J. M., et al. (2015). Structure and Reactivity of Alucone-Coated Films on Si and Li_x Si_y Surfaces. *ACS Appl. Mater. Inter.* 7 (22), 11948–11955. doi:10.1021/acsami.5b01917
- Meng, X. (2017). An Overview of Molecular Layer Deposition for Organic and Organic-Inorganic Hybrid Materials: Mechanisms, Growth Characteristics, and Promising Applications. *J. Mater. Chem. A* 5 (35), 18326–18378. doi:10.1039/c7ta04449f
- Multia, J., Heiska, J., Khayyami, A., and Karppinen, M. (2020). Electrochemically Active *In Situ* Crystalline Lithium-Organic Thin Films by ALD/MLD. *ACS Appl. Mater. Inter.* 12 (37), 41557–41566. doi:10.1021/acsami.0c11822
- Nisula, M., and Karppinen, M. (2016). Atomic/Molecular Layer Deposition of Lithium Terephthalate Thin Films as High Rate Capability Li-Ion Battery Anodes. *Nano Lett.* 16 (2), 1276–1281. doi:10.1021/acs.nanolett.5b04604
- Nisula, M., and Karppinen, M. (2018). *In Situ* lithiated Quinone Cathode for ALD/MLD-fabricated High-Power Thin-Film Battery. *J. Mater. Chem. A* 6 (16), 7027–7033. doi:10.1039/c8ta00804c
- Obrovac, M. N., and Chevrier, V. L. (2014). Alloy Negative Electrodes for Li-Ion Batteries. *Chem. Rev.* 114 (23), 11444–11502. doi:10.1021/cr500207g
- Østreg, E., Sønsteby, H. H., Øien, S., Nilsen, O., and Fjellvåg, H. (2014). Atomic Layer Deposition of Sodium and Potassium Oxides: Evaluation of Precursors and Deposition of Thin Films. *Dalton Trans.* 43 (44), 16666–16672. doi:10.1039/c4dt01930j
- Oudenhoven, J. F. M., Baggetto, L., and Notten, P. H. L. (2011). All-Solid-State Lithium-Ion Microbatteries: A Review of Various Three-Dimensional Concepts. *Adv. Energ. Mater.* 1 (1), 10–33. doi:10.1002/aenm.201000002
- Pearse, A. J., Schmitt, T. E., Fuller, E. J., El-Gabaly, F., Lin, C.-F., Gerasopoulos, K., et al. (2017). Nanoscale Solid State Batteries Enabled by Thermal Atomic Layer Deposition of a Lithium Polyphosphazene Solid State Electrolyte. *Chem. Mater.* 29 (8), 3740–3753. doi:10.1021/acs.chemmater.7b00805
- Pearse, A., Schmitt, T., Sahadeo, E., Stewart, D. M., Kozen, A., Gerasopoulos, K., et al. (2018). Three-Dimensional Solid-State Lithium-Ion Batteries Fabricated by Conformal Vapor-phase Chemistry. *ACS Nano* 12 (5), 4286–4294. doi:10.1021/acsnano.7b08751
- Perrotta, A., Berger, R., Muralter, F., and Coclite, A. M. (2019a). Mesoporous ZnO Thin Films Obtained from Molecular Layer Deposited “Zincones”. *Dalton Trans.* 48 (37), 14178–14188. doi:10.1039/c9dt02824b
- Perrotta, A., Pilz, J., Pachmajer, S., Milella, A., and Coclite, A. M. (2019b). On the Transformation of “Zincones”-like into Porous ZnO Thin Films from Sub-saturated Plasma Enhanced Atomic Layer Deposition. *Beilstein J. Nanotechnol.* 10, 746–759. doi:10.3762/bjnano.10.74
- Piper, D. M., Travis, J. J., Young, M., Son, S.-B., Kim, S. C., Oh, K. H., et al. (2014). Reversible High-Capacity Si Nanocomposite Anodes for Lithium-Ion Batteries Enabled by Molecular Layer Deposition. *Adv. Mater.* 26 (10), 1596–1601. doi:10.1002/adma.201304714
- Roberts, M., Johns, P., Owen, J., Brandell, D., Edstrom, K., El Enany, G., et al. (2011). 3D Lithium Ion Batteries-From Fundamentals to Fabrication. *J. Mater. Chem.* 21 (27), 9876. doi:10.1039/c0jm04396f
- Rowden, B., and Garcia-Araez, N. (2020). A Review of Gas Evolution in Lithium Ion Batteries. *Energ. Rep.* 6, 10–18. doi:10.1016/j.egy.2020.02.022
- Scott, I. D., Jung, Y. S., Cavanagh, A. S., Yan, Y., Dillon, A. C., George, S. M., et al. (2011). Ultrathin Coatings on Nano-LiCoO₂ for Li-Ion Vehicular Applications. *Nano Lett.* 11 (2), 414–418. doi:10.1021/nl1030198
- Sheil, R., and Chang, J. P. (2020). Synthesis and Integration of Thin Film Solid State Electrolytes for 3D Li-Ion Microbatteries. *J. Vacuum Sci. Tech. A* 38 (3), 032411. doi:10.1116/1.5142859
- Son, S.-B., Wang, Y., Xu, J., Li, X., Groner, M., Stokes, A., et al. (2017). Systematic Investigation of the Alucone-Coating Enhancement on Silicon Anodes. *ACS Appl. Mater. Inter.* 9 (46), 40143–40150. doi:10.1021/acsami.7b08960
- Sundberg, P., and Karppinen, M. (2014). Organic and Inorganic-Organic Thin Film Structures by Molecular Layer Deposition: A Review. *Beilstein J. Nanotechnol.* 5, 1104–1136. doi:10.3762/bjnano.5.123
- Van De Kerckhove, K., Barr, M. K. S., Santinacci, L., Vereecken, P. M., Dendooven, J., and Detavernier, C. (2018). The Transformation Behaviour of “Alucones”, Deposited by Molecular Layer Deposition, in Nanoporous Al₂O₃ Layers. *Dalton Trans.* 47 (16), 5860–5870. doi:10.1039/c8dt00723c
- Van De Kerckhove, K., Mattelaer, F., Deduytsche, D., Vereecken, P. M., Dendooven, J., and Detavernier, C. (2016). Molecular Layer Deposition of “titanicone”, a Titanium-Based Hybrid Material, as an Electrode for Lithium-Ion Batteries. *Dalton Trans.* 45 (3), 1176–1184. doi:10.1039/c5dt03840e
- Van De Kerckhove, K., Mattelaer, F., Dendooven, J., and Detavernier, C. (2017). Molecular Layer Deposition of “vanadicone”, a Vanadium-Based Hybrid Material, as an Electrode for Lithium-Ion Batteries. *Dalton Trans.* 46 (14), 4542–4553. doi:10.1039/c7dt00374a
- Wang, H., Gregorczyk, K. E., Lee, S. B., Rubloff, G. W., and Lin, C.-F. (2020). Li-Containing Organic Thin Film-Structure of Lithium Propane Dioxide via Molecular Layer Deposition. *J. Phys. Chem. C* 124 (12), 6830–6837. doi:10.1021/acs.jpcc.9b11868
- Weimer, A. W. (2019). Particle Atomic Layer Deposition. *J. Nanopart. Res.* 21 (1). doi:10.1007/s11051-018-4442-9
- Xiao, X., Lu, P., and Ahn, D. (2011). Ultrathin Multifunctional Oxide Coatings for Lithium Ion Batteries. *Adv. Mater.* 23 (34), 3911–3915. doi:10.1002/adma.201101915
- Xu, L., Tang, S., Cheng, Y., Wang, K., Liang, J., Liu, C., et al. (2018). Interfaces in Solid-State Lithium Batteries. *Joule* 2 (10), 1991–2015. doi:10.1016/j.joule.2018.07.009
- Yan, P., Zheng, J., Liu, J., Wang, B., Cheng, X., Zhang, Y., et al. (2018). Tailoring Grain Boundary Structures and Chemistry of Ni-Rich Layered Cathodes for Enhanced Cycle Stability of Lithium-Ion Batteries. *Nat. Energ.* 3 (7), 600–605. doi:10.1038/s41560-018-0191-3
- Zhao, Y., Goncharova, L. V., Sun, Q., Li, X., Lushington, A., Wang, B., et al. (2018a). Robust Metallic Lithium Anode Protection by the Molecular-Layer-Deposition Technique. *Small Methods* 2 (5), 1700417. doi:10.1002/smt.201700417
- Zhao, Y., Goncharova, L. V., Zhang, Q., Kaghazchi, P., Sun, Q., Lushington, A., et al. (2017). Inorganic-Organic Coating via Molecular Layer Deposition

- Enables Long Life Sodium Metal Anode. *Nano Lett.* 17 (9), 5653–5659. doi:10.1021/acs.nanolett.7b02464
- Zhao, Y., Zhang, L., Liu, J., Adair, K., Zhao, F., Sun, Y., et al. (2021). Atomic/molecular Layer Deposition for Energy Storage and Conversion. *Chem. Soc. Rev.* 50, 3889–3956. doi:10.1039/d0cs00156b
- Zhao, Y., Zheng, K., and Sun, X. (2018b). Addressing Interfacial Issues in Liquid-Based and Solid-State Batteries by Atomic and Molecular Layer Deposition. *Joule* 2 (12), 2583–2604. doi:10.1016/j.joule.2018.11.012
- Zhu, H., Aboonassr Shiraz, M. H., Yao, L., Adair, K., Wang, Z., Tong, H., et al. (2020). Molecular-layer-deposited Tincone: a New Hybrid Organic-Inorganic Anode Material for Three-Dimensional Microbatteries. *Chem. Commun.* 56 (86), 13221–13224. doi:10.1039/d0cc03869e
- Zhu, S., Liu, J., and Sun, J. (2019a). Growth of Ultrathin SnO₂ on Carbon Nanotubes by Atomic Layer Deposition and Their Application in Lithium Ion Battery Anodes. *Appl. Surf. Sci.* 484, 600–609. doi:10.1016/j.apsusc.2019.04.163
- Zhu, S., Liu, J., and Sun, J. (2019b). Precise Growth of Al₂O₃/SnO₂/CNTs Composites by a Two-step Atomic Layer Deposition and Their Application as an Improved Anode for Lithium Ion Batteries. *Electrochimica Acta* 319, 490–498. doi:10.1016/j.electacta.2019.07.027
- Conflict of Interest:** The authors declare that the research was conducted in the absence of any commercial or financial relationships that could be construed as a potential conflict of interest.

Copyright © 2021 Liu and Wang. This is an open-access article distributed under the terms of the Creative Commons Attribution License (CC BY). The use, distribution or reproduction in other forums is permitted, provided the original author(s) and the copyright owner(s) are credited and that the original publication in this journal is cited, in accordance with accepted academic practice. No use, distribution or reproduction is permitted which does not comply with these terms.



Exploring the Thermodynamic Limits of Enhanced H₂ Recovery With Inherent Carbon Removal From Low Value Aqueous Biomass Oxygenate Precursors

Prince Ochonma¹, Claire Blaudeau², Rosalie Krasnoff³ and Greeshma Gadikota^{1,2*}

¹Robert Frederick Smith School of Chemical and Biomolecular Engineering, Cornell University, Ithaca, NY, United States, ²School of Civil and Environmental Engineering, Cornell University, Ithaca, NY, United States, ³Department of Earth and Environmental Engineering, Columbia University, New York, NY, United States

OPEN ACCESS

Edited by:

Andreas Borgschulte,
Swiss Federal Laboratories for
Materials Science and Technology,
Switzerland

Reviewed by:

Federico Rossi,
University of Siena, Italy
Zaki Yamani Zakaria,
University of Technology Malaysia,
Malaysia

*Correspondence:

Greeshma Gadikota
gg464@cornell.edu

Specialty section:

This article was submitted to
Bioenergy and Biofuels,
a section of the journal
Frontiers in Energy Research

Received: 16 July 2021

Accepted: 30 August 2021

Published: 29 September 2021

Citation:

Ochonma P, Blaudeau C, Krasnoff R
and Gadikota G (2021) Exploring the
Thermodynamic Limits of Enhanced
H₂ Recovery With Inherent Carbon
Removal From Low Value Aqueous
Biomass Oxygenate Precursors.
Front. Energy Res. 9:742323.
doi: 10.3389/fenrg.2021.742323

Rational integration of chemical pathways at the molecular scale to direct thermodynamically favorable enhanced H₂ production with inherent carbon removal from low-value substrates can be guided by exploring the thermodynamic limits of feasibility. The substrates of interest are biomass oxygenates that are water-soluble and uneconomical for separation from water. In this study, we investigate the thermodynamic feasibility of recovering H₂ with inherent carbon removal from biomass oxygenates such as ethanol, methanol, glycerol, ethylene glycol, acetone, and acetic acid. The influence of biomass oxygenate-to-water ratios, reaction temperature of 150°C–325°C, and CaO or Ca(OH)₂ as the alkalinity source on the yields of H₂, CH₄, CO₂, and Ca-carbonate are investigated. By maintaining the fluids in the aqueous phase under pressure, energy needs associated with vaporization are circumvented. The hypothesis that enhanced alkalinity favors the preferential formation of CO (precursor for CO₂ formation) over CH₄ and aids the formation of calcium carbonate is investigated. The findings from these studies inform the feasibility, design of experiments, and the tuning of reaction conditions for enhanced H₂ recovery with inherent carbon removal from biomass oxygenate sources.

Keywords: hydrogen, carbon removal, biomass oxygenates, calcium carbonate, thermodynamics

INTRODUCTION

Decarbonizing energy carriers such as H₂ while upcycling abundant low value resources is crucial for a sustainable energy, environmental, and climate future. This approach addresses our societal mission of lifting millions of people out of energy poverty globally (WHO, 2009) while limiting detrimental environmental impacts including the rise of global temperatures (Masson-Delmotte

Abbreviations: ΔH_{298}^0 , standard heat of reaction at 298 K; G_i^0 , Gibbs free energy of species i at its standard state; T , temperature; R , universal gas constant; $z_i P$, partial pressure of species i in the gas phase; n_i , number of moles of species i ; α_{ik} , number of atoms of k th component present in each molecules of species i ; b_k , total number of atomic masses of k th component in the system; BO_{in} , amount of biomass oxygenates fed into the system; BO_{out} , amount of biomass oxygenates unconverted; SR, H₂/BO stoichiometric ratio.

TABLE 1 | Concentration of methanol, ethanol, glycerol, ethylene glycol, acetone, and acetic acid in waste streams.

Biomass oxygenate of interest	Waste source	Concentration in mg/L	References
Methanol	Wastewater algae	0.022–0.5	Mincer and Aicher (2016)
	Industrial wastewater	1,000	Novak et al. (1985)
	Municipal wastewater	0.145–0.203	Kim et al. (2018)
Ethanol	Wastewater algae	30–530	Ellis et al. (2012)
	Industrial wastewater	18,500–49,400	Abanoz et al. (2012)
	Municipal wastewater	235–245	Ajao et al. (2019)
	Food waste	58,000	Uçkun Kiran and Liu (2015)
		84,850–89,890	Yan et al. (2012)
Glycerol	Municipal wastewater	400–420	Ajao et al. (2019)
	Industrial wastewater (bio-diesel)	75,680–202,312	Thompson and He (2006)
Ethylene Glycol	Industrial wastewater	30–1,050	Qi et al. (2020)
Acetone	Wastewater algae	450–1,430	Ellis et al. (2012)
Acetic acid	Municipal wastewater	1884–2,520	Badawi et al. (1992)
	Food waste	12,810–25,880	Li et al. (2015)

et al., 2018). Currently, more than 85% of H₂ is produced *via* steam methane reforming (SMR) and the water gas shift reaction (WGSR) as represented by the following reactions: CH₄ + H₂O → CO + 3H₂ (SMR) and CO + H₂O → CO₂ + H₂ (WGSR). Producing H₂ from renewable natural gas (e.g., biogas) and removing CO₂ is one approach to produce decarbonized fuels (Gadikota, 2020, 2021).

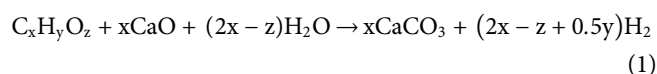
Conventional approaches to capture CO₂ using adsorption, (Sayari et al., 2011) absorption, (Rochelle, 2009), and membrane separations (Khalilpour et al., 2015) are being realized at the commercial scale. Once CO₂ is captured, it is compressed and stored in geologic formations (Benson and Surles, 2006). However, the availability of appropriate reservoirs for geologic storage of CO₂ is essential. In places that do not have access to appropriate geologic formations, alternative technologies are needed for storing CO₂ as inorganic carbonates. Further, energy carriers such as H₂ can be produced from distributed bio-based feedstocks with inherent carbon removal.

Significant advancements have been made in harnessing hydrogen from bio-based sources. Technologies to harness H₂ from gaseous and solid biomass-based feedstocks include steam reforming (SR) in which light hydrocarbons are reacted with steam to produce H₂ and CO₂, usually in the presence of a catalyst (Ross, 1984; Ming et al., 2002), partial oxidation in which biomass is partial combusted with limited amount of O₂ to produce synthetic gas (a mixture of CO and H₂) (Dissanayake et al., 1991; Hohn and Schmidt, 2001), and autothermal reforming (ATR) in which biomass is mixed with steam, and a limited amount of O₂ to produce synthetic gas and CO₂ (Dissanayake et al., 1991; Joensen and Rostrup-Nielsen, 2002; Deluga et al., 2004). Alkaline hydrothermal treatment (ATT) of wet biomass has been extensively reported to enhance H₂ generation from wet biomass with inherent CO₂ capture to produce inorganic carbonates (Stonor et al., 2017a; Zhang et al., 2020). However, few approaches have addressed strategies to harness H₂ from aqueous biomass oxygenate streams.

Biomass oxygenates soluble in water are important because they can be readily obtained from low value biomass feedstocks

such as food or municipal waste generated in urban or rural environments, algal sources, and industrial wastewater polluted streams as shown in **Table 1**. These feedstocks are also available in large quantities. For example, more than 40% of the food produced in the United States, and 44 million m³/day of wastewater generated in India, eventually returns to the environment as waste (Ranade and Bhandari, 2014; NRDC, 2021). Novel conversion pathways that can be easily adapted to accommodate a wide range of aqueous feedstocks are required, given the increasing scientific viability of producing simpler biomass oxygenates from waste streams, (Badawi et al., 1992; Thompson and He, 2006; Abanoz et al., 2012; Ellis et al., 2012; Yan et al., 2012; Li et al., 2015; Uçkun Kiran and Liu, 2015; Mincer and Aicher, 2016; Kim et al., 2018; Ajao et al., 2019; Qi et al., 2020; Arora et al., 2021) and from the chemical deconstruction of biomass (Brandt et al., 2013).

One such approach is aqueous phase reforming (APR) in which bio-derived aqueous feedstocks can be converted to H₂ in a pressurized environment. (Shabaker et al., 2003; Wen et al., 2008; Cortright et al., 2010). Compared to the other energy conversion approaches, APR occurs at 200–250°C which is significantly lower than temperatures >500°C for other biomass conversion approaches. The water gas shift reaction (WGSR) is integral to APR and catalysts are harnessed to direct the conversion of biomass oxygenates into H₂. APR reactions are represented as follows: C_nH_{2y}O_n + nH₂O → nCO₂ + (y + n)H₂ (Davda et al., 2005). The approach of maintaining water in the aqueous phase as opposed to in the gas phase enables the scientific possibility of integrating with carbon mineralization reaction to remove CO₂ with H₂ recovery from biomass oxygenates (see **Figure 1**). The reaction representing H₂ recovery with inherent carbon removal is shown as follows:



The standard heats of reaction (ΔH_{298}^0) for methanol, ethanol, glycerol, ethylene glycol, acetone, and acetic acid are exothermic as shown in **Table 2**.

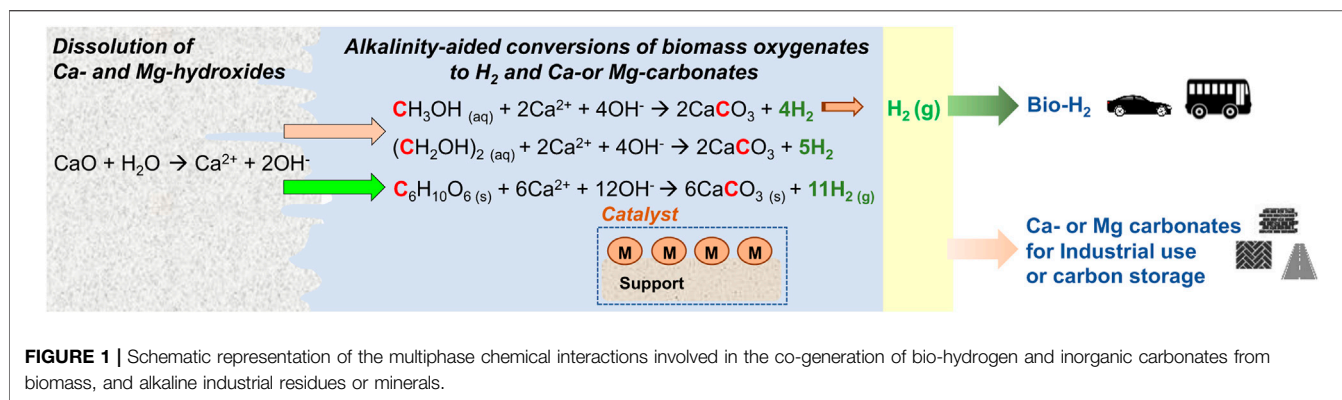


TABLE 2 | Standard heats of reaction (kJ/mol) for H₂ recovery from aqueous biomass oxygenates with inherent carbon removal: $\text{C}_x\text{H}_y\text{O}_z(\text{l}) + x\text{CaO}_{(\text{s})} + (2x - z)\text{H}_2\text{O}_{(\text{l})} \rightarrow x\text{CaCO}_{3(\text{s})} + (2x - z + 0.5y)\text{H}_{2(\text{g})}$. Heat of formations for reacting and product species was obtained from (Williams, 1996).

Biomass oxygenate	Standard heats of reaction (kJ/mol)	Heat of reaction at 500 K (227°C) (kJ/mol)
Methanol	-47.7	-65.6
Ethanol	-10.4	-63.3
Glycerol	-191.1	-254.7
Ethylene glycol	-113.8	-153.0
Acetone	-40.7	-134.0
Acetic acid	-89.5	-128.1

Despite the simplicity of this stoichiometric representation, this reaction pathways are complex and involve several multiphase chemical interactions including: (i) cleavage of biomass oxygenate molecules, (ii) competitive formation of CO versus CH₄, and (iii) conversion of CO to CO₂ followed by the subsequent dissolution of CO₂ to produce inorganic carbonates. These reactions are sensitive to temperature, pH, and solid and water compositions (in addition to catalyst compositions and uses). Further the anomalous solubility of calcium carbonate which decreases with increase in temperature and the dissolution behavior of the alkaline sources (e.g., Ca- or Mg-rich residues and minerals) in these multiphase chemical environments needs to be considered. The thermodynamic basis for these experimental investigations needs to be developed prior to demonstrating experimental feasibility. Therefore, the aim of this study is to develop the thermodynamic limits for enhanced H₂ recovery with inherent carbon removal from aqueous biomass oxygenates and alkaline sources such as calcium oxide (CaO). CaO is abundant in ash, slags, and kiln dusts recovered from industrial processes (Gadikota et al., 2015). The biomass oxygenates of interest are methanol (CH₃OH), ethanol (C₂H₅OH), glycerol [C₃H₅(OH)₃], ethylene glycol [C₂H₄(OH)₂], acetone (CH₃COCH₃), and acetic acid (CH₃COOH), because these oxygenates have been frequently used as model compounds, during aqueous phase reforming at low temperatures (< 500°C) (Davda et al., 2005; Cortright et al., 2010; Coronado et al., 2016; NRDC, 2021). Also, these oxygenates are readily available in low value aqueous streams such as wastewater from biomass processing as shown in Table 1.

Prior studies focused on enhanced H₂ conversion from biomass feedstocks at high temperature and low pressure conditions in which steam is the dominant reacting phase as opposed to water. Temperatures in the range of 427°C–627°C and steam-to-biomass ratios greater than five resulted in highly selective H₂ production over CH₄ formation. However, this approach is accompanied by significant evolution of CO₂ and CO in the product stream (Cohce et al., 2010). H₂ with purity of 99.97% or higher is needed for fuel cell applications. Even low concentrations of CO to the order of 100 ppm can inhibit the use of fuel cells (Baschuk and Li, 2001; U.S. Department of Energy et al., 2016).

Thermodynamic analyses of methanol reforming found that temperatures of 246°C and steam-to-methanol ratio of 5.6 resulted in a maximized H₂ yield of 4.28% with methanation CH₄ and 99.7% without methanation reactions. Further, CO product formation at atmospheric pressure was minimized (Özcan and Akin, 2019). Coupling these reactions with CO₂ capture can ensure high purity H₂ yields for use in fuel cell applications. To investigate the influence of inherent CO₂ capture during H₂ recovery from biomass oxygenates, sorption-enhanced steam methane reforming was investigated. Equilibrium H₂ concentrations of over 97% were observed for reforming with water-to-oxygenate ratio of 6, 9, 4, and 12 for ethanol, glycerol, methanol, and n-butanol respectively, in the presence of CaO at 500°C, and at an elevated pressure of 5 bar (Lima Da Silva and Müller, 2011).

Furthermore, experimental studies building on similar conditions have reported better H₂ yields using catalysts that suppress CH₄ formation and favor more H₂ production. For example, H₂ yield of 63% was noted using 10 wt% aqueous glycerol in the presence of CaO and Pt-Ni catalyst at 230°C and initial N₂ pressure of 30 bar (He et al., 2015). Maintaining the fluid in the aqueous phase favors accelerated carbon mineralization *via* enhanced dissolution and carbonate formation. Extensive studies reported the use of appropriate catalysts for aqueous phase reforming (Davda et al., 2005; Luo et al., 2008; Menezes et al., 2011; De Vlieger et al., 2012; Roy et al., 2012). Catalysts that preferentially direct the formation of CO over CH₄ in aqueous phase reforming were reported. However, comprehensive analyses exploring the thermodynamic limits of enhanced H₂ recovery with CO₂ capture from biomass

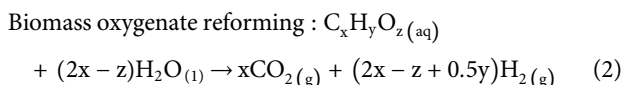
oxygenates and the corresponding physico-chemical parameters have not been reported in prior literature. This information is essential for developing the rational basis for enhanced H₂ recovery from biomass oxygenates with inherent carbon removal while maintaining the fluid in the aqueous phase.

In this study, the compositions of H₂, CO, CO₂, and CH₄ in the gas phase are determined as a function of temperature, water-to-oxygenate ratios, and CaO compositions for various biomass oxygenates such as ethanol, methanol, glycerol, ethylene glycol, acetic acid, and acetone. Specifically, the enhancement in H₂ yield due to inherent carbon removal via calcium carbonate formation is the focus of these investigations. These studies provide the basis for experimental studies for probing enhanced H₂ yield from biomass oxygenates with inherent carbonate formation.

METHODS

Reactions Involved in Enhanced H₂ Recovery With Inherent Carbon Removal From Aqueous Biomass Oxygenates

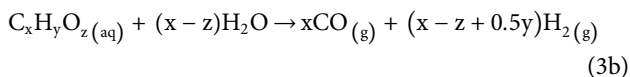
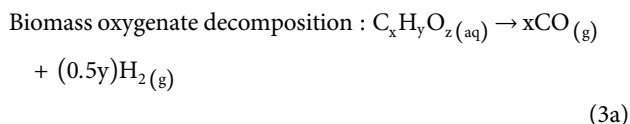
Several reactions and intermediate steps are involved in the recovery of H₂ from biomass oxygenates with the inherent removal of CO₂. These reactions are incorporated into the models for exploring thermodynamic limits for enhanced H₂ recovery with carbon removal via mineralization. Reaction 2 represents the deconstruction of biomass oxygenates to produce CO₂ and H₂. This reaction represents the overall pathway for biomass oxygenate refining without CO₂ capture.



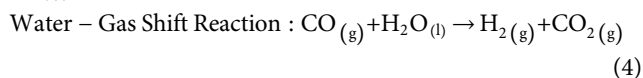
Standard heat of reaction (ΔH_{500}^0) = 108.6^a, 285.2^b, 268.1^c, 195.5^d, 388.7^e, 220.3^f kJ mol⁻¹

a, b, c, d, e, f corresponds to methanol, ethanol, glycerol, ethylene glycol, acetone, and acetic acid, respectively.

Reaction 2 involves several intermediate steps as described below. The first step in this pathway is the preferential formation of CO through bio-oxygenate decomposition as shown in Eq. 3a for C:O molar ratio of 1:1, and hydrolysis as shown in Eq. 3b for C:O molar ratios greater than 1:1. The CO produced then undergoes an exothermic water gas shift reaction (WGSR) to produce H₂ and CO₂.

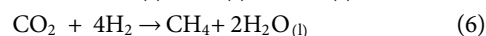
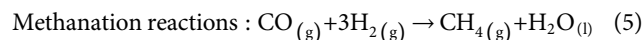


$$\Delta H_{500}^0 = 127.1^g, 322.2^b, 323.6^c, 232.5^h, 444.2^e, 257.2^i \text{ kJmol}^{-1}$$



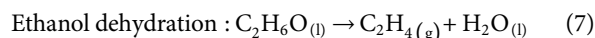
$$\Delta H_{500}^0 = -18.5 \text{ kJmol}^{-1}$$

Competing reactions that result in CH₄ formation as opposed to H₂ formation need to be incorporated (see reactions 5 and 6). Compared to WGS reactions, methanation reactions are more exothermic which make them favorable at low temperatures.

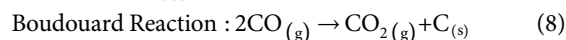


$\Delta H_{500}^0 = -235.6 \text{ kJmol}^{-1}$ and $\Delta H_{500}^0 = -217.1 \text{ kJmol}^{-1}$ for Eqs 5, 6 respectively.

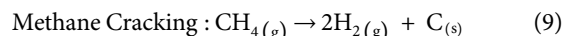
Furthermore, bio-derived oxygenates and their intermediate products can undergo dehydration, cracking, decomposition, and reduction to produce more undesired products such as CH₄, CO, solid C, and C₂H₄, as shown by reactions 7–11 below.



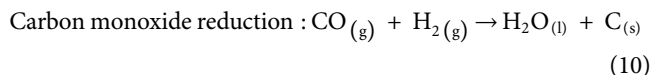
$$\Delta H_{500}^0 = 58.4 \text{ kJmol}^{-1}$$



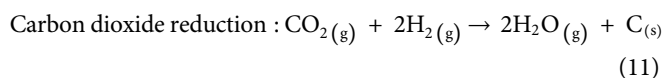
$$\Delta H_{500}^0 = -173.8 \text{ kJmol}^{-1}$$



$$\Delta H_{500}^0 = 80.3 \text{ kJmol}^{-1}$$

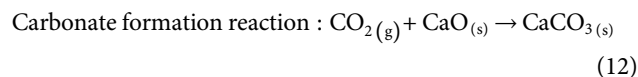


$$\Delta H_{500}^0 = -155.3 \text{ kJmol}^{-1}$$



$$\Delta H_{500}^0 = -136.8 \text{ kJmol}^{-1}$$

Bio-oxygenate reforming reactions can be endothermic. Therefore, coupling these with exothermic carbon mineralization reactions (Eq. 12) enhances the overall spontaneity of these reactions. The overall exothermicity resulting from the coupling of these reaction is shown in Eq. 1, and the heat of reactions at 500 K for methanol, ethanol, glycerol, ethylene glycol, acetone, and acetic acid is presented in Table 2.



$$\Delta H_{500}^0 = -174.3 \text{ kJmol}^{-1}$$

Thermodynamic Modelling and Simulation Methodology

The equilibrium compositions of various reacting processes are determined using the Gibbs energy minimization method. A more detailed description of this methodology was described by Lima *et al.* (Lima da Silva *et al.*, 2009; Lima Da Silva and Müller, 2011). The advantage of this approach is that it addresses systems with potential for simultaneous reactions. The objective function shown in Eq. 14 is minimized subject to the elemental balance constraint in Eq. 15,

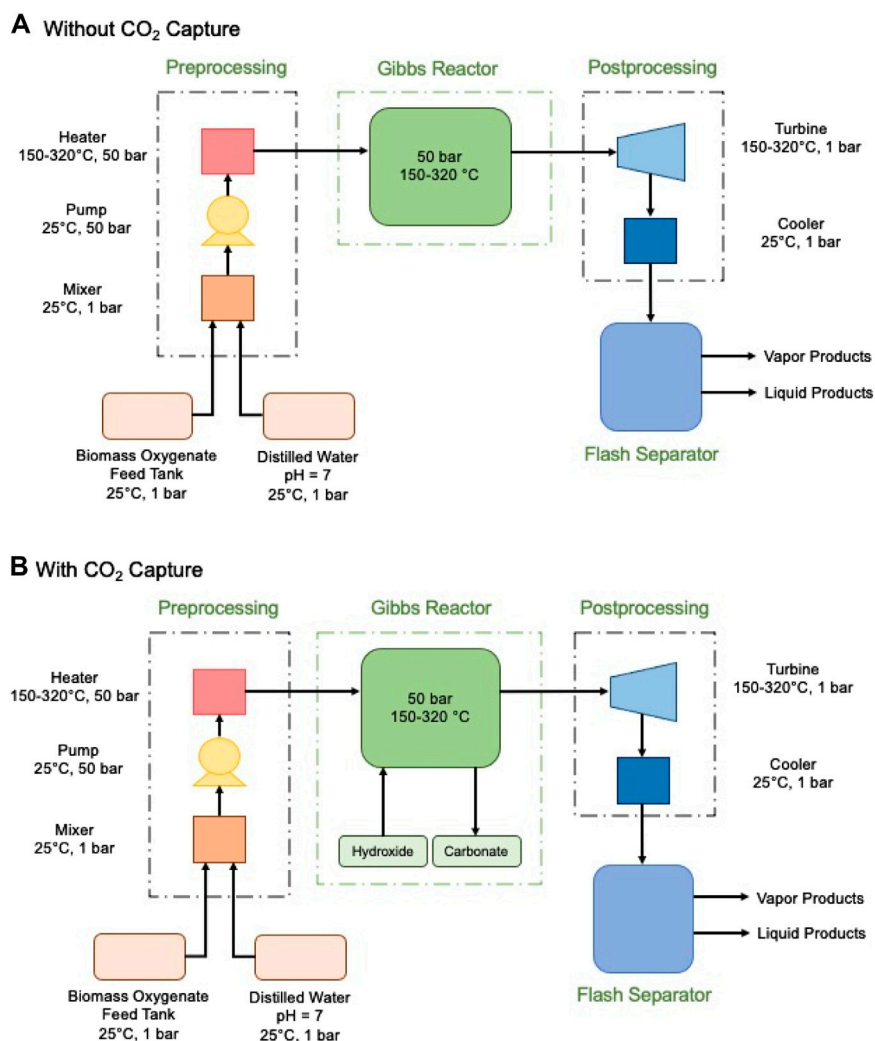


FIGURE 2 | Process flow diagram of simulation environment **(A)** without *in-situ* CO₂ capture, **(B)** with *in-situ* CO₂ capture. The thermodynamic feasibility of enhancing H₂ recovery with inherent carbon removal using aqueous biomass oxygenate sources are based on the reactions taking place in the Gibbs reactor.

$$\frac{G}{RT} = \left\{ \sum_{i=1}^N n_i \left[\frac{G_i^0}{RT} + \ln(z_i P) \right] \right\} + \frac{1}{RT} \sum_{j=1}^N n_j G_j^0 \quad (14)$$

$$\sum_{j=1}^N n_i \alpha_{ik} + \sum_{j=1}^N n_j \alpha_{jk} = b_k \quad K = 1 \dots M \quad (15)$$

Where G , G_i^0 , T , R , z_i , P , n_j , α_{jk} , and b_k represents the total Gibbs free energy of the system, Gibbs free energy of species i at its standard state, temperature of the system, universal gas constant, mole fraction of species i in the gas phase, pressure of the system, number of atoms of k th component present in each molecules of species i , and the total number of atomic masses of k th component in the system, respectively.

Minimizing the objective function of the system indicates that a mixture of chemical species approaches an equilibrium state. These equilibrium calculations were performed and simulated using ASPEN[®] Plus V8.6 process simulation software. The Gibbs reactor (see **Figure 2A,B**) was modelled as an Isothermal

equilibrium reactor, which calculates the equilibrium composition of product species using the Gibbs energy minimization method at various operating conditions, keeping our reaction temperature constant, while accounting for the heat of reactions. The Peng-Robinson (Peng-Rob) equations of state were used to model the property parameter (Peng and Robinson, 1976). This property method has been widely used for processes containing oxygenates, water, and combustion gases (Fateen et al., 2013; Ali et al., 2014; Jimmy et al., 2017).

Prior to been fed into the reactor, biomass oxygenate, and water is mixed, pressurized, and heated using a mixer, pump, and heater, respectively. In cases where the effect of alkalinity was investigated, the alkaline source was fed directly into the reactor at its specified temperature and pressure. It was found that the temperature of the input feed stream does not affect the thermodynamic results, because fixing the reactor parameters produces the equilibrium effect determined by the set

temperature and pressure. However, the configuration was still used to ensure proper representation of the real batch reformer, as it would account for the energy required to heat the feedstock to the desired temperature and cool the products before analysis. Using this setup, H₂ evolution with varying biomass oxygenate-to-water ratios in the range of 5–95%, a low temperature range of 150–325°C, and varying alkaline sources, was studied at 50 bar. Prior studies have shown that methanation reactions can also be effectively suppressed using catalysts (Davda et al., 2005; Coronado et al., 2016). We also investigated the influence of 1) methanation and 2) suppressed methanation. Both cases were also investigated with and without CO₂ capture *via* carbon mineralization. This approach provides the optimal and sub-optimal scenarios that are dependent on the activity of the catalysts.

The equilibrium conversions of biomass oxygenates to products and associated product yields were defined as follows:

$$\begin{aligned} &\% \text{ Conversion of Biomass Oxygenates (BO)} \\ &= \frac{\text{BO}_{\text{in}} - \text{BO}_{\text{out}}}{\text{BO}_{\text{in}}} \times 100 \end{aligned} \quad (17)$$

$$\begin{aligned} &\% \text{H}_2 \text{ yield} \\ &= \left[\frac{\text{Moles of H}_2 \text{ produced}}{\text{Moles of biomass oxygenate fed} \times \text{Stoichiometric Ratio (SR)}} \right] \times 100 \end{aligned} \quad (18)$$

$$\% \text{CO, CO}_2 \text{ and alkanes yield} = \frac{\text{Moles of C in compound produced}}{\text{Moles of C atoms in BO fed}} \times 100 \quad (19)$$

RESULTS AND DISCUSSION

Effect of Water-to-Biomass Oxygenate Ratio on H₂ Recovery With Carbon Removal

Water plays a synergistic role in enhanced H₂ recovery with inherent carbon removal from biomass oxygenates. Water facilitates the dissolution of calcium oxide to release calcium ions that can readily react with the evolved CO₂ to produce inorganic carbonates, as opposed to steam. The enhanced ion transport in gas-liquid-solid environments as opposed to in gas-solid environments favors accelerated formation of carbonates at lower temperatures as opposed to sorption-enhanced steam methane reforming that occurs at higher temperatures (Wang et al., 2008; Lindén et al., 2011). Further, the need for additional energy input in the form of latent heat of vaporization is avoided by maintaining water in the aqueous phase. To harness these advantages and resolve the compositions of the product stream, simulations were performed at 227°C, N₂ pressure of 50 bar, with and without stoichiometric amounts of CaO as defined by reaction 1 and 13. H₂, CH₄, and CO₂ yields with and without CaO are shown in **Figures 3–8** for methanol, ethanol, glycerol, ethylene glycol, acetone, and acetic acid, respectively.

In the absence of CaO for CO₂ capture, the yields of H₂ and CH₄ remain unaffected by an increase in the concentration of methanol and ethanol up to 40 wt% (See **Figures 3A,C, 4A,C**). Further increases in the concentrations of methanol and ethanol led to an increase in CH₄ yield and a simultaneous decrease in the production of hydrogen.

Decrease in H₂ yield is accompanied by a decrease in the production of gaseous CO₂ gas, which can be attributed to the limited amount of H₂O available to undergo a water gas shift reaction as shown in **Eq. 4**. Limited water concentration cause a thermodynamic shift to favor CH₄ production *via* CO methanation reaction at equilibrium. When CaO was introduced to capture CO₂, H₂ concentrations decreased after methanol and ethanol concentrations exceeded 20 wt% (See **Figures 3B,D, 4B,D**). This change is attributed to the use of water for the water gas shift reaction and the dissolution of CaO to produce calcium carbonate.

The hypothesis that CaO significantly enhances H₂ yields and suppresses CH₄ yields was shown to be true since H₂ yields exceeding 75% were achieved around 20 wt% for all the biomass oxygenates reported in this study (**Figures 3B–8B**). In the absence of CaO, less than 2% yield of H₂ was noted (**Figures 3A–8A**). However, methane yields either remained unchanged at low biomass oxygenate concentrations or increased in most cases except for acetone. At acetone concentrations of 80 wt% or higher, H₂ yields approached zero and methane yields decreased significantly. Also, the concentration of unreacted acetone in the product stream rapidly increased indicating low conversions of acetone (19–81%) at concentrations of 80wt% or higher, elsewhere the conversion was 100%. The observed anomaly could imply a different reaction mechanism caused by inadequate amounts of water leading to acetone decomposition to produce unstable radicals described as (CH₃COCH₃ → 2CH₃[•] + CO) (Spence and Wild, 1936; Smith and Hinshelwood, 1944). Further, the absence of H₂O or H₂ for the CO produced during this reaction to undergo WGS reactions or methanation reaction as described in reactions 4) and 5) shifts the equilibrium back to acetone production at room temperature, leading to low conversions. With all the biomass oxygenates investigated, non-monotonic relationships between the concentrations of biomass oxygenates and the yields of H₂ and CH₄ were noted.

It was interesting to note a significantly lower yield of H₂ at biomass oxygenate concentrations exceeding 60% for all the biomass oxygenates reported in this study which are methanol, ethanol, glycerol, ethylene glycol, acetone, and acetic acid. However, the trends in the concentrations of H₂ and CH₄ at biomass oxygenate concentrations below 60 wt% differ. The effectiveness of using stoichiometric amounts of CaO is evident from the negligibly low concentrations of CO₂ in the gas phase to the order of 10^{−12} mol of CO₂ per mole of biomass oxygenate fed after CO₂ capture (**Figures 3D–8D**). At biomass oxygenate concentrations of 20 wt% or less, near complete conversions of CaO to CaCO₃ are noted (**Figures 3D–9D**). In addition to aiding the separation of CO₂, the heat generated during carbon mineralization aids the water gas shift reaction for enhanced H₂ conversion.

Effect of Temperature on H₂ Recovery With Carbon Removal

Temperature has a significant effect on coupled multiphase chemical interactions involved in enhanced H₂ recovery with inherent CO₂ removal from biomass oxygenate precursors.

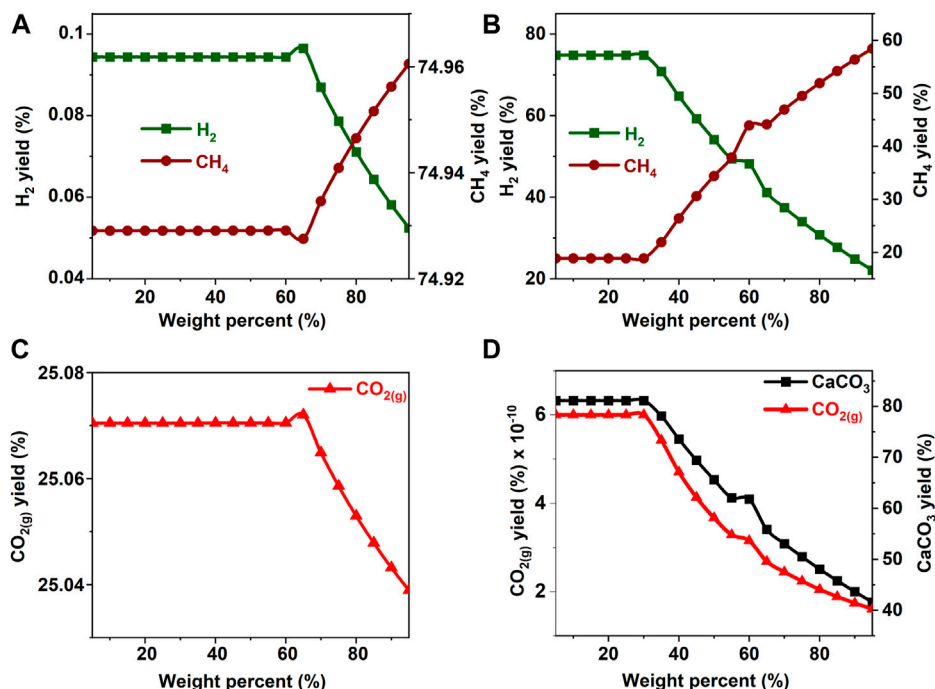


FIGURE 3 | Effect of methanol concentration on the product yield (A, C) in the absence and (B) in the presence of calcium oxide. The yield of CO₂ post capture to produce calcium carbonate is represented in 1 (D). These calculations are performed with temperatures of 227°C and pressures of 50 bar.

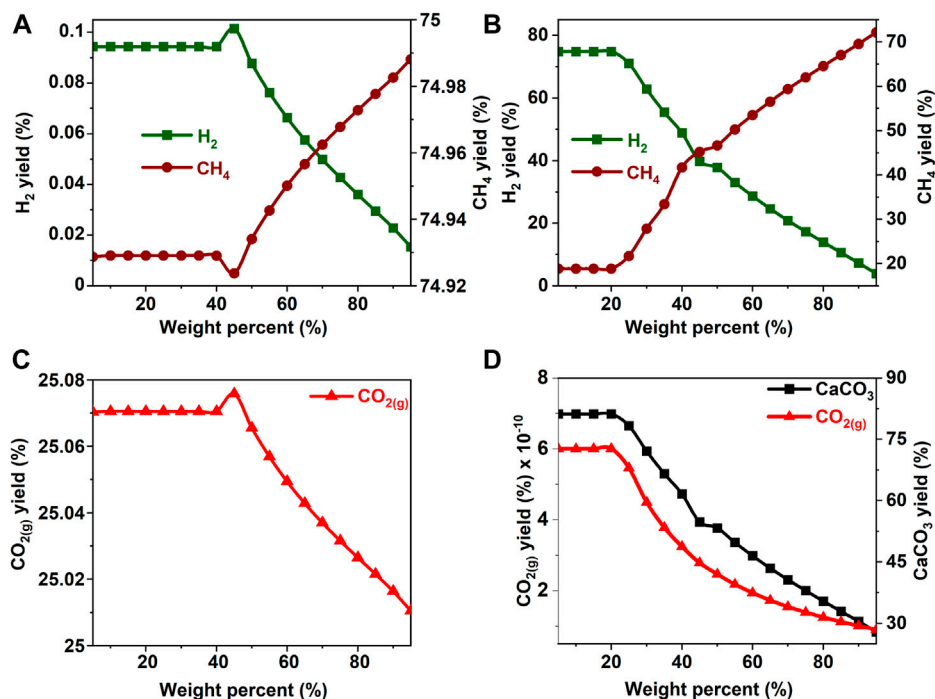


FIGURE 4 | Effect of ethanol concentration on the product yield (A, C) in the absence and (B) in the presence of calcium oxide. The yield of CO₂ post capture to produce calcium carbonate is represented in 2 (D). These calculations are performed with temperatures of 227°C and pressures of 50 bar.

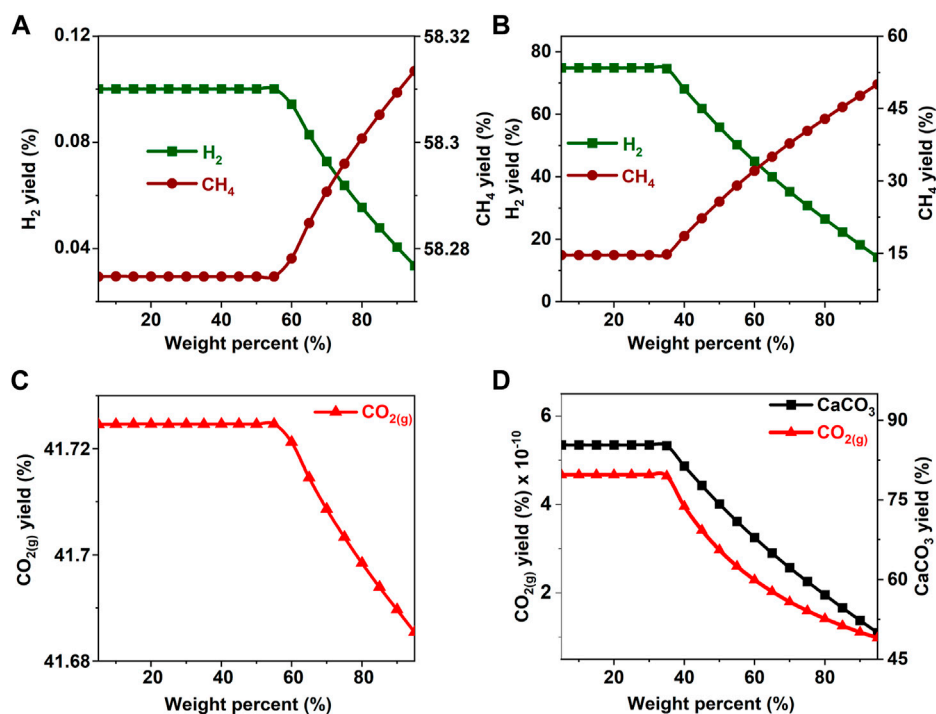


FIGURE 5 | Effect of glycerol concentration on the product yield (A, C) in the absence and (B) in the presence of calcium oxide. The yield of CO₂ post capture to produce calcium carbonate is represented in 3(D). These calculations are performed with temperatures of 227°C and pressures of 50 bar.

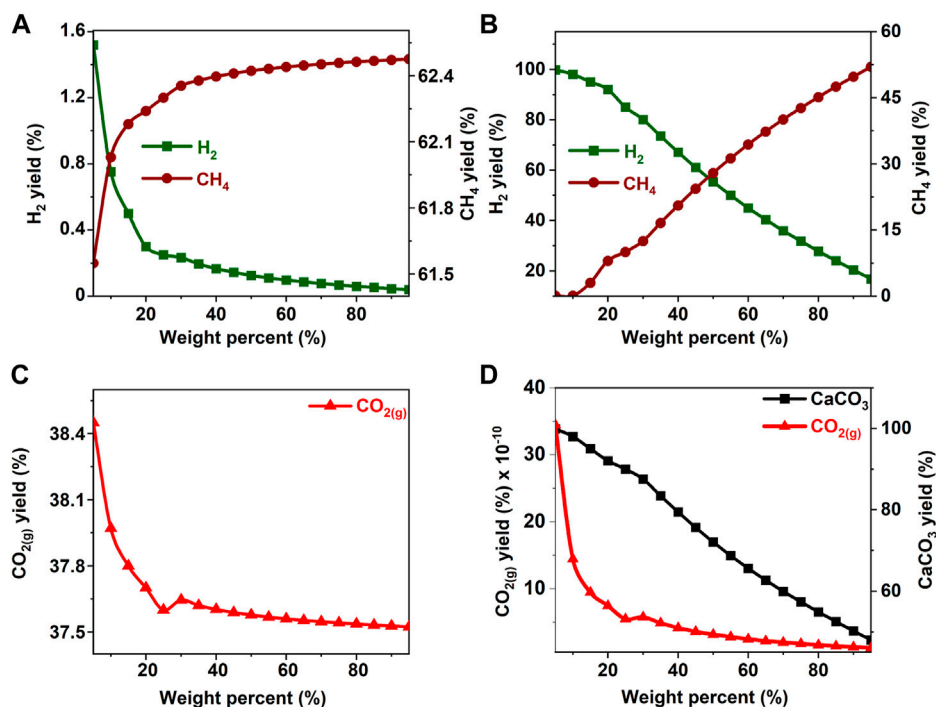


FIGURE 6 | Effect of ethylene glycol concentration on the product yield (A, C) in the absence and (B) in the presence of calcium oxide. The yield of CO₂ post capture to produce calcium carbonate is represented in 4(D). These calculations are performed with temperatures of 227°C and pressures of 50 bar.

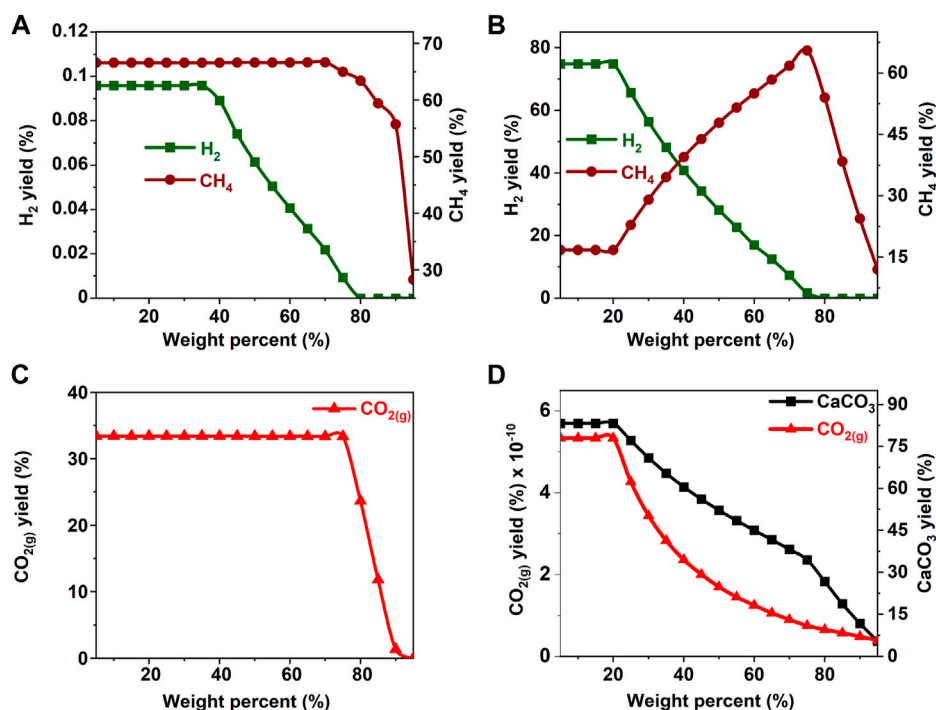


FIGURE 7 | Effect of acetone concentration on the product yield (A, C) in the absence and (B) in the presence of calcium oxide. The yield of CO₂ post capture to produce calcium carbonate is represented in 5(D). These calculations are performed with temperatures of 227°C and pressures of 50 bar.

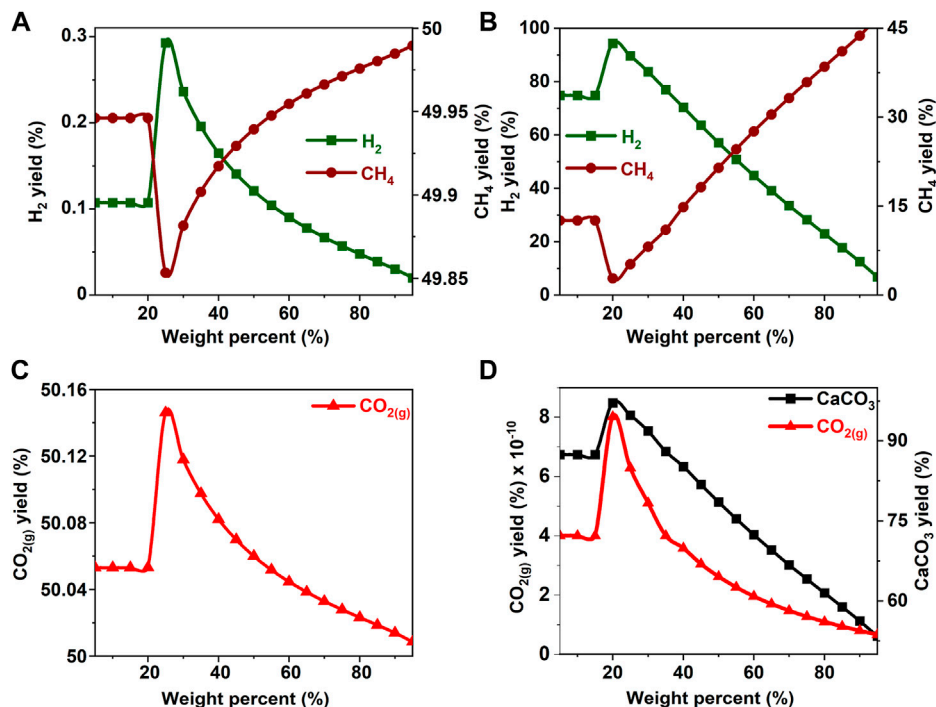


FIGURE 8 | Effect of acetic acid concentration on the product yield (A, C) in the absence and (B) in the presence of calcium oxide. The yield of CO₂ post capture to produce calcium carbonate is represented in 6(D). These calculations are performed with temperatures of 227°C and pressures of 50 bar.

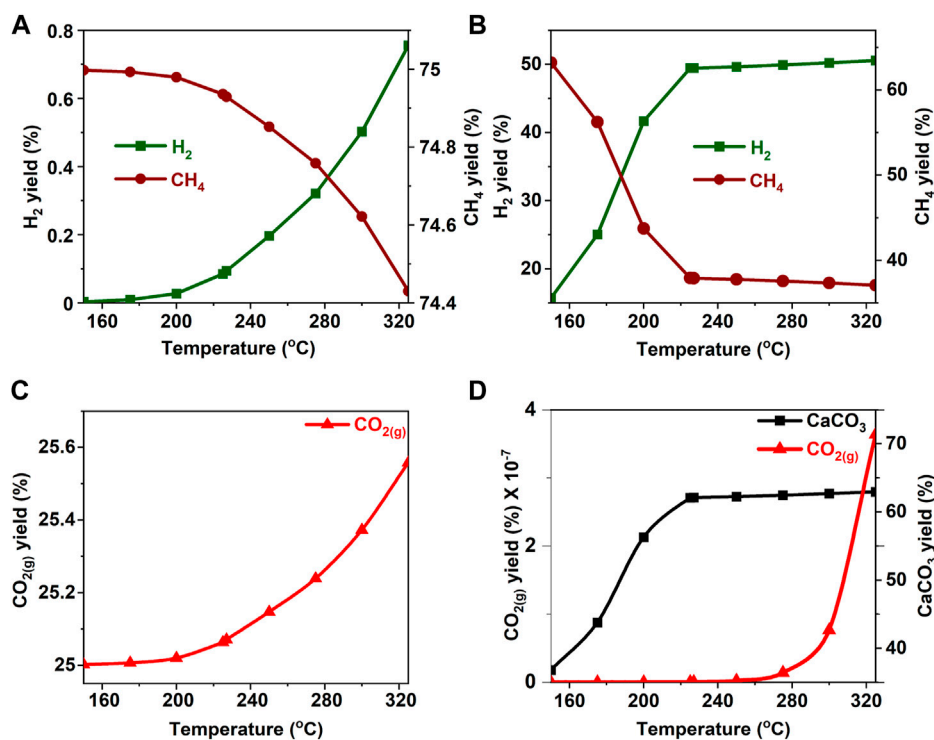


FIGURE 9 | Effect of temperature on the product yield from methanol (**A, C**) in the absence and (**B**) in the presence of calcium oxide. The yield of CO₂ post capture to produce calcium carbonate is represented in **7(D)**. These calculations are performed with temperatures of 227°C and pressures of 50 bar.

Increase in temperature favors product and reactant formation in endothermic and exothermic reactions, respectively. Further, the solubility of calcium carbonate decreases with temperature which favors the removal of CO₂. Aqueous biomass oxygenate decomposition is an endothermic reaction (see Reaction 3) and higher temperatures are expected to aid the decomposition behavior. In contrast, the conversion of CO and H₂ to CH₄ is exothermic (and higher temperatures may shift the equilibrium towards the reactants, which favors H₂ yield. Coupling the exothermic water-gas-shift reaction (see Reaction 4) with the carbon mineralization reaction removes CO₂ from the product stream and pushes the equilibrium to the products. This coupling of reactions counterbalances the effect of temperature which is to push the equilibrium towards the products. To investigate the hypothesis that the reaction temperature has a significant effect on enhanced H₂ formation with inherent carbon removal, the gas compositions were determined at temperatures in the range of 150°C–325°C, while all other conditions such as the biomass oxygenate composition and the N₂ pressure were held constant at 50 wt% and 50 bar.

In the absence of a catalyst and CaO for CO₂ capture, H₂ yields are less than 1% for all the biomass oxygenates and CH₄ yields exceed 49% in the temperature range of 150°C–325°C (**Figures 9A–14A**). H₂ and CO₂ yields increase monotonically with temperature (**Figures 9A,C–14A,C**). The yields of CH₄ decrease monotonically with temperature at these conditions (**Figures 9A–14A**). In the presence of CaO for CO₂ capture, H₂ yields of 46–65% or higher are achieved at temperatures

exceeding 220°C. At these conditions, CH₄ yields are 30% or lower at temperatures exceeding 220°C (**Figures 9B–14B**). These data suggest that alkaline environments (bearing CaO in this case) favor alkaline hydrolysis that contributes to the cleavage of C–C bonds as opposed to acid hydrolysis that results in C–O cleavage which promotes alkane formation. (Davda et al., 2005). Further, CO yields to the order of 10^{−3}% and 10^{−9}% were noted in the absence and presence of CaO, suggesting that the removal of CO₂ from the gas phase accelerates the conversion of CO to CO₂ (See **Supplementary Figure S2A–F**).

Unlike the cases without CaO, where we obtained a constant increase in H₂ yield, an asymptotic pattern was observed in cases with *in-situ* CO₂ capture for temperatures greater than 225°C. Furthermore, despite the low amounts of CO being produced, there was a sharp increase CO formation with increasing temperature between 225°C and 320°C. These observations imply that biomass oxygenate decomposition is aided at higher temperatures to produce CO. However, the low concentrations of CO and higher temperatures do not favor product formation in the exothermic water-gas-shift and methanation reactions. These factors contribute to the asymptotic behavior of H₂ above 225°C which also corresponds to the near complete uptake of CO₂ to produce CaCO₃ (**Figures 9D–14D**). Negligible concentrations of CO₂ to the order 10^{−7}–10^{−10}% were found in the product gas stream for all cases of biomass oxygenates studied after CO₂ capture using CaO (See **Figures 9D–14D**).

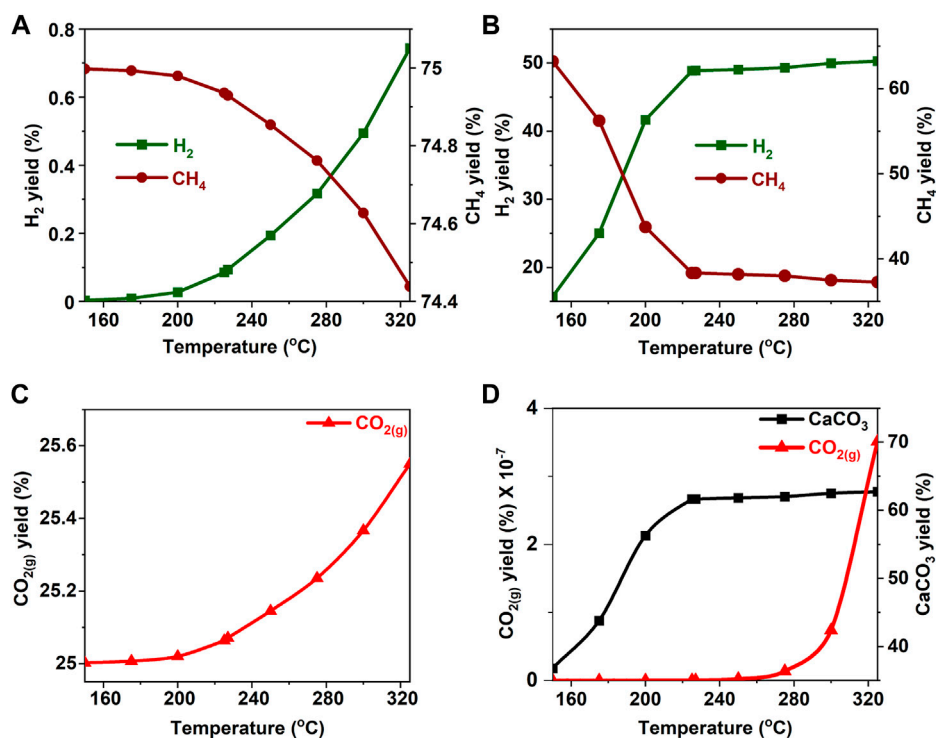


FIGURE 10 | Effect of temperature on the product yield from ethanol (A, C) in the absence and (B) in the presence of calcium oxide. The yield of CO₂ post capture to produce calcium carbonate is represented in 8(D). These calculations are performed with temperatures of 227°C and pressures of 50 bar.

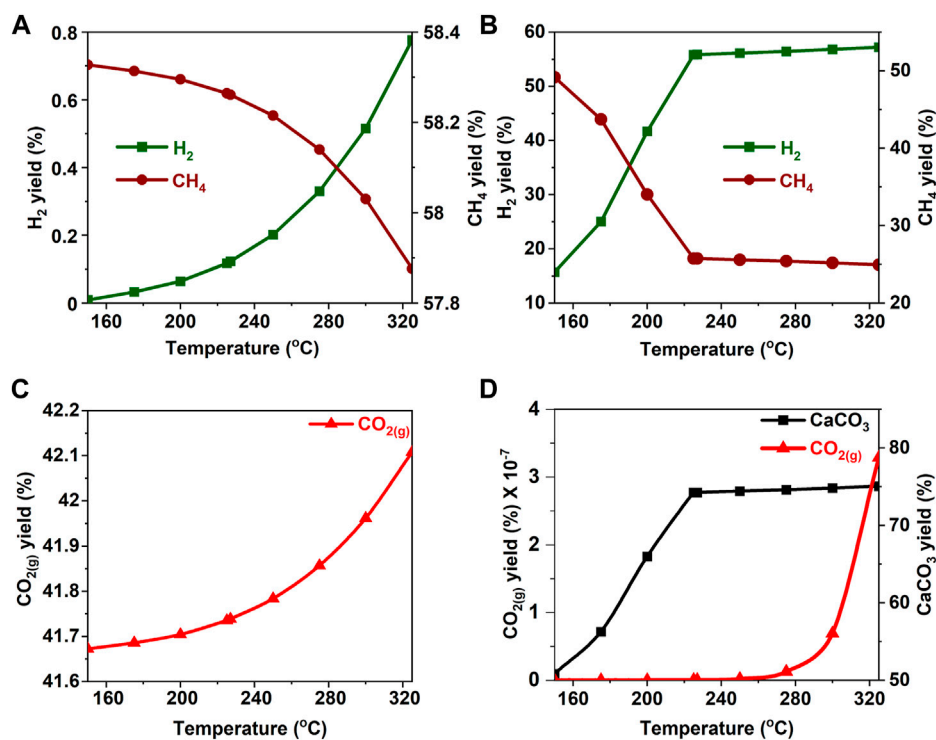


FIGURE 11 | Effect of temperature on the product yield from glycerol (A, C) in the absence and (B) in the presence of calcium oxide. The yield of CO₂ post capture to produce calcium carbonate is represented in 9(D). These calculations are performed with temperatures of 227°C and pressures of 50 bar.

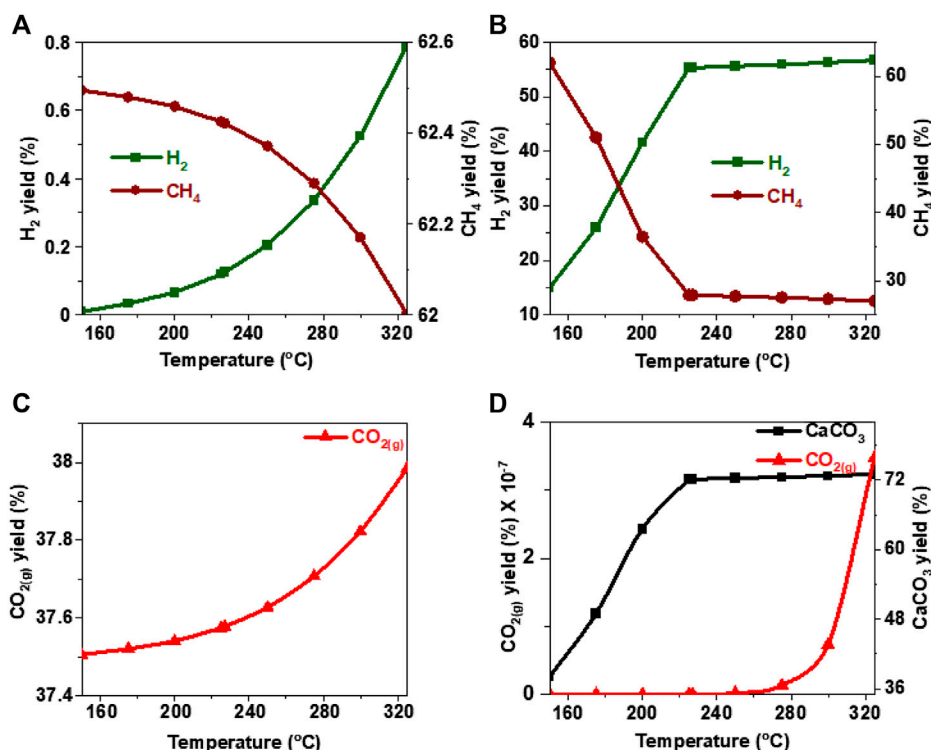


FIGURE 12 | Effect of temperature on the product yield from ethylene glycol (A, C) in the absence and (B) in the presence of calcium oxide. The yield of CO₂ post capture to produce calcium carbonate is represented in 10(D). These calculations are performed with temperatures of 227°C and pressures of 50 bar.

Effect of Methanation on H₂ Recovery With Carbon Removal

The key limiting factor in accelerating H₂ recovery from biomass oxygenates is the formation of CH₄. CH₄ is produced from CO or CO₂ and H₂ as building blocks via exothermic reaction pathways (see Reactions 5 and 6). One approach to limit CH₄ formation is to use catalysts that favor C-C bond cleavage and the water gas shift (WGS) reaction over C-O bond cleavage and methanation reactions (Davda et al., 2003; Davda et al., 2005; Coronado et al., 2016). Some examples of these catalysts include rare earth metals supported catalysts such as Pt/SiO₂, Pd/Al₂O₃, and Ru/C. Further, catalysts that have a basic character or operate in alkaline environments such as earth abundant Ni catalysts have also been shown to be effective in aiding H₂ evolution (Stonor et al., 2017b).

In this study, we build on these observations to investigate the influence of methanation and its suppression on H₂, CH₄, CO, CO₂, and CaCO₃ yields. In the suppressed methanation case, the reactions associated with CH₄ formation from CO and CO₂ precursors are not included in the model. The studies are conducted at 227°C, N₂ pressure of 50 bar, and biomass oxygenate concentrations of 20 wt%, with and without CO₂ capture. For cases with CO₂ capture, we used a stoichiometric amounts of CaO as defined by (reaction 13). In this study, we consider four scenarios for hydrothermal biomass oxygenate reactions: 1) with methanation, 2) without methanation, 3) alkaline treatment with methanation, and 4) alkaline treatment without methanation reactions (Figure 15).

In the scenario with methanation and without a catalyst, CH₄ and CO₂ compositions are dominant and H₂ yields are less than 0.3%. In the scenario where methanation is suppressed by using a catalyst, H₂ and CO₂ yields are dominant, while CO formation is suppressed and there is no CH₄ observed. For alkaline treatment with methanation, more than 70% conversion of H₂ and CaCO₃, and substantial CH₄ yields are noted. No CO formation is noted in this case. For alkaline treatment without methanation, H₂ and CaCO₃ are the dominant phases. These results demonstrate that strategies to harness biomass oxygenates for H₂ recovery with CO₂ removal need to incorporate catalysts to suppress methane formation and alkaline sources for *in-situ* CO₂ capture.

Analysis of the product streams provided further insights into the reactivities of various biomass oxygenates. The reactivities of the functional groups proceed in the descending order of OH > COOH > COR. This trend was similar with experimental results obtained by Fu and co-workers (Fu et al., 2020) who investigated the steam reforming of bio-oil and its derivatives and reported the highest H₂ yield from reforming of ethylene glycol, followed by acetic acid, and acetone. Additionally, the separation of CO₂ from the gas phase in the alkaline environment greatly limits methanation kinetically at low and moderate temperatures (less than 227°C) and enhances H₂ production. The lower temperatures are potentially beneficial to catalyst life, and they significantly reduce cost. Furthermore, trace amounts of CO (10⁻¹² %) were evident in all cases studied, implying that these processes are effective for generating hydrogen with CO content within the 20 ppm limit for fuel cell applications.

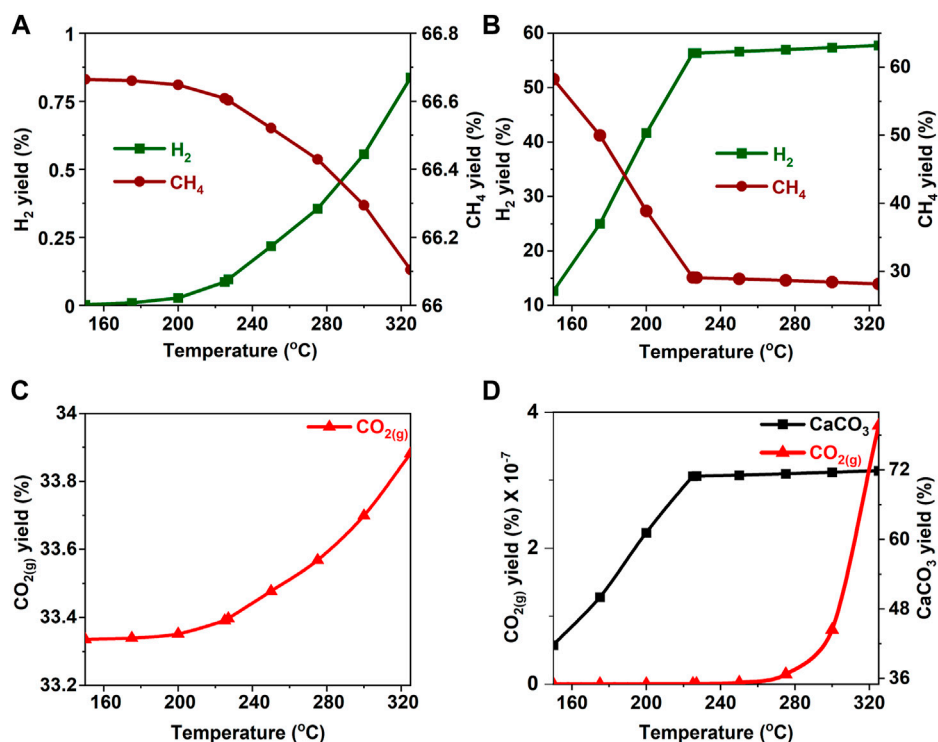


FIGURE 13 | Effect of temperature on the product yield from acetone (A, C) in the absence and (B) in the presence of calcium oxide. The yield of CO₂ post capture to produce calcium carbonate is represented in 11(D). These calculations are performed with temperatures of 227°C and pressures of 50 bar.

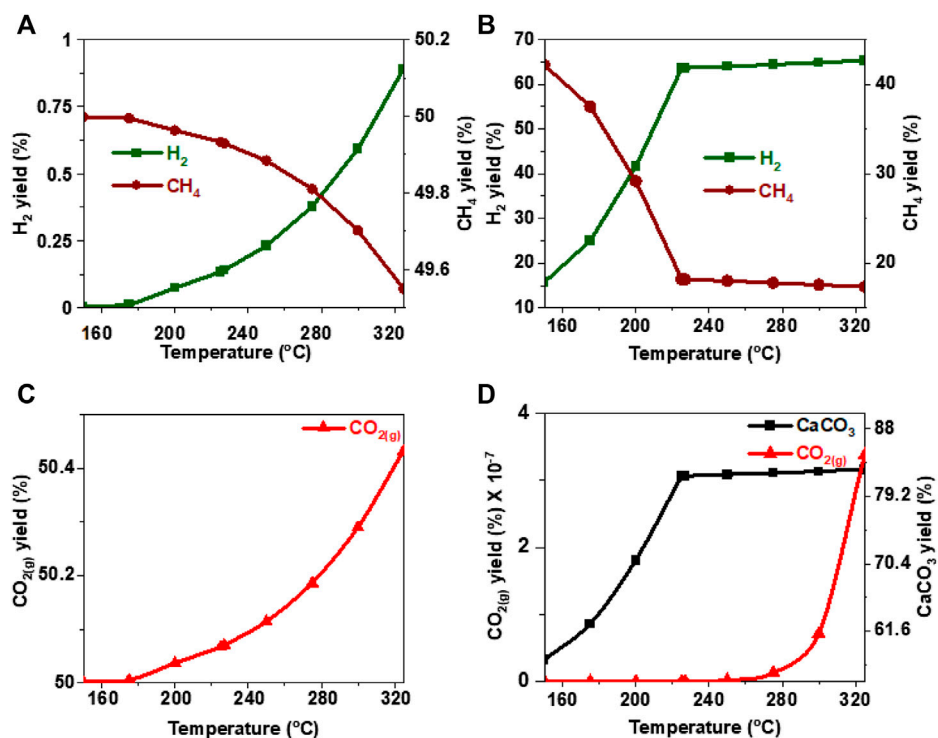


FIGURE 14 | Effect of temperature on the product yield from acetic acid (A, C) in the absence and (B) in the presence of calcium oxide. The yield of CO₂ post capture to produce calcium carbonate is represented in 13(D). These calculations are performed with temperatures of 227°C and pressures of 50 bar.

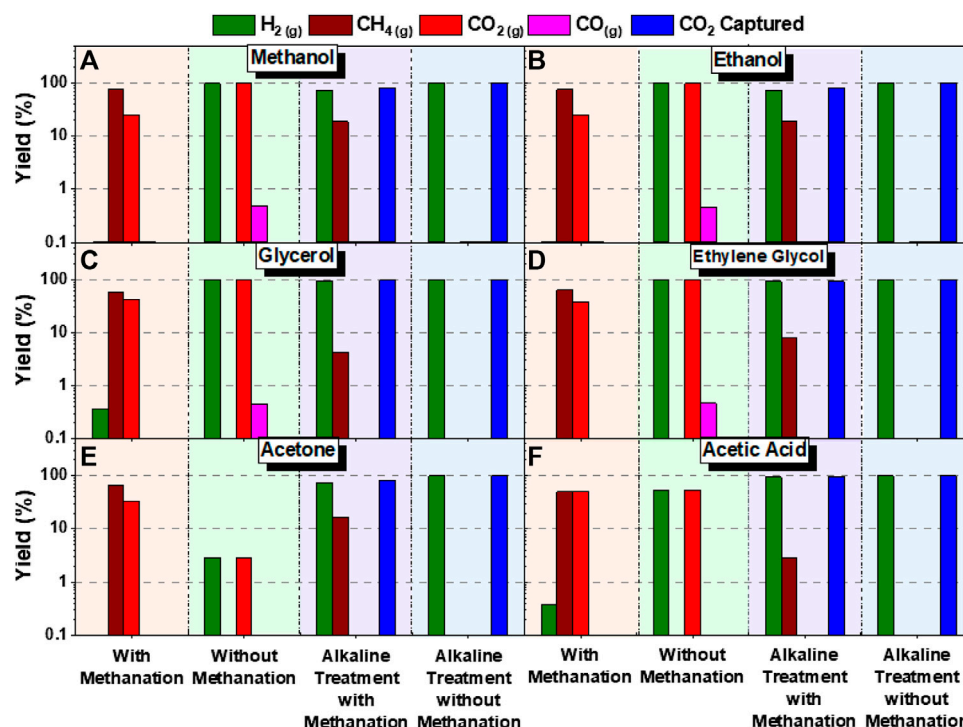


FIGURE 15 | Comparison of theoretical product yields with 20 wt% of (A) methanol, (B) ethanol, (C) glycerol, (D) ethylene glycol, (E) acetone, (F) acetic acid. Thermodynamic product yield was computed for cases with methanation, catalytic effect (without methanation reactions), alkaline treatment with methanation, and alkaline treatment with catalytic effect (without methanation reactions). These calculations are performed with temperatures of 227°C and pressures of 50 bar.

CONCLUSION

In this study, the thermodynamic limits for enhanced H₂ recovery with inherent CO₂ removal from various biomass oxygenate sources such as methanol, ethanol, glycerol, ethylene glycol, acetone, and acetic acid are reported. The effects of biomass oxygenate-to-water ratio, temperature, and suppression of the limiting methanation reactions on the yields of H₂ and other associated compositions are investigated. As opposed to conventional high temperature reforming processes (> 500°C) at atmospheric pressure, we investigated the effect of maintaining fluids in the aqueous phase on under N₂ pressure of 50 bar and at significantly lower temperatures <325°C. The effect of coupling thermodynamically downhill carbon mineralization reactions for *in-situ* CO₂ capture to enhance H₂ evolution was also studied. Higher H₂ yields with *in-situ* CO₂ capture were achieved with biomass oxygenate concentrations lower than 30 wt%. Water is needed as a reactant for the water gas shift reaction and to facilitate the dissolution of CaO for carbon mineralization. Temperatures around 220–230°C yielded high H₂ conversion with *in-situ* CO₂ capture. Further increases in temperature did not contribute to a significant enhancement in CO₂ capture. The suppression of methanation reactions and *in-situ* CO₂ capture to produce inorganic carbonates is crucial for producing high purity H₂ that can be used in a fuel cell. The thermodynamic feasibility of these reaction pathways demonstrates that low value residues such as Ca-rich alkaline residues and wastewater streams bearing biomass oxygenates can be successfully upcycled to produce high value H₂ with inherent CO₂ removal.

DATA AVAILABILITY STATEMENT

The original contributions presented in the study are included in the article/**Supplementary Material**, further inquiries can be directed to the corresponding author.

AUTHOR CONTRIBUTIONS

PO conducted the analyses and completed the initial draft. CB and RK contributed to the resource assessments. GG conceptualized the study and contributed towards writing and editing.

FUNDING

This work was supported as part of the Cornell Atkinson Small Grant Program through the Reducing Climate Risk initiative funded by the Cornell Atkinson Center for Sustainability, Cornell University.

SUPPLEMENTARY MATERIAL

The Supplementary Material for this article can be found online at: <https://www.frontiersin.org/articles/10.3389/fenrg.2021.742323/full#supplementary-material>

REFERENCES

- Abanoz, K., Stark, B. C., and Akbas, M. Y. (2012). Enhancement of Ethanol Production from Potato-Processing Wastewater by Engineering *Escherichia coli* Using Vitreoscilla Haemoglobin. *Lett. Appl. Microbiol.* 55, 436–443. doi:10.1111/lam.12000
- Ajao, V., Millah, S., Gagliano, M. C., Bruning, H., Rijnaarts, H., and Temmink, H. (2019). Valorization of Glycerol/ethanol-Rich Wastewater to Biofloculants: Recovery, Properties, and Performance. *J. Hazard. Mater.* 375, 273–280. doi:10.1016/j.jhazmat.2019.05.009
- Ali, E., Hadj-Kali, M. K., Mulyono, S., Alnashif, I., Fakeeha, A., Mjalli, F., et al. (2014). Solubility of CO₂ in Deep Eutectic Solvents: Experiments and Modelling Using the Peng-Robinson Equation of State. *Chem. Eng. Res. Des.* 92, 1898–1906. doi:10.1016/j.cherd.2014.02.004
- Arora, K., Kaur, P., Kumar, P., Singh, A., Patel, S. K. S., Li, X., et al. (2021). Valorization of Wastewater Resources into Biofuel and Value-Added Products Using Microalgal System. *Front. Energ. Res.* 9, 1–25. doi:10.3389/feng.2021.646571
- Badawi, M. A., El-Shinnawi, M. M., Blanc, F. C., Wise, D. L., and El-Shimi, S. A. (1992). Production of Acetic Acid from Thermally Treated Sewage Sludge in an Upflow Anaerobic Reactor. *Resour. Conserv. Recycl.* 7, 201–212. doi:10.1016/0921-3449(92)90017-V
- Baschuk, J. J., and Li, X. (2001). Carbon Monoxide Poisoning of Proton Exchange Membrane Fuel Cells. *Int. J. Energ. Res.* 25, 695–713. doi:10.1002/er.713
- Benson, S. M., and Surles, T. (2006). Carbon Dioxide Capture and Storage: An Overview with Emphasis on Capture and Storage in Deep Geological Formations. *Proc. IEEE* 94, 1795–1804. doi:10.1109/JPROC.2006.883718
- Brandt, A., Gräsvik, J., Hallett, J. P., and Welton, T. (2013). Deconstruction of Lignocellulosic Biomass with Ionic Liquids. *Green. Chem.* 15, 550–583. doi:10.1039/c2gc36364j
- Coché, M. K., Dincer, I., and Rosen, M. A. (2010). Thermodynamic Analysis of Hydrogen Production from Biomass Gasification. *Int. J. Hydrogen Energ.* 35, 4970–4980. doi:10.1016/j.ijhydene.2009.08.066
- Coronado, I., Stekrova, M., Reinikainen, M., Simell, P., Lefferts, L., and Lehtonen, J. (2016). A Review of Catalytic Aqueous-phase Reforming of Oxygenated Hydrocarbons Derived from Biorefinery Water Fractions. *Int. J. Hydrogen Energ.* 41, 11003–11032. doi:10.1016/j.ijhydene.2016.05.032
- Cortright, R. D., Davda, R. R., and Dumesic, J. A. (2010). Hydrogen from Catalytic Reforming of Biomass-Derived Hydrocarbons in Liquid Water. *Mater. Sustain. Energ. A Collect. Peer-Reviewed Res. Rev. Artic. Nat. Publ. Gr.* 418, 289–292. doi:10.1142/9789814317665_0043
- Davda, R. R., Shabaker, J. W., Huber, G. W., Cortright, R. D., and Dumesic, J. A. (2003). Aqueous-phase Reforming of Ethylene Glycol on Silica-Supported Metal Catalysts. *Appl. Catal. B Environ.* 43, 13–26. doi:10.1016/S0926-3373(02)00277-1
- Davda, R. R., Shabaker, J. W., Huber, G. W., Cortright, R. D., and Dumesic, J. A. (2005). A Review of Catalytic Issues and Process Conditions for Renewable Hydrogen and Alkanes by Aqueous-phase Reforming of Oxygenated Hydrocarbons over Supported Metal Catalysts. *Appl. Catal. B Environ.* 56, 171–186. doi:10.1016/j.apcatb.2004.04.027
- De Vlieger, D. J. M., Mojet, B. L., Lefferts, L., and Seshan, K. (2012). Aqueous Phase Reforming of Ethylene Glycol - Role of Intermediates in Catalyst Performance. *J. Catal.* 292, 239–245. doi:10.1016/j.jcat.2012.05.019
- Deluga, G. A., Salge, J. R., Schmidt, L. D., and Verykios, X. E. (2004). Renewable Hydrogen from Ethanol by Autothermal Reforming. *Science* 303, 993–997. doi:10.1126/science.1093045
- Dissanayake, D., Rosynek, M. P., Kharas, K. C. C., and Lunsford, J. H. (1991). Partial Oxidation of Methane to Carbon Monoxide and Hydrogen over a Ni/Al₂O₃ Catalyst. *J. Catal.* 132, 117–127. doi:10.1016/0021-9517(91)90252-Y
- Ellis, J. T., Hengge, N. N., Sims, R. C., and Miller, C. D. (2012). Acetone, Butanol, and Ethanol Production from Wastewater Algae. *Bioresour. Technol.* 111, 491–495. doi:10.1016/j.biortech.2012.02.002
- Fateen, S. E. K., Khalil, M. M., and Elnabawy, A. O. (2013). Semi-empirical correlation for binary interaction parameters of the Peng-Robinson equation of state with the van der Waals mixing rules for the prediction of high-pressure vapor-liquid equilibrium. *J. Adv. Res.* 4, 137–145. doi:10.1016/j.jare.2012.03.004
- Fu, P., Zhang, A., Luo, S., Yi, W., and Zhang, Y. (2020). Comparative Study on the Catalytic Steam Reforming of Biomass Pyrolysis Oil and its Derivatives for Hydrogen Production. *RSC Adv.* 10, 12721–12729. doi:10.1039/d0ra01409e
- Gadikota, G., Park, A., and hyung, A. (2015). *Accelerated Carbonation of Ca- and Mg-Bearing Minerals and Industrial Wastes Using CO₂*. Elsevier B.V. doi:10.1016/B978-0-444-62746-9.00008-6
- Gadikota, G. (2020). Multiphase Carbon Mineralization for the Reactive Separation of CO₂ and Directed Synthesis of H₂. *Nat. Rev. Chem.* 4, 78–89. doi:10.1038/s41570-019-0158-3
- Gadikota, G. (2021). Carbon Mineralization Pathways for Carbon Capture, Storage and Utilization. *Commun. Chem.* 4, 1–5. doi:10.1038/s42004-021-00461-x
- He, C., Zheng, J., Wang, K., Lin, H., Wang, J. Y., and Yang, Y. (2015). Sorption Enhanced Aqueous Phase Reforming of Glycerol for Hydrogen Production over Pt-Ni Supported on Multi-Walled Carbon Nanotubes. *Appl. Catal. B Environ.* 162, 401–411. doi:10.1016/j.apcatb.2014.07.012
- Hohn, K. L., and Schmidt, L. D. (2001). Partial Oxidation of Methane to Syngas at High Space Velocities over Rh-Coated Spheres. *Appl. Catal. A Gen.* 211, 53–68. doi:10.1016/S0926-860X(00)00835-8
- Jimmy, U., Mohamedali, M., and Ibrahim, H. (2017). Thermodynamic Analysis of Autothermal Reforming of Synthetic Crude Glycerol (Scg) for Hydrogen Production. *ChemEngineering* 1, 1–12. doi:10.3390/chemengineering1010004
- Joensen, F., and Rostrup-Nielsen, J. R. (2002). Conversion of Hydrocarbons and Alcohols for Fuel Cells. *J. Power Sourc.* 105, 195–201. doi:10.1016/S0378-7753(01)00939-9
- Khalilpour, R., Mumford, K., Zhai, H., Abbas, A., Stevens, G., and Rubin, E. S. (2015). Membrane-based Carbon Capture from Flue Gas: A Review. *J. Clean. Prod.* 103, 286–300. doi:10.1016/j.jclepro.2014.10.050
- Kim, I. T., Yoo, Y. S., Yoon, Y. H., Lee, Y. E., Jo, J. H., Jeong, W., et al. (2018). Bio-Methanol Production Using Treated Domestic Wastewater with Mixed Methanotroph Species and Anaerobic Digester Biogas. *Water (Switzerland)* 10, 1414. doi:10.3390/w10101414
- Li, Y., He, D., Niu, D., and Zhao, Y. (2015). Acetic Acid Production from Food Wastes Using Yeast and Acetic Acid Bacteria Micro-aerobic Fermentation. *Bioproc. Biosyst. Eng.* 38, 863–869. doi:10.1007/s00449-014-1329-8
- Lima Da Silva, A., and Müller, I. L. (2011). Hydrogen Production by Sorption Enhanced Steam Reforming of Oxygenated Hydrocarbons (Ethanol, Glycerol, N-Butanol and Methanol): Thermodynamic Modelling. *Int. J. Hydrogen Energ.* 36, 2057–2075. doi:10.1016/j.ijhydene.2010.11.051
- Lima da Silva, A., Malfatti, C. de F., and Müller, I. L. (2009). Thermodynamic Analysis of Ethanol Steam Reforming Using Gibbs Energy Minimization Method: A Detailed Study of the Conditions of Carbon Deposition. *Int. J. Hydrogen Energ.* 34, 4321–4330. doi:10.1016/j.ijhydene.2009.03.029
- Lindén, I., Backman, P., Brink, A., and Hupa, M. (2011). Influence of Water Vapor on Carbonation of CaO in the Temperature Range 400–550 °C. *Ind. Eng. Chem. Res.* 50, 14115–14120. doi:10.1021/ie2009795
- Luo, N., Fu, X., Cao, F., Xiao, T., and Edwards, P. P. (2008). Glycerol Aqueous Phase Reforming for Hydrogen Generation over Pt Catalyst - Effect of Catalyst Composition and Reaction Conditions. *Fuel* 87, 3483–3489. doi:10.1016/j.fuel.2008.06.021
- Masson-Delmotte, V., Zhai, P., Pörtner, H.-O., Roberts, D., Skea, J., Shukla, P. R., et al. (2018). IPCC Report Global Warming of 1.5°C. *Ipcc - Sr15* 2, 17–20. Available at: www.environmentalgraphiti.org.
- Menezes, A. O., Rodrigues, M. T., Zimmaro, A., Borges, L. E. P., and Fraga, M. A. (2011). Production of Renewable Hydrogen from Aqueous-phase Reforming of Glycerol over Pt Catalysts Supported on Different Oxides. *Renew. Energ.* 36, 595–599. doi:10.1016/j.renene.2010.08.004
- Mincer, T. J., and Aicher, A. C. (2016). Methanol Production by a Broad Phylogenetic Array of marine Phytoplankton. *PLoS One* 11, 1–17. doi:10.1371/journal.pone.0150820
- Ming, Q., Healey, T., Allen, L., and Irving, P. (2002). Steam Reforming of Hydrocarbon Fuels. *Catal. Today* 77, 51–64. doi:10.1016/S0920-5861(02)00232-8
- Novak, J. T., Goldsmith, C. D., Benoit, R. E., and O'Brien, J. H. (1985). Biodegradation of Methanol and Tertiary Butyl Alcohol in Subsurface Systems. *Water Sci. Technol.* 17, 71–85. doi:10.2166/wst.1985.0083
- NRDC (2021). Food Waste in Cities. Available at: <https://www.nrdc.org/food-matters> (Accessed July 10, 2021).

- Özcan, O., and Akin, A. N. (2019). Thermodynamic Analysis of Methanol Steam Reforming to Produce Hydrogen for HT-PEMFC: An Optimization Study. *Int. J. Hydrogen Energ.* 44, 14117–14126. doi:10.1016/j.ijhydene.2018.12.211
- Peng, D. Y., and Robinson, D. B. (1976). A New Two-Constant Equation of State. *Ind. Eng. Chem. Fundam.* 15, 59–64. doi:10.1021/i160057a011
- Qi, K., Li, Z., Zhang, C., Tan, X., Wan, C., Liu, X., et al. (2020). Biodegradation of Real Industrial Wastewater Containing Ethylene Glycol by Using Aerobic Granular Sludge in a Continuous-Flow Reactor: Performance and Resistance Mechanism. *Biochem. Eng. J.* 161, 107711. doi:10.1016/j.bej.2020.107711
- Ranade, V. V., and Bhandari, V. M. (2014). Industrial Wastewater Treatment, Recycling, and Reuse: An Overview. *Ind. Wastewater Treat. Recycl. Reuse*, 1–80. doi:10.1016/B978-0-08-099968-5.00001-5
- Rochelle, G. T. (2009). Amine Scrubbing for CO₂ Capture. *Science* 325, 1652–1654. doi:10.1126/science.1176731
- Ross, R. H. J. (1984). *Catal. Sci. Technol.* 5. doi:10.1016/s0166-9834(00)83350-3
- Roy, B., Martinez, U., Loganathan, K., Datye, A. K., and Leclerc, C. A. (2012). Effect of Preparation Methods on the Performance of Ni/Al₂O₃ Catalysts for Aqueous-phase Reforming of Ethanol: Part I-Catalytic Activity. *Int. J. Hydrogen Energ.* 37, 8143–8153. doi:10.1016/j.ijhydene.2012.02.056
- Sayari, A., Belmabkhout, Y., and Serna-Guerrero, R. (2011). Flue Gas Treatment via CO₂ Adsorption. *Chem. Eng. J.* 171, 760–774. doi:10.1016/j.cej.2011.02.007
- Shabaker, J. W., Huber, G. W., Davda, R. R., Cortright, R. D., and Dumesic, J. A. (2003). Aqueous-phase Reforming of Ethylene Glycol over Supported Platinum Catalysts. *Catal. Lett.* 88, 1–8. doi:10.1023/A:1023538917186
- Smith, J. R. E., and Hinshelwood, C. N. (1944). The thermal Decomposition of Acetone. *Proc. R. Soc. Lond. Ser. A. Math. Phys. Sci.* 183, 33–37. doi:10.1098/rspa.1944.0019
- Spence, R., and Wild, W. (1936). Mechanism of the Photo-Decomposition of Acetone. *Nature* 138, 206. doi:10.1038/138206b0
- Stonor, M. R., Chen, J. G., and Park, A. H. A. (2017a). Bio-Energy with Carbon Capture and Storage (BECCS) Potential: Production of High Purity H₂ from Cellulose via Alkaline Thermal Treatment with Gas Phase Reforming of Hydrocarbons over Various Metal Catalysts. *Int. J. Hydrogen Energ.* 42, 25903–25913. doi:10.1016/j.ijhydene.2017.08.059
- Stonor, M. R., Ouassil, N., Chen, J. G., and Park, A. H. A. (2017b). Investigation of the Role of Ca(OH)₂ in the Catalytic Alkaline Thermal Treatment of Cellulose to Produce H₂ with Integrated Carbon Capture. *J. Energ. Chem.* 26, 984–1000. doi:10.1016/j.jechem.2017.07.013
- Thompson, J. C., and He, B. B. (2006). Characterization of Crude Glycerol from Biodiesel Production from Multiple Feedstocks. 22, 261–265. doi:10.13031/2013.20272
- U.S. Department of Energy (2016). *Hydrogen Fuel Quality Specifications for Polymer Electrolyte Fuel Cells in Road Vehicles*. Safety, Codes Stand. Progr, 1–72.
- Uçkun Kiran, E., and Liu, Y. (2015). Bioethanol Production from Mixed Food Waste by an Effective Enzymatic Pretreatment. *Fuel* 159, 463–469. doi:10.1016/j.fuel.2015.06.101
- Wang, C., Jia, L., Tan, Y., and Anthony, E. J. (2008). Carbonation of Fly Ash in Oxy-Fuel CFB Combustion. *Fuel* 87, 1108–1114. doi:10.1016/j.fuel.2007.06.024
- Wen, G., Xu, Y., Ma, H., Xu, Z., and Tian, Z. (2008). Production of Hydrogen by Aqueous-phase Reforming of Glycerol. *Int. J. Hydrogen Energ.* 33, 6657–6666. doi:10.1016/j.ijhydene.2008.07.072
- WHO (2009). *The Energy Access Situation in Developing Countries*. UNDP WHO New York, 142. Available at: http://www.who.int/indoorair/publications/PowerPoint_Energy_Access_paper-lr.pdf?0Ahttp://scholar.google.com/scholar?hl=en&btnG=Search&q=intitle:THE+ENERGY+ACCESS+SITUATION+IN+DEVELOPING+COUNTRIES+A+Review+Focusing+on+the#0.
- Williams, M. L. (1996). CRC Handbook of Chemistry and Physics. *Occup. Environ. Med.* 53, 504. doi:10.1136/oem.53.7.504
- Yan, S., Chen, X., Wu, J., and Wang, P. (2012). Ethanol Production from Concentrated Food Waste Hydrolysates with Yeast Cells Immobilized on Corn Stalk. *Appl. Microbiol. Biotechnol.* 94, 829–838. doi:10.1007/s00253-012-3990-7
- Zhang, K., Kim, W. J., and Park, A. H. A. (2020). Alkaline thermal Treatment of Seaweed for High-Purity Hydrogen Production with Carbon Capture and Storage Potential. *Nat. Commun.* 11. doi:10.1038/s41467-020-17627-1

Conflict of Interest: The authors declare that the research was conducted in the absence of any commercial or financial relationships that could be construed as a potential conflict of interest.

Publisher's Note: All claims expressed in this article are solely those of the authors and do not necessarily represent those of their affiliated organizations, or those of the publisher, the editors and the reviewers. Any product that may be evaluated in this article, or claim that may be made by its manufacturer, is not guaranteed or endorsed by the publisher.

Copyright © 2021 Ochonma, Blaudeau, Krasnoff and Gadikota. This is an open-access article distributed under the terms of the Creative Commons Attribution License (CC BY). The use, distribution or reproduction in other forums is permitted, provided the original author(s) and the copyright owner(s) are credited and that the original publication in this journal is cited, in accordance with accepted academic practice. No use, distribution or reproduction is permitted which does not comply with these terms.



Energetics of Li⁺ Coordination with Asymmetric Anions in Ionic Liquids by Density Functional Theory

Drace Penley¹, Stephen P. Vicchio², Rachel B. Getman² and Burcu Gurkan^{1*}

¹Chemical and Biomolecular Engineering, Case Western Reserve University, Cleveland, OH, United States, ²Chemical and Biomolecular Engineering, Clemson University, Clemson, SC, United States

OPEN ACCESS

Edited by:

Ah-Hyung Alissa Park,
Columbia University, United States

Reviewed by:

Hailei Zhao,
University of Science and Technology
Beijing, China

Shrihari Sankarasubramanian,
University of Texas at San Antonio,
United States

*Correspondence:

Burcu Gurkan
beg23@case.edu

Specialty section:

This article was submitted to
Electrochemical Energy Conversion
and Storage,
a section of the journal
Frontiers in Energy Research

Received: 14 June 2021

Accepted: 10 September 2021

Published: 15 October 2021

Citation:

Penley D, Vicchio SP, Getman RB and
Gurkan B (2021) Energetics of Li⁺
Coordination with Asymmetric Anions
in Ionic Liquids by Density
Functional Theory.
Front. Energy Res. 9:725010.
doi: 10.3389/fenrg.2021.725010

The energetics, coordination, and Raman vibrations of Li solvates in ionic liquid (IL) electrolytes are studied with density functional theory (DFT). Li⁺ coordination with asymmetric anions of cyano(trifluoromethanesulfonyl)imide ([CTFSI]) and (fluorosulfonyl)(trifluoro-methanesulfonyl)imide ([FTFSI]) is examined in contrast to their symmetric analogs of bis(trifluoromethanesulfonyl)imide ([TFSI]), bis(fluorosulfonyl)imide ([FSI]), and dicyanamide ([DCA]). The dissociation energies that can be used to describe the solvation strength of Li⁺ are calculated on the basis of the energetics of the individual components and the Li solvate. The calculated dissociation energies are found to be similar for Li⁺-[FTFSI], Li⁺-[TFSI], and Li⁺-[FSI] where only Li⁺-O coordination exists. Increase in asymmetry and anion size by fluorination on one side of the [TFSI] anion does not result in significant differences in the dissociation energies. On the other hand, with [CTFSI], both Li⁺-O and Li⁺-N coordination are present, and the Li solvate has smaller dissociation energy than the solvation by [DCA] alone, [TFSI] alone, or a 1:1 mixture of [DCA]/[TFSI] anions. This finding suggests that the Li⁺ solvation can be weakened by asymmetric anions that promote competing coordination environments through enthalpic effects. Among the possible Li solvates of (Li[CTFSI]_n)⁻⁽ⁿ⁻¹⁾, where $n = 1, 2, 3, \text{ or } 4$, (Li[CTFSI]₂)⁻¹ is found to be the most stable with both monodentate and bidentate bonding possibilities. Based on this study, we hypothesize that the partial solvation and weakened solvation energetics by asymmetric anions may increase structural heterogeneity and fluctuations in Li solvates in IL electrolytes. These effects may further promote the Li⁺ hopping transport mechanism in concentrated and multicomponent IL electrolytes that is relevant to Li-ion batteries.

Keywords: ionic liquid electrolytes, lithium solvation, concentrated electrolytes, lithium-ion battery, *ab initio* thermodynamics

INTRODUCTION

The structure of Li⁺ solvates in concentrated electrolytes has a significant impact on Li⁺ transport and is influential in the rate capability of rechargeable lithium ion batteries (LIBs) (Borodin et al., 2018; Yamada et al., 2019; Krachkovskiy et al., 2020; Pham et al., 2021). ILs present an extreme case of a concentrated electrolyte where the electrolyte is made entirely of discrete ions and lacks neutral solvent molecules. Generally, ILs are known to have high ionic conductivity, large electrochemical windows, and negligible volatility (Bae et al., 2013; Navarra, 2013). These properties are desirable for lithium battery systems and thus are of great interest for safe, high-density energy storage devices (Galinski et al., 2006; Bae et al., 2013; Navarra, 2013; Eftekhari et al., 2016). However, Li⁺ transport in

ILs is complex and hindered by the high viscosity, mainly due to Coulombic interactions and specific Li^+ -anion interactions, which leads to the formation of clusters that decrease the mobility of Li^+ in the bulk liquid (Lesch et al., 2014; Pham et al., 2021). Li^+ transport in ILs has been studied mostly by Raman spectroscopy, nuclear magnetic resonance spectroscopy, transference measurements, density functional theory (DFT), and classical molecular dynamic (MD) simulations (Borodin et al., 2006; Umebayashi et al., 2007; Duluard et al., 2008; Lassègues et al., 2009; Umebayashi et al., 2010; Castiglione et al., 2011; Fujii et al., 2013; Haskins et al., 2014; Borodin et al., 2018). In this study, the DFT approach is employed to understand the impact of anion asymmetry and the presence of binary anions on the structure and energetics of the first solvation shell of Li^+ in IL electrolytes.

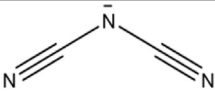
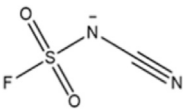
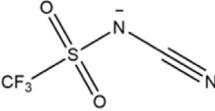
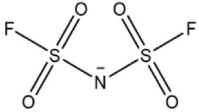
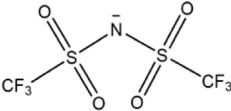
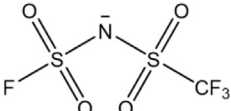
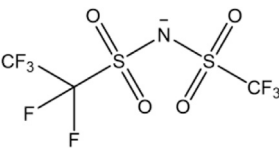
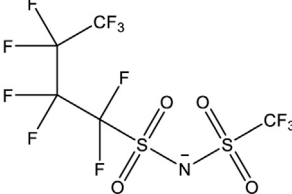
The bis(trifluoromethanesulfonyl)imide, [TFSI], anion and its respective ILs have been widely studied as potential electrolytes for lithium metal batteries and LIBs, and were shown to improve battery performance over the state-of-the-art organic carbonate electrolytes with $\text{Li}[\text{PF}_6]$ (Sakaebe and Matsumoto, 2003; Garcia et al., 2004; Armand et al., 2009). Fundamental studies of IL electrolytes with [TFSI] anion showed that Li^+ coordinates with anionic oxygen atoms where on average slightly less than four oxygen atoms are involved (Borodin et al., 2006), leading to two anions in the first solvation shell where *cis* conformation is favored with increased Li salt doping (Umebayashi et al., 2010). These studies were focused on Li salt mole fraction of $x_{\text{Li}^+} < 0.2$. In the similar Li salt concentration range, Fujii et al. showed that in the case of [FSI], the solvation number increases to three anions in the first shell where both monodentate and bidentate bonds coexist (Fujii et al., 2013; Lesch et al., 2016). Later, Lesch et al. (2016) showed that when both [TFSI] and [FSI] anions are available, Li^+ prefers to coordinate with [TFSI] and forms $\text{Li}^+ \cdot [\text{TFSI}] \cdot \text{Li}^+$ dimers which move on a similar timescale as $\text{Li}^+ \cdot [\text{TFSI}]$ aggregates. Haskins et al. (2014) studied the Li^+ solvation and transport in pyrrolidinium ILs with [TFSI] and [FSI] anions, and imidazolium IL with tetrafluoroborate $[\text{BF}_4]$ anion, with each system having 0.5 molal Li-salt concentration. When examining the solvation structures, they observed that the binding distances increased in the order of $\text{Li}^+ \cdot [\text{FSI}] > \text{Li}^+ \cdot [\text{TFSI}] > \text{Li}^+ \cdot [\text{BF}_4]$, where the system with $[\text{BF}_4]$ had the strongest binding energy and the system with [FSI] had the weakest binding energy. Different than previous studies, Haskins et al. reported that three [TFSI] anions coordinate with Li^+ through two monodentate and two bidentate bonds, while the coordination with $[\text{BF}_4]$ and [FSI] involved four anions with each having monodentate binding. The differences from the previous reports were attributed to the higher Li salt concentrations in their study ($x_{\text{Li}^+} \sim 0.33$) and difficulty in characterizing the coordination environment with experimental spectroscopy in the previous reports. At high Li salt concentrations, Li et al. (2012) also showed increased [TFSI] coordination with fewer bidentate and more monodentate bonds. Haskins et al. also studied the residence time of neighboring ions to Li^+ among other transport parameters, including Li^+ diffusivity and conductivity. The correlated ion motion that corresponds to the vehicular motion was decreased with increasing Li salt concentration, suggesting that Li^+ moves through the liquid by anion exchange. They concluded that the majority (60%) of the

transport occurred *via* vehicular motion, while Li^+ hopping was found to gain more significance with large-sized anions and increased Li^+ concentration. Therefore, the promotion of the hopping mechanism *via* anion exchange is the key for enhanced Li^+ mobility in concentrated electrolytes such as ILs considering the limitations of the vehicular mobility in the presence of Li^+ aggregates at $x_{\text{Li}^+} > 0.05$ (Brinkkötter et al., 2018; McEldrew et al., 2021).

Decreasing the solvation strength and the lifetime of coordinated species in LIB electrolytes have been suggested to play an important role in improving Li^+ mobility. Borodin et al. (2017) demonstrated the promotion of Li^+ transport in concentrated electrolytes where nano-heterogeneity decouples cations from anion cages. In other examples where heterogeneity was achieved by simple mixtures, Li^+ solvation was shown to weaken in binary organic carbonate mixtures (Matsuda et al., 2002), and the solvation shell was found to be more rigid in cyclic carbonates than in their linear counterparts (Fulfer and Kuroda, 2016). Shim (2018) studied the solvation structure and dynamics of a mixture of ethylmethyl carbonate (EMC), dimethyl carbonate (DMC), and ethylene carbonate (EC) with the $\text{Li}[\text{PF}_6]$ salt by MD simulations. They reported that as the EC concentration increased, the solvent fluctuations in Li solvates decreased due to the preferred coordination of Li^+ with EC and increased local density by the ring structure of EC, which was consistent with the reports by Yang et al. (2010). The decreased solvent fluctuations resulted in increased viscosity and reduced Li^+ diffusion. Similar to organic mixture electrolytes, mixtures of ILs have been studied to increase conductivity by Li solvate structural fluctuations and reduced solvation strength (Yang et al., 2010; Kerner et al., 2015; Huang et al., 2019a; Huang et al., 2019b; Chen and Forsyth, 2019).

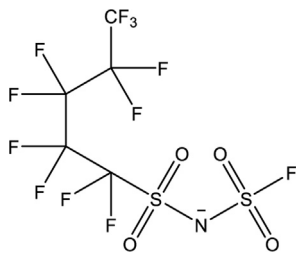
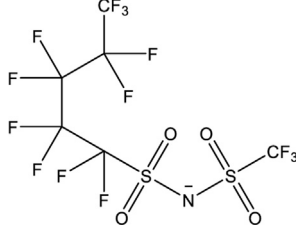
IL mixtures with [TFSI]/[FSI] anions have been studied the most to date due to the superior electrochemical properties of ILs paired with these anions. The [DCA] anion has also garnered attention due to its lower viscosity and higher conductivity than [TFSI]- and [FSI]-based ILs. In a study by Yoon et al. (2013), the [DCA] anion paired with a pyrrolidinium cation in a $\text{Li}|\text{LiFePO}_4$ cell showed stable cycling at elevated temperatures. Huang et al. (2019b) showed by a combined Raman spectroscopy and MD simulations study that at $x_{\text{Li}^+} < 0.2$, Li^+ coordinates on average with four [DCA] anions *via* monodentate bonds in a binary Li salt/IL mixture with [DCA] anion as well as a Li salt/IL/IL ternary mixture with [TFSI]/[DCA] anions. Using attenuated total reflectance far-ultraviolet and deep-ultraviolet spectroscopy, Imai et al. (2020) reported similar results for the first solvation shell of Li^+ in the Li salt/IL binary electrolyte with [DCA] anions. Huang et al. (2019b) also studied the ion pair lifetimes by MD and Li^+ transference by an experimental polarization method employed in Li-Li symmetrical cells. It was found that Li^+ coordination was not a strong function of the Li salt in the ternary mixture with [TFSI]/[DCA] anions, in contrast to Li-salt/IL binary electrolytes with [TFSI]. The ion pair lifetime of $\text{Li}^+ \cdot [\text{TFSI}]$ decreased with increasing [TFSI] concentration in the ternary electrolyte. This result was attributed to Li^+ preferring to coordinate with [DCA] and the addition of the [TFSI] anion breaking down the rigid first solvation shell due to the weaker coordination bond.

TABLE 1 | Anions of interest with full name as well as an abbreviation used within the study.

Anion	Full name	Structure
[DCA]	Dicyanamide	
[CFSI]	Cyano(fluorosulfonyl)imide	
[CTFSI]	Cyano(trifluoromethanesulfonyl)imide	
[FSI]	Bis(fluorosulfonyl)imide	
[TFSI]	Bis(trifluoromethanesulfonyl)imide	
[FTFSI]	(fluorosulfonyl) (trifluoromethanesulfonyl)imide	
[PFTFSI]	(pentafluoroethanesulfonyl) (trifluoromethanesulfonyl)imide	
[HFTFSI]	(heptafluoropropanesulfonyl) (trifluoromethanesulfonyl)imide	

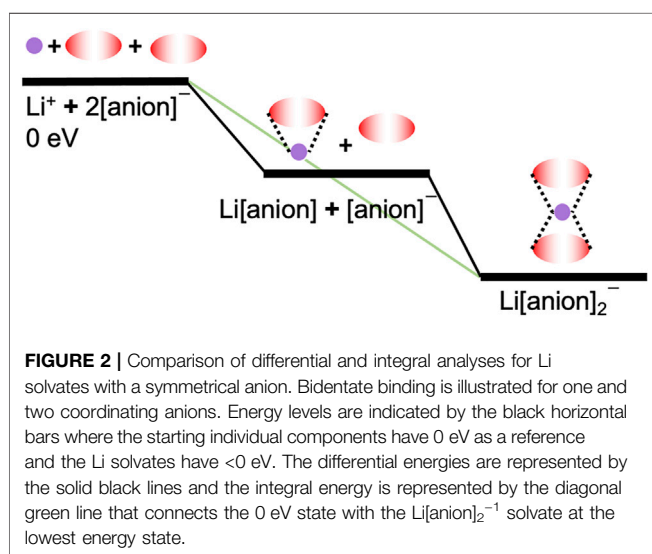
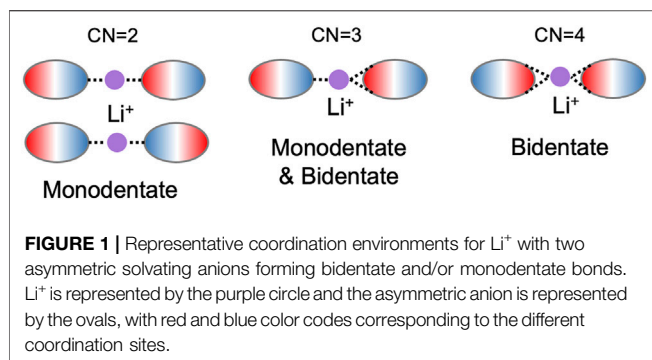
(Continued in next column)

TABLE 1 | (Continued) Anions of interest with full name as well as an abbreviation used within the study.

Anion	Full name	Structure
[NFFSI]	(nonafluorobutanesulfonyl) (fluorosulfonyl)imide	
[NFTFSI]	(nonafluorobutanesulfonyl) (trifluoromethanesulfonyl)imide	

Very recently, Nurnberg et al. (2020) studied the Li^+ solvation and transport in IL electrolytes ($x_{\text{Li}^+} = 0.1\text{--}0.7$) with the [CTFSI] anion by Raman spectroscopy and pulsed gradient NMR measurements. This anion is an asymmetric analog to both [TFSI] and [DCA] anions. They found that the [CTFSI]-based electrolyte had lower conductivity than the [TFSI] system. However, a pronounced transition from vehicular to structural diffusion (hopping) was noted for the asymmetric anion. Studies on such asymmetric anions are scarce, and mixture anions in IL electrolytes are relatively recently being explored. Understanding the Li^+ coordination environments and the solvation energies in the case of asymmetric anions are important for tuning concentrated electrolytes for future energy storage devices. In this study, we calculated the optimized geometries, Raman vibrations, and the Li solvate energies by DFT to understand the effect of anion functionality in IL mixtures with Li salts. Several asymmetric anions based on [FSI], [TFSI], and [DCA] parent anions were studied and compared in terms of the anion size, extent of fluorination, and coordination chemistry. The structures of the studied anions as well as their abbreviation are listed in **Table 1**.

The bulk properties and electrochemical applications of the three asymmetric anions such as [NFTFSI], [CTFSI], and [FTFSI] are relatively unexplored when compared to their parent anions. The [CTFSI] anion in an IL electrolyte has shown promise in LIBs, with improved thermal and anodic stability, and exhibited higher room temperature conductivity than [DCA] and [TFSI] parent anions (Hoffknecht et al., 2017). However, the structure of the Li solvate was not studied, and it is not clear what the role of the liquid structure is on the improved performance. An investigation on the [FTFSI]-based IL electrolyte showed that



the vehicular motion dominates due to the formation of Li^+ aggregates until 0.4 mole fraction of the Li salt after which the transport of Li^+ *via* hopping increases (Brinkkötter et al., 2018). [NFTFSI] is unique in that rather than combining the functionality of two parent IL anions, the fluoromethane group on [TFSI] is replaced with a fluorobutane. This provides the ability to quantify how the increased fluorination impacts the structure and transport properties. There has been little investigation of the [NFTFSI] and [NFFSI] anions in the past. Palumbo et al. (2017) studied the conformer structures of [NFTFSI] in a pyrrolidinium IL. Han et al. (2011) utilized 1M $\text{Li}[\text{NFFSI}]$ as the conducting salt in organic carbonates (EC/EMC 3:7 v/v) to improve high temperature performance of LIBs. $\text{Li}[\text{NFFSI}]$ showed similar conductivity as $\text{Li}[\text{ClO}_4]$ and slightly lower than $\text{Li}[\text{PF}_6]$; however, $\text{Li}[\text{NFFSI}]$ did not corrode the aluminum current collector of the graphite/ LiCoO_2 cell with 63% capacity retention over 100 cycles at 60°C, while the cell with $\text{Li}[\text{PF}_6]$ failed rapidly. Therefore, how the length of fluorination impacts the stability of LIBs is important to understand for extreme temperature conditions. In order to do so, we need a better understanding of how these fluorinated anions solvate and interact with Li^+ in the bulk electrolyte. The [CFSI], [PFTFSI], and [HFTFSI] anions were studied here to explore how

the degree of fluorination of the asymmetric anions impacts solvation strength. Previously, it was found that the binding energies of Li solvates with organic ligands decreased with increased fluorination (Bauschlicher, 2018). It was also shown that with reduced dipole moment and an increased ligand size, the ligand–ligand repulsion was increased. This was discussed to possibly lead to different structures than the non-fluorinated analogs. In this study, we show how the strength of solvation is impacted by the asymmetry of the coordinating anions and how the anion mixtures compare to the analogous asymmetric anion that has binary coordination with Li^+ . We report the strength of the first solvation shell of Li^+ in ILs without the impacts of the IL cation through DFT calculations and suggest which anions may help promote Li^+ transport based on this first principles study.

METHODS

Computational Details

Dissociation energies (E_D) were used to assess the thermodynamic favorabilities of the different Li^+ -anion systems. E_D represents the amount of energy it takes to break Li^+ -anion clusters into their constituents (i.e., the difference in energy going from the Li^+ -anion cluster to the individual components of Li^+ and the anion at infinite separation). They were calculated using quantum mechanics in the absence of solvation, similar to a prior study on Li^+ transport in cross-linked polymer electrolytes with ILs (Elmore et al., 2018), according to the equation:

$$E_D = \left[E_{\text{Li}^+} + \sum_i \gamma (E_{\text{anion}})_i \right] - E_{\text{Li-solvate}}, \quad (1)$$

where E_{Li^+} is the electronic energy of the lithium ion, E_{anion} is the electronic energy of the isolated anion i , γ is the number of anion i in the solvate structure, and $E_{\text{Li-solvate}}$ is the electronic energy of the Li solvate. In this study, $1 \leq \gamma \leq 4$. The isolated Li^+ is modeled with a +1 charge, and each anion is modeled with a net charge of −1. The net charge of the Li solvate can hence be 0, −1, −2, and −3, depending on the number of coordinating anions. This analysis is limited to a maximum number of coordinating anions of four due to the repulsive forces between anions when the first solvation shell includes five anions or greater, resulting in concentrated environments of $0.20 \leq x_{\text{Li}^+} \leq 0.50$. According to Eq. 1, positive values of E_D are favorable, with increasing values of E_D indicating stronger Li^+ ion bonds. Thus, a more positive E_D value is interpreted as a more stable Li solvate, and a more negative E_D value is interpreted as less stable, which would allow for faster breakdown of the first solvation shell and thus quicker exchange of anions within this shell.

Quantum mechanics calculations were carried out in the Gaussian 16 program (Frisch et al., 2016) using the three-parameter Becke model with the Lee–Yang–Par modification (B3LYP) (Lee et al., 1988) functional for exchange and correlation and the 6-311G(d,p) (Ditchfield et al., 1971) basis set. Structures of the isolated anions and Li^+ solvate systems and their associated electronic energies were obtained using geometry optimizations with default convergence criteria; as the Li^+ system does not require geometry optimization, its electronic energy was

calculated as a “single point.” Frequency calculations were carried out at the same level of theory in order to obtain thermodynamic and Raman spectroscopic data. Raman frequencies were scaled by a factor of 0.964 (Palafox, 2018). An example Gaussian input file for a geometry optimization and frequency calculation is provided in the supplementary.

Coordination Number and Li Solvate Structures

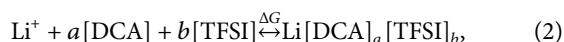
It is important to note the distinction between the number of anions coordinating with Li^+ and the coordination number (CN) associated with this first solvation shell. An anion can have more than one bonding site for Li^+ in which case CN will be a greater number than the number of coordinating anions. For example, the *cis* and *trans* conformation of [TFSI] can yield bidentate and monodentate bonds which can result in CN of 1–4 as [TFSI] has four oxygen atoms that can coordinate with Li^+ . **Figure 1** demonstrates the possible monodentate and bidentate binding with two coordinating anions. The represented anions are asymmetric as illustrated by the color code (blue and red). Thus, with two coordinating asymmetric anions, a CN of two, three, or four is possible.

Differential vs. Integral Analysis

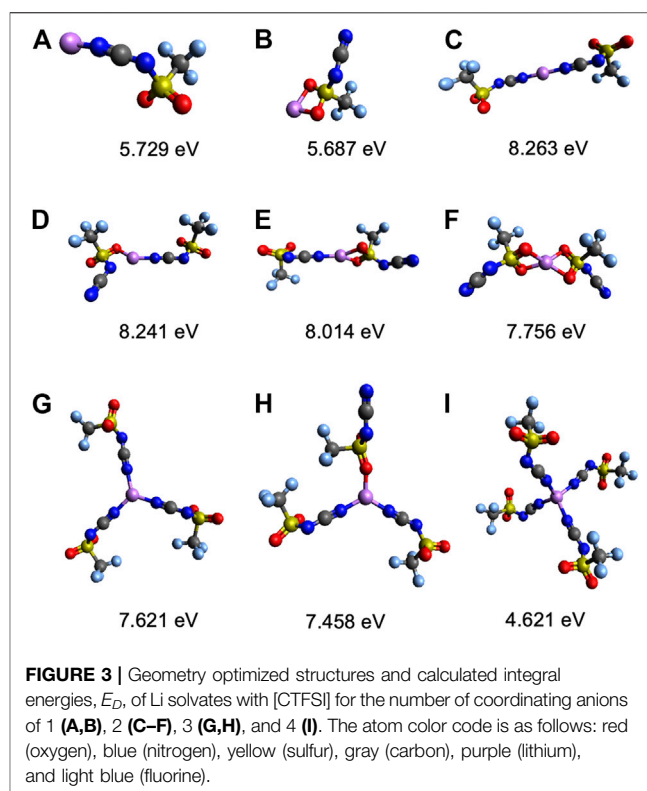
Two methods were used to determine the energy difference associated with adding a new anion to the first solvation shell of Li^+ . These methods can be visualized in **Figure 2** for a symmetric anion such as [TFSI] coordination with Li^+ . The integral binding energy, which is equal to $-1 \times E_D$, is shown *via* the green diagonal line. It refers to the energy to add n anions to Li^+ , for example, $\text{Li}^+ + 2[\text{anion}]^- \rightarrow \text{Li}[\text{anion}]_2^-$. In contrast, the differential binding energy is the energy to add one anion at a time, for example, $\text{Li}[\text{anion}] + [\text{anion}]^- \rightarrow \text{Li}[\text{anion}]_2^-$. The differential binding energy is useful for assessing the maximum number of anions that will coordinate to Li^+ , whereas the integral binding energy is useful for assessing relative stabilities. A detailed example of the asymmetric [CTFSI] and [FTFSI] differential vs. integral analysis can be seen in **Supplementary Tables S1, S2**.

Ab Initio Thermodynamic Analysis

The thermodynamic stabilities of structurally and compositionally different Li solvates were calculated using an *ab initio* thermodynamic analysis (Soon et al., 2007; Getman et al., 2008; Grundner et al., 2015; Paolucci et al., 2016). This analysis was performed specifically for [TFSI]- and [DCA]-containing solvates. The *ab initio* thermodynamic analysis calculates the free energy of formation for different Li solvates at different mole fractions of [DCA] and [TFSI] in solution according to the following equation:



where a is the number of [DCA] anions and b is the number of [TFSI] anions that coordinate to a single Li^+ cation. We used a library for the analysis that includes all [DCA]-only ($1 \leq a \leq 4$; $b = 0$), [TFSI]-only ($a = 0$; $1 \leq b \leq 3$), and [DCA]/[TFSI] ($1 \leq a + b \leq$



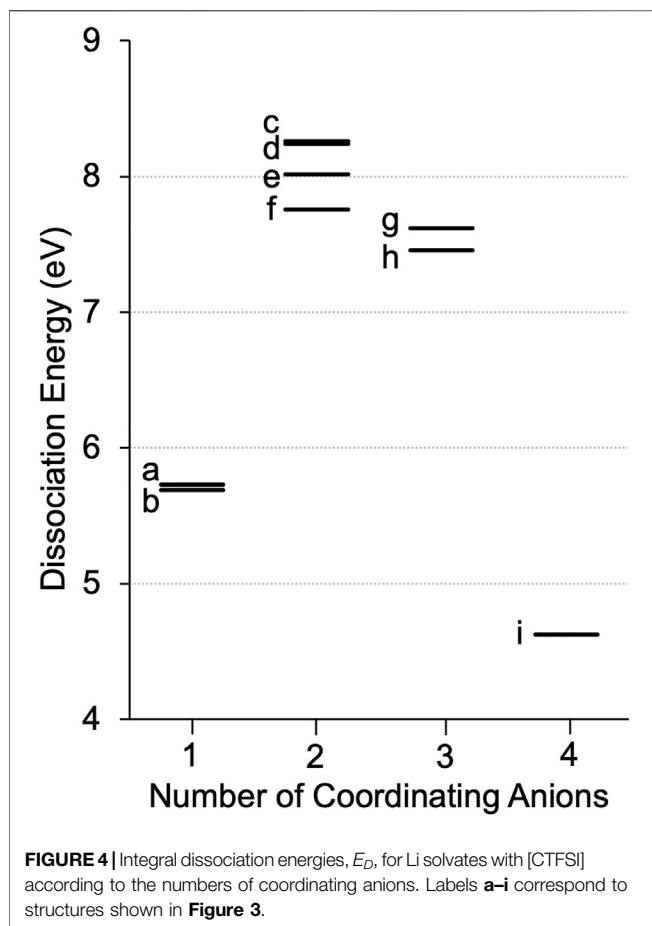
3) structures. According to the *ab initio* thermodynamic analysis, the free energy of formation for compositionally different structures ($\text{Li}[\text{DCA}]_a[\text{TFSI}]_b$) is calculated by transforming the free energy of a fixed number of species, $\Delta G(T, P, N_{\text{Li}^+}, N_{[\text{TFSI}]}, N_{[\text{DCA}]})$, where * denotes that the anion species is coordinated with the Li^+ cation, to a fixed chemical potential using Legendre's transformations (see Supporting Information for more details). In this study, we transform $N_{[\text{TFSI}]}$ and $N_{[\text{DCA}]}$ to $\mu_{[\text{TFSI}]}$ and $\mu_{[\text{DCA}]}$; the resulting free energy of formation is denoted as $\Delta G^{(2)}$ (where the 2 superscript denotes two variables were transformed) and is given by the following equation:

$$\Delta G^{(2)}(T, P, N_{\text{Li}^+}, \mu_{[\text{TFSI}]}, \mu_{[\text{DCA}]}) = (\Delta E) - (\mu_{[\text{TFSI}]}) (N_{[\text{TFSI}]}^*) - (\mu_{[\text{DCA}]}) \times (N_{[\text{DCA}]}^*), \quad (3)$$

where ΔE is the difference in electronic energy between a $\text{Li}[\text{DCA}]_a[\text{TFSI}]_b$ structure and the isolated Li^+ cation. Chemical potentials of [DCA] and [TFSI] are calculated (Starzak, 2010; Moučka et al., 2015) as follows:

$$\mu_i^*(T, x_i) = E_i + RT \ln(\gamma_i x_i), \quad (4)$$

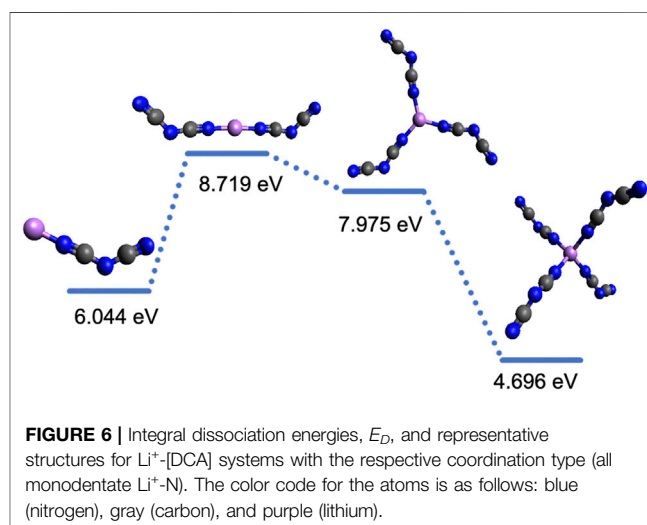
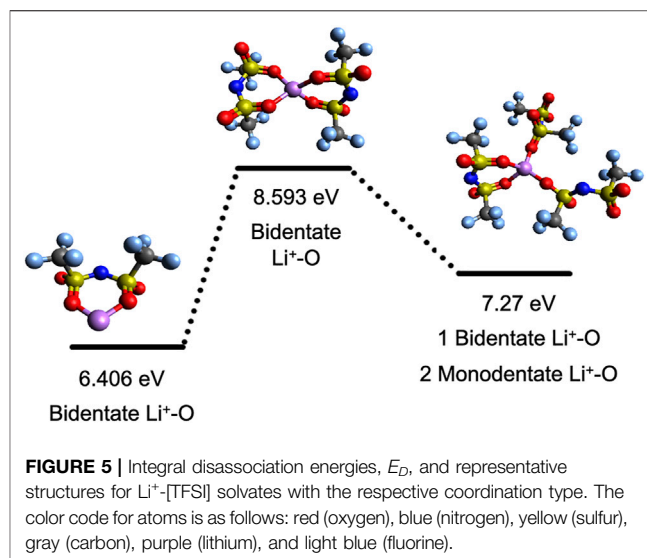
where E_i is the electronic energy of the anion ($i = \text{DCA}$ or TFSI), x_i is the mole fraction in solution, R is the gas constant, and γ_i is the activity coefficient. We assume a temperature of 298 K for all calculations and that all activity coefficients are equal to unity (Noda et al., 2001; Sun et al., 2018). The influence of this choice is detailed in the Supporting Information.



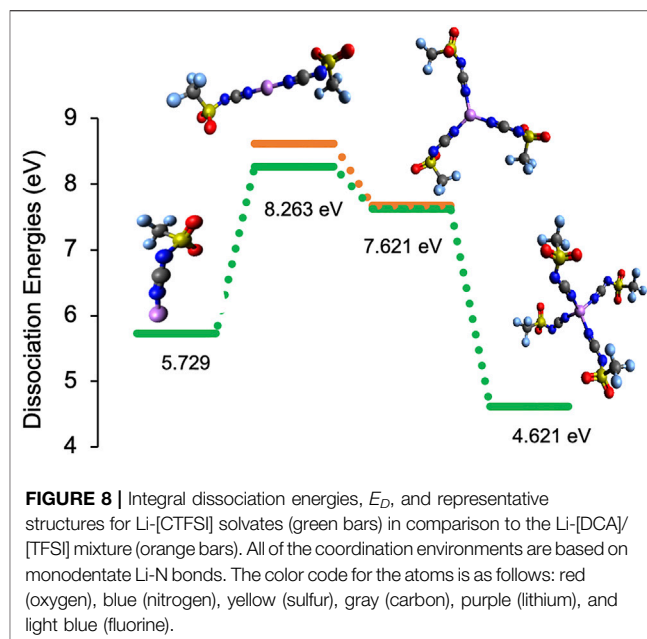
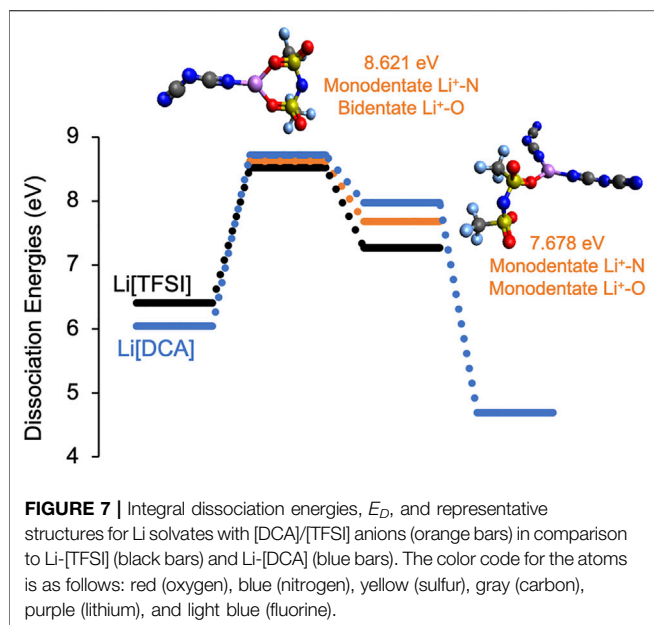
RESULTS AND DISCUSSION

Thermodynamically Favored Structure

The Li^+ solvation in the electrolyte is dynamic, and different populations of multiple solvate structures may be present. In order to determine the most likely configurations, dissociation energies were calculated for all of the possible monodentate and bidentate coordination environments while incrementally increasing the number of anions around Li^+ . The list of calculated E_D 's for all of the Li solvates studied is in **Supplementary Table S3**. For the asymmetric [CTFSI], it is determined that Li^+ can coordinate with up to four anions where CN varies from one to four, as shown in **Figure 3**. Both the oxygen on the sulfonyl ($\text{Li}^+\text{-O}$) and the nitrogen on the cyano group ($\text{Li}^+\text{-N}$) can coordinate with Li^+ . Therefore, when there is one [CTFSI] coordinating with Li^+ , two configurations are possible, as seen in **Figures 3A,B**. With two coordinating anions, there are four possible configurations, as seen in **Figures 3C–F**. With three [CTFSI] anions, there are only two possible structures: all cyano coordination with monodentate bonds or two cyano and one sulfonyl oxygen coordination each with monodentate bonds, as shown in **Figures 3G,H**. Finally, moving to four coordinating anions, the only possible structure is seen in **Figure 3I** *via* monodentate $\text{Li}^+\text{-N}$ bonds. The calculated

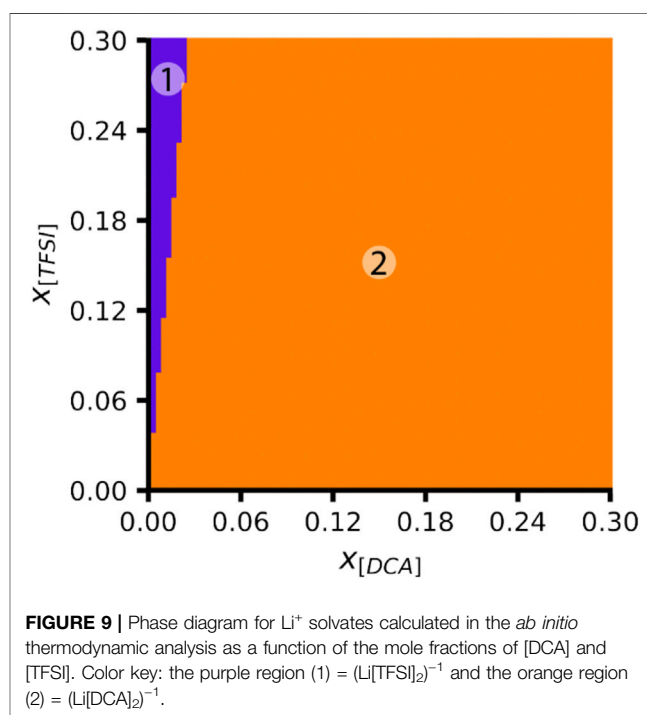


E_D 's for these Li solvate structures at differing numbers of coordinating anions are shown in **Figure 4**. It is interpreted that the structure with the highest E_D is the most stable since it requires more energy to break the coordination. Therefore, Li solvates with the highest E_D (strongest) among the multiple possible configurations for a specific coordination are said to be thermodynamically favored. According to the energies in **Figure 4**, for both Li[CTFSI] and $(\text{Li[CTFSI]}_2)^{-1}$, Li^+ prefers to coordinate with [CTFSI] *via* the cyano group ($\text{Li}^+\text{-N}$) over the sulfonyl oxygen atoms ($\text{Li}^+\text{-O}$). The most optimal Li solvate is $(\text{Li[CTFSI]}_2)^{-1}$ where Li^+ coordinates with two cyano groups each through monodentate conformation as in **Figure 3C** and/or one monodentate with cyano and another monodentate with sulfonyl, as in **Figure 3D**. Based on the three and four anion systems relying solely on $\text{Li}^+\text{-N}$ coordination, all $\text{Li}^+\text{-N}$ coordinated $(\text{Li[CTFSI]}_2)^{-1}$ are used for further analysis. This methodology for selecting the thermodynamically favored structures was implemented for all of the anions investigated in this study.



To better understand the change in solvation energy with the asymmetric anion in comparison to the symmetric anions, the Li^+ -[CTFSI] system was compared with the Li^+ -[TFSI] and Li^+ -[DCA] which are more widely studied experimentally (Sakaebe and Matsumoto, 2003; Garcia et al., 2004; Borgel et al., 2009; Yoon et al., 2013; Shen et al., 2015).

Further, the Raman frequencies of [TFSI], [DCA], and [CTFSI] with and without Li^+ coordination were calculated (spectra shown in **Supplementary Figures S1–S3**). The prominent vibrations were of the S-N-S and S=O bonds of [TFSI], and the C-N-C bond of [DCA]. For [CTFSI], the vibrations of interest are S-N- C_{CN} , S=O, and $\text{C}\equiv\text{N}$. With Li^+ coordination, the symmetric S-N-S stretch of *cis*-[TFSI] at 735 cm^{-1} experiences a blue shift by 10 cm^{-1} , which is consistent with previously reported experiments (Huang et al., 2019a; Huang et al., 2019b; Nurnberg et al., 2020). The S=O symmetric stretch appears at $1,132$ and $1,148\text{ cm}^{-1}$. With Li^+ coordination (structure in **Figure 5** with single [TFSI] coordinated to Li^+), the S=O peaks shift to $1,100$ and $1,111\text{ cm}^{-1}$. These vibrations have similar trends with [CTFSI]. Specifically, the S-N- C_{CN} peak in [CTFSI] at 762 cm^{-1} shifts to 779 cm^{-1} with Li^+ coordination (structure in **Figure 3B**). The S=O vibration of [CTFSI] at $1,118\text{ cm}^{-1}$ shifts to $1,099\text{ cm}^{-1}$. Similarly, the C-N-C asymmetric and symmetric stretches of [DCA] at $2,183$ and $2,199\text{ cm}^{-1}$ show blue shifts by 15 and 45 cm^{-1} (structure in **Figure 6** with single [DCA] coordinated to Li^+), respectively, which are also consistent with previous experimental findings (Huang et al., 2019b). [CTFSI] shows a similar peak location as [DCA] for the $\text{C}\equiv\text{N}$ symmetric stretch at $2,195\text{ cm}^{-1}$, with a blue shift of 42 cm^{-1} with Li^+ coordination (structure in **Figure 3A**), which is similar to the previous experimental findings (Nurnberg et al., 2020). The overall consistency of the peak locations and shifts when moving from the pure anion to the Li solvate provide confidence that our converged structures closely match with the known experimental reports.



Li^+ Solvation by [TFSI], [DCA], and [CTFSI]

Figures 5, 6 show the dissociation energies and structures for Li solvates with the [TFSI] and [DCA] anions, respectively. Li^+ has a CN of four with both [TFSI] and [DCA], according to the number of coordination sites. However, the number of anions in the first solvation shell for [TFSI] is three, while it is four for [DCA]. This is a result of [TFSI] coordination *via* the oxygen atoms on the same anion where the two Li^+ -O coordination *via* bidentate bonds with two [TFSI] anions yield a CN of four, as seen in

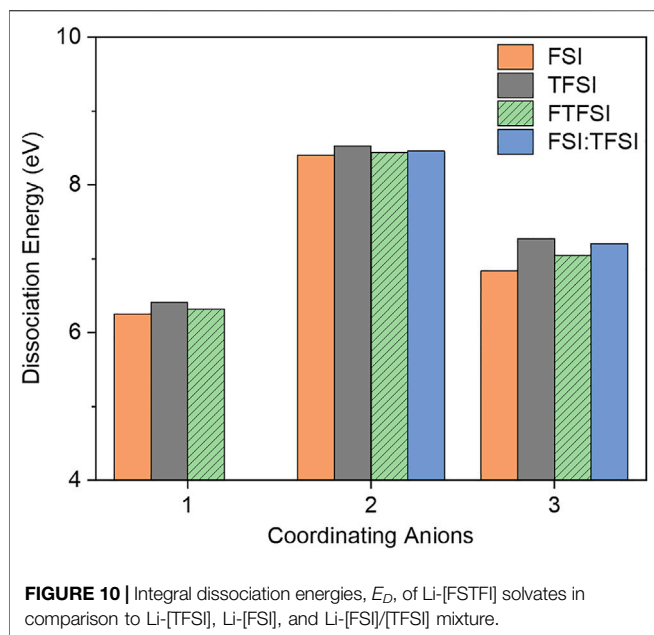


Figure 5. Previously, the integral binding energy for Li solvates with two [TFSI] anions calculated at the DFT/6-311+(d) level of theory was reported as -792.5 kJ/mol (8.2 eV) (Umebayashi et al., 2007), which is in reasonable agreement with our calculated Li [TFSI] $_2^{-1}$ (middle structure in **Figure 5**) E_D of 8.59 eV (828.8 kJ/mol). For [DCA], there is Li $^{+}$ -N interaction *via* monodentate bonds; therefore, four [DCA] anions yield a CN of four, as seen in **Figure 6**. Based on these results, Li $^{+}$ -N coordination is stronger than Li $^{+}$ -O, especially when solvates with 2–3 anions are compared, which is consistent with previously reported results (Huang et al., 2019b). Therefore, one can suggest that Li solvates with a [DCA] anion will be more rigid, and this can hinder Li $^{+}$ hopping in comparison to Li solvates with [TFSI]. This is counterintuitive to the low viscosities that are promoted with [DCA] anion in ILs. It should be recalled that while smaller and more rigid Li solvates may have higher vehicular motion, the hopping mechanism can prevail at high Li salt concentrations with weaker solvate structures.

To further understand the relationship of how the differing anions affect the strength of the interaction between Li $^{+}$ and the [TFSI] and [DCA] anions, the E_D of the mixture system, [TFSI]/[DCA], as well as the individual anions are compared, as in **Figure 7**.

It should be noted that the minimum number of solvating anions for the [DCA]/[TFSI] system studied is two since a single anion would not capture the mixture behavior. Additionally, Li $^{+}$ solvation by three anions can either contain two [DCA] and one [TFSI] or *vice versa*; however, Li $^{+}$ coordination with two [DCA] anions provided a more thermodynamically favored structure (as shown in **Figure 7**). Comparing the Li $^{+}$ solvation energies of the [DCA]/[TFSI] mixture with those of [DCA]-only and [TFSI]-only systems, it is seen that with a CN of three, the mix-anion system (represented by orange bars in **Figure 7**) has a weaker E_D than Li-[DCA] (blue bars) and a stronger E_D than Li-[TFSI]

(black) systems. For a perspective on how the mix-anion system of [DCA]/[TFSI] compares with the asymmetric analog of [CTFSI], the calculated dissociation energies are shown in **Figure 8**.

Based on the lower dissociation energies of Li solvates with the [CTFSI] anion, it can be said that the solvation cage is weakened by the anion asymmetry and the presence of competing coordination sites for Li $^{+}$. For example, comparing systems with two total solvation anions around Li $^{+}$, (Li[CTFSI] $_2$) $^{-1}$ has the most facile E_D of 8.26 eV in comparison to 8.59 eV for (Li[TFSI] $_2$) $^{-1}$, 8.62 eV for (Li[DCA][TFSI]) $^{-1}$, and 8.72 eV for (Li[DCA] $_2$) $^{-1}$. When [CTFSI] was compared with a slightly different asymmetric anion [CFSI], similar results were obtained, where Li-[CFSI] has more facile E_D than the solvates with [FSI] or [DCA] alone. Further, Li-[CFSI] solvates had slightly reduced E_D when compared to [CTFSI] (see **Supplementary Figure S4**). To understand the influence of solution composition on the Li $^{+}$ solvate, we performed an *ab initio* thermodynamic analysis of the mix-anion [DCA]/[TFSI] system. The thermodynamic stability for the anionic [DCA]/[TFSI] system as a function of [DCA] and [TFSI] mole fraction is presented in **Figure 9**. Indeed, these results indicate that (Li[DCA] $_2$) $^{-1}$ is thermodynamically most preferred except for very low mole fractions of [DCA], where (Li[TFSI] $_2$) $^{-1}$ is preferred. None of the mix-anion structures are thermodynamically preferred according to the *ab initio* thermodynamic analysis.

Taken together, the above analysis suggests that assessment of ion pair lifetimes and measurement of the Li $^{+}$ transport when solvated by asymmetric anions would be interesting and necessary to understand the transport mechanism as these

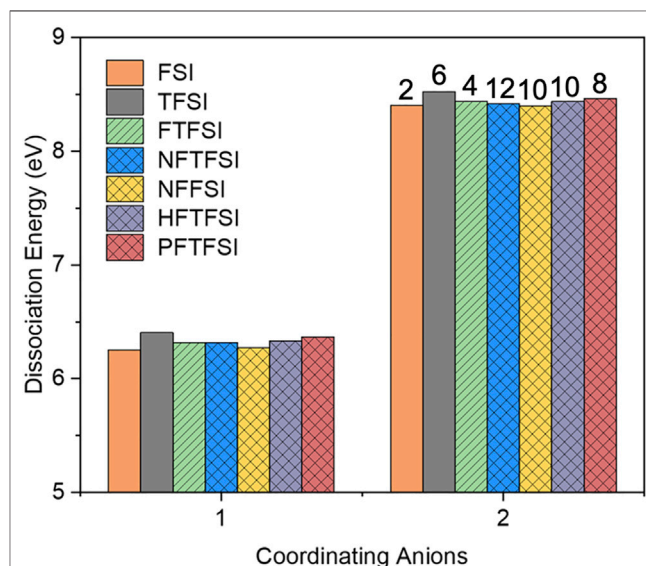


FIGURE 11 | Integral dissociation energies with respect to the number of coordinating asymmetric anions. [FTFSI] anion is highlighted with slashes, and all other asymmetric fluorinated anions are highlighted with crosshatches. PF, NF, and HF nomenclatures in front of TFSI or FSI stand for C $_2$ F $_5$, C $_3$ F $_7$, and C $_4$ F $_9$ chains, respectively. The numbers on top of the bars indicate the number of total fluorines in the anion.

studies may provide a method to tune Li^+ hopping in concentrated electrolytes.

Li^+ solvation by [FSI], [TFSI], and [FTFSI]

Li solvates with the asymmetric anion [FTFSI] were also studied in comparison to [TFSI], [FSI], and the [FSI]/[TFSI] mixture. It has been shown that Li^+ transport is enhanced in ILs with [FSI]/[TFSI] mix-anions, resulting in improved battery cycling over the Li-IL binary mixtures with either the [FSI] or the [TFSI] anion (Lux et al., 2009; Bayley et al., 2011; Huang et al., 2019a). In order to understand whether the improvements in LIBs with these electrolytes originated from a change in solvation energies, we calculated the dissociation energies for this system, similar to the analysis performed for Li^+ -[CTFSI]. **Figure 10** shows that the asymmetric [FTFSI] behaves similarly to [FSI] and the [FSI]/[TFSI] mixture. It should be noted that the Li solvate with the [FSI]/[TFSI] mixture and three coordinating anions consists of two [TFSI] and one [FSI], as this produced the more thermodynamically favored structure. The other configuration with two [FSI] and one [TFSI] system resulted in a dissociation energy of 6.907 eV, which is slightly lower than coordination with three [FTFSI] anions for $(\text{Li}^+ - [\text{FTFSI}]_3)^{-2}$ at 7.045 eV. Unlike the [CTFSI] asymmetric anion, Li solvates with [FTFSI] have higher E_D than that of its parent anion [FSI], and the E_D of all configurations is similar. This is due to the single coordination chemistry through the sulfonyl oxygen in all of the cases considered in **Figure 10**. The most significant difference among Li solvates with [TFSI], [FSI], and [FTFSI] is that with three coordinating anions, [FSI] has all monodentate $\text{Li}^+ - \text{O}(=\text{S})$ coordination, leading to a CN of three, while [FTFSI] and [TFSI] have one bidentate and two monodentate bonds, respectively, leading to a CN of four, as seen in **Supplementary Figure S5**. All other structures demonstrated bidentate configurations where CN was two for a single solvating anion and four for two solvating anions. Due to the similarities in the solvation structure, the only impact on the solvation strength comes from the fluorinated groups, either F-S ([FSI]) or CF_3 -S ([TFSI] and [FTFSI]).

Fluorination Effects

The impacts of the length of fluorination and the degree of asymmetry on the calculated dissociation energies for Li solvates are captured in **Figure 11**. The asymmetry of the anions represented by the patterned bars in **Figure 11** is dictated by the length of the fluorinated alkyl chain on either the [FSI] or the [TFSI] parent anion. Specifically, the PF, NF, and HF nomenclatures in front of TFSI stand for C_2F_5 , C_3F_7 , and C_4F_9 chains, respectively, on the one side of the derivatized [TFSI] anion. As seen, there are no significant differences in E_D . The lowest dissociation energy is with [NFFSI] which has the longest fluorinated alkyl chains (C_4F_9) on the one side, with the other side being F-S.

While these results cannot point to a specific advantage of the longer fluorinated anions since they have the same enthalpic effects on Li^+ coordination, we expect to find entropic effects in solution which are not present in gas phase energy evaluations. In the case of [NFTFSI] and

[NFFSI], the long fluorinated butane chains of each anion align with each other when the Li solvate has two anions with a CN of four *via* two bidentate bonds (**Supplementary Figure S6**). This alignment of the fluorinated alkyl chains may have a significant impact on the bulk liquid structure that cannot be evaluated by gas phase DFT calculations. We expect that the increase in the fluorination length will improve the viscosity and the solvation dynamics more than the enthalpic contributions to the dissociation energies, due to the delocalization of charge along the alkyl chain and inability of fluorochains solvating Li^+ . In particular, the treatment of the entire system with IL cation and other cosolvents, if present, can provide more realistic solvate structures when longer chain fluorinated asymmetric anions are solvating Li^+ . By studying these systems with MD simulations and experimental spectroscopic studies (Raman and NMR), the impact of fluorination on the bulk solvation and transport properties can be probed to a greater extent.

CONCLUSION

The solvation structure and energies of Li^+ with solvating anions of [TFSI], [DAC], [CTFSI], and [FTFSI] and a number of longer fluorinated anions with $\text{Li}^+ - \text{O}$ and $\text{Li}^+ - \text{N}$ coordination capability were calculated. The anions studied produced Li solvate structures with CNs of 2–4 depending on the size and functionality of the anion. Li solvates with a CN of two resulted in the highest dissociation energies (most stable conformers). Li solvates with a CN of one resulted in the lowest E_D with the exception of [DCA] and [CTFSI]. [DCA] and [CTFSI] were able to coordinate with four anions, and these Li solvates produced the lowest E_D (weakest). Through the E_D analysis, we found that the asymmetric [CTFSI] anion coordination with Li^+ is weaker than [TFSI] and [DCA] anions as well as the [TFSI]/[DCA] mixture. There are a larger number of solvate structures for Li-[CTFSI] solvate than those for [TFSI] and [DCA]. We suspect that this heterogeneity in the first solvation shell may lead to increased fluidity and structural diffusion (hopping) of Li^+ compared to solvates with [TFSI] and [DCA]. The [FTFSI] anion showed very similar results in terms of E_D as the [TFSI] and [FSI] parent anions due to the similar coordination environments between the three anions. However, [FTFSI] yielded slightly lower E_D than that of the Li^+ solvate with the parent anion mixture of [TFSI]/[FSI]. Given the weakened solvation energies, it would be interesting to study the impact of IL electrolytes with asymmetric anion on the Li^+ transference and performance of LIBs. The impact of fluorination length seems to have limited impact on E_D , with the longer fluorinated chains having slightly lower E_D than [TFSI]. However, we anticipate that these long fluorinated alkyl chains will have more significant entropic effects, which are not captured in gas phase DFT calculations. By studying these systems with MD simulations and experimental spectroscopic studies (Raman and NMR), the impact of fluorination on the bulk solvation and transport

properties can be probed to a greater extent. It will also be crucial for future studies to evaluate the impact of IL cations as well as the electric field present in Li batteries on the solvation structure and dynamics of Li^+ .

DATA AVAILABILITY STATEMENT

The original contributions presented in the study are included in the article/**Supplementary Material**; further inquiries can be directed to the corresponding author.

AUTHOR CONTRIBUTIONS

DP performed the DFT calculations for geometries, vibrations, and dissociation energies. SV performed the *ab initio* thermodynamic analysis. RG supervised the *ab initio* thermodynamic analysis and contributed to the discussions. BG developed the plan, supervised DFT calculations, and

contributed to the discussions. All authors contributed to the writing of the manuscript.

FUNDING

BG would like to acknowledge funding from the National Science Foundation (CBET, Award No. 1903259). BG and DP would also like to acknowledge the High Performance Computing Resource in the Core Facility for Advanced Research Computing at Case Western Reserve University. SV is supported by a GAANN Fellowship (Award Number: P200A180076) from the United States Department of Education.

SUPPLEMENTARY MATERIAL

The Supplementary Material for this article can be found online at: <https://www.frontiersin.org/articles/10.3389/fenrg.2021.725010/full#supplementary-material>

REFERENCES

- Armand, M., Endres, F., MacFarlane, D. R., Ohno, H., and Scrosati, B. (2009). Ionic-Liquid Materials for the Electrochemical Challenges of the Future. *Nat. Mater.* 8 (8), 621–629. doi:10.1038/nmat2448
- Bae, S.-Y., Shim, E.-G., and Kim, D.-W. (2013). Effect of Ionic Liquid as a Flame-Retarding Additive on the Cycling Performance and thermal Stability of Lithium-Ion Batteries. *J. Power Sourc.* 244, 266–271. doi:10.1016/j.jpowsour.2013.01.100
- Bauschlicher, C. W. (2018). Li+-Ligand Binding Energies and the Effect of Ligand Fluorination on the Binding Energies. *Chem. Phys. Lett.* 694, 86–92. doi:10.1016/j.cplett.2018.01.047
- Bayley, P. M., Best, A. S., MacFarlane, D. R., and Forsyth, M. (2011). Transport Properties and Phase Behaviour in Binary and Ternary Ionic Liquid Electrolyte Systems of Interest in Lithium Batteries. *ChemPhysChem* 12 (4), 823–827. doi:10.1002/cphc.201000909
- Borgel, V., Markevich, E., Aurbach, D., Semrau, G., and Schmidt, M. (2009). On the Application of Ionic Liquids for Rechargeable Li Batteries: High Voltage Systems. *J. Power Sourc.* 189 (1), 331–336. doi:10.1016/j.jpowsour.2008.08.099
- Borodin, O., Giffin, G. A., Moretti, A., Haskins, J. B., Lawson, J. W., Henderson, W. A., et al. (2018). Insights into the Structure and Transport of the Lithium, Sodium, Magnesium, and Zinc Bis(trifluoromethanesulfonyl)imide Salts in Ionic Liquids. *J. Phys. Chem. C* 122 (35), 20108–20121. doi:10.1021/acs.jpcc.8b05573
- Borodin, O., Smith, G. D., and Henderson, W. (2006). Li+ Cation Environment, Transport, and Mechanical Properties of the LiTFSI Doped N-Methyl-N-alkylpyrrolidinium+TFSI- Ionic Liquids. *J. Phys. Chem. B* 110 (34), 16879–16886. doi:10.1021/jp061930t
- Borodin, O., Suo, L., Gobet, M., Ren, X., Wang, F., Faraone, A., et al. (2017). Liquid Structure with Nano-Heterogeneity Promotes Cationic Transport in Concentrated Electrolytes. *ACS Nano* 11 (10), 10462–10471. doi:10.1021/acsnano.7b05664
- Brinkkötter, M., Giffin, G. A., Moretti, A., Jeong, S., Passerini, S., and Schönhoff, M. (2018). Relevance of Ion Clusters for Li Transport at Elevated Salt Concentrations in [Pyr12O1][TFSI] Ionic Liquid-Based Electrolytes. *Chem. Commun.* 54, 4278–4281. doi:10.1039/C8CC01416G
- Castiglione, F., Ragg, E., Mele, A., Appetecchi, G. B., Montanino, M., and Passerini, S. (2011). Molecular Environment and Enhanced Diffusivity of Li+ Ions in Lithium-Salt-Doped Ionic Liquid Electrolytes. *J. Phys. Chem. Lett.* 2 (3), 153–157. doi:10.1021/jz101516c
- Chen, F., and Forsyth, M. (2019). Computational Investigation of Mixed Anion Effect on Lithium Coordination and Transport in Salt Concentrated Ionic Liquid Electrolytes. *J. Phys. Chem. Lett.* 10 (23), 7414–7420. doi:10.1021/acs.jpclett.9b02416
- Ditchfield, R., Hehre, W. J., and Pople, J. A. (1971). Self-Consistent Molecular-Orbital Methods. IX. An Extended Gaussian-Type Basis for Molecular-Orbital Studies of Organic Molecules. *J. Chem. Phys.* 54 (2), 724. doi:10.1063/1.1674902
- Duluard, S., Grondin, J., Bruneel, J.-L., Pianet, I., Grélaud, A., Campet, G., et al. (2008). Lithium Solvation and Diffusion in the 1-Butyl-3-Methylimidazolium Bis(trifluoromethanesulfonyl)imide Ionic Liquid. *J. Raman Spectrosc.* 39 (5), 627–632. doi:10.1002/jrs.1896
- Eftekhari, A., Liu, Y., and Chen, P. (2016). Different Roles of Ionic Liquids in Lithium Batteries. *J. Power Sourc.* 334, 221–239. doi:10.1016/j.jpowsour.2016.10.025
- Elmore, C., Seidler, M., Ford, H., Merrill, L., Upadhyay, S., Schneider, W., et al. (2018). Ion Transport in Solvent-free, Crosslinked, Single-Ion Conducting Polymer Electrolytes for Post-Lithium Ion Batteries. *Batteries* 4 (2), 28. doi:10.3390/batteries4020028
- Frisch, M. J., Trucks, G. W., Schlegel, H. B., Scuseria, G. E., Robb, M. A., Cheeseman, J. R., et al. (2016). *Gaussian 16 Rev. C.01*. Wallingford, CT.
- Fujii, K., Hamano, H., Doi, H., Song, X., Tsuzuki, S., Hayamizu, K., et al. (2013). Unusual Li+ Ion Solvation Structure in Bis(fluorosulfonyl)amide Based Ionic Liquid. *J. Phys. Chem. C* 117 (38), 19314–19324. doi:10.1021/jp4053264
- Fulfer, K. D., and Kuroda, D. G. (2016). Solvation Structure and Dynamics of the Lithium Ion in Organic Carbonate-Based Electrolytes: A Time-dependent Infrared Spectroscopy Study. *J. Phys. Chem. C* 120 (42), 24011–24022. doi:10.1021/acs.jpcc.6b08607
- Galiński, M., Lewandowski, A., and Stepniak, I. (2006). Ionic Liquids as Electrolytes. *Electrochimica Acta* 51 (26), 5567–5580. doi:10.1016/j.electacta.2006.03.016
- Garcia, B., Lavallée, S., Perron, G., Michot, C., and Armand, M. (2004). Room Temperature Molten Salts as Lithium Battery Electrolyte. *Electrochim. Acta* 49 (26), 4583–4588. doi:10.1016/j.electacta.2004.04.041
- Getman, R. B., Xu, Y., and Schneider, W. F. (2008). Thermodynamics of Environment-dependent Oxygen Chemisorption on Pt(111). *J. Phys. Chem. C* 112 (26), 9559–9572. doi:10.1021/jp800905a
- Grundner, S., Markovits, M. A. C., Li, G., Tromp, M., Pidko, E. A., Hensen, E. J. M., et al. (2015). Single-site Trinuclear Copper Oxygen Clusters in Mordenite for Selective Conversion of Methane to Methanol. *Nat. Commun.* 6 (1), 7546. doi:10.1038/ncomms8546
- Han, H., Guo, J., Zhang, D., Feng, S., Feng, W., Nie, J., et al. (2011). Lithium (Fluorosulfonyl)(nonafluorobutanesulfonyl)imide (LiFNFESI) as Conducting Salt to Improve the High-Temperature Resilience of Lithium-Ion Cells. *Electrochem. Commun.* 13 (3), 265–268. doi:10.1016/j.elecom.2010.12.030
- Haskins, J. B., Bennett, W. R., Wu, J. J., Hernández, D. M., Borodin, O., Monk, J. D., et al. (2014). Computational and Experimental Investigation of Li-Doped Ionic

- Liquid Electrolytes: [pyr14][TFSI], [pyr13][FSI], and [EMIM][BF₄]. *J. Phys. Chem. B* 118 (38), 11295–11309. doi:10.1021/jp5061705
- Hoffknecht, J.-P., Drews, M., He, X., and Paillard, E. (2017). Investigation of the N-Butyl-N-Methyl Pyrrolidinium Trifluoromethanesulfonyl-N-cyanoamide (PYR 14 TFSAM) Ionic Liquid as Electrolyte for Li-Ion Battery. *Electrochim. Acta* 250, 25–34. doi:10.1016/j.electacta.2017.08.020
- Huang, Q., Lee, Y.-Y., and Gurkan, B. (2019a). Pyrrolidinium Ionic Liquid Electrolyte with Bis(trifluoromethylsulfonyl)imide and Bis(fluorosulfonyl)imide Anions: Lithium Solvation and Mobility, and Performance in Lithium Metal-Lithium Iron Phosphate Batteries. *Ind. Eng. Chem. Res.* 58, 22587–22597. doi:10.1021/acs.iecr.9b03202
- Huang, Q., Lourenço, T. C., Costa, L. T., Zhang, Y., Maginn, E. J., and Gurkan, B. (2019b). Solvation Structure and Dynamics of Li⁺ in Ternary Ionic Liquid-Lithium Salt Electrolytes. *J. Phys. Chem. B* 123 (2), 516–527. doi:10.1021/acs.jpbc.8b08859
- Imai, M., Tanabe, I., Ikehata, A., Ozaki, Y., and Fukui, K.-i. (2020). Attenuated Total Reflectance Far-Ultraviolet and Deep-Ultraviolet Spectroscopy Analysis of the Electronic Structure of a Dicyanamide-Based Ionic Liquid with Li⁺. *Phys. Chem. Chem. Phys.* 22 (38), 21768–21775. doi:10.1039/D0CP03865B
- Kerner, M., Plylahan, N., Scheers, J., and Johansson, P. (2015). Ionic Liquid Based Lithium Battery Electrolytes: Fundamental Benefits of Utilising Both TFSI and FSI Anions. *Phys. Chem. Chem. Phys.* 17 (29), 19569–19581. doi:10.1039/C5CP01891A
- Krachkovskiy, S., Dontigny, M., Rochon, S., Kim, C., Trudeau, M. L., and Zaghib, K. (2020). Determination of Binary Diffusivities in Concentrated Lithium Battery Electrolytes via NMR and Conductivity Measurements. *J. Phys. Chem. C* 124 (45), 24624–24630. doi:10.1021/acs.jpcc.0c07383
- Lassègues, J.-C., Grondin, J., Aupetit, C., and Johansson, P. (2009). Spectroscopic Identification of the Lithium Ion Transporting Species in LiTFSI-Doped Ionic Liquids. *J. Phys. Chem. A* 113 (1), 305–314. doi:10.1021/jp806124w
- Lee, C., Yang, W., and Parr, R. G. (1988). Development of the Colle-Salvetti Correlation-Energy Formula into a Functional of the Electron Density. *Phys. Rev. B* 37 (2), 785–789. doi:10.1103/physrevb.37.785
- Lesch, V., Jeremias, S., Moretti, A., Passerini, S., Heuer, A., and Borodin, O. (2014). A Combined Theoretical and Experimental Study of the Influence of Different Anion Ratios on Lithium Ion Dynamics in Ionic Liquids. *J. Phys. Chem. B* 118 (26), 7367–7375. doi:10.1021/jp501075g
- Lesch, V., Li, Z., Bedrov, D., Borodin, O., and Heuer, A. (2016). The Influence of Cations on Lithium Ion Coordination and Transport in Ionic Liquid Electrolytes: a MD Simulation Study. *Phys. Chem. Chem. Phys.* 18 (1), 382–392. doi:10.1039/C5CP05111H
- Li, Z., Smith, G. D., and Bedrov, D. (2012). Li⁺ Solvation and Transport Properties in Ionic Liquid/Lithium Salt Mixtures: A Molecular Dynamics Simulation Study. *J. Phys. Chem. B* 116 (42), 12801–12809. doi:10.1021/jp3052246
- Lux, S. F., Schmuck, M., Appetecchi, G. B., Passerini, S., Winter, M., and Balducci, A. (2009). Lithium Insertion in Graphite from Ternary Ionic Liquid-Lithium Salt Electrolytes: II. Evaluation of Specific Capacity and Cycling Efficiency and Stability at Room Temperature. *J. Power Sourc.* 192 (2), 606–611. doi:10.1016/j.jpowsour.2009.02.066
- Matsuda, Y., Fukushima, T., Hashimoto, H., and Arakawa, R. (2002). Solvation of Lithium Ions in Mixed Organic Electrolyte Solutions by Electrospray Ionization Mass Spectroscopy. *J. Electrochem. Soc.* 149 (8), A1045. doi:10.1149/1.1489687
- McEldrew, M., Goodwin, Z. A. H., Bi, S., Kornyshev, A. A., and Bazant, M. Z. (2021). Ion Clusters and Networks in Water-In-Salt Electrolytes. *J. Electrochem. Soc.* 168 (5), 050514. doi:10.1149/1945-7111/abf975
- Moučka, F., Nezbeda, I., and Smith, W. R. (2015). Chemical Potentials, Activity Coefficients, and Solubility in Aqueous NaCl Solutions: Prediction by Polarizable Force Fields. *J. Chem. Theor. Comput.* 11 (4), 1756–1764. doi:10.1021/acs.jctc.5b00018
- Navarra, M. A. (2013). Ionic Liquids as Safe Electrolyte Components for Li-Metal and Li-Ion Batteries. *MRS Bull.* 38 (7), 548–553. doi:10.1557/mrs.2013.152
- Noda, A., Hayamizu, K., and Watanabe, M. (2001). Pulsed-Gradient Spin-Echo 1H and 19F NMR Ionic Diffusion Coefficient, Viscosity, and Ionic Conductivity of Non-chloroaluminate Room-Temperature Ionic Liquids. *J. Phys. Chem. B* 105 (20), 4603–4610. doi:10.1021/jp004132q
- Nürnberg, P., Lozinskaya, E. I., Shaplov, A. S., and Schönhoff, M. (2020). Li Coordination of a Novel Asymmetric Anion in Ionic Liquid-In-Li Salt Electrolytes. *J. Phys. Chem. B* 124 (5), 861–870. doi:10.1021/acs.jpbc.9b11051
- Palafox, M. A. (2018). DFT Computations on Vibrational Spectra: Scaling Procedures to Improve the Wavenumbers. *Phys. Sci. Rev.* 3 (6), 1–30. doi:10.1515/psr-2017-0184
- Palumbo, O., Trequattrini, F., Appetecchi, G., and Paolone, A. (2017). A Study of the Conformers of the (Nonafluorobutanesulfonyl)imide Ion by Means of Infrared Spectroscopy and Density Functional Theory (DFT) Calculations. *Challenges* 8 (1), 7. doi:10.3390/challe8010007
- Paolucci, C., Parekh, A. A., Khurana, I., Di Iorio, J. R., Li, H., Albarracín Caballero, J. D., et al. (2016). Catalysis in a Cage: Condition-dependent Speciation and Dynamics of Exchanged Cu Cations in SSZ-13 Zeolites. *J. Am. Chem. Soc.* 138 (18), 6028–6048. doi:10.1021/jacs.6b02651
- Pham, T. D., Bin Faheem, A., Chun, S. Y., Rho, J. R., Kwak, K., and Lee, K. K. (2021). Synergistic Effects on Lithium Metal Batteries by Preferential Ionic Interactions in Concentrated Bisalt Electrolytes. *Adv. Energ. Mater.* 11 (11), 2003520. doi:10.1002/aenm.202003520
- Sakaebé, H., and Matsumoto, H. (2003). N-Methyl-N-propylpiperidinium Bis(trifluoromethanesulfonyl)imide (PP13-TFSI) - Novel Electrolyte Base for Li Battery. *Electrochem. Commun.* 5 (7), 594–598. doi:10.1016/s1388-2481(03)00137-1
- Shen, S., Fang, S., Qu, L., Luo, D., Yang, L., and Hirano, S.-i. (2015). Low-viscosity Ether-Functionalized Pyrazolium Ionic Liquids Based on Dicyanamide Anions: Properties and Application as Electrolytes for Lithium Metal Batteries. *RSC Adv.* 5 (114), 93888–93899. doi:10.1039/C5RA17539A
- Shim, Y. (2018). Computer Simulation Study of the Solvation of Lithium Ions in Ternary Mixed Carbonate Electrolytes: Free Energetics, Dynamics, and Ion Transport. *Phys. Chem. Chem. Phys.* 20 (45), 28649–28657. doi:10.1039/C8CP05190A
- Soon, A., Todorova, M., Delley, B., and Stampfl, C. (2007). Surface Oxides of the Oxygen-Copper System: Precursors to the Bulk Oxide Phase?. *Surf. Sci.* 601 (24), 5809–5813. doi:10.1016/j.susc.2007.06.062
- Starzak, M. E. (2010). *Energy and Entropy*. New York, NY: Springer-Verlag.
- Sun, Y., Xin, N., and Prausnitz, J. M. (2018). Solubilities of Five Lithium Salts in 1-Butyl-3-Methylimidazolium Dicyanamide and in 1-Butyl-3-Methylimidazolium Tetrafluoroborate from 298.15 to 343.15 K. *J. Chem. Eng. Data* 63 (12), 4524–4531. doi:10.1021/acs.jced.8b00618
- Umebayashi, Y., Mitsugi, T., Fukuda, S., Fujimori, T., Fujii, K., Kanzaki, R., et al. (2007). Lithium Ion Solvation in Room-Temperature Ionic Liquids Involving Bis(trifluoromethanesulfonyl) Imide Anion Studied by Raman Spectroscopy and DFT Calculations. *J. Phys. Chem. B* 111 (45), 13028–13032. doi:10.1021/jp076869m
- Umebayashi, Y., Mori, S., Fujii, K., Tsuzuki, S., Seki, S., Hayamizu, K., et al. (2010). Raman Spectroscopic Studies and *Ab Initio* Calculations on Conformational Isomerism of 1-Butyl-3-Methylimidazolium Bis-(trifluoromethanesulfonyl) amide Solvated to a Lithium Ion in Ionic Liquids: Effects of the Second Solvation Sphere of the Lithium Ion. *J. Phys. Chem. B* 114 (19), 6513–6521. doi:10.1021/jp100898h
- Yamada, Y., Wang, J., Ko, S., Watanabe, E., and Yamada, A. (2019). Advances and Issues in Developing Salt-Concentrated Battery Electrolytes. *Nat. Energ.* 4 (4), 269–280. doi:10.1038/s41560-019-0336-z
- Yang, L., Xiao, A., and Lucht, B. L. (2010). Investigation of Solvation in Lithium Ion Battery Electrolytes by NMR Spectroscopy. *J. Mol. Liquids* 154 (2), 131–133. doi:10.1016/j.molliq.2010.04.025
- Yoon, H., Lane, G. H., Shekibi, Y., Howlett, P. C., Forsyth, M., Best, A. S., et al. (2013). Lithium Electrochemistry and Cycling Behaviour of Ionic Liquids Using Cyano Based Anions. *Energy Environ. Sci.* 6 (3), 979–986. doi:10.1039/C3EE23753B

Conflict of Interest: The authors declare that the research was conducted in the absence of any commercial or financial relationships that could be construed as a potential conflict of interest.

Publisher's Note: All claims expressed in this article are solely those of the authors and do not necessarily represent those of their affiliated organizations, or those of the publisher, the editors, and the reviewers. Any product that may be evaluated in this article, or claim that may be made by its manufacturer, is not guaranteed or endorsed by the publisher.

Copyright © 2021 Penley, Vicchio, Getman and Gurkan. This is an open-access article distributed under the terms of the Creative Commons Attribution License (CC BY). The use, distribution or reproduction in other forums is permitted, provided the original author(s) and the copyright owner(s) are credited and that the original publication in this journal is cited, in accordance with accepted academic practice. No use, distribution or reproduction is permitted which does not comply with these terms.



The Origins of Ion Conductivity in MOF-Ionic Liquids Hybrid Solid Electrolytes

Roman Zettl¹ and Ilie Hanzu^{1,2*}

¹Institute for Chemistry and Technology of Materials, Graz University of Technology (NAWI Graz), Graz, Austria, ²Alistore – ERI European Research Institute, CNRS FR3104, Amiens, France

OPEN ACCESS

Edited by:

Shripad T Revankar,
Purdue University, United States

Reviewed by:

Sheng S. Zhang,
United States Army Research
Laboratory, United States
Uwe Schröder,
Technische Universität Braunschweig,
Germany

*Correspondence:

Ilie Hanzu
hanzu@tugraz.at

Specialty section:

This article was submitted to
Electrochemical Energy Conversion
and Storage,
a section of the journal
Frontiers in Energy Research

Received: 25 May 2021

Accepted: 22 September 2021

Published: 08 October 2021

Citation:

Zettl R and Hanzu I (2021) The Origins
of Ion Conductivity in MOF-Ionic
Liquids Hybrid Solid Electrolytes.
Front. Energy Res. 9:714698.
doi: 10.3389/fenrg.2021.714698

Fast Li⁺ solid ion conductors are a key component of all-solid-state batteries, a technology currently under development. The possible use of metallic lithium as active material in solid-state batteries warrants a quantum step improvement of battery specific energy, enabling further electric vehicles application. Hereby, we report the synthesis and ion conduction properties of a new solid hybrid electrolyte based on the MIL-121 metal organic framework (MOF) structure. After an ion exchange procedure that introduces Li⁺ in the structure, a known quantity of a soaking electrolyte is incorporated. The soaking electrolyte is based on the EMIM-TFSI ionic liquid, thus we can classify our formulation as a MOF-ionic liquid hybrid solid electrolyte. Electrical conductivity is investigated by impedance spectroscopy and preliminary studies of ion dynamics are conducted by ⁷Li NMR. The field of MOF-based ion conductors remains in incipient stages of research. Our report paves the way towards the rational design of new solid-state ion conductors.

Keywords: ion conduction, metal organic framework (MOF), solid electrolytes, solid-state batteries, conductivity spectroscopy, ionic Liquids

1 INTRODUCTION

Energy storage is one of the key technological challenges of our society. Unsurprisingly, many research efforts are oriented towards advanced battery systems. (Kim et al., 2019). One critical component of electrochemical systems and devices is the electrolyte. Electrolytes must be conductive for electroactive species, such as Li⁺, and insulating with respect to electrons. There are major interests in finding solid electrolytes with high conductivity; (Zhang et al., 2018; Zhao et al., 2019); on the long term they are considered better alternatives to the current liquid electrolytes used in commercial Li-ion battery systems.

The motivation is at least two-fold. First, the current commercial liquid electrolyte formulations are flammable, which may lead to dangerous situations in case of an electrolyte leak. A solid electrolyte would obviously eliminate leakage problems and would be safer, although safety largely depends on the type of compound used. (Chung and Kang, 2017; Chen et al., 2020). Second, the use of metallic lithium as an active material would be desired as a high capacity replacement for graphite. Graphite has reached its maximum technological development limit. Higher capacity materials would be required to further improve the specific energy of batteries. In spite of 40 years of research, it remains hitherto impractical to use Li metal anodes with liquid electrolytes in rechargeable lithium cells. Li dendrite growth and pulverisation of the anode upon repeated stripping and plating cycles are preventing the use of metallic lithium in batteries with liquid electrolyte. (Zheng J. et al., 2020).

Nowadays, much hope is put on Li⁺ conducting solid electrolytes and composites; this is a highly dynamic and rapidly expanding field. (Zheng Y. et al., 2020). Solid electrolytes are expected to

prevent lithium dendrite growth; yet it seems that this is not an *a priori* property of solid electrolytes. (Porz et al., 2017). However, with careful engineering and keeping the current density low, solid electrolytes can at least alleviate the issue of lithium dendrite growth, if not eliminating it completely. Finding suitable solid lithium ion conductors remains a challenging task, although there are several compounds showing high conductivity; the list is currently expanding. (Zheng et al., 2018).

Metal-organic frameworks (MOF), also called coordination polymers, are a class of microporous organic-inorganic compounds developed initially for their gas adsorption properties, especially for catalysis and for separation technologies. Since then, the range of MOF applications has been significantly extended. A MOF structure is built of metal centres or metal clusters connected to a bi- or multidentate organic molecule called a linker. The metal centres and the linkers may form 2D or 3D structures having long range crystalline ordering, very often with a well-defined pore size and a high specific surface area. One of the key characteristics of MOF structures is the large choice of ligands that can be used to build MOFs. The size and chemical structure of the MOF linker will determine the crystal structure as well as the shape and the volume of the pores. The chemical functionality of the ligand offers many possibilities for tuning the MOF's physical and chemical properties. In addition, the number of combinations between suitable metal centres and linkers is enormous. Thanks to these features, MOFs emerged as a development platform currently used to create, to explore and to adjust functional materials.

Lithium ion conductors based on metal organic framework (MOF) structures are a relatively new research field. While MOF proton conductors are known for a while, (Sadakiyo and Kitagawa, 2021), the first Li^+ MOF ion conductor was found only 10 years ago (Wiers et al., 2011). Although further developments were reported, (Ameloot et al., 2013; Park et al., 2017; Miner et al., 2019), the field of MOF Li^+ conductors is in its infancy and there are plenty of possibilities to explore. One characteristic of the few MOF ion conductors reported so far, is the use of a soaking electrolyte or small solvent molecules that fill the pores of the MOF ion conductor. As the pores of MOF materials tend to be large with respect to the small size of Li^+ ions, a small Li^+ solvating molecule is necessary to enhance Li^+ mobility. However, only few solvent molecules may actually reside in a typical MOF cage or pore as the space is very limited in a nanopore. Therefore, one cannot describe these small molecules embedded in the pores as a liquid phase; a closer description would be that of adsorbed molecules confined in the pores. Unfortunately, adsorption of chemical species on MIL-121 is an aspect more complicated than for other MOFs. Not all species may be adsorbed in the MIL-121 structure, even if they are certainly small. For instance, specific surface area determination of the MIL-121 by the Brunauer-Emmett-Teller (BET) method using nitrogen adsorption shows a very low specific surface area, simply because the non-polar N_2 molecules cannot properly enter the pores that are obstructed by the free carboxylic units. (Chen et al., 2019).

Nevertheless, it is not quite clear how the electric dipole moment of the adsorbing species influences the adsorption properties of MIL-121.

In a recent publication, we reported the functionalization of the MIL-121 MOF (Zettl et al., 2021) with Li^+ and Na^+ by ion exchange. With a soaking electrolyte containing propylene carbonate (PC) solvent, that is present in the pores in the nanofluid (or adsorbed) form mentioned above, we reached high conductivities for both Li^+ and Na^+ . While the PC proved to be an excellent solvent that significantly increases Li^+ mobility in the MOF structure, it also has a low, yet not negligible, vapour pressure and it is susceptible to slow evaporation from the structure. This property may raise additional issues during manufacturing, storage and operation of this hybrid solid electrolyte.

In this report we investigate the use of an ionic liquid, namely 1-ethyl-3-methylimidazolium bis(trifluoromethylsulfonyl)imide (EMIM-TFSI) as a soaking electrolyte in a MIL-121 MOF that was functionalized with Li^+ cations. Ionic liquids are known for their extremely low vapour pressure, EMIM-TFSI is no exception. We hereby report on the ionic conduction properties of these materials and we take a glimpse into the ion dynamics of these materials by ^7Li nuclear magnetic resonance (NMR) spectroscopy.

2 MATERIALS AND METHODS

Lithiated MIL-121 was prepared by an ion exchange reaction with lithium acetate (LiAc). The solution was stirred overnight in a closed container. Details about the synthesis of MIL-121 and the post-synthetic modification with LiAc can be found elsewhere. (Zettl et al., 2021). Before the soaking electrolyte was added, all samples were activated at 300°C at a pressure of 10^{-3} mbar for 24 h. Elemental analysis was carried out using inductively coupled plasma mass spectrometry (ICPMS, Agilent 7700); we used a microwave heated pressurized autoclave digestion system (Ultraclave IV, MLS ICPMS 7700x Agilent Technologies). An aliquot (0.02 g) of the rinsed and dried (see above) MIL-121/Li sample was mixed with 5 ml HNO_3 heated in a MLS UltraClave. The temperature program consisted of a ramp, heating the sample in 30 min from room temperature to 250°C and then holding for 30 min at 250°C . For the analysis, the samples were further diluted. The results are shown in **Supplementary Table S1** (see Supplementary Material).

Soaking of MIL-121/Li was done with a 0.4 M solution of LiTFSI (lithium bis(trifluoromethanesulfonyl)imide) in EMIM-TFSI (1-ethyl-3-methylimidazolium-bis(trifluoromethylsulfonyl)imide). EMIM-TFSI ionic liquid is further abbreviated as IL. The addition of the soaking electrolyte was carried out on the ion exchanged MOF in powder form, followed by vigorous mixing of the powder to homogenize the mixture. After resting for at least 24 h in a closed container in the drying oven, this powder was further used for pressing pellets and for NMR measurements. The soaking electrolyte was added in such an amount that the liquid content equalled 30 wt% of the solid content. This corresponds to

TABLE 1 | Sample abbreviations and compositions of the samples prepared and investigated.

Sample ID	Composition
MIL-121/Li	MIL-121 with 1/3 of free carboxylic protons exchanged with Li ⁺
MIL-121/Li + IL	77 wt% MIL-121/Li, 23 wt% EMIM-TFSI ionic liquid
MIL-121/Li + IL + LiTFSI	77 wt% MIL-121/Li, 23 wt% 0.4 M LiTFSI in EMIM-TFSI solution
MIL-121 + IL + LiTFSI	77 wt% MIL-121 (no Li), 23 wt% 0.4 M LiTFSI in EMIM-TFSI solution
MIL-121 + IL	77 wt% MIL-121 (no Li), 23 wt% EMIM-TFSI ionic liquid

a content of 23 wt% ionic liquid or soaking electrolyte, while the MOF fraction of the samples with IL or soaking electrolyte was always 77 wt%.

In order to check the influence of Li⁺ at the carboxylic groups of MIL-121 and the role of the Li salt (*i.e.* LiTFSI), on the ionic conductivity, different pellet samples were prepared for impedance spectroscopy. MIL-121/Li, MIL-121/Li + IL, MIL-121/Li + IL + LiTFSI, MIL-121 + IL + LiTFSI and MIL-121 + IL were pressed into pellets at a load of 0.3 tons and sputtered with Au electrodes that act as blocking electrodes for Li ions. The pellets had a diameter of 5 mm with a thickness of about 1 mm. Measurements were carried out in coin cells in order to keep samples free from moisture and air. A Concept 80 impedance spectrometer (Novocontrol) equipped with an Alpha-A impedance analyzer in combination with an active ZGS sample cell was used. Frequencies covered a range from 10⁷ to 10⁻² Hz; the amplitude of the applied AC voltage was 0.1 V and the temperature domain was between -90 and 110°C. Conductivity data points for the calculation of the activation energy were taken from the DC plateaus of conductivity isotherms. Isotherms were recorded every 20°C during the

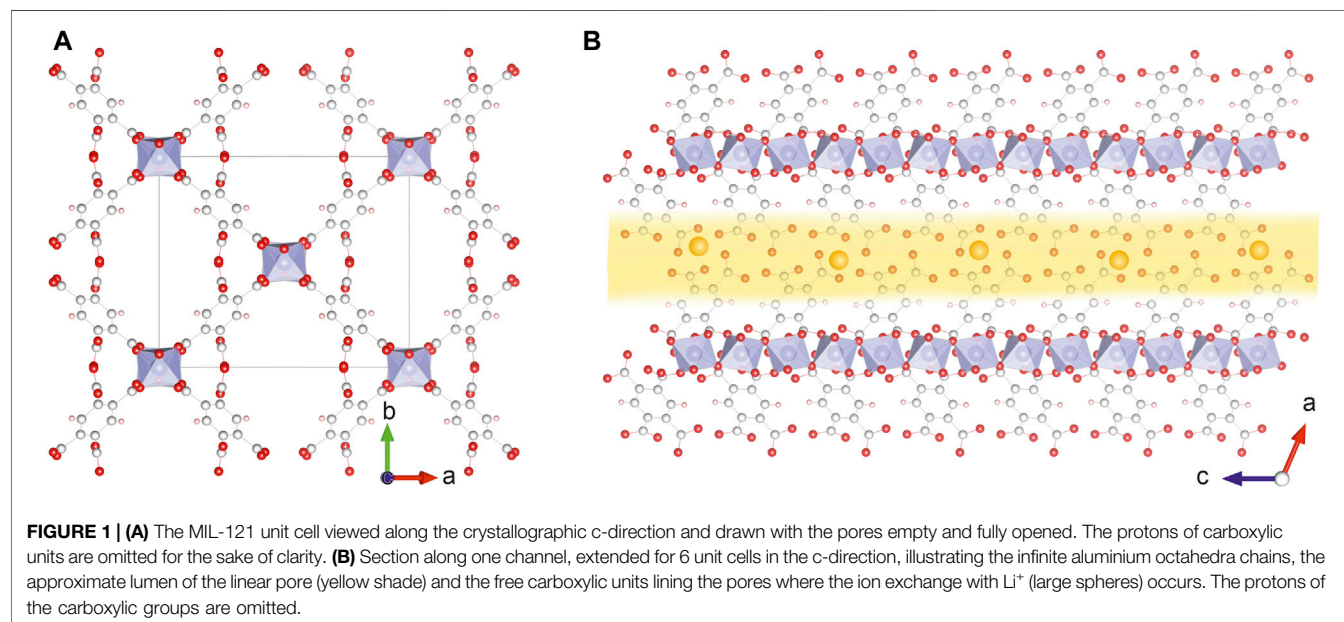
cooling run, which was started after the temperature reached 110°C.

Variable-temperature ⁷Li NMR lines were recorded with a spectrometer from Bruker (Avance III 300). A 7.0 T cryomagnet field strength results in a resonance frequency of 116.59 MHz for ⁷Li nucleus. The lines were recorded under static conditions, with 90° pulse lengths in the order of 2–3 μs and a recycle delay of 10 s. 128 FIDs (free induction decays) were accumulated to achieve an acceptable signal-to-noise ratio. Prior to NMR measurements, the various samples were filled in Duran tubes and fire sealed to keep them free of moisture and air. A summary of the sample compositions and the abbreviations used in this report is shown in Table 1.

3 RESULTS AND DISCUSSION

The MIL-121 MOF is formed by the coordination of aluminum metal centres with 1,2,4,5-benzenetetracarboxylic acid, also known as pyromellitic acid. Only two of the four carboxylic functional groups participate in building the MOF structure, the other two are free and situated along the linear pores characteristic to the MIL-121 structure, as shown in Figure 1. The protons of these free carboxylic units can be exchanged partially with Li⁺ ions. With the lithium acetate solution (see *Materials and Methods*), we reach a degree of ion exchange of approximately one third, the other two thirds of the carboxylic units remain protonated.

Conductivity isotherms of the lithiated MIL-121 sample, thoroughly dried and without any ionic liquid, are presented in Figure 2A). MIL-121/Li is a very poor conductor, it behaves like an insulator up to 90°C. Only at 100°C and above there are indications of very poor ion transport. Yet, at a conductivity of 10⁻¹² S cm⁻¹ measured at the very faint DC plateau seen at 110°C, the material can hardly be classified as an ionic conductor. Very likely, the



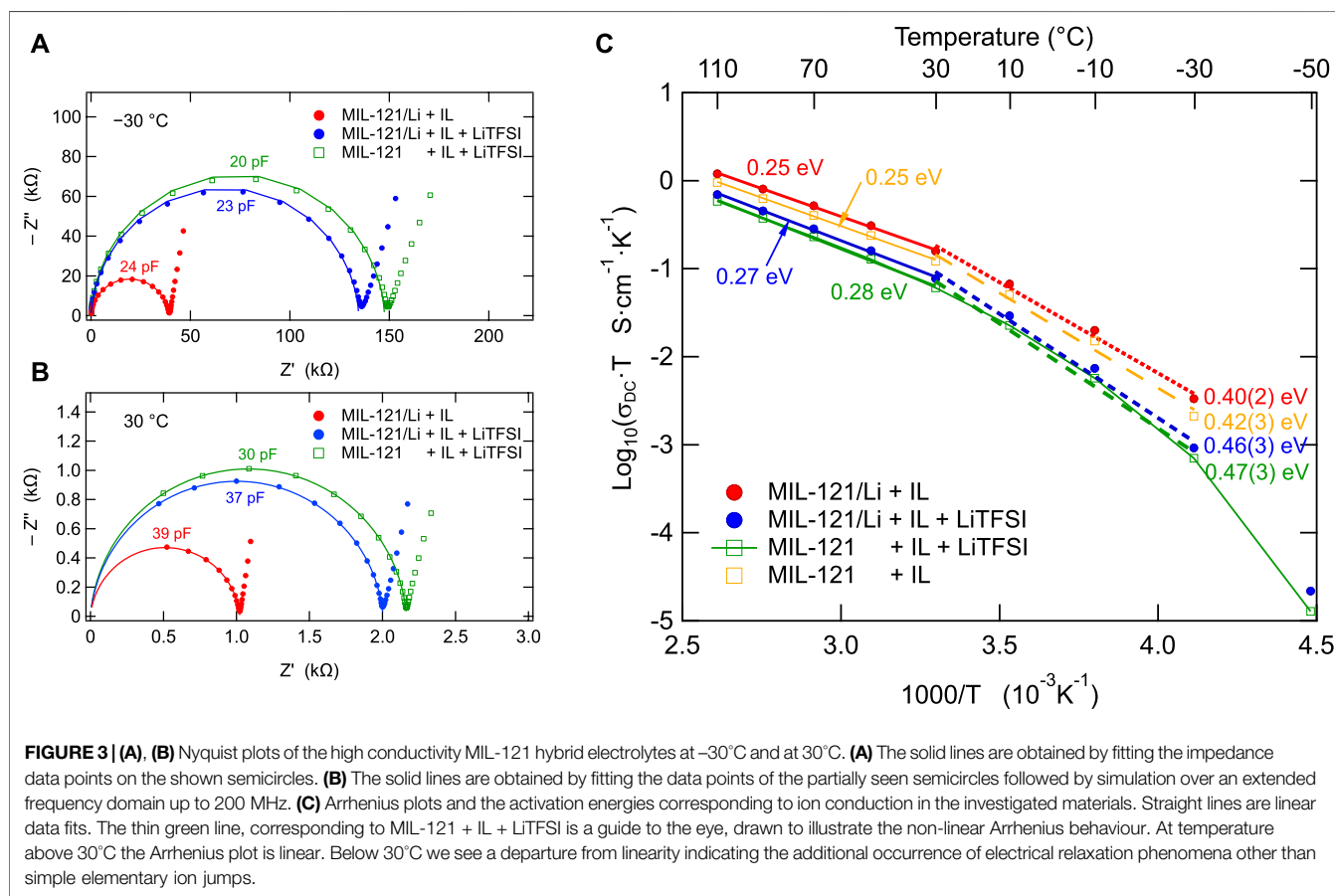
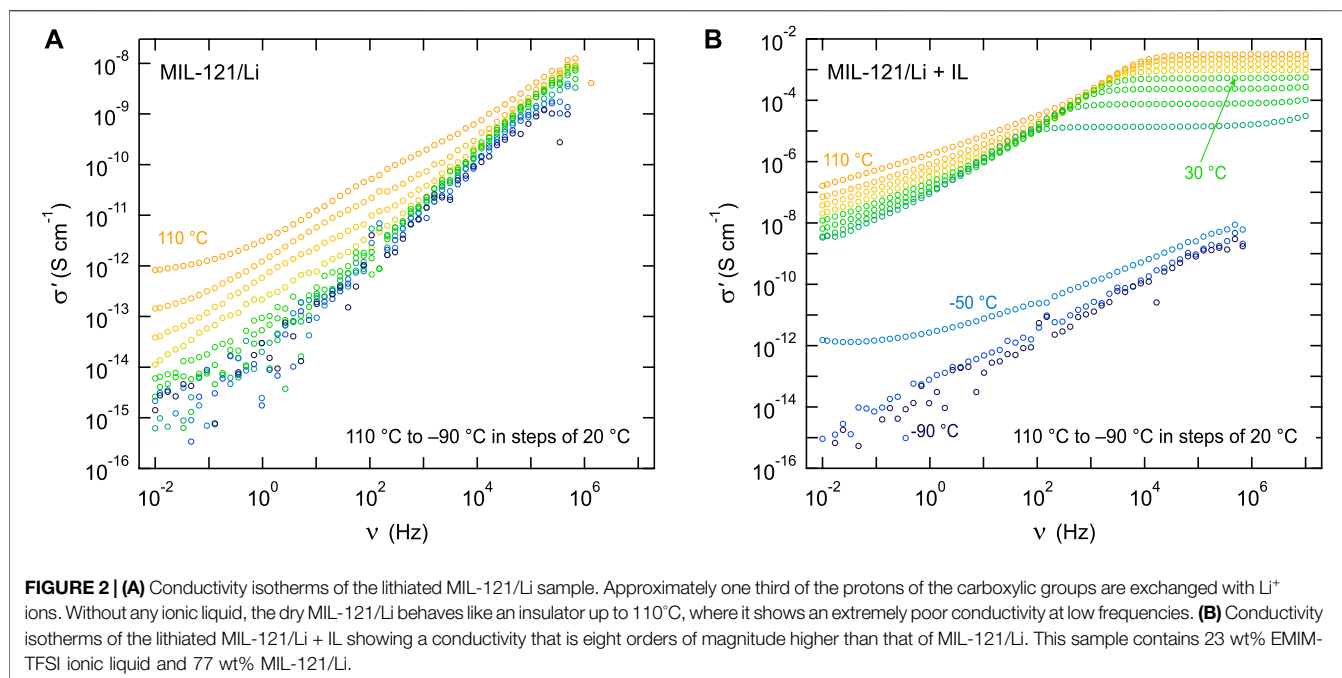


TABLE 2 | Parameters obtained by fitting the impedance semicircles in **Figures 3B,C** with a constant phase element (CPE) in parallel to a resistor R_p . C_p is the capacitance and a is the exponent of the CPE.

Temperature	−30°C			30°C		
Sample ID	$C_p(\text{pF})$	a	$R_p(\text{k}\Omega)$	$C_p(\text{pF})$	a	$R_p(\text{k}\Omega)$
MIL-121/Li + IL	24	0.96	39.09	39	0.94	1.023
MIL-121/Li + IL + LiTFSI	23	0.96	134.6	37	0.94	2.004
MIL-121 + IL + LiTFSI	20	0.97	147.5	30	0.95	2.164
MIL-121 + IL	24	0.97	44.38	36	0.95	1.016

Li^+ in the structure is too strongly bonded to the carboxylic group, resulting in negligible mobility. One option would be the addition of a solvent or a soaking electrolyte that may enter the pores and solvate the Li^+ ions. For this purpose, we investigated the addition of EMIM-TFSI ionic liquid-based soaking electrolyte.

As shown in **Figure 2B**, adding 23 wt% EMIM-TFSI ionic liquid to the lithium exchanged MOF increases the conductivity to 0.5 mS cm^{-1} at 30°C . Compared to MIL-121/Li, this jump in DC conductivity corresponds to an increase by more than eight orders of magnitude. While the MIL-121/Li + IL contains 23% by mass EMIM-TFSI ionic liquid, the sample keeps a true solid appearance, is not waxy and can be pressed into pellets.

The dry MIL-121/Li presents a faint second DC plateau in the region 10^4 – 10^2 Hz. This may be attributed to some local electrical relaxation processes, for instance localized ion dynamics, such as ion motion within the boundaries of a confining potential energy well, or cavity, of the structure. This weak contribution also shows up on the electric modulus plot, see **Supplementary Figure S1 D**). The absence of a corresponding perturbation on the imaginary part of the impedance (Z'') confirms the localized nature of the electrical relaxation process.

Nyquist plots of MIL-121/Li + IL are shown in **Figures 3A,B**) which correspond to temperatures of -30°C and 30°C , respectively. The semicircles can be fitted with a simple equivalent circuit consisting of a constant phase element in parallel to a resistor. We may remind that the impedance of a constant phase element is given by $Z = 1/[C_p(j\omega)^a]$, where j is the imaginary unit, $\omega = 2\pi\nu$ is the angular frequency, C_p is the capacitance of the constant phase element and a is the exponent of the constant phase element. For $a = 1$, the constant phase element reverts to an ideal capacitor. For $a < 1$, the behaviour deviates from that of a capacitor and the “capacitance” of the constant phase element is correctly expressed in $F/s^{(1-a)}$. However, in practice, for $a \approx 1$, the behaviour of the constant phase element would be very close to that of a capacitor and we may express the capacitance in F (Farads).

Indeed, the Nyquist plots shown in **Figures 3A,B**) show almost perfectly shaped semicircles, indicating an almost ideal Debye behaviour. The values of the constant phase element exponent, a , are close to 1 (see **table 2**), which indicates a behaviour very close to that of an ideal capacitor. In addition, capacitances ranging from 20–40 pF reveal that the electrical relaxation phenomena involved are bulk processes, in accordance to the model of Irvine and West. (Irvine et al., 1990).

The Arrhenius plots of all samples containing ionic liquids are shown in **Figure 3C**). Above 30°C , $\sigma_{DC}T$ follows an Arrhenius

behaviour characterized by activation energies ranging from 0.25 to 0.28 eV for all the samples that contain EMIM-TFSI ionic liquid. An interesting feature is the appearance of a kink at 30°C . At lower temperatures the situation changes significantly. Not only that the activation energies sensibly increase, but also the electric relaxation mechanism very likely changes. Indeed, we see a small, but clear departure from linear Arrhenius behaviour, indicating that, at lower temperatures, electric relaxation may occur also by other phenomena than ion transport in the material. Such a behaviour is known for some polymer electrolytes, where the Vogel-Fulcher-Tammann (VFT) equation is commonly used instead of the Arrhenius equation. (Ratner and Shriver, 1988). Here, this non-linear behaviour may also be an expression of the increasing viscosity with the decreasing temperature, (Tammann and Hesse, 1926), although this aspect requires further clarifying investigations.

Surprisingly, there is no significant variation of conductivity when more Li^+ ions are included in the system by dissolving LiTFSI in EMIM-TFSI. Moreover, modifying the MOF, *i.e.* introducing Li^+ ions into the structure via an ion exchange reaction, does not lead to a decisive enhancement in conductivity. If we compare the MIL-121/Li + IL with MIL-121/Li + IL + LiTFSI and with MIL-121 + IL + LiTFSI we see a change by a factor of two, the conductivity of MIL-121/Li + IL turned out to be slightly higher. The conductivity isotherms of MIL-121 + IL + LiTFSI and MIL-121/Li + IL + LiTFSI are shown in **Supplementary Figure S1A, B**. Even more surprising is the absence of clear differences between a sample that contains a lithiated MOF and a sample that does not contain a lithiated MOF, while both contain the same amount of 0.4 M LiTFSI in EMIM-TFSI electrolyte.

To estimate the self-diffusivity of Li^+ in the materials we carried out nuclear magnetic resonance (NMR) measurements. The ^7Li NMR line-width depends on the mobility of Li^+ in the material and thus on temperature. A narrow NMR line is a clear indication of rapid lithium ion exchange processes. This phenomenon, called motional line narrowing, can be used to estimate the relative number of ion jumps per second, also known as the jump rate. Thus, by looking at the relative widths of the NMR lines it is possible to distinguish between slow and fast ion conductors. (Wilkening et al., 2008; Kuhn et al., 2011).

^7Li NMR line measurements are shown in **Figure 4** for all the samples containing Li^+ . Please note that, in these samples, there are two sources of Li^+ . The first is the ion exchange process, see MIL-121/Li, **Figure 4A**). The second is the Li^+ -containing ionic liquid that was added to both the ion-exchanged sample, see MIL-121/Li + IL + LiTFSI on **Figure 4B**), and also to the Li-free MOF structure, that was not previously ion-exchanged, see MIL-121 + IL + LiTFSI **Figure 4C**).

We see in **Figure 4C**) that, for MIL-121 + IL + LiTFSI, the ^7Li NMR line is fully narrowed already at -20°C , with negligible narrowing above this temperature. At -60°C a broad line is recorded because of the solidification of the 0.4 M LiTFSI in EMIM-TFSI solution. This sample has no lithium from the ion-exchange procedure, all lithium originates from the 23 wt% Li^+ containing ionic liquid soaking electrolyte that was added. This indicates that all Li^+ species are already mobile above -20°C .

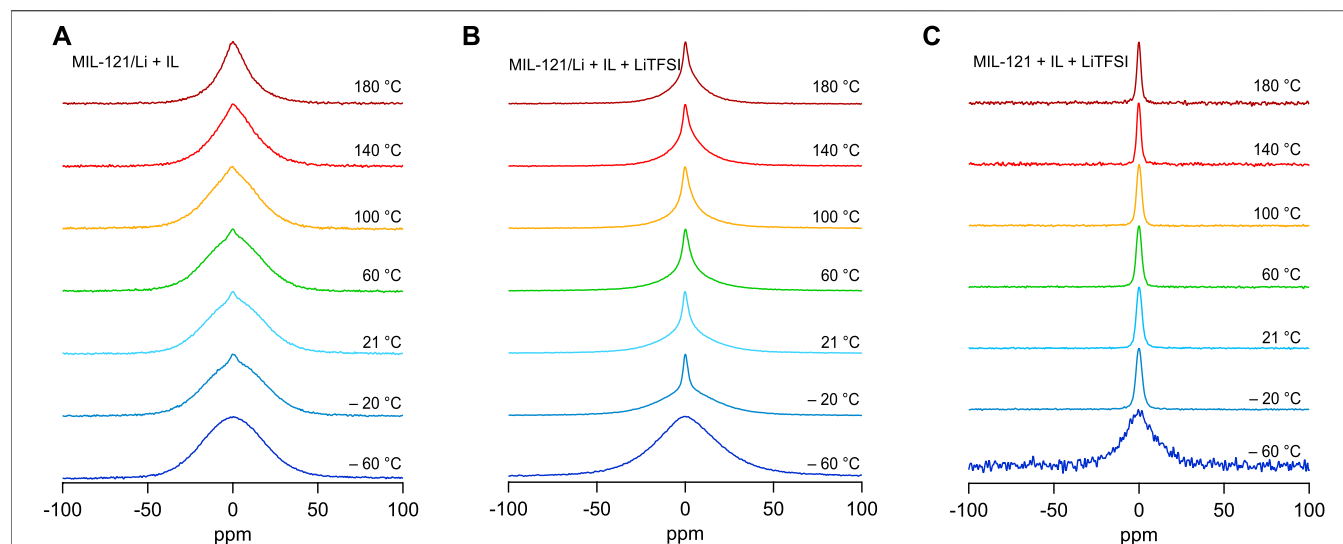


FIGURE 4 | (A) ^7Li NMR lines acquired in a magnetic field strength $B_0 = 7$ T for which the ^7Li NMR central resonance frequency is 116.59 MHz. **(A)** The ^7Li NMR line width of MIL-121/Li + IL shows little motional narrowing with increasing temperature. However, a small narrower line that can be assigned to faster jumping Li^+ ions is visible on top of the broad ^7Li signal. The broad line can probably be assigned to the slow jumping of Li^+ contained in the functionalized MOF. **(B)** The ^7Li NMR lines at various temperature of a sample that contains 77 wt% MIL-121/Li and 23 wt% solution of 0.4 M LiTFSI in EMIM-TFSI. **(C)** The ^7Li NMR lines at various temperature of a sample that contains 77 wt% MIL-121 (pure activated MOF) and 23 wt% solution of 0.4 M LiTFSI in EMIM-TFSI.

For the sample where all the Li^+ originates from the ion-exchange procedure, *i.e.* MIL-121/Li + IL, see **Figure 4A**), we see a much different behaviour. ^7Li NMR lines are broad over the entire domain and a very small narrowed line appears on top of the broad contribution at temperatures above -20°C . This indicates the existence of two lithium spin reservoirs in the material. One lithium spin reservoir shows low Li^+ jump rates, whereas the other is very likely a faster ion conductor characterized by much higher Li^+ jump rates. However, the fraction of fast Li^+ ions appears small in comparison to the slow, poorly mobile Li^+ species.

Thus, most of Li^+ ions from the MIL-121/Li structure do not change their ion dynamics properties by the addition of EMIM-TFSI ionic liquid. Nevertheless, for few of the Li^+ there is a significant increase in jump rates when pure EMIM-TFSI ionic liquid is added. This is a plausible indication that only Li^+ from the surface, or near-surface, regions of the MIL-121/Li particles interact significantly with the ionic liquid.

For the sample MIL-121/Li + IL + LiTFSI, where lithium originates from both the ion-exchange procedure and from the addition of 0.4 M LiTFSI in EMIM-TFSI soaking electrolyte, we see an intermediary situation. On top of a broad ^7Li NMR line we have a significantly narrower line, corresponding to a higher fraction of fast Li^+ species, see **Figure 4B**). Of course, as the Li^+ content in the ionic liquid is high and comparable to the Li^+ content in the MOF structure, the area fraction under the narrow line is large.

Therefore, the high conductivity of the samples can be assigned mostly to the ionic liquid added to the MOF. The Li^+ species originating from the ion exchange procedure do not appear to contribute significantly to the total conductivity of the samples. In spite of MIL-121/Li containing a significant

quantity of Li^+ , these ions are not mobile and they cannot be made mobile by simply adding EMIM-TFSI ionic liquid. It would appear then, that the high conductivity of the MIL-121/Li + IL sample does not stem from the high Li^+ ion mobility in the sample, but from the inherent high conductivity of the EMIM-TFSI ionic liquid itself, see the conductivity of MIL-121 + IL shown in **Supplementary Figure S1C**).

The bulk conduction process that appears in impedance measurements of all samples (see **Figures 3A,B**) and **table 2**) does not correspond to conduction in the MOF, but to conduction on the surface of the MOF or in the ionic liquid only. While further investigations are necessary, we note that the occurrence of a capacitance contribution that closely approaches the behaviour of a capacitor would be unusual for a highly porous sample characterized by nano-domains and uniformly filled with mobile adsorbed molecules or mobile ions. Thus, it may happen that the ionic liquid does not enter the linear pores of the MIL-121 structure.

Moreover, the decrease in conductivity when LiTFSI is added to the MIL-121/Li + IL, as seen in **Figures 3A,B**), is typical to the behaviour of a salt dissolved in an ionic liquid. In fact, the conductivity of the pure ionic liquid (EMIM-TFSI) is known to be higher than the conductivity of a LiTFSI solution in EMIM-TFSI. The LiTFSI solution in EMIM-TFSI has a higher viscosity than the pure ionic liquid and hence the solution has a lower conductivity than the pure ionic liquid. (Wu et al., 2013). Thus, we see a typical ionic liquid solution behaviour, which does not appear to be visibly altered by the presence of lithiated MIL-121 particles. This behaviour could be very well explained if the ionic liquid species do not enter the pores of the MOF.

The MIL-121 samples consist of well grown and crystallized particles that are in the order of $10\ \mu\text{m}$. If the ionic liquid does not go

significantly inside the pores, then it must reside on the outer surface area of the MOF and in the voids between MOF particles. Thus, the bulk electrical relaxation process seen for all the samples containing an ionic liquid, very likely corresponds almost exclusively to the bulk conductivity of the ionic liquid phase itself.

4 CONCLUSION

MIL-121 metal organic frameworks were prepared and their ion conduction properties were investigated. Following an ion-exchanged procedure, one third of the protons on the free carboxylic groups in the MOF were exchanged with Li^+ ions. The conductivity of the dry ion-exchanged sample is very low. We found that by the addition of an ionic liquid or an ionic liquid-based Li^+ electrolyte, the DC conductivity (σ_{DC}) of the MOF materials increase by eight orders of magnitude. There are indications that, the ionic liquid does not increase the mobility of a significant fraction of Li^+ ions from the ion-exchanged MOF structure. Thus, the origin of conductivity in MIL-121 functionalized with Li^+ and soaked with ionic liquids is in fact, to a very large extent, due to the ionic liquid located outside of the solid MOF particles. The majority of Li^+ ions in the MOF structure are rather slow and do not significantly participate in long range ion transport. Also, we found indications that by soaking the MIL-121 MOF in EMIM-TFSI ionic liquid, the ionic liquid does not enter the pores of the material to a significant extent. This observation requires, however, further work for a definite confirmation.

DATA AVAILABILITY STATEMENT

The raw data supporting the conclusions of this article will be made available by the authors, without undue reservation.

REFERENCES

- Ameloot, R., Aubrey, M., Wiers, B. M., Gómora-Figueroa, A. P., Patel, S. N., Balsara, N. P., et al. (2013). Ionic Conductivity in the Metal-Organic Framework UiO-66 by Dehydration and Insertion of Lithiumtert-Butoxide. *Chem. Eur. J.* 19, 5533–5536. doi:10.1002/chem.201300326
- Chen, R., Nolan, A. M., Lu, J., Wang, J., Yu, X., Mo, Y., et al. (2020). The Thermal Stability of Lithium Solid Electrolytes with Metallic Lithium. *Joule* 4, 812–821. doi:10.1016/j.joule.2020.03.012
- Chen, S., Mukherjee, S., Lucier, B. E. G., Guo, Y., Wong, Y. T. A., Terskikh, V. V., et al. (2019). Cleaving Carboxyls: Understanding Thermally Triggered Hierarchical Pores in the Metal-Organic Framework MIL-121. *J. Am. Chem. Soc.* 141, 14257–14271. doi:10.1021/jacs.9b06194
- Chung, H., and Kang, B. (2017). Mechanical and Thermal Failure Induced by Contact between a $\text{Li}_1.5\text{Al}_0.5\text{Ge}_1.5(\text{PO}_4)_3$ Solid Electrolyte and Li Metal in an All Solid-State Li Cell. *Chem. Mater.* 29, 8611–8619. doi:10.1021/acs.chemmater.7b02301
- Irvine, J. T. S., Sinclair, D. C., and West, A. R. (1990). Electroceramics: Characterization by Impedance Spectroscopy. *Adv. Mater.* 2, 132–138. doi:10.1002/adma.19900020304
- Kim, T., Song, W., Son, D.-Y., Ono, L. K., and Qi, Y. (2019). Lithium-ion Batteries: Outlook on Present, Future, and Hybridized Technologies. *J. Mater. Chem. A* 7, 2942–2964. doi:10.1039/C8TA10513H

AUTHOR CONTRIBUTIONS

RZ synthesized the MOFs and prepared the investigated materials, conducted the impedance and NMR measurements and plotted the data. IH conceived and supervised this research. IH and RZ interpreted the data and wrote the manuscript together. IH acquired the funding for this investigation.

FUNDING

This research received funding from Land Steiermark through Zukunftsfonds Steiermark (project Hybrid-Solarzellenbatterie, grant no. 1341) and from the FFG (K-project Safe Battery, grant no. 856234).

ACKNOWLEDGMENTS

We thank Prof. H. Martin R. Wilkening for many useful discussions and for allowing us to use his impedance equipment and NMR spectrometer in Graz. We thank Prof. W. Gössler and S. Meschnark for the elemental analysis (Karl Franzens University Graz). The Deutsche Forschungsgemeinschaft (DFG) (FOR 1227 MoLiFe, project LIDINAM, grant HA6966/1-2) and Austrian Research Promotion Agency (FFG) (project SolaBat, grant 853627) are kindly acknowledged.

SUPPLEMENTARY MATERIAL

The Supplementary Material for this article can be found online at: <https://www.frontiersin.org/articles/10.3389/fenrg.2021.714698/full#supplementary-material>

- Kuhn, A., Narayanan, S., Spencer, L., Goward, G., Thangadurai, V., and Wilkening, M. (2011). Li Self-Diffusion in Garnet-type $\text{Li}_7\text{La}_3\text{Zr}_2\text{O}_{12}$ Probed Directly by Diffusion-induced $\text{Li}^{7\text{spin}}$ -Lattice Relaxation NMR Spectroscopy. *Phys. Rev. B* 83, 094302. doi:10.1103/PhysRevB.83.094302
- Miner, E. M., Park, S. S., and Dincă, M. (2019). High Li^+ and Mg^{2+} Conductivity in a Cu-Azolate Metal-Organic Framework. *J. Am. Chem. Soc.* 141, 4422–4427. doi:10.1021/jacs.8b13418
- Park, S. S., Tulchinsky, Y., and Dincă, M. (2017). Single-Ion Li^+ , Na^+ , and Mg^{2+} Solid Electrolytes Supported by a Mesoporous Anionic Cu-Azolate Metal-Organic Framework. *J. Am. Chem. Soc.* 139, 13260–13263. doi:10.1021/jacs.7b06197
- Porz, L., Swamy, T., Sheldon, B. W., Rettenwander, D., Frömling, T., Thaman, H. L., et al. (2017). Mechanism of Lithium Metal Penetration through Inorganic Solid Electrolytes. *Adv. Energ. Mater.* 7, 1701003. doi:10.1002/aenm.201701003
- Ratner, M. A., and Shriver, D. F. (1988). Ion Transport in Solvent-free Polymers. *Chem. Rev.* 88, 109–124. doi:10.1021/cr00083a006
- Sadakiyo, M., and Kitagawa, H. (2021). Ion-conductive Metal-Organic Frameworks. *Dalton Trans.* 50, 5385–5397. doi:10.1039/D0DT04384B
- Tammann, G., and Hesse, W. (1926). Die Abhängigkeit der Viscosität von der Temperatur bei unterkühlten Flüssigkeiten. *Z. Anorg. Allg. Chem.* 156, 245–257. doi:10.1002/zaac.19261560121
- Wiers, B. M., Foo, M.-L., Balsara, N. P., and Long, J. R. (2011). A Solid Lithium Electrolyte via Addition of Lithium Isopropoxide to a Metal-Organic Framework with Open Metal Sites. *J. Am. Chem. Soc.* 133, 14522–14525. doi:10.1021/ja205827z

- Wilkening, M., Epp, V., Feldhoff, A., and Heitjans, P. (2008). Tuning the Li Diffusivity of Poor Ionic Conductors by Mechanical Treatment: High Li Conductivity of Strongly Defective LiTaO₃ Nanoparticles. *J. Phys. Chem. C* 112, 9291–9300. doi:10.1021/jp801537s
- Wu, T. Y., Hao, L., Chen, P. R., and Liao, J. W. (2013). Ionic Conductivity and Transporting Properties in LiTFSI-Doped Bis(trifluoromethanesulfonyl)imide-Based Ionic Liquid Electrolyte. *Int. J. Electrochem. Sci.* 8, 2606–2624.
- Zettl, R., Lunghammer, S., Gadermaier, B., Boulaoued, A., Johansson, P., Wilkening, H. M. R., et al. (2021). High Li + and Na + Conductivity in New Hybrid Solid Electrolytes Based on the Porous MIL-121 Metal Organic Framework. *Adv. Energ. Mater.* 11, 2003542. doi:10.1002/aenm.202003542
- Zhang, Z., Shao, Y., Lotsch, B., Hu, Y.-S., Li, H., Janek, J., et al. (2018). New Horizons for Inorganic Solid State Ion Conductors. *Energy Environ. Sci.* 11, 1945–1976. doi:10.1039/C8EE01053F
- Zhao, W., Yi, J., He, P., and Zhou, H. (2019). Solid-State Electrolytes for Lithium-Ion Batteries: Fundamentals, Challenges and Perspectives. *Electrochem. Energ. Rev.* 2, 574–605. doi:10.1007/s41918-019-00048-0
- Zheng, F., Kotobuki, M., Song, S., Lai, M. O., and Lu, L. (2018). Review on Solid Electrolytes for All-Solid-State Lithium-Ion Batteries. *J. Power Sourc.* 389, 198–213. doi:10.1016/j.jpowsour.2018.04.022
- Zheng, J., Kim, M. S., Tu, Z., Choudhury, S., Tang, T., and Archer, L. A. (2020a). Regulating Electrodeposition Morphology of Lithium: towards Commercially Relevant Secondary Li Metal Batteries. *Chem. Soc. Rev.* 49, 2701–2750. doi:10.1039/c9cs00883g
- Zheng, Y., Yao, Y., Ou, J., Li, M., Luo, D., Dou, H., et al. (2020b). A Review of Composite Solid-State Electrolytes for Lithium Batteries: Fundamentals, Key Materials and Advanced Structures. *Chem. Soc. Rev.* 49, 8790–8839. doi:10.1039/d0cs00305k
- Conflict of Interest:** The authors declare that the research was conducted in the absence of any commercial or financial relationships that could be construed as a potential conflict of interest.
- Publisher's Note:** All claims expressed in this article are solely those of the authors and do not necessarily represent those of their affiliated organizations, or those of the publisher, the editors and the reviewers. Any product that may be evaluated in this article, or claim that may be made by its manufacturer, is not guaranteed or endorsed by the publisher.

Copyright © 2021 Zettl and Hanzu. This is an open-access article distributed under the terms of the Creative Commons Attribution License (CC BY). The use, distribution or reproduction in other forums is permitted, provided the original author(s) and the copyright owner(s) are credited and that the original publication in this journal is cited, in accordance with accepted academic practice. No use, distribution or reproduction is permitted which does not comply with these terms.



Surface Properties of LaNi_5 and TiFe —Future Opportunities of Theoretical Research in Hydrides

Zbigniew Łodziana*

Institute of Nuclear Physics Polish Academy of Sciences, Kraków, Poland

OPEN ACCESS

Edited by:

Ah-Hyung Alissa Park,
Columbia University, United States

Reviewed by:

Terry David Humphries,
Curtin University, Australia
Sukanta Dash,
Pandit Deendayal Petroleum
University, India

*Correspondence:

Zbigniew Łodziana
Zbigniew.Lodziana@ifj.edu.pl

Specialty section:

This article was submitted to
Hydrogen Storage and Production,
a section of the journal
Frontiers in Energy Research

Received: 02 June 2021

Accepted: 10 September 2021

Published: 20 October 2021

Citation:

Łodziana Z (2021) Surface Properties
of LaNi_5 and TiFe —Future
Opportunities of Theoretical Research
in Hydrides.
Front. Energy Res. 9:719375.
doi: 10.3389/fenrg.2021.719375

Hydrogen in the solid state compounds is still considered as a safe method of energy storage. The ultimate metal hydrides or other materials that can be used for this purpose remain unknown. Such metal hydrides shall have favorable thermodynamics and kinetics of hydrogen ad/desorption, and it shall be resistant to contamination of H_2 and should not constitute any environmental hazards. Theoretical investigations, based on quantum mechanics approach, have a well-established position in modern materials research; however, their application for design of new alloys with tailored properties for reversible hydrogen storage is rarely present in the literature. The mainstream research deals with accurate prediction of thermodynamic and structural properties of hydrides as a function of composition or external parameters. On the other hand, the kinetic effects related to hydrogen transport or interaction between solid and pure or contaminated H_2 are more demanding. They cannot be easily automated. We present calculations of the equilibrium crystal shapes for LaNi_5 and TiFe —two important materials that show reversible hydrogen cycling near ambient conditions. Understanding of the surface properties is crucial for development of materials with better cyclability or resistance to hydrogen impurities. Indeed, the calculated adsorption energy of carbon oxides or water is stronger than hydrogen. These molecules block the active sites for H_2 dissociation, leading to formation of surface oxides. Particularly strong adsorption of CO/CO_2 on TiFe explains large degradation of hydrogen storage capacity of this compound by carbon oxides. Over-representation of La on exposed facets of LaNi_5 is related to formation of La_2O_3 and $\text{La}(\text{OH})_3$. Such examples show that the present development of computational methods allows reliable studies of intermetallic properties related to their surface or novel catalytic applications.

Keywords: metal hydride, surface energy, LaNi_5 alloy, TiFe alloy, DFT, hydrogen storage

1 INTRODUCTION

Alloys and intermetallic compounds have been for a long time and they still are considered as promising hydrogen storage materials (Ivey and Northwood, 1983; Sakintuna et al., 2007; Joubert et al., 2021). These claims and hopes are based on the fact that in contact with the surface of these compounds, the bond between hydrogen atoms in the H_2 molecule is broken [H_2 dissociation energy 4.477 eV (Herzberg and Monfils, 1961)], and hydrogen atoms diffuse into the bulk forming a stable compound—a metal hydride. This process can be reversed at mild conditions and gaseous hydrogen is extracted from the hydride. Multiple repetitions of such procedure, without significant degradation

of kinetic and thermodynamic parameters, are very appealing for practical applications. As a matter of fact, many decades of metal hydride research, numerous real live applications, and enormous literature on this subject justify hopes for applications (Fukai, 2005; Sakintuna et al., 2007; Züttel et al., 2008; Mohtadi and Orimo, 2017; Fuel Cells Bulletin, 2018; Modi and Aguey-Zinsou, 2021). Hydrogen is able to form stable hydrides with variety of metals as well as intermetallic compounds. These compounds are traditionally denoted as AB, AB₂, A₂B, or AB₅. The key aspect of hydride formation is related to the so-called pressure composition isotherms that reveal enthalpy of formation (ΔH^0) and entropy of formation (ΔS^0) as well as the hydride stoichiometry or an insight into kinetic parameters. There are, however, very stable hydrides such as AlH₃ (Saitoh et al., 2008), MgH₂ (Baran and Polański, 2020), or LiH (Jain et al., 2016) that cannot be formed by simple exposition of metals to hydrogen because the dissociation of H₂ does not easily occur at the surface, and pressures of dozens of kbar with elevated temperature are required in order to form a hydride.

The mainstream literature on metal hydrides (Fukai, 2005; Züttel et al., 2008; Broom, 2011) details all aspects of general reaction $M + \frac{x}{2}H_2 \leftrightarrow MH_x + \Delta H^0$, modification of the equilibrium pressures, and temperatures by appropriate alloy doping or processing. Tuning thermodynamic properties of metal hydrides is a longstanding research effort. Over the decades, it was directed by the empirical models such as Hume–Rothery rules (the model is based on similarity of atomic radii, electronegativity of constituting elements, and crystal structure) (Hume–Rothery et al., 1934) and the Miedema model (which is based on the charge density and the work function of metals contained in a hydride) (Boer et al., 1988). Another approach called Pettifor structure maps introduces a chemical scale χ for ordering elements in the Mendeleev table (Pettifor, 1986). The use of metal hydrides in electrochemical systems is another important application (Joubert et al., 2021).

Metal hydrides have great potential to be used as distributed stationary hydrogen (energy) storage; however, some aspects not directly related to their hydrogen capacity, operating conditions, or thermodynamic properties gain importance. As an example, one can mention cyclic stability, cycle life, or sensitivity to hydrogen impurities. It was recognized in the early years of the hydride research that intermetallics and alloys are vulnerable to hydrogen contamination by impure gases such as CO, CO₂, O₂, H₂O, CH₄, and others (Sandrock and Goodell, 1980; Block and Bahs, 1983). Their minimal content (on ppm level) in H₂ may diminish hydrogenation kinetics or even irreversibly block formation of the hydride (Sandrock and Goodell, 1984; Corré et al., 1997; Schweppe et al., 1997; Hanada et al., 2015; Dematteis et al., 2021). Hydrogen purification is an energetically expensive process, especially on the small scale (Du et al., 2021), and thus, understanding of the problems related to alloy and hydride degradation is crucial in practical applications. The dissociation of H₂ requires that active sites for this process are present at the surface, and they are accessible to hydrogen (Züttel et al., 2008). For example, the ideal clean surface of Pd requires at least three empty surface sites to allow hydrogen dissociation (Mitsui et al., 2003; Lopez et al., 2004). As the

hydrogen impurity molecules interact with the surface, they might block the active sites for H₂ dissociation or a protective layer, that is, oxide, hydroxide, and sulfide might be formed. Such a layer prevents transport or dissociation/association of H₂ molecules (Sandrock and Goodell, 1980).

Metal hydrides might act as a catalyst, for example, the for hydrogenation reaction of C₂H₄ over LaNi₅ (Soga et al., 1977). It was reported that the reaction rate was two orders of magnitude higher on hydrogenated alloy (LaNi₅H_{2.4}). LaNi₄X (X = Ni, Cr, Al, and Cu) were reported as catalysts for CO₂ methanation (Ando et al., 1995) with significant activity of LaNi₅ and LaNi₄Cr. The activity is postulated due to the presence of Ni, known as the methanation catalyst (Aziz et al., 2015). To best of our knowledge, no atomistic understanding of mechanisms beyond these catalytic aspects or poisoning mechanism of LaNi₅ exists. Empirical models of LaNi₅ surfaces and a chemical analysis indicate that the surface is enriched in La, La₂O₃, and La(OH)₃ (Wallace et al., 1979; Selvam et al., 1991). This oxide layer is permeable for hydrogen; thus, H₂ can reach Ni atoms underneath, dissociate there, and form a hydride. Similar situation occurs for TiFe; however, permeability of the oxide layer is low for hydrogen (Edalati et al., 2013). One important difference between two compounds is that unlike LaNi₅ TiFe is far more sensitive to CO or CO₂, even a small amount of these gasses passivates or poisons this compound. Energetically demanding heat treatment is required to reactivate TiFe (Sandrock and Goodell, 1980; Block and Bahs, 1983). The so-called activation process required for utilization of the alloy's full potential for reversible hydrogen storage is mostly related to formation of exposed active sites for hydrogen dissociation by perturbing any protective layer that covers them (Schlapbach and Brundle, 1981; Kisi et al., 1992; Edalati et al., 2013). The alloy contamination primarily occurs at the surface or, in general, at the interface between solid and gaseous hydrogen. Therefore, a reliable picture of the alloy's surface is required for understanding its interaction with gasses.

Gas interactions with surfaces are well studied for heterogeneous catalytic and electrocatalytic systems, where insight from theoretical methods already guides discoveries of new catalysts (Greeley et al., 2006; Nørskov et al., 2009; Seh et al., 2017; Pérez-Ramírez and López, 2019). In particular, it is well known that surface modifications by alloying (restricted to top atomic layers) have a strong influence on surface reactivity (Christensen et al., 1997; Greeley et al., 2006). However, atomistic investigations of the bulk alloy surfaces are at an early stage, in particular, due to the difficulties related to segregation, dealloying, and other processes occurring at the surface (Cao et al., 2019; Mamun et al., 2019).

The quantum mechanics-based research in metal hydrides is rather scarce, taking into account a growing impact of theoretical, atomistic calculations on materials science. Such calculations for compounds relevant for hydrogen storage were pioneered decades ago (Malik et al., 1982; Satterthwaite and Jena, 1983). New developments or predictions of metal hydride properties are still far beyond these for secondary batteries or even the so-called complex hydrides, where hydrogen atoms are incorporated into a molecule or ion like BH₄⁻, AlH₄⁻, and NH₄⁺. This is likely due to

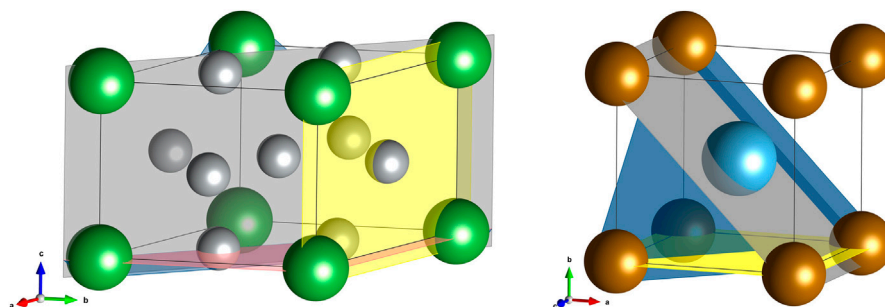


FIGURE 1 | (A) The crystal structure of LaNi_5 . Green spheres are for La and grey for Ni; examples of (0001), (01-10), and (11-20) lattice planes are shown in red, yellow, and grey, respectively. **(B)** The crystal structure of TiFe. Brown spheres are for Fe and blue one for Ti. Examples of (010), (110), and (111) lattice planes are shown in yellow, grey, and blue, respectively.

very complex electronic or magnetic properties of intermetallic compounds that contain transition and rare Earth metals. For example, the electronic structure, elastic properties, hydrogen diffusion in the bulk, and stoichiometric modifications were reported for LaNi_5 (Tatsumi et al., 2001; Hector et al., 2003; Han et al., 2008; Tezuka et al., 2010; Łodziana et al., 2019) or for TiFe (Mankovsky et al., 1997; Canto and de Coss, 2000; Sahara et al., 2015). The calculations of the surface properties are even more rare, and the simplest crystal terminations were considered like (0001)/(10-10) for LaNi_5 (Han et al., 2008; Hanada et al., 2015; Łodziana et al., 2019) or (001) for the face of TiFe (Mankovsky et al., 1997; Canto and de Coss, 2000). A detailed surface analysis of TiFe or LaNi_5 is not present in the literature, to the best of our knowledge.

Hereby, we want to pave the way toward the description of the surface properties of LaNi_5 and TiFe by calculating the surface energy for a variety of low index facets and an analysis of the simplest gas adsorption processes for exposed facets. This requires a series of practical simplifications that will be described below. In the era of advanced computational screening and machine learning methods, these examples might seem trivial. In fact, they are not as the formulation of the realistic models of the surface cannot yet be automated, except for elemental metals or non-metallic elements (Tran et al., 2016). After presentation of methods, the surface energies and the equilibrium crystal shapes for LaNi_5 and TiFe are presented for the first time. Adsorption energies for simple molecules like H_2 , CO, CO_2 , and H_2O complement the surface calculations.

2 METHODS

LaNi_5 has a hexagonal structure (symmetry $P6/mmm$) (Kisi et al., 1992) with a fraction of Ni located at $2c$ Wyckoff positions, sharing the (ab)-plane with La, and there are three La nearest neighbors 2.9 \AA apart from Ni. The second site occupied by Ni is $3g$ placed within the (ab)-plane in between La layers, and there are four La nearest neighbors separated by 3.2 \AA from Ni (**Figure 1**). TiFe (cubic, $Pm\bar{3}m$ symmetry) (Thompson et al., 1989) is an

example of a bcc structure with different elements ordered on two sublattices (**Figure 1**).

All calculations were performed within spin polarized density functional theory (DFT) with a periodic plane wave basis set as implemented in the Vienna *ab initio* Simulation Package (Kresse and Furthmüller, 1996b,a). The calculation parameters were the cutoff energy for the basis set expansion 500 eV , the k-point sampling with density $k \cdot a \geq 60$, the convergence criteria for electronic degrees of freedom 10^{-6} eV/\AA , a conjugated gradient method for atomic relaxation and convergence criteria 10^{-2} eV/\AA , Projected Augmented Wave (PAWs) potentials (Blöchl, 1994; Kresse and Joubert, 1999) for atoms, and the Perdew–Burke–Ernzerhof (PBE) exchange–correlation functional (Perdew et al., 1996). The surface calculations were performed in the slab geometry with minimum 12 \AA of vacuum separating slab images. The slab geometry for each facet was created using a Pymatgen package (Sun and Ceder, 2013; Tran et al., 2016); the slab thickness was minimum 15 \AA . Only stoichiometric slabs were considered; for facets where two or more possible surface terminations exist, all of them were taken into account, and the reported surface energies are for terminations that are the most stable. None of the LaNi_5 surface terminations has the inversion symmetry; thus, the surfaces are different on both sides of the slab. We did not consider possible surface reconstructions or off-stoichiometry, and the reported data are the effective surface energies when both surfaces are exposed. Similar procedure was applied for TiFe; however, for this compound, facets with indexes (110), (211), (310), (321), and (332) possess inversion symmetry/mirror plane parallel to the surface. The surface energies were calculated with the approach of (Fiorentini and Methfessel, 1996). Gas molecule adsorption studies were done on the one side of the slab; the adsorption energy is defined as $E_{ads} = E_{tot} - (E_{slab} + E_X)$, where E_{tot} is the energy of the slab with adsorbed X ($X = \text{H}_2$, CO, CO_2 , and H_2O molecule), E_{slab} is the total energy of the slab, and E_X is the ground state energy for the X molecule (calculated in cubic box with edge of 12 \AA). For adsorption studies, three atomic layers on the bottom side of the slab were frozen and a 2×2 surface supercell was used.

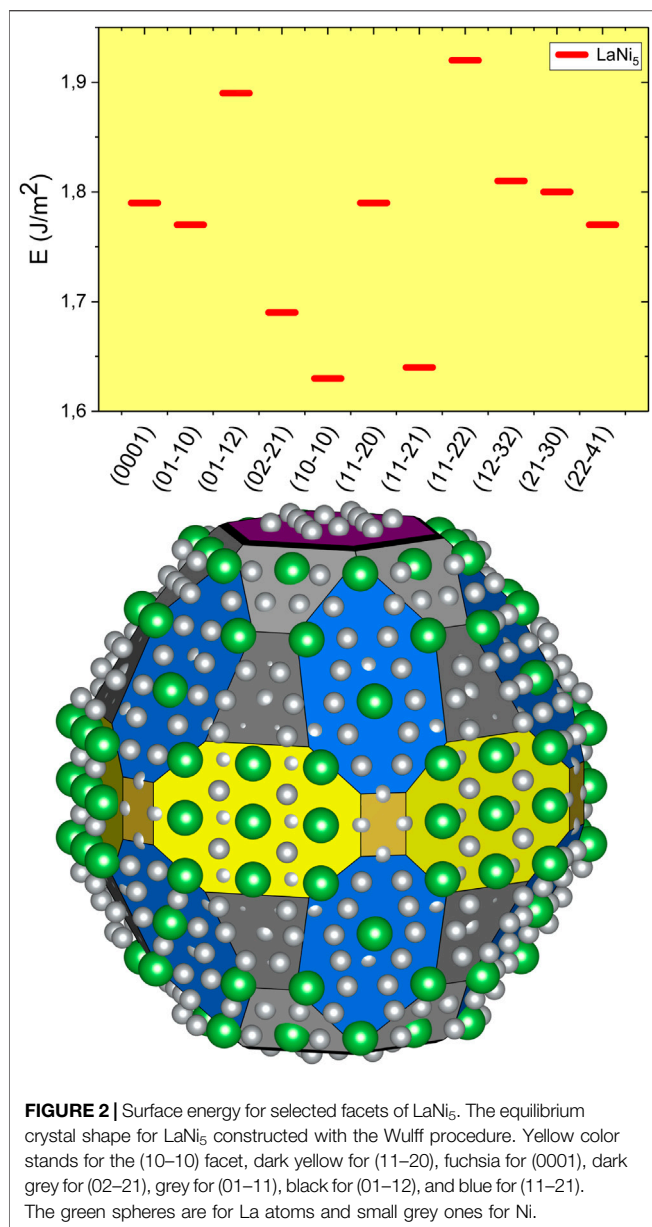


FIGURE 2 | Surface energy for selected facets of LaNi₅. The equilibrium crystal shape for LaNi₅ constructed with the Wulff procedure. Yellow color stands for the (10-10) facet, dark yellow for (11-20), fuchsia for (0001), dark grey for (02-21), grey for (01-11), black for (01-12), and blue for (11-21). The green spheres are for La atoms and small grey ones for Ni.

3 RESULTS

The calculated ground state lattice parameters for LaNi₅ are $a = 5.001$ Å and $c = 3.986$ Å. This compares well with experimental data $a = 5.0125$ Å and $c = 3.9873$ Å (Kisi et al., 1992) or previous calculations $a = 5.008$ Å and $c = 3.967$ Å (Hector et al., 2003). For TiFe, the calculated lattice constant is $a = 2.946$ Å, and it can be compared to experimental $a = 2.9789$ Å (Thompson et al., 1989). The optimized structures were used for construction of the surfaces for both compounds and calculations of the equilibrium crystal shapes.

3.1 Surface Energy

Calculated surface energies are presented in **Figure 2** and **Figure 3**. The surface energy for constituent metals is in the

range 0.7–0.8 J/m² for La, 1.9–2.4 J/m² for Ni, 1.9–2.3 J/m² for Ti, and 2.4–3.4 J/m² for Fe (Tran et al., 2016). The weighted average of elemental surface energies for LaNi₅ ranges from 1.7 J/m² to 2.13 J/m² that covers the range of its surface energies calculated here, with three exceptions (10-10), (02-21), and (11-21). For these facets, lanthanum is over-represented (**Figure 1**); moreover, such crystal planes are different from the (0001) face often considered in the literature.

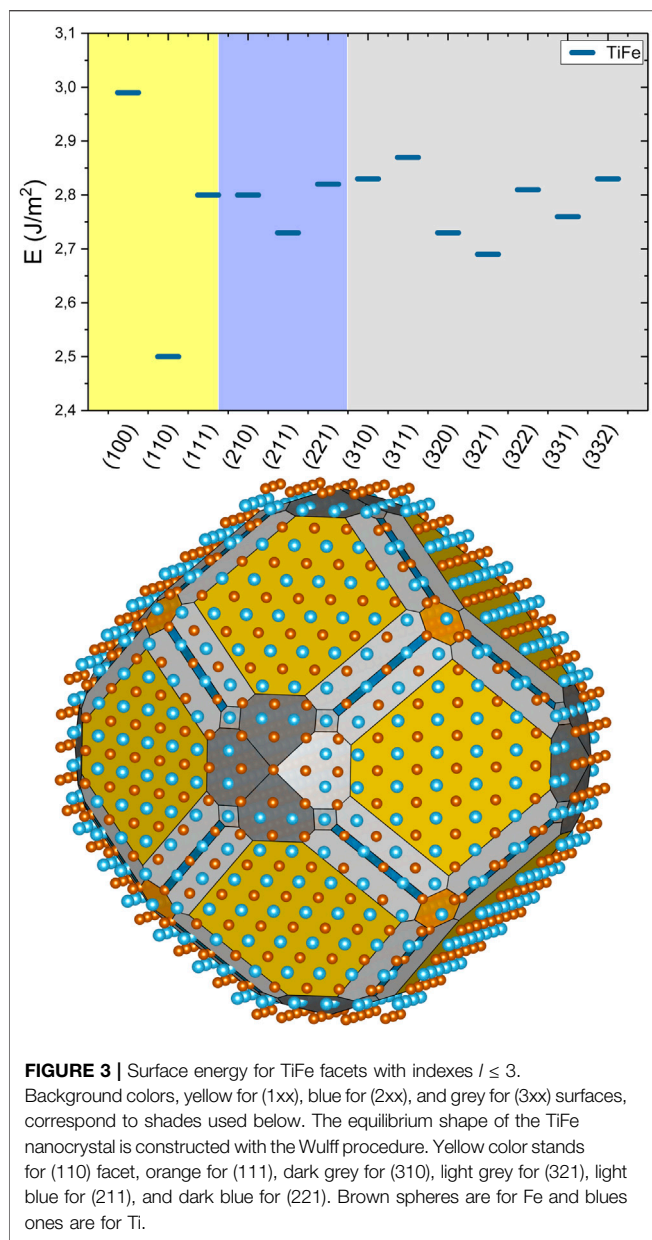
Based on the calculated surface energies, we have constructed the equilibrium shape of the LaNi₅ nano-crystal with the Wulff method (Wulff, 1901; Barmbaris et al., 2015). The crystal symmetry was used for determination of equivalent facets; the nano-crystallite shape is presented in **Figure 2**. In the equilibrium crystal shape, only 7.7% of the exposed surface belongs to (0001) termination, and the largest fraction of 40.4% is the (11-21) facet. Other exposed surface terminations are (10-10), 20.9%; (01-11), 14.1%; and (02-21), 13.4%. Possible atomic compositions of the surface are shown in **Figure 2**; for facets like (10-10), La is over-represented at the surface and it might already seed the surface oxidation and formation of La₂O₃. This can be accompanied by further segregation and La diffusion toward the surface. Observed La₂O₃ and La (OH)₃ can be explained by the composition of most exposed surfaces of LaNi₅. The formation of oxide shifts the surface stability toward the stability of the interface, a thermodynamically driven process of self-limiting passivation.

The surface energies of TiFe are generally larger than these for LaNi₅, and they fall in the average energies for constituting elements, that is, 2.15 J/m² to 2.85 J/m², except the (100) facet.

The (100) surface has usually very large surface energy for bcc metals (Fe, Cr) unlike for alkali metals where the surface energy is very low for all surface terminations (Tran et al., 2016). The lowest surface energy for the (110) crystal plane is not surprising. This is the bcc lattice plane with the densest atom packing. The calculated equilibrium crystal shape is dominated with (110) surface family (50% of all exposed surface); however, surface terminations with higher indexes are largely represented. Such facets expose under-coordinated atoms that are very reactive (Nørskov et al., 2009; Seh et al., 2017) contributing to strong passivation and difficult activation of TiFe alloys. In theoretical calculations, surface terminations with indexes larger than two are rarely used, except for the analysis of highly reactive surfaces (Honkala et al., 2005).

3.2 Gas Adsorption

In order to probe the surface properties, we have calculated the adsorption energies for H₂, CO, CO₂, and H₂O molecules at the (0001) surface of LaNi₅ and (110) surface of TiFe, **Figure 4**. For each molecule, we have considered associative and dissociative adsorption and a variety of adsorption sites. For each compound, it is possible to distinguish on top, bridge, and threefold adsorption sites usually considered in the literature. Due to composition, a top site can be over La, Ni, or Ti, Fe; the bridge site splits into La–Ni and Ni–Ni or Ti–Ti, Fe–Fe, or Ti–Fe. Threefold site consists of 2Ni–La, 2Fe–Ti, or 2Ti–Fe. All adsorption possibilities were considered and the most stable adsorbate configurations are shown in **Figure 4**. For LaNi₅, additional coverage dependence of adsorption energy was considered for H₂ and CO.



For the low coverage limit [$\frac{1}{4}$ monolayer (ML)], dissociative adsorption of H₂ with $\Delta E = -1.67$ eV/H₂ and hydrogen in the bridge positions between two Ni atoms is the most stable one. For 1 ML of hydrogen, the bridge site remains the most stable, and $\Delta E = -1.37$ eV/H₂ (the adsorption energy is given per H₂ molecule here for ease of comparison; in the literature, the adsorption energy is often reported per atom, that is, $\frac{1}{2}$ H₂). For CO, the adsorption energy drops from $\Delta E = -2.06$ eV at $\frac{1}{4}$ ML to $\Delta E = -1.77$ eV for 1 ML (Figure 4). The adsorption site changes from the bridge position to the top of the Ni position at 1 ML of CO; this effect was reported previously (Han et al., 2008). Dissociative adsorption of CO₂ with CO at the top position and oxygen at the Ni–Ni bridge position is $\Delta E = -2.30$ eV; this configuration is more stable than associative adsorption of

CO₂ with $\Delta E = -1.62$ eV where carbon is at the Ni–Ni bridge position and oxygen points toward La. We have not considered energy barriers that might hinder CO₂ molecule dissociation.

In general, the CO₂ dissociation process is very complex. It can lead to formation of nickel carbonyls (NiCO₄), formate anions, or radicals (COOH[•]) or dissociation into elements C and O. Such processes are beyond the scope of this study; however, here we show that dissociative adsorption of CO₂ on LaNi₅ is thermodynamically stable, and thus, it opens a route for catalytic transformation of this gas and indicates that surface oxidation can be related to the presence of CO/CO₂. The adsorption energy for the water molecule is $\Delta E = -0.37$ eV/H₂O on top of La, and for dissociation to OH and H, the adsorption energy is $\Delta E = -1.96$ eV/H₂O (see Figure 4).

For TiFe, only a low coverage adsorption ($\frac{1}{4}$ ML) regime was considered. Hydrogen atoms adsorbed at 2Ti–Fe threefold sites have $\Delta E = -2.03$ eV/H₂; on top of iron is the most stable adsorption site for CO, $\Delta E = -2.54$ eV; for dissociative adsorption of CO + O, $\Delta E = -3.98$ eV, and for OH + H, $\Delta E = -3.00$ eV. The adsorption energy of the CO₂ molecule is $\Delta E = -2.30$ eV with carbon at the Fe–Fe bridge site and O pointing toward Ti; thus, the dissociated state is more stable.

In order to bring calculated adsorption energies into a broader context, one can notice that hydrogen adsorption energies calculated here are generally larger than these calculated for pure elements [–1.29 eV at Ni (100), –1.63 eV at Fe (111), and –2.01 eV at Ti (0001)] (Winther et al., 2019; Billeter et al., 2021). We have found a small activation barrier for H₂ dissociation at TiFe (110) (0.07 eV). For CO, reported molecular adsorption energies are of the range –1.53 eV at the Fe (211) surface or –1.96 eV at the Co₃Ti (111) facet. For water molecules, adsorption energies strongly depend on particular surface geometry, for example, energies of –0.52 eV and –1.72 eV are reported for Fe (211) and molecular or dissociated (OH + H) state, respectively. For the (111) surface of Fe, these energies are lower: –0.09 eV and –0.60 eV, respectively (Winther et al., 2019). Thus, adsorption energies for carbon oxides and H₂O on TiFe (110) calculated here are rather large. However, adsorption of these molecules on binary alloys can result in adsorption energies as large as –5.35 eV for CO₂ on FeZr (Mamun et al., 2019). Such large adsorption energies for CO and CO₂ are in line with a particularly strong poisoning effect of these gasses on TiFe. In fact, the intrinsic nature of the gas adsorption on binary alloy surfaces still poses many open questions. Two types of atoms constituting an alloy bring the reactivity of dense and flat surfaces toward this of high index facets for late transition metals.

4 DISCUSSION

Calculated surface energies and equilibrium crystal shapes for LaNi₅ and TiFe indicate that theoretical models for the surface-related properties in these two intermetallics have to be created with care, as the exposed facets differ from those of elemental metals. Intermetallics and metal hydrides are subject to the mass transport during hydrogen ad/desorption. Within this process, a fresh surface of either phase is formed. The main driving force for

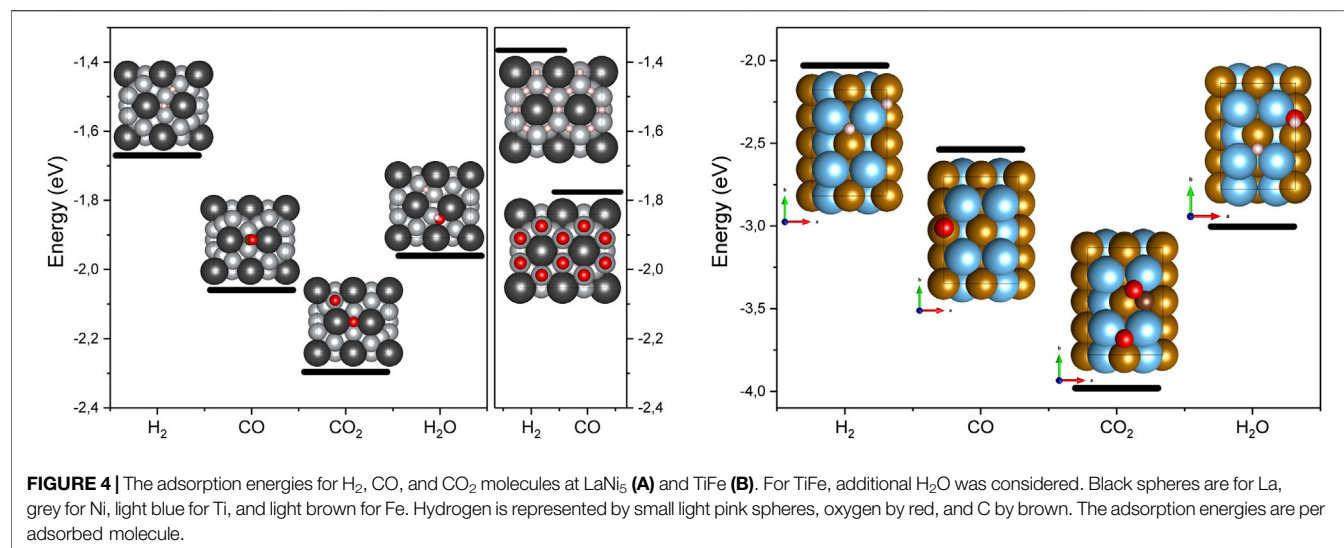


TABLE 1 | Bader charges in *e* calculated for LaNi₅ (0001), and TiFe (110) surfaces. The asterisk is for the dissociated state.

	LaNi ₅	TiFe
H ₂	-0.74*; -0.02	-0.95*; -0.1
H ₂ O	-1.05*; -0.1	-1.11*; -0.05
CO	-0.61	-0.71
CO ₂	-1.66*; -1.11	-2.16*; -1.39

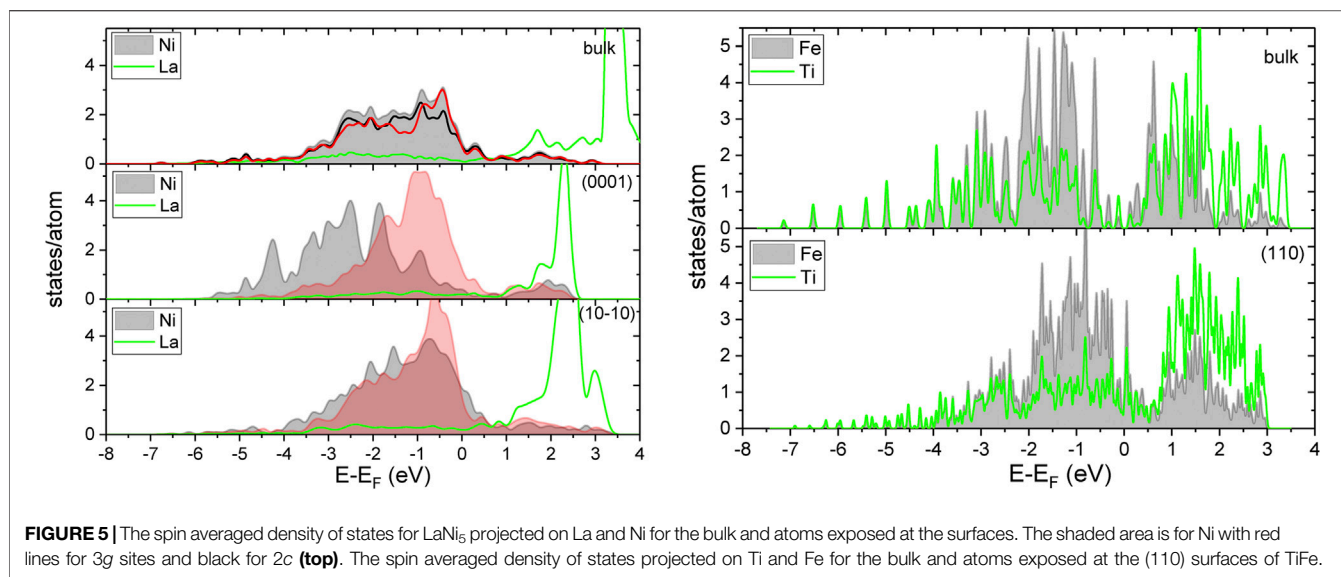
the type of surface is related to thermodynamic stability as exemplified with Wulff construction. Thus, the equilibrium nanocrystal shapes are not only a theoretical concept. To the best of our knowledge, there are no reports of direct observation of the nanocrystalline shapes of LaNi₅ that allows comparison. However, an indirect indication of preferential exposure of the (10–10) surface of LaNi₅ can be deduced from the report of dislocations moving on (10–10) slip planes (Inui et al., 1998). The slip plane must be a low energy surface termination, and indeed, it is such a surface, as presented in **Figure 2**. For TiFe, one can refer to a detailed transmission electron microscopy study of crystallites as small as 7 nm (Emami et al., 2015). Preferential exposure of the (110) surface family is clearly observed there, and the crystallite shape agrees well with this in **Figure 3**. Our analysis brings other facets that are exposed at the edges; these facets with high indexes possess under-coordinated atoms that are more reactive (Nørskov et al., 2009) and constitute 50% of the surface. The change of the surface properties between metal and metal hydride is also related to the degradation processes. With repetitive cycling, it can be strongly affected by formation of oxides, hydroxides, or carbides. Further studies are required in this direction.

Calculated adsorption energies for hydrogen, CO, CO₂, and H₂O molecules indicate that the binding energy for larger molecules is stronger than H₂. The physisorption (for weak interactions) or chemisorption (strong interaction) describes

interactions of gasses with surfaces. Strong interactions are accompanied by the charge transfer between solid and adsorbed molecules, and once charge donation from the surface to bonding molecular orbitals occurs, the molecule dissociation or transformation might take place. We have performed the charge distribution analysis for adsorbed molecules according to the Bader method (Henkelman et al., 2006) (see **Table 1**). For dissociative adsorption, the sum of charges for all adsorbed species is reported in **Table 1**. The charge donation is observed for all adsorbed molecules and for all surfaces considered here. The charge transfer is systematically larger for TiFe as the adsorption energies are larger too.

Such electron donation leads to bond breaking in H₂ (this process is not activated on LaNi₅ and calculated activation energy on TiFe is 0.07 eV) or formation of CO₂ radical anions. These radical anions are no longer straight, and the O–C–O angle is of the order 130° (Álvarez et al., 2017). In the present calculations, the bend angle of CO₂ is 123° for adsorption on LaNi₅ and 118° for TiFe. Such large deformation of the CO₂ molecule is due to the composition of the surface and geometrical factors. The length of CO₂ is 2.32 Å; once adsorbed, the carbon atom locates in the bridge site and oxygen points toward the second element. For LaNi₅, the Ni–Ni bridge site for C is preferred and oxygen is oriented toward La, and nearest La atoms are separated by 5.0 Å. On TiFe, the carbon atom is at the Fe–Fe bridge site and oxygen points toward Ti that are separated by 4.3 Å, and the CO₂ bending angle is larger for this case. The dissociation of carbon dioxide is an activated process (Liu et al., 2012), and in order to fully understand the interaction of carbon oxides with surfaces considered here, the separate study are required that shall include activation energies and formation of Ni/Fe carbonyls, formate radicals, and other molecules or oxidation.

Adsorption energies calculated here bring important information for the compound property. The firm



conclusion from this study is that large adsorption energies for CO , CO_2 , and H_2O shall lead to accumulation of these molecules at the surface, even if they are present in very small concentrations. Such accumulation blocks surface sites that are necessary for H_2 dissociation or trigger surface reactions that potentially form even stronger protective layers at the surface. For example, all metals that constitute presented alloys form stable oxides. Their enthalpy of formation varies strongly with the element, and the most stable is La_2O_3 [$\Delta H^0 = -1791.6 \text{ kJ/mol}$ (Konings et al., 2014)]; for TiO_2 (rutile), $\Delta H^0 = -944.747 \text{ kJ/mol}$ (Chase, 1998), for NiO , $\Delta H^0 = -239.74 \text{ kJ/mol}$ (Boyle et al., 1954), and for Fe_2O_3 , $\Delta H^0 = -825.503 \text{ kJ/mol}$ (Chase, 1998). Additionally stable carbides like TiC [$\Delta H^0 = -184.096 \text{ kJ/mol}$ (Chase, 1998)] can be formed. Dissociative adsorption of water or carbon oxides will, thus, result in very strongly bound oxygen or oxide layers for large coverage. Large adsorption energies for CO and CO_2 on TiFe explain sensitivity of this compound to such impurities in H_2 .

Adsorption of molecules or atoms at transition metal surfaces is successfully described by correlation of the adsorption energy and center of d-band (Newns, 1969; Nørskov et al., 2009). The density of states for the bulk and surface are shown in **Figure 5**. For LaNi_5 , it can be seen that the center of the valence band for Ni strongly depends on the exposed facet and the site symmetry of Ni. For the (0001) surface, the Ni valence d-band is shifted to lower energies. This effect is less pronounced for the (10-10) surface. As the La electronic states are located above the Fermi level, the reactivity of the surface is related to exposed nickel and La can be oxidized.

Besides the stoichiometric composition of the surface where La is over-represented and oxidation of this element occurs, the modification of the electronic structure is an additional factor of the surface reactivity of resistivity for hydrogen contamination. For TiFe , the modification of the valence band at the surface is

also present; here, the center of the valence band moves to higher energies at the surface, and the shifts of the band position are similar for Ti and Fe.

5 SUMMARY

In the present study, we have shown an example of the surface energy calculations for alloys relevant for hydrogen storage. The equilibrium crystal shapes were determined for LaNi_5 and TiFe . The composition of exposed surfaces of LaNi_5 indicates over-representation of La which can be oxidized. The strong binding energies of CO , CO_2 , and H_2O at the surfaces of compounds considered here indicate that they accumulate at the surface, blocking the active sites for hydrogen adsorption/dissociation or became precursors for catalytic activity of intermetallics. Large adsorption energies for carbon oxides on TiFe (110) can explain a very high sensitivity of this material to hydrogen contaminations by CO/CO_2 . Understanding of the processes at the surface is one of the key points for improvement of the cyclic stability of metal hydrides or finding new applications for catalyzed reactions. The future calculations in this direction shall bring significant advances in material design for efficient hydrogen storage or catalytic transformations with metal hydrides.

DATA AVAILABILITY STATEMENT

The raw data supporting the conclusion of this article will be made available by the authors, without undue reservation.

AUTHOR CONTRIBUTIONS

The author confirms being the sole contributor of this work and has approved it for publication.

FUNDING

This manuscript is the results of the research project funded by the NCBiR project BIOSTRATEG2/297310/13/NCBR/2016.

REFERENCES

- Álvarez, A., Borges, M., Corral-Pérez, J. J., Olcina, J. G., Hu, L., Cornu, D., et al. (2017). CO₂ Activation over Catalytic Surfaces. *ChemPhysChem* 18, 3135–3141. doi:10.1002/cphc.201700782
- Ando, H., Fujiwara, M., Matsumura, Y., Miyamura, H., Tanaka, H., and Souma, Y. (1995). Methanation of Carbon Dioxide over LaNi₄X-type Intermetallic Compounds as Catalyst Precursor. *J. Alloys Compd.* 223, 139–141. doi:10.1016/0925-8388(94)01488-4
- Aziz, M. A. A., Jalil, A. A., Triwahyono, S., and Ahmad, A. (2015). CO₂ Methanation over Heterogeneous Catalysts: Recent Progress and Future Prospects. *Green. Chem.* 17, 2647–2663. doi:10.1039/C5GC00119F
- Baran, A., and Polański, M. (2020). Magnesium-Based Materials for Hydrogen Storage-A Scope Review. *Materials* 13, 3993. doi:10.3390/ma13183993
- Barmaris, G. D., Łodziana, Z., Lopez, N., and Remedakis, I. N. (2015). Nanoparticle Shapes by Using Wulff Constructions and First-Principles Calculations. *Beilstein J. Nanotechnol.* 6, 361–368. doi:10.3762/bjnano.6.35
- Billeter, E., Łodziana, Z., and Andreas, B. (2021). Surface Properties of the Hydrogen - Titanium Nsystem. submitted
- Blöchl, P. E. (1994). Projector Augmented-Wave Method. *Phys. Rev. B* 50, 17953–17979. doi:10.1103/physrevb.50.17953
- Block, F. R., and Bahr, H.-J. (1983). Investigation of Selective Absorption of Hydrogen by Lani₅ and Fet_i. *J. Less Common Met.* 89, 77–84. doi:10.1016/0022-5088(83)90251-5
- Boer, F. d., Mattens, W., Boom, R., Miedema, A., and Niessen, A. (1988). *Cohesion in Metals*. Netherlands: North-Holland.
- Boyle, B. J., King, E. G., and Conway, K. C. (1954). Heats of Formation of Nickel and Cobalt Oxides (Nio and Co) of Combustion Calorimetry. *J. Am. Chem. Soc.* 76, 3835–3837. doi:10.1021/ja01643a072
- Broom, D. P. (2011). *Hydrogen Storage Materials*. London, United Kingdom: Springer-Verlag London. doi:10.1007/978-0-85729-221-6
- Canto, G., and de Coss, R. (2000). Tight-binding Electronic Structure Calculations for the TiFe(001) Surface. *Surf. Sci.* 465, 59–64. doi:10.1016/S0039-6028(00)00662-2
- Cao, L., Niu, L., and Mueller, T. (2019). Computationally Generated Maps of Surface Structures and Catalytic Activities for alloy Phase Diagrams. *Proc. Natl. Acad. Sci. USA* 116, 22044–22051. doi:10.1073/pnas.1910724116
- Chase, M. (1998). *NIST-JANAF Thermochemical Tables*. 4th Edition. Washington, DC: American Institute of Physics.
- Christensen, A., Ruban, A. V., Stoltze, P., Jacobsen, K. W., Skriver, H. L., Nørskov, J. K., et al. (1997). Phase Diagrams for Surface Alloys. *Phys. Rev. B* 56, 5822–5834. doi:10.1103/PhysRevB.56.5822
- Corrê, S., Gotoh, Y., Sakaguchi, H., Fruchart, D., and Adachi, G.-Y. (1997). The Hydrogen Confinement in Lani₅ and Lani₅zr_{0.1} Hydrides Using Poisonous Gases. *J. Alloys Compd.* 255, 117–121. doi:10.1016/S0925-8388(96)02869-1
- Dematteis, E. M., Berti, N., Cuevas, F., Latroche, M., and Baricco, M. (2021). Substitutional Effects in TiFe for Hydrogen Storage: a Comprehensive Review. *Mater. Adv.* 2, 2524–2560. doi:10.1039/D1MA00101A
- Du, Z., Liu, C., Zhai, J., Guo, X., Xiong, Y., Su, W., et al. (2021). A Review of Hydrogen Purification Technologies for Fuel Cell Vehicles. *Catalysts* 11, 393. doi:10.3390/catal11030393
- Edalati, K., Matsuda, J., Arita, M., Daio, T., Akiba, E., and Horita, Z. (2013). Mechanism of Activation of TiFe Intermetallics for Hydrogen Storage by Severe Plastic Deformation Using High-Pressure Torsion. *Appl. Phys. Lett.* 103, 143902. doi:10.1063/1.4823555
- Emami, H., Edalati, K., Matsuda, J., Akiba, E., and Horita, Z. (2015). Hydrogen Storage Performance of TiFe after Processing by ball Milling. *Acta Material.* 88, 190–195. doi:10.1016/j.actamat.2014.12.052
- Fiorentini, V., and Methfessel, M. (1996). Extracting Convergent Surface Energies from Slab Calculations. *J. Phys. Condens. Matter* 8, 6525–6529. doi:10.1088/0953-8984/8/36/005

ACKNOWLEDGMENTS

CPU allocation at the PL-Grid infrastructure is kindly acknowledged.

- Fuel Cells Bulletin (2018). Doosan Starts Installation of Hydrogen-Fueled 50 Mw Fuel Cell Power Plant in south korea. *Fuel Cell Bull.* 2018, 1. doi:10.1016/S1464-2859(18)30270-0
- Fukai, Y. (2005). *The Metal-Hydrogen System*. Berlin, Heidelberg: Springer. doi:10.1007/3-540-28883-X
- Greeley, J., Jaramillo, T. F., Bonde, J., Chorkendorff, I., and Nørskov, J. K. (2006). Computational High-Throughput Screening of Electrocatalytic Materials for Hydrogen Evolution. *Nat. Mater.* 5, 909–913. doi:10.1038/nmat1752
- Han, S., Zhang, X.-B., Shi, S.-Q., Kohyama, M., Tanaka, H., Kuriyama, N., et al. (2008). CO Adsorption on a LaNi₅Hydrogen Storage Alloy Surface: A Theoretical Investigation. *ChemPhysChem* 9, 1564–1569. doi:10.1002/cphc.200800080
- Hanada, N., Nakagawa, T., Asada, H., Ishida, M., Takahashi, K., Isobe, S., et al. (2015). Dependence of Constituent Elements of AB₅ Type Metal Hydrides on Hydrogenation Degradation by CO₂ Poisoning. *J. Alloys Compd.* 647, 198–203. doi:10.1016/j.jallcom.2015.05.253
- Hector, L. G., Herbst, J. F., and Capehart, T. W. (2003). Electronic Structure Calculations for LaNi₅ and LaNi₅H₇: Energetics and Elastic Properties. *J. Alloys Compd.* 353, 74–85. doi:10.1016/S0925-8388(02)01324-5
- Henkelman, G., Arnaldsson, A., and Jónsson, H. (2006). A Fast and Robust Algorithm for Bader Decomposition of Charge Density. *Comput. Mater. Sci.* 36, 354–360. doi:10.1016/j.commatsci.2005.04.010
- Herzberg, G., and Monfils, A. (1961). The Dissociation Energies of the H₂, HD, and D₂ Molecules. *J. Mol. Spectrosc.* 5, 482–498. doi:10.1016/0022-2852(61)90111-4
- Honkala, K., Hellman, A., Remedakis, I. N., Logadottir, A., Carlsson, A., Dahl, S., et al. (2005). Ammonia Synthesis from First-Principles Calculations. *Science* 307, 555–558. doi:10.1126/science.1106435
- Hume-Rothery, W., Mabbott, W., GilbertChannel Evans, K. M., and Carpenter, H. C. H. (1934). The Freezing Points, Melting Points, and Solid Solubility Limits of the Alloys of Silver and Copper with the Elements of the B Sub-groups. *Phil. Trans. R. Soc. Lond. A.* 233, 1–97. doi:10.1098/rsta.1934.0014
- Inui, H., Yamamoto, T., Di, Z., and Yamaguchi, M. (1998). C-type Dislocations Emitted from Cracks Introduced in a Thin Foil of Lani₅. *J. Alloys Compd.* 269, 294–296. doi:10.1016/S0925-8388(98)00164-9
- Ivey, D. G., and Northwood, D. O. (1983). Storing Energy in Metal Hydrides: a Review of the Physical Metallurgy. *J. Mater. Sci.* 18, 321–347. doi:10.1007/BF00560621
- Jain, A., Miyaoka, H., and Ichikawa, T. (2016). Destabilization of Lithium Hydride by the Substitution of Group 14 Elements: A Review. *Int. J. Hydrogen Energ.* 41, 5969–5978. doi:10.1016/j.ijhydene.2016.02.069
- Joubert, J.-M., Paul-Boncour, V., Cuevas, F., Zhang, J., and Latroche, M. (2021). LaNi₅ Related AB₅ Compounds: Structure, Properties and Applications. *J. Alloys Compd.* 862, 158163. doi:10.1016/j.jallcom.2020.158163
- Kisi, E. H., Buckley, C. E., and Gray, E. M. (1992). The Hydrogen Activation of LaNi₅. *J. Alloys Compd.* 185, 369–384. doi:10.1016/0925-8388(92)90484-Q
- Konings, R. J. M., Beneš, O., Kovács, A., Manara, D., Sedmidubský, D., Gorokhov, L., et al. (2014). The Thermodynamic Properties of Thf-Elements and Their Compounds. Part 2. The Lanthanide and Actinide Oxides. *J. Phys. Chem. Reference Data* 43, 013101. doi:10.1063/1.4825256
- Kresse, G., and Furthmüller, J. (1996a). Efficiency of Ab-Initio Total Energy Calculations for Metals and Semiconductors Using a Plane-Wave Basis Set. *Comput. Mater. Sci.* 6, 15–50. doi:10.1016/0927-0256(96)00008-0
- Kresse, G., and Furthmüller, J. (1996b). Efficient Iterative Schemes Forab Initio Total-Energy Calculations Using a Plane-Wave Basis Set. *Phys. Rev. B* 54, 11169–11186. doi:10.1103/physrevb.54.11169
- Kresse, G., and Joubert, D. (1999). From Ultrasoft Pseudopotentials to the Projector Augmented-Wave Method. *Phys. Rev. B* 59, 1758–1775. doi:10.1103/physrevb.59.1758

- Liu, C., Cundari, T. R., and Wilson, A. K. (2012). Co₂ Reduction on Transition Metal (Fe, Co, Ni, and Cu) Surfaces: In Comparison with Homogeneous Catalysis. *J. Phys. Chem. C* 116, 5681–5688. doi:10.1021/jp210480c
- Lopez, N., Łodziana, Z., Illas, F., and Salmeron, M. (2004). When Langmuir Is Too Simple: H₂ Dissociation on Pd(111) at High Coverage. *Phys. Rev. Lett.* 93, 146103. doi:10.1103/PhysRevLett.93.146103
- Malik, S. K., Arlinghaus, F. J., and Wallace, W. E. (1982). Calculation of the Spin-Polarized Energy-Band Structure of LaNi₅ and GdNi₅. *Phys. Rev. B* 25, 6488–6491. doi:10.1103/PhysRevB.25.6488
- Mamun, O., Winther, K. T., Boes, J. R., and Bligaard, T. (2019). High-throughput Calculations of Catalytic Properties of Bimetallic alloy Surfaces. *Sci. Data* 6, 76. doi:10.1038/s41597-019-0080-z
- Mankovsky, S., Ostrokhov, A., Floka, V., and Cherepin, V. (1997). The Electronic Structure and Magnetic Properties of (100) Surface of TiFe alloy. *Vacuum* 48, 245–247. doi:10.1016/S0042-207X(96)00265-5
- Mitsui, T., Rose, M. K., Fomin, E., Ogletree, D. F., and Salmeron, M. (2003). Dissociative Hydrogen Adsorption on Palladium Requires Aggregates of Three or More Vacancies. *Nature* 422, 705–707. doi:10.1038/nature01557
- Modi, P., and Aguey-Zinsou, K.-F. (2021). Room Temperature Metal Hydrides for Stationary and Heat Storage Applications: A Review. *Front. Energ. Res.* 9, 128. doi:10.3389/fenrg.2021.616115
- Mohtadi, R., and Orimo, S.-i. (2017). The Renaissance of Hydrides as Energy Materials. *Nat. Rev. Mater.* 2, 16091. doi:10.1038/natrevmats.2016.91
- Newns, D. M. (1969). Self-consistent Model of Hydrogen Chemisorption. *Phys. Rev.* 178, 1123–1135. doi:10.1103/PhysRev.178.1123
- Nørskov, J. K., Bligaard, T., Rossmeisl, J., and Christensen, C. H. (2009). Towards the Computational Design of Solid Catalysts. *Nat. Chem.* 1, 37–46. doi:10.1038/nchem.121
- Perdew, J. P., Burke, K., and Ernzerhof, M. (1996). Generalized Gradient Approximation Made Simple. *Phys. Rev. Lett.* 77, 3865–3868. doi:10.1103/physrevlett.77.3865
- Pérez-Ramírez, J., and López, N. (2019). Strategies to Break Linear Scaling Relationships. *Nat. Catal.* 2, 971–976. doi:10.1038/s41929-019-0376-6
- Pettifor, D. G. (1986). The Structures of Binary Compounds. I. Phenomenological Structure Maps. *J. Phys. C: Solid State. Phys.* 19, 285–313. doi:10.1088/0022-3719/19/3/002
- Sahara, R., Emura, S., and Tsuchiya, K. (2015). Theoretical Investigation of Effect of Alloying Elements on Phase Stability in Body-Centered Cubic Ti-X Alloys (X = V, Cr, Fe, Co, Nb, and Mo). *J. Alloys Compd.* 634, 193–199. doi:10.1016/j.jallcom.2015.02.005
- Saitoh, H., Machida, A., Katayama, Y., and Aoki, K. (2008). Formation and Decomposition of AlH₃ in the Aluminum-Hydrogen System. *Appl. Phys. Lett.* 93, 151918. doi:10.1063/1.3002374
- Sakintuna, B., Lamaridarkrim, F., and Hirscher, M. (2007). Metal Hydride Materials for Solid Hydrogen Storage: A Review. *Int. J. Hydrogen Energ.* 32, 1121–1140. doi:10.1016/j.ijhydene.2006.11.022
- Sandrock, G. D., and Goodell, P. D. (1984). Cyclic Life of Metal Hydrides with Impure Hydrogen: Overview and Engineering Considerations. *J. Less Common Met.* 104, 159–173. doi:10.1016/0022-5088(84)90452-1
- Sandrock, G. D., and Goodell, P. D. (1980). Surface Poisoning of LaNi₅, FeTi and (Fe,mn)Ti by O₂, Co and H₂O. *J. Less Common Met.* 73, 161–168. doi:10.1016/0022-5088(80)90355-0
- Satterthwaite, C., and Jena, P. (1983). *Electronic Structure and Properties of Hydrogen in Metals*. New York: Springer US.
- Schlapbach, L., and Brundle, C. R. (1981). XPS Study of the Chemisorption Induced Surface Segregation in LaNi₅ and ThNi₅. *J. Phys. France* 42, 1025–1028. doi:10.1051/jphys:019810042070102500
- Schweppe, F., Martin, M., and Fromm, E. (1997). Hydrogen Absorption of LaNi₅ Powders Precovered with O₂, Co, H₂s, Co₂ or N₂. *J. Alloys Compd.* 253–254, 511–514. doi:10.1016/S0925-8388(96)03002-2
- Seh, Z. W., Kibsgaard, J., Dickens, C. F., Chorkendorff, I., Nørskov, J. K., and Jaramillo, T. F. (2017). Combining Theory and experiment in Electrocatalysis: Insights into Materials Design. *Science* 355, eaad4998. doi:10.1126/science.aad4998
- Selvam, P., Viswanathan, B., Swamy, C., and Srinivasan, V. (1991). Surface Properties of LaNi₅: A Reinvestigation. *Int. J. Hydrogen Energ.* 16, 23–33. doi:10.1016/0360-3199(91)90057-P
- Soga, K., Imamura, H., and Ikeda, S. (1977). Hydrogenation of Ethylene over Lanthanum-Nickel (LaNi₅) alloy. *J. Phys. Chem.* 81, 1762–1766. doi:10.1021/j100533a010
- Sun, W., and Ceder, G. (2013). Efficient Creation and Convergence of Surface Slabs. *Surf. Sci.* 617, 53–59. doi:10.1016/j.susc.2013.05.016
- Tatsumi, K., Tanaka, I., Inui, H., Tanaka, K., Yamaguchi, M., and Adachi, H. (2001). Atomic Structures and Energetics of LaNi₅-H solid Solution and Hydrides. *Phys. Rev. B* 64, 184105. doi:10.1103/PhysRevB.64.184105
- Tezuka, A., Wang, H., Ogawa, H., and Ikeshoji, T. (2010). Potential Energy Surface and Hopping Path for Hydrogen in LaNi₅. *Phys. Rev. B* 81, 134304. doi:10.1103/PhysRevB.81.134304
- Thompson, P., Reilly, J. J., and Hastings, J. M. (1989). The Application of the Rietveld Method to a Highly Strained Material with Microtwins: TiFeD_{1.9}. *J. Appl. Cryst.* 22, 256–260. doi:10.1107/S002188988801430X
- Tran, R., Xu, Z., Radhakrishnan, B., Winston, D., Sun, W., Persson, K. A., et al. (2016). Surface Energies of Elemental Crystals. *Sci. Data* 3, 160080. doi:10.1038/sdata.2016.80
- Wallace, W. E., Karlick, R. F., and Imamura, H. (1979). Mechanism of Hydrogen Absorption by Lanthanum-Nickel (LaNi₅). *J. Phys. Chem.* 83, 1708–1712. doi:10.1021/j100476a006
- Winther, K. T., Hoffmann, M. J., Boes, J. R., Mamun, O., Bajdich, M., and Bligaard, T. (2019). Catalysis-hub.org, an Open Electronic Structure Database for Surface Reactions. *Sci. Data* 6, 75. doi:10.1038/s41597-019-0081-y
- Wulff, G. (1901). XXV. Zur Frage der Geschwindigkeit des Wachstums und der Auflösung der Krystallflächen. *Z. Kristallogr. Cryst. Mater.* 34, 449–530. doi:10.1524/zkri.1901.34.1.449
- Züttel, A., Schlapbach, L., and Borgschulte, A. (2008). *Hydrogen as a Future Energy Carrier*. Weinheim: John Wiley & Sons. doi:10.1002/9783527622894.fmatter
- Łodziana, Z., Dębski, A., Cios, G., and Budziak, A. (2019). Ternary LaNi_{4.75}Mn_{0.25} Hydrogen Storage Alloys: Surface Segregation, Hydrogen Sorption and Thermodynamic Stability. *Int. J. Hydrogen Energ.* 44, 1760–1773. doi:10.1016/j.ijhydene.2018.11.104

Conflict of Interest: The author declares that the research was conducted in the absence of any commercial or financial relationships that could be construed as a potential conflict of interest.

Publisher's Note: All claims expressed in this article are solely those of the authors and do not necessarily represent those of their affiliated organizations, or those of the publisher, the editors, and the reviewers. Any product that may be evaluated in this article, or claim that may be made by its manufacturer, is not guaranteed or endorsed by the publisher.

Copyright © 2021 Łodziana. This is an open-access article distributed under the terms of the Creative Commons Attribution License (CC BY). The use, distribution or reproduction in other forums is permitted, provided the original author(s) and the copyright owner(s) are credited and that the original publication in this journal is cited, in accordance with accepted academic practice. No use, distribution or reproduction is permitted which does not comply with these terms.



Degradation Comparison of Cyclic and Linear Siloxane Contamination on Solid Oxide Fuel Cells Ni-YSZ Anode

Jiashen Tian and Ryan J. Milcarek*

School for Engineering of Matter, Transport and Energy, Arizona State University, Tempe, AZ, United States

OPEN ACCESS

Edited by:

Uwe Schröder,
University of Greifswald, Germany

Reviewed by:

Stephen Skinner,
Imperial College London,
United Kingdom
Aleksy Yaremchenko,
University of Aveiro, Portugal

*Correspondence:

Ryan J. Milcarek
Ryan.Milcarek@asu.edu

Specialty section:

This article was submitted to
Fuel Cells,
a section of the journal
Frontiers in Energy Research

Received: 29 July 2021

Accepted: 11 October 2021

Published: 22 October 2021

Citation:

Tian J and Milcarek RJ (2021)
Degradation Comparison of Cyclic and
Linear Siloxane Contamination on Solid
Oxide Fuel Cells Ni-YSZ Anode.
Front. Energy Res. 9:749771.
doi: 10.3389/fenrg.2021.749771

The solid oxide fuel cell (SOFC) nickel-yttria stabilized zirconia (Ni-YSZ) anode degradation due to different types of siloxane contamination is investigated. A cyclic structure siloxane, octamethylcyclotetrasiloxane (D4), and a linear structure siloxane, decamethyltetrasiloxane (L4), are mixed with H_2+N_2 as the fuel for SOFCs at 750°C. The electrochemical characterization results after stability experiments suggest that the SOFC contaminated with cyclic siloxane, D4, had higher degradation. Pure YSZ pellets with different surface hydroxylation extents were also tested to investigate the D4/L4 adsorption and deposition process. Postmortem SEM/WDS, XRD and Raman analysis all indicate that cyclic siloxane has more deposition than linear siloxane on the anode. Further analysis demonstrates that high adsorption and low desorption rates of cyclic siloxane on YSZ are linked to the degradation. Besides the silicon deposition, SiC and amorphous carbon deposition were also observed from the XRD and Raman analysis.

Keywords: solid oxide fuel cell (SOFC), siloxane, biogas, degradation, D4, L4, carbon deposition

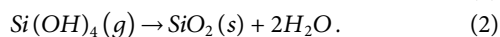
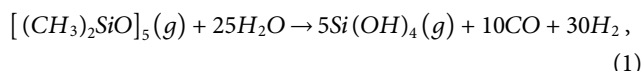
INTRODUCTION

Biogas is generated during the natural degradation of organic material by microorganisms under anaerobic conditions. Wastewater treatment plants utilize the anaerobic digestion process converting organic material in wastewater to biogas. Similarly, the organic composition of the solid waste in landfills decomposes to produce biogas (Park and Shin, 2001). The biogas collected from wastewater treatment plants and landfills is considered a renewable fuel that could be used to produce electricity, heat or as vehicle fuel (Scarlat et al., 2018). Biogas from organic waste digesters usually contains from 60 to 70% methane, from 30 to 40% carbon dioxide and <1% nitrogen. In landfills, methane concentration is usually from 45 to 55%, carbon dioxide from 30 to 40% and nitrogen from 5 to 15% (Jonsson et al., 1997). Generally, biogas also contains impurities such as hydrogen sulfide, siloxanes, aromatics and halogenated compounds. The concentration of the main impurities are 0.005–2 vol% hydrogen sulfide, 0–0.02 vol% siloxanes, <1 vol% ammonia, and <0.6 vol% halogenated compounds (Ryckebosch et al., 2011).

Prime movers, as a source of motive power, can be used to convert biogas to useful work. Gas turbines, micro-turbines, reciprocating internal combustion engines and Stirling engines are common prime movers utilized extensively (Riley et al., 2020). Solid oxide fuel cells (SOFCs) are an alternative prime mover that can utilize biogas, the use of which results in higher electrical efficiency, reduced NO_x and lower carbon emissions (Rillo et al., 2017; Gandiglio et al., 2020). Despite potential for direct use of biogas, challenges remain with impurities like hydrogen sulfide and siloxanes. These impurities, even at low concentrations, can potentially damage the prime movers which becomes the main barrier for biogas applications (Papurello et al., 2014; Papurello et al., 2016).

Utilizing biogas directly without purification causes serious damage to prime movers after long-term operation. Among the impurities, H_2S contamination causes temporary and permanent performance degradation of SOFCs. SOFC degradation due to H_2S contamination was studied extensively at different temperatures, operating current/voltage, operating time and H_2S concentration (0.02–240 ppm) (Rasmussen and Hagen, 2009). In comparison, research on siloxane, which has been reported as the main impurity causing failure of common prime movers (Trendewicz and Braun, 2013), has not received as much attention. There are many different kinds of siloxane that exist in biogas and they can be sorted based on cyclic or linear structure. Cyclic siloxanes are designated by a “D” for cyclic structure and a number indicating how many silicon atoms per molecule. Hexamethylcyclotrisiloxane (D3), Octamethylcyclotetrasiloxane (D4) and Decamethylcyclopentasiloxane (D5) are the cyclic structure siloxanes typically found in biogas with the highest concentration. Linear siloxanes are designated by a “L” for linear structure and a number indicating how many silicon atoms per molecule. For linear siloxanes, trace levels of hexamethyldisiloxane (L2), octamethyltrisiloxane (L3) and decamethyltetrasiloxane (L4) can be detected in biogas (Rücker and Kümmerer, 2015).

The concentration of each type of siloxane in biogas from wastewater treatment plants differs significantly. For example, smaller molecule siloxane, like D3, L3, and L2, can only exist in a limited amount because of high volatility which leads to vaporization prior to the anaerobic digester. There are also only small amounts of larger siloxane, such as D6, in biogas due to low volatility and low partial pressure in the active sludge (Dewil et al., 2007). As a result, cyclic siloxanes D5 and D4, which have stable molecular structure, typically have higher concentration and thus are often selected to represent all siloxanes in biogas for SOFCs contamination studies. For example, Haga et al. (2008) reported fatal degradation of the Ni/ScSZ anode SOFC due to 10 ppm D5 contamination in 30–50 h. In that study, the authors also hypothesized a two-step siloxane deposition reaction shown in Eqs 1, 2 resulting in siloxane conversion to silicon dioxide (Haga et al., 2008).



Similar to the study by K. Haga et al., Kikuchi et al. (2017) also tested the Ni/ScSZ anode SOFC with the 60 ppm D5 as the impurity. After a 100 h experiment, significant SOFC degradation was observed. Madi et al. (2015b), Madi et al. (2015a) reported 50% degradation (voltage decrease at constant current density) per 1,000 h for a SOFC with Ni/YSZ anode utilizing simulated reformed biogas mixed with ppm level D4. Furthermore, Papurello and Lanzini (2018) reported that even ppb level D4 could cause obvious degradation of an SOFC with Ni/YSZ anode after 50 h operation. The author's recent work (Tian and Milcarek, 2020; Tian and Milcarek, 2021) reported significant Ni/YSZ anode SOFC degradation with ppm level D4

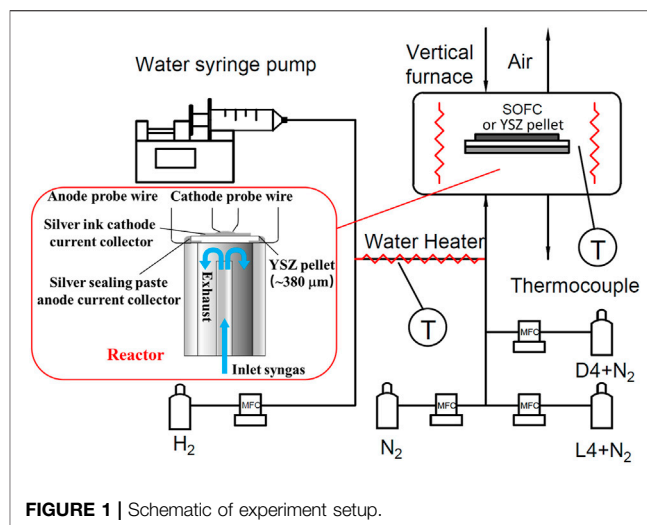


FIGURE 1 | Schematic of experiment setup.

contamination in different fuel compositions. Besides silicon deposition, carbon deposition was observed and hypothesized to be an essential factor causing SOFC performance degradation.

The previous studies only focus on SOFC degradation due to cyclic siloxanes instead of linear siloxanes. This is due to the higher concentration of cyclic siloxanes (D4 and D5) and the fact that linear siloxanes are considered to be decomposed easier than cyclic structure in the digester due to instability. However, the concentration of smaller linear siloxanes in landfill gas are comparable or can be higher than cyclic siloxanes such as D4 and D5 (Lu et al., 2011; Wang et al., 2020). For biogas from a wastewater treatment plant, siloxane concentration is also influenced by multiple factors such as digester type, location, and season. In some cases, high concentrations of linear structure siloxanes were also reported (Lanzini et al., 2017). To improve the utilization of biogas from landfill and wastewater treatment plants, investigation of SOFC degradation due to linear siloxane contamination is necessary.

In this study, linear structure siloxane, L4, was selected as the contamination source and is compared with a cyclic siloxane, D4. L4 and D4 were chosen as they have different structure, but the same number of silicon atoms per molecule of siloxane. Stability tests are conducted to compare SOFC degradation and contamination on YSZ pellets. The experimental results of D4/L4 were analyzed and compared to reveal the mechanism of the SOFC degradation due to different siloxane contamination.

EXPERIMENTAL SETUP

Fuel Cell and Pellets Fabrication and Experimental Setup

The SOFCs were fabricated with LSCF $[(\text{La}_{0.60}\text{Sr}_{0.40})_{0.95}\text{Co}_{0.20}\text{Fe}_{0.80}\text{O}_{3-x}]$ Fuelcellmaterials + SDC $(\text{Sm}_{0.20}\text{Ce}_{0.80}\text{O}_{2-x})$ mid grade powder, Fuelcellmaterials cathode (7:3 w/w), SDC buffer layer, YSZ $[(\text{Y}_2\text{O}_3)_{0.08}(\text{ZrO}_2)_{0.92}]$ spray dried grade powder, Fuelcellmaterials electrolyte and NiO (standard grade

TABLE 1 | Flow rate (sccm) of anode side gases supplied to YSZ pellet during different experiments.

Experiment conditions	H ₂	H ₂ O	N ₂	Siloxane + N ₂
N ₂ +D4	NA	NA	10.67	9.33
H ₂ + N ₂ +D4	7	NA	3.67	9.33
H ₂ +N ₂ +H ₂ O+D4	7	2	1.67	9.33
N ₂ +L4	NA	NA	10.07	9.93
H ₂ + N ₂ +L4	7	NA	3.07	9.93
H ₂ +N ₂ +H ₂ O+L4	7	2	1.07	9.93

powder, Fuelcellmaterials) + YSZ anode (60:40 w/w). NiO/YSZ was dry pressed and pre-fired (final thickness of 380 μm). The YSZ electrolyte and SDC buffer layers were sprayed on the surface of NiO/YSZ green body and sintered at 1,400°C with ~ 10 and ~ 3 μm thickness, respectively. LSCF + SDC cathode was hand sprayed on the SDC buffer layer and sintered at 1,100°C (final thickness ~ 17 μm). More details about the fabrication method can be found in previous literature (Tian and Milcarek, 2020). YSZ pellets (380 μm thick) were also dry pressed and sintered to investigate the siloxane degradation mechanism.

Figure 1 shows the experimental setup which was built for investigating the influence of the type of siloxane (cyclic or linear) contamination on the Ni-YSZ SOFC anode. According to previous work (Tian and Milcarek, 2020), dry fuel mixed with siloxane can increase SOFC performance degradation compared to adding H₂O. As a result, for the SOFC test, H₂ (ultra high purity grade, Airgas) + N₂ (ultra high purity grade, Airgas) +siloxane was selected as the fuel. To regulate the flow of H₂, N₂, L4 and D4, Brooks Delta II smart mass flow controllers (MFCs) with LabView interface were utilized. The H₂ flow rate was fixed at 7 standard cubic centimeters per minute (sccm). The certified D4 (5.358 ppm_v, Airgas) and L4 (5.034 ppm_v, Airgas) cylinders balanced with N₂ were mixed with research grade N₂ to fix the concentration of D4 and L4 to 2.5 ppm. The total gas flow rate to the anode was 20 sccm for all experiments. For YSZ pellet experiments, which included tests with steam, water was delivered by a syringe pump (PumpSystems Inc.). Resistive heaters wrapped on the fuel delivery pipe were used to vaporize the deionized water and maintain vapor phase. To ensure the steam remained in vapor phase, T-type thermocouples (Omega) were mounted on the pipe to monitor the temperature. Air was delivered to the cathode through the vertical furnace by natural convection.

Based on previous siloxane deposition studies (Finocchio et al., 2008; Vaiss et al., 2020), siloxanes prefer to chemisorb on metal oxide surfaces, like γ -Al₂O₃, due to reactions with hydroxyl groups present. As a result, YSZ grains are hypothesized as one of the locations where siloxane deposits initially in the Ni-YSZ anode. To test this theory, siloxane (L4/D4) deposition on a YSZ pellet was conducted. To control the amount of hydroxyl groups on the YSZ pellet surface, different gas compositions were chosen for L4 and D4 contamination studies. The details of these experimental conditions are show in **Table 1**. In order to remove hydroxyl groups present on the surface of YSZ pellets before the experiment, the pellets were heated to 850°C and maintained at that temperature for 1 h with 20 sccm pure N₂ on the bottom side.

For the SOFC and YSZ pellet experiments, the SOFCs (or pellets) were sealed on a quartz tube with silver paste. The cathode (or the cathode side of the pellet surface) was printed with silver ink as the current collector with an active area of 0.712 cm². Silver wires connected with the anode and cathode were utilized for the electrochemical characterization. The operating temperature was fixed at 750°C with 5°C per minute heating rate for all experiments.

Characterization Methods

In order to evaluate the performance degradation of SOFCs under L4 and D4 contamination, the fuel cells' polarization (I-V) curves were acquired by a digital SourceMeter (Keithley 2460) interfaced with LabView on the computer with four-probe technique. The electrochemical characterization of the entire SOFC and YSZ pellets were conducted by electrochemical impedance spectroscopy (EIS). The impedance spectra were obtained by an Electrochemical Impedance Analyzer (Solartron Analytical Energylab XM) with ac amplitude of 10 mV and a frequency range of 10⁶ Hz–0.1 Hz. The distribution of relaxation time (DRT) method was utilized to analyze EIS data by a MATLAB GUI program (DRTtools) (Ciucci and Chen, 2015; Wan et al., 2015; Effat and Ciucci, 2017). The regularization parameter is selected as 10^{−3} for DRT calculation.

Several techniques were used to characterize the morphology and composition of the silicon containing deposits. The morphologies of L4 and D4 deposition under different experimental conditions on YSZ pellets were conducted by a field emission scanning electron microscope (FESEM, JEOL JXA-8530F electron microprobe) equipped with an energy-dispersive spectrometer (EDS) and wavelength-dispersive spectrometer (WDS). As the Y and Si signals are not well separated with EDS, WDS was utilized to obtain the elemental analysis of the sample. To determine the L4 and D4 deposition compositions on the YSZ pellets, X-ray diffractometer (XRD) system was utilized for the deposition crystalline structure characterization. The XRD patterns were obtained using the X-ray diffractometer (PANalytical X' Pert Pro MRD) with a Cu K α (K-Alpha2/K-Alpha2 = 0.5) radiation source. To obtain more composition information for the L4 and D4 deposition on the YSZ pellets, Raman test was conducted on an Acton 300i spectrograph and a back thinned Princeton Instruments liquid nitrogen cooled CCD detector with a 532 nm laser as excitation source. The power was kept at 6 mW.

RESULTS

SOFC Degradation due to Siloxane Contamination

As shown in **Figure 2A**, the polarization curves of the SOFC after 20 and 40 h D4 contamination are compared with the initial fuel cell performance after intrinsic degradation. In order to eliminate the influence of SOFCs' intrinsic degradation, the SOFCs have been operated with clean fuel for 48 h. This data provides a useful reference for the SOFC degradation without siloxane contamination, as shown in **Table 2**. After 20 h D4

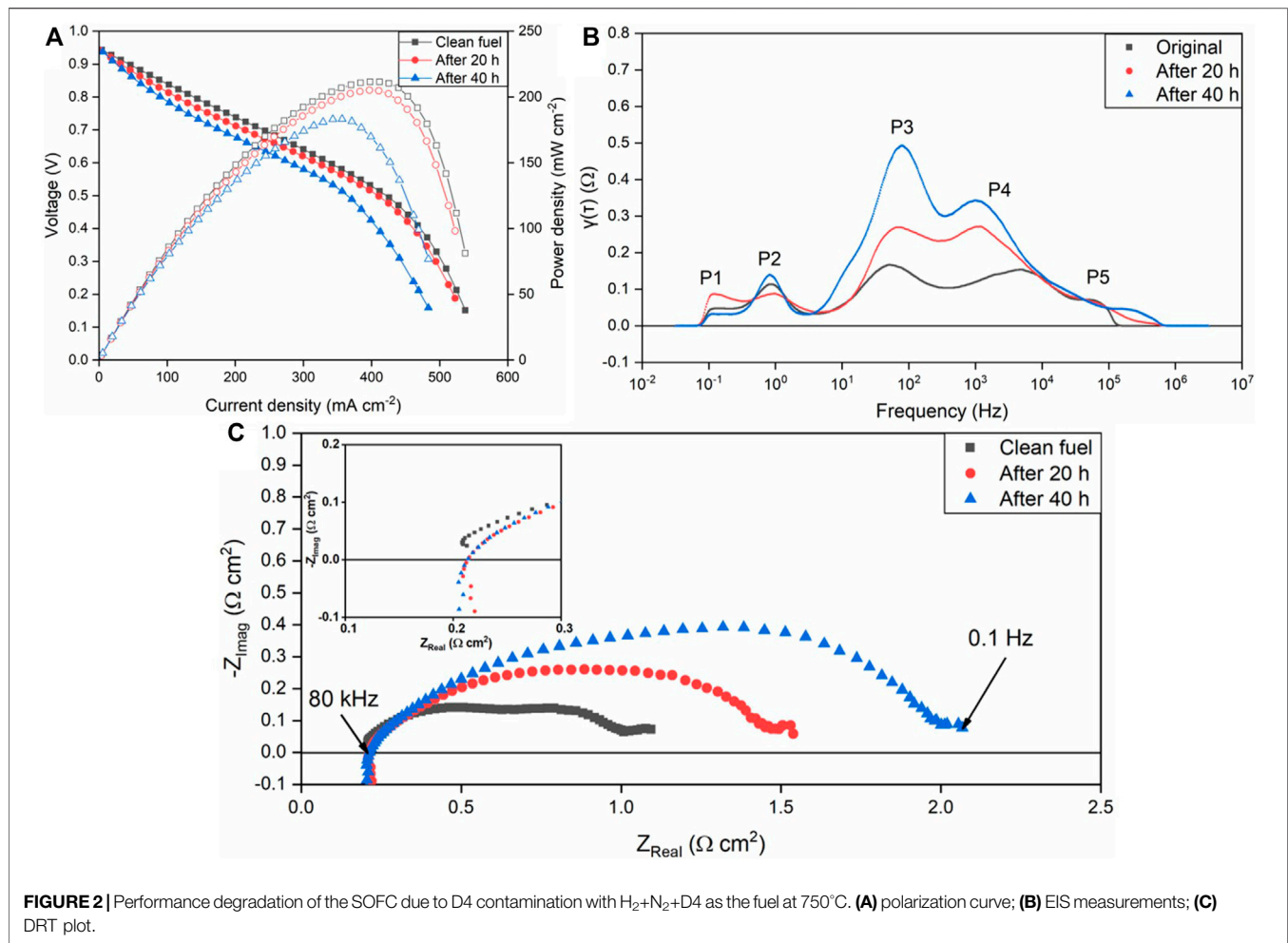
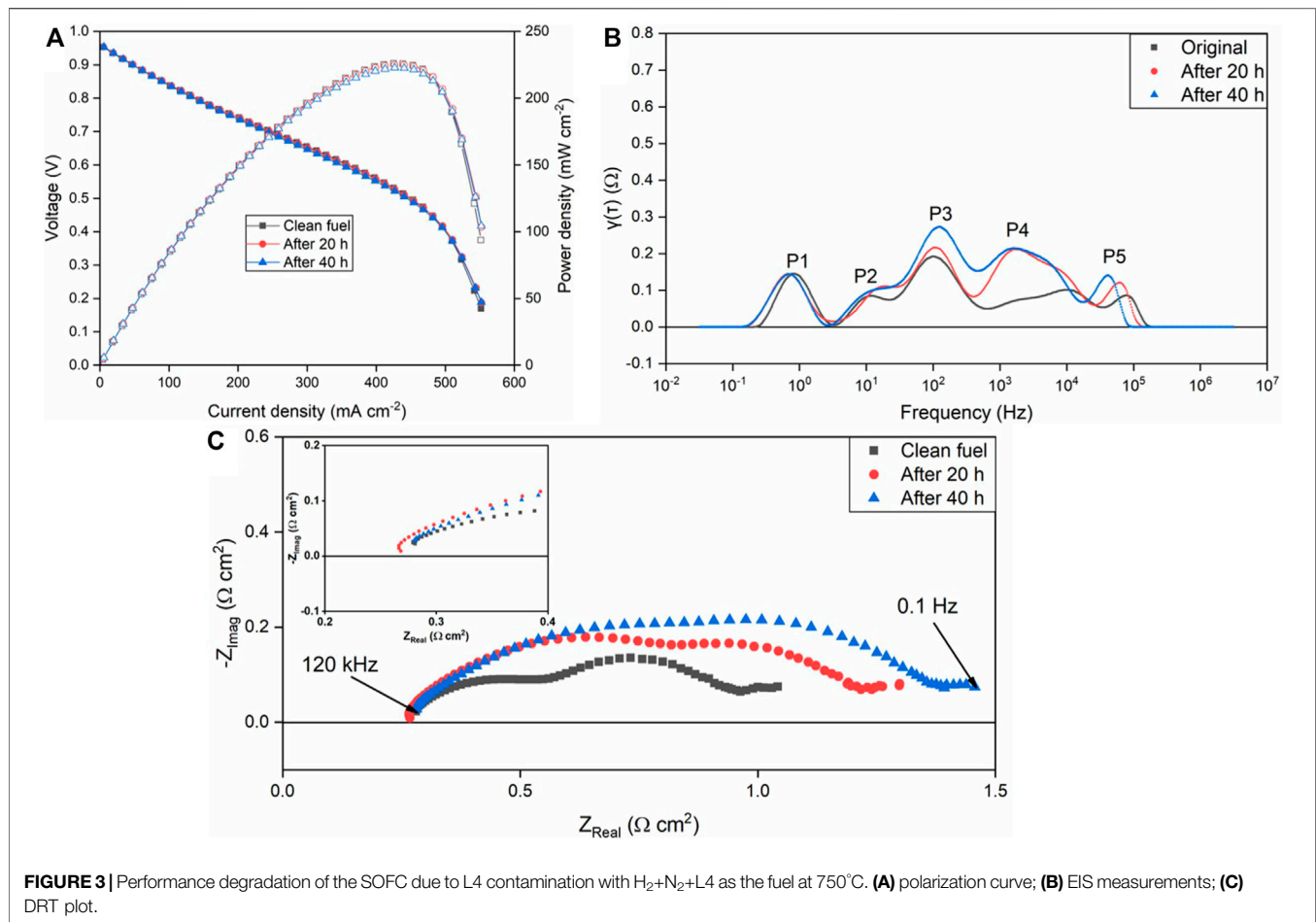


TABLE 2 | Maximum power density decrease and increase in area specific resistance (ASR) calculated from characterization results.

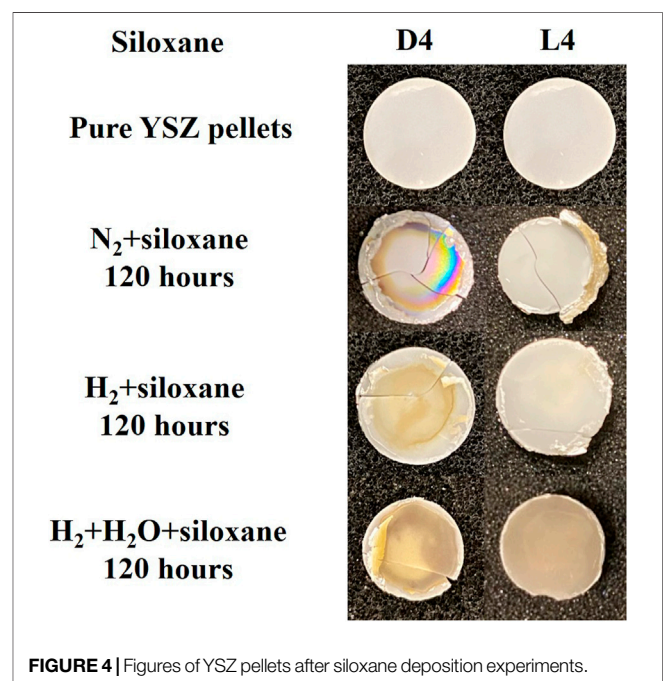
	Original	Clean fuel 48 h	After 20 h siloxane	After 40 h siloxane	Power density decrease after contaminations
D4 maximum power density ($mW\ cm^{-2}$)	215.5	211.5	205.1	183.2	28.3
L4 maximum power density ($mW\ cm^{-2}$)	229.6	226.0	225.0	222.8	3.2
					ASR increase after contaminations
D4 experiment	0.75	0.87	1.32	1.85	0.98
ASR ($\Omega\ cm^2$)					
L4 experiment	0.60	0.67	1.03	1.18	0.41
ASR ($\Omega\ cm^2$)					

contamination, the maximum power density of the fuel cell decreased from 211.5 to 205.1 $mW\ cm^{-2}$. In comparison, the maximum power density of the fuel cell during the next 20 h (40 h total contamination) decreased to 183.16 $mW\ cm^{-2}$ from 205.1 $mW\ cm^{-2}$. A similar trend of degradation was also observed in the EIS results. The obvious impedance increase after D4 contamination can be noticed from **Figure 2C**. DRT analysis was conducted to identify the characteristic distribution of the SOFC EIS results. Among the five main discrete peaks (P1~P5)

in **Figure 2B**, P1 and P2 (0.1–1 Hz) at low frequency are considered as the gas diffusion process for the cathode, based on previous DRT analysis (Tian and Milcarek, 2021). P3 and P4 at medium frequency (1 Hz–10 kHz) are related to the gas diffusion process for the anode. P5 (>10 kHz) at high frequency is attributed to charge transfer. With minor change of cathode and charge transfer process (P1, P2, P5), the main performance degradation of the SOFC results from anode processes (P3 and P4) (Caliandro et al., 2019; Hong et al., 2020; Sumi et al., 2020).



The electrochemical characterization results for the L4 contamination experiment are shown in **Figure 3**. The obvious degradation rate difference from D4 and L4 can be observed from power density and EIS results after 40 h in **Figure 3**. From **Figure 3A**, no obvious degradation can be found in the polarization curve. From the EIS results in **Figure 3C**, a relatively small impedance increase is observed. Similar to the DRT results from D4 contamination, L4 contamination results also illustrate the main degradation occurred in anode process as shown by P3 and P4 increase. More details comparing L4 versus D4 results are shown in **Table 2**. From the results of **Table 2**, which show power density change and area specific resistance (ASR) increase, the SOFC under L4 contamination has noticeably less degradation than with D4 contamination. Although SOFCs with the same fabrication process and materials were utilized, the EIS and polarization results before D4/L4 contamination are also slightly different. In this situation, there are some experimental setup factors that may influence the results such as current collector coating, wires, sealing, etc. Considering the appearance of inductance in one data set one possibility is that the wires, which can introduce distortion by inductance, may play a part in this process, which has been reported before (Nielsen and Hjelm, 2014).



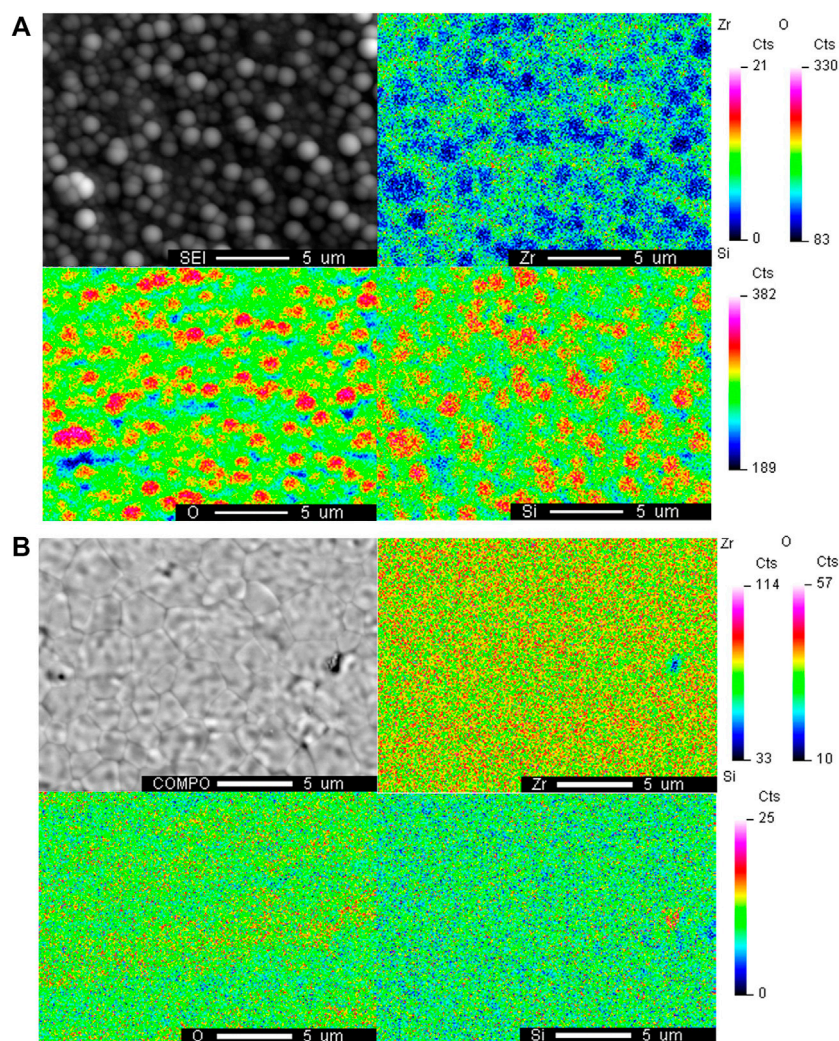


FIGURE 5 | WDS elemental mapping of the surface of YSZ pellet with H_2+N_2 +siloxane contamination after (A) D4 contamination and (B) L4 contamination at 750°C.

Pellet Degradation due to Siloxane Contamination

Figure 4 shows photos of the YSZ pellets after the D4/L4 exposure experiments. The mechanical damage of SOFCs occurred during the dismounting process from the silver sealing. As shown, the color of pellets, under certain conditions, has been converted from white (clean YSZ) to yellow/brown which indicates the deposition of siloxanes. Generally, the experiments with D4 as impurity had more deposition compared with L4. The siloxane deposition for the experiments with wet fuel (H_2+H_2O + siloxane) was larger than the experiments with dry fuel (H_2 + siloxane, N_2 + siloxane). Furthermore, some details shown in the photos should also be highlighted. For L4 contamination experiments, besides the test involving H_2O mixed with the fuel, there is little siloxane deposition on the YSZ pellets' surface. However, after adding H_2O , significant deposition was observed. For N_2 +D4

experiment, there is no obvious deposition that can be noticed in the center of the pellet. However, siloxane was deposited on the edge of the pellet near the silver sealing/current collector.

The morphology and elemental mapping of YSZ pellets were investigated after the contamination test utilizing SEM and WDS. **Figure 5** shows the WDS map of the Zr, O and Si elements on the surface of the YSZ pellets under the H_2+N_2 +D4/L4 conditions. As shown in **Figure 5B**, which shows the surface after L4 contamination, the fine YSZ grains and grain boundaries can be observed and there is no obvious silicon deposition. In comparison the sphere shape depositions (in **Figure 5A**) whose diameters are around 1 μm completely covered the surface of the YSZ pellet after D4 contamination experiment. Thus, the clear grains and grain boundaries shown in **Figure 5B** cannot be detected. The presence of strong overlapping signals of Si and O was observed with WDS elements mapping, indicating silicon dioxide formation in the H_2+N_2 +D4 experiment.

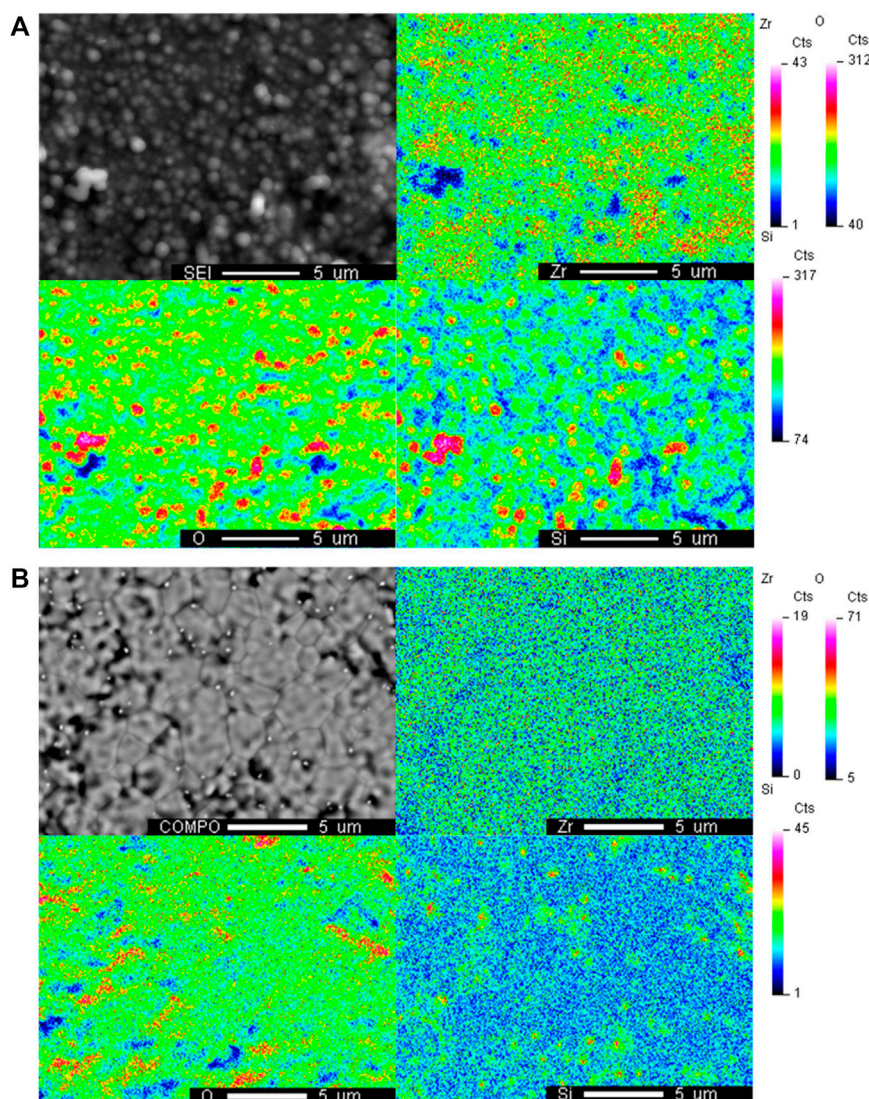
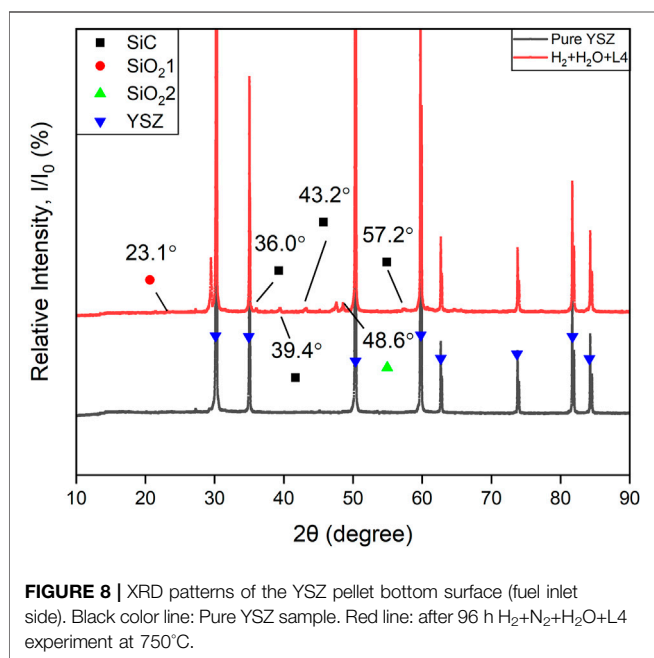
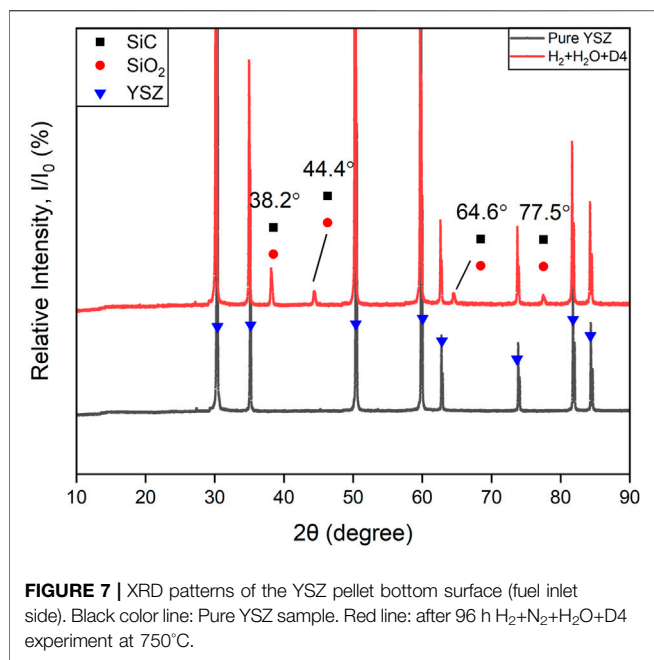


FIGURE 6 | WDS elemental mapping of the surface of YSZ pellet with $\text{H}_2 + \text{H}_2\text{O} + \text{N}_2 + \text{siloxane}$ contamination after **(A)** D4 contamination and **(B)** L4 contamination at 750°C .

For the $\text{H}_2 + \text{N}_2 + \text{H}_2\text{O} + \text{D4/L4}$ experiments, generally, heavier siloxane deposition can be noticed than the $\text{H}_2 + \text{N}_2 + \text{D4/L4}$ experiments. Similar to the $\text{H}_2 + \text{N}_2 + \text{D4}$ experiment, overlapping silicon and oxygen signals can also be found in element mapping for $\text{H}_2 + \text{N}_2 + \text{H}_2\text{O} + \text{D4}$ experiment in **Figure 6A** which indicates the composition is silicon dioxide. Compared with the regular sphere deposition observed in **Figure 5A**, irregular or less structured deposition was formed with wet fuel likely due to more total deposition on the surface. For the $\text{H}_2 + \text{N}_2 + \text{H}_2\text{O} + \text{L4}$ experiment, also like the dry fuel experiments, less total deposition was observed than the D4 experiment. In **Figure 6B**, the surface grain boundaries of YSZ can be detected. Silicon deposition was observed after the $\text{H}_2 + \text{N}_2 + \text{H}_2\text{O} + \text{L4}$ experiment primarily at the grain boundaries where small Si/O deposits initiate.

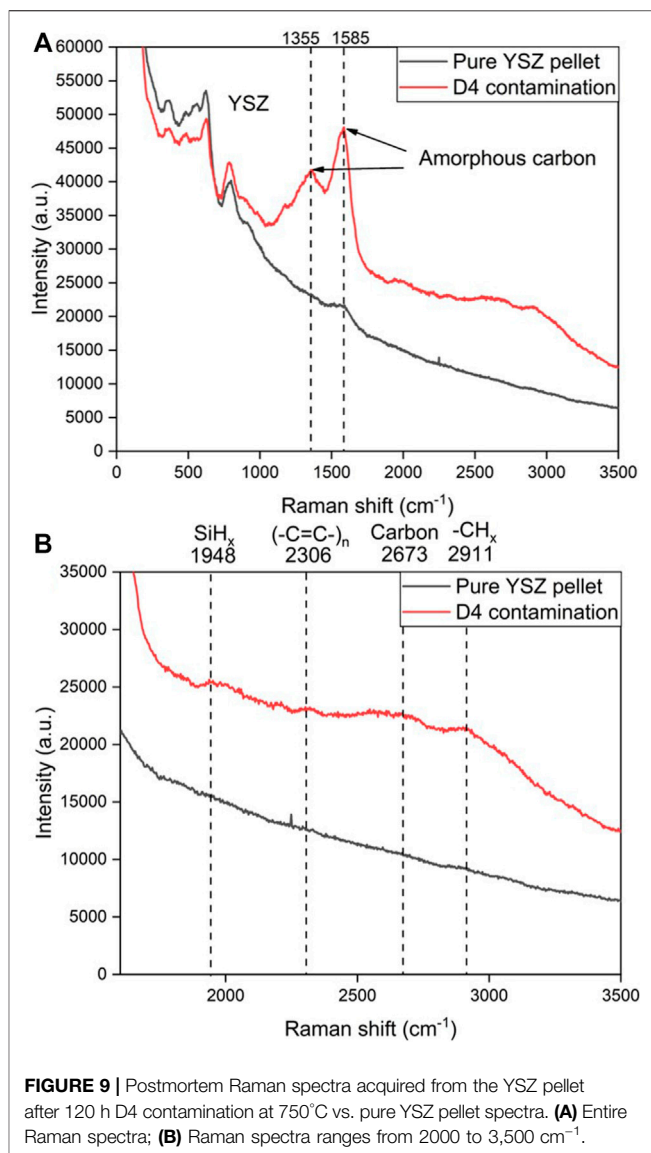
Figure 7 shows the XRD pattern of the YSZ pellet before and after exposure to the fuel which was composed of $\text{H}_2 + \text{N}_2 + \text{H}_2\text{O} + \text{D4}$. New peaks appearing at 38.2° , 44.4° , 64.6° , and 77.5° (2θ) were found after contamination, which indicate siloxane deposition. Based on the Si, C and O present in siloxane, the deposition corresponding to the peaks can be attributed to both cubic crystal structure SiO_2 (melanophlogite, PDF#01-080-4051) and silicon carbide SiC (3C-SiC, PDF#00-049-1623).

According to the observed extent of deposition on the YSZ pellets in **Figure 4** and SEM/WDS analysis, the deposition from L4 was much less compared with D4. Similar trends can also be found in the XRD result for the $\text{H}_2 + \text{N}_2 + \text{H}_2\text{O} + \text{L4}$ experiment. In **Figure 8**, much weaker deposition peaks are observed at 23.1° , 36° , 43.2° , 48.6° and 57.2° (2θ) in the pattern. They correspond to a hexagonal crystal structure SiC (moissanite-18H, PDF#01-089-2217), a tetragonal structure SiO_2 (α -cristobalite, PDF#04-018-0233) and a cubic



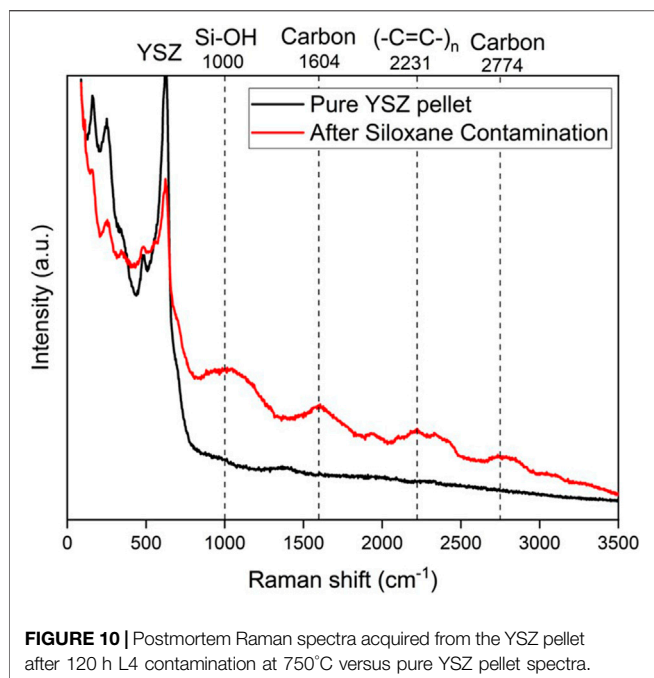
crystal structure SiO_2 (melanophlogite, PDF#01-080-4051). For the two different polymorphs of SiO_2 , melanophlogite, which is always correlated to organic matter decomposition, can exist steadily under 800°C (Skinner and Appleman, 1963). The α -cristobalite may originate from β -cristobalite after cooling below 250°C from high temperature at ambient pressure (Downs and Palmer, 1994). These two kinds of polymorphs of SiO_2 can exist together as a result of the siloxane deposition.

There is a comparatively strong peak at $2\theta = 29.4^\circ$ in **Figure 8**. Considering its relative signal strength and the position, which is



very close to the main peak of YSZ, it may be a result of the Zr, Y, O ratio change in the surface of YSZ pellet. There is also an unlabelled weak peak around 27° in both **Figure 7** and **Figure 8**. Considering the presence of this peak before and after siloxane contamination and without significant increase from the patterns, it should not be associated with the siloxane deposition process. It may originate from secondary peaks of main components or noise.

Figure 9A shows postmortem Raman spectra from the YSZ pellets after 120 h D4 contamination with $H_2+N_2+H_2O$ as fuel. For poly-aromatic hydrocarbons the appearance of D and G peaks in Raman spectroscopy are common. D peak originates from the breathing modes of sp^2 atoms in rings. The G peak is generated by all pairs of sp^2 atoms bond stretching in both rings and chains (Ferrari, 2007). Compared with the pure YSZ pellet without D4 contamination, emergence of G peak observed in all sp^2 carbon systems near 1,600 cm^{-1} and D peak around



1,350 cm^{-1} both indicate the presence of amorphous carbon deposition after exposure to D4 contamination. Besides the strong amorphous carbon signal, some weaker peaks corresponding to different chemical groups were observed as shown in **Figure 9B**. Methyl/methylene (CH_x) group vibrational bands can be noticed at 2,911 cm^{-1} . SiH_x , $(-\text{C}=\text{C}-)_n$ groups can be observed at 1,948 and 2,306 cm^{-1} . The secondary order D peak 2D can also be found at 2,673 cm^{-1} (Jereng et al., 2011; Yu et al., 2013; Bouhamed, 2017).

In **Figure 10**, Raman spectra have been obtained from the YSZ pellet surface exposed to $\text{H}_2+\text{N}_2+\text{H}_2\text{O}+\text{L4}$ fuel. Besides YSZ, no strong signals like observed in **Figure 9A**, were detected. This also confirms the trend that D4 contamination has more deposition than L4. The band at 1,604 and 2,774 cm^{-1} are attributed to carbon deposition. Similarly in **Figure 9B**, the $(-\text{C}=\text{C}-)_n$ groups can be also found at 2,231 cm^{-1} . For the silicon deposition, Si-OH bond can be observed at 1,000 cm^{-1} (da Silva

et al., 2006; Lanzini et al., 2017). These results are important because they emphasize the role of carbon deposition in the siloxane deposition process.

Besides the deposition composition analysis, electrochemical analysis of the pellets experiment was also conducted to obtain more details about the degradation process. **Figure 11** shows the Nyquist plots of the impedance of YSZ pellets under L4 contamination with $\text{H}_2+\text{N}_2+\text{H}_2\text{O}$ as fuel at 750°C. An obvious impedance increase can be observed after siloxane contamination. The EIS results were also fitted based on an equivalent circuit with the program LEVM embedded to Solartron Analytical EnergyLab XM software (Macdonald and Garber, 1977). The CPE is a constant phase element, whose characterization can be determined by two parameters, T and n . The effective capacitance, C , for the RQ circuit was calculated by **Eq. 3** (Yan et al., 2013). T is the frequency-independent constant, and n represents the non-ideal factor. The electrochemical process for the YSZ pellet can be reflected in the magnitude of C (Yuan et al., 2020).

$$C = (R^{1-n}T)^{1/n}. \quad (3)$$

According to previous EIS studies of YSZ pellets (Van Herle and McEvoy, 1994; Mondal et al., 1999; Guo, 2001; Guo and Waser, 2006), there are two semicircles assigned to the impedance response of the gases chemisorption on the silver electrode, diffusion of gases through the silver electrode and gas conversion process in the silver electrode, respectively. The intercept R_s with the real axis at high frequency is related to the YSZ electrolyte resistance. Fitting the experimental impedance spectra with an equivalent circuit, the resistances and capacitances from diffusion (R_D and C_D), chemisorption (R_A and C_A) and conversion (R_C and C_C) are shown in **Table 3** (Yan et al., 2013). Consistent with a previous study (Van Herle and McEvoy, 1994), the resistance corresponding to the gas diffusion through electrodes is much larger than chemisorption resistance and gas conversion resistance. Resistance increase is observed in all the elements in the equivalent circuit after L4 contamination. The diffusion resistance increase is more dominant than the other types. This illustrates that besides deposition on the pellets' surface, the siloxane deposition also prefers to cover the silver current

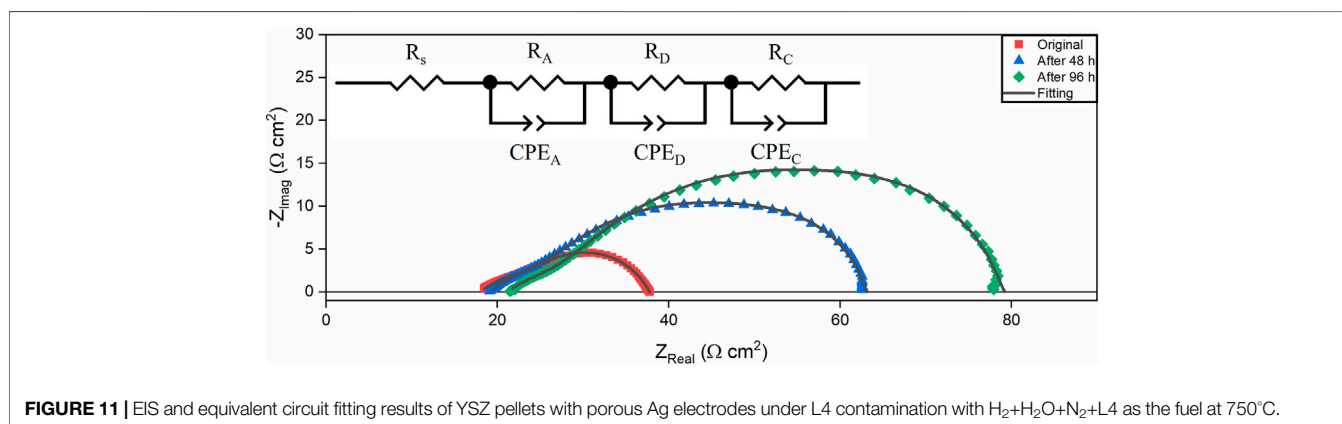


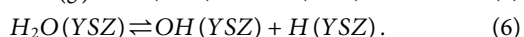
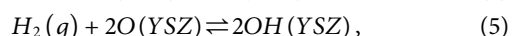
TABLE 3 | Equivalent circuit fitting results from EIS results.

Experiment conditions	R_s (Ω)	R_A (Ω)	C_A (10^{-3} F)	R_D (Ω)	C_D (10^{-5} F)	R_C (Ω)	C_C (10^{-6} F)
Original	25.56	13.53	0.21	9.75	3.35	4.18	1.40
48 h	26.97	15.23	1.71	38.04	9.11	8.58	2.80
96 h	29.65	16.93	2.60	51.08	13.21	13.62	5.83

collector which is also the electrode in this setup. As a result, the diffusion process through the electrode is blocked due to siloxane deposition around silver, eventually causing a significant increase in the diffusion impedance. Besides the diffusion process, a slight ohmic resistance and gas conversion resistance increase can also be noticed from the change of R_s and R_C . For ohmic resistance, it is likely due to the obstruction of the conductive network among the silver grains associated with the siloxane deposition process. When the gas concentration cannot be maintained in the electrodes, the gas conversion loss appears. The increase of the gas conversion resistance indicates the concentration change of gases supplied to the surface of the electrode. The siloxane deposition may prevent sufficient flow of gases through the electrodes. This is also in good agreement with the results found in **Figure 4** that show siloxane deposition is more significant around the edge of the pellet covered by silver.

DISCUSSION

Based on the SOFC siloxane contamination studies, the experiment with L4 as contamination source had less performance degradation compared with D4. To confirm this phenomenon and also investigate the mechanism causing cyclic and linear structure siloxane deposition, the YSZ pellet experiments were completed. From previous siloxane adsorption studies (Finocchio et al., 2008; Vaiss et al., 2020), hydroxyl groups play an important role in the siloxane chemical adsorption process. It has been established in previous research that YSZ has hydroxyl groups on its surface (Kogler et al., 2014). To assess the role of hydroxyl groups on the YSZ surface in the siloxane chemisorption process, different fuel mixtures were prepared. Based on the experimental conditions, the quantity of hydroxyl groups on the YSZ pellets' surface should follow the sequence: $H_2+N_2+H_2O+siloxane > H_2+N_2+siloxane > N_2+siloxane$. Hydroxyl groups can be formed on YSZ, based on **Eqs 4, 5**, through reduction of YSZ by hydrogen, which only occurs near the surface, or through reaction with oxygen ions transported through the YSZ (Ong et al., 2016). Alternatively, H_2O can form hydroxyl groups directly according to **Eq. 6** at a faster rate compared to the previous mechanism.



Based on the photos of YSZ pellets after experiments (shown in **Figure 4**) and the SEM/WDS results (shown in **Figures 5, 6**),

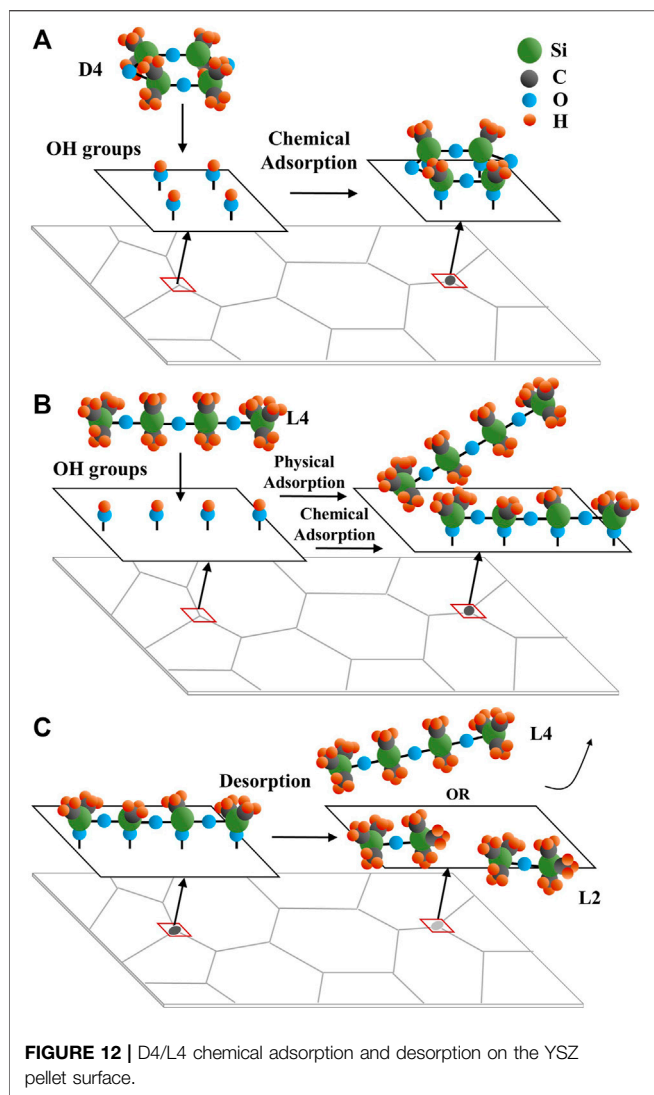
the extent of surface hydroxylation influences the siloxane deposition. The experiment with $H_2+N_2+H_2O+siloxane$ as the fuel, which is considered to have the maximum hydroxyl groups among all conditions, had the most serious siloxane deposition on the pellets' surface. In comparison, with $N_2+siloxane$ as the fuel, which does not result in any surface hydroxyl groups, no significant siloxane deposition is observed in the middle of the YSZ pellet surface. This demonstrates that siloxane chemical adsorption is essential to the entire deposition process.

Following the same trend with the SOFC results, L4 contamination experiments also had less siloxane deposition on the YSZ pellet surface than D4. This phenomenon can also be verified by XRD and Raman results in **Figures 5–10**, in which the YSZ pellet with D4 deposition always resulted in stronger signal during characterization than the YSZ pellet with L4 deposition. From a chemical reaction perspective, L4 as a linear structure siloxane is less stable compared with D4, with its cyclic structure (Gun'ko et al., 2007). As a result, L4 as a linear structure siloxane can be dissociated more easily compared to the stable D4 structure (Gun'ko et al., 2007). However, the results are opposite of what might be expected. Considering the influence of hydroxyl groups on the siloxane deposition, the chemical adsorption process should be the rate determining step for the siloxane deposition reaction. This can also be proved by results in **Figure 4**.

The deposition in **Figure 4** appears as a yellow/brown color. The visual inspection of the color change may only provide qualitative analysis. From XRD results in **Figure 7** and **Figure 8**, SiC and SiO_2 are deposited on the surface. Considering the interaction of atoms and their electrons with light waves, the band gap of a semi-conductor material can determine its color. For 3C-SiC, which correlates to 3.26 eV bandgap value, its color should be in the range of yellow to green (Zhao and Bagayoko, 2000). In this case, the color of deposition may determine the extent of SiC deposition. However, SiO_2 is always reported as white or colorless crystalline. Different colors can also be observed because of light scattering from the small particles. In this case, further quantitative analysis of deposition extent can be conducted in future work.

For the experiment with $H_2+N_2+siloxane$ and $N_2+siloxane$ as the fuel, which had lower hydroxylation of the surface, deposition resulting from L4 is much less than from D4. After introducing H_2O in the fuel, which results in more hydroxyl groups, the chemical adsorption process accelerated and the extent of L4 deposition increased significantly.

M. Schweigkofler et al. reported that compared with linear siloxanes, many types of absorbents, including silicon and carbon-based material, show higher adsorption ability for



cyclic siloxanes (Schweigkofler and Niessner, 2001). Besides the adsorption process, linear siloxanes also have much higher desorption efficiency than cyclic siloxanes because linear siloxanes can also be absorbed physically without any transformation. In some cases, large molecule linear siloxanes can convert to L2 after desorption from absorbents (Soreanu et al., 2011). Based on this insight, the assumed L4 and D4 adsorption and desorption processes on the YSZ pellet surface are presented in Jonsson **Figure 12**. The D4 contamination is believed to result in more degradation for SOFCs' anode due to its high adsorption and low desorption ability on YSZ compared to L4. The pellets' XRD results with D4 and L4 contamination in **Figure 7** and **Figure 8** show different deposition peak positions for SiO_2 and SiC. The different positions refer to crystalline differences resulting from D4 and L4 deposition, even though they have similar composition. This may also be explained by the adsorption and desorption process difference for D4 and L4 on the YSZ pellets. As the initial step of siloxane deposition, the adsorption

process difference may cause significant divergence in next deposition reaction steps.

Several evidences including previous studies along with the SOFC and pellet experimental results in this study derive the assumed mechanism. Direct evidence such as high spatial resolution imaging of the adsorption process by techniques like transmission electron microscopy (TEM) is still needed to prove the assumption. More studies like XPS analysis of deposition on SOFC and pellet surfaces and exhaust gas composition analysis from the SOFC experiment can also aid in understanding the siloxane deposition process.

Besides the differences in D4 versus L4 deposition, there are other interesting results to discuss. For siloxane pellet experiments, introducing H_2O to the fuel accelerates the siloxane deposition which can be explained from the chemical adsorption process as discussed in the previous section. However, this can't explain why the wet fuel reduces performance degradation with siloxane contamination which has been reported in previous work (Tian and Milcarek, 2020). There must be other factors also resulting in Ni/YSZ anode degradation besides siloxane deposition on the YSZ. Our previous work (Tian and Milcarek, 2020) suggested that sufficient H_2O in the fuel could prevent carbon deposition on the Ni which is considered as a good catalyst for hydrocarbon reforming reactions (Hecht et al., 2005). In this study, some evidence can also be provided. For siloxane deposition composition analysis tests, XRD and Raman tests both show carbon-based compounds, such as SiC in XRD tests and strong amorphous carbon signals in Raman test after D4 deposition. Existing $(-\text{C}=\text{C}-)_n$ and CH_x groups on YSZ surface are also evidence of early stages of carbon deposition.

Besides carbon deposition, degradation of silver current collector (also considered as electrode for pellet experiments) due to siloxane contamination is also demonstrated by this study. Silver, also known as an interaction catalyst of oxygen (Nagy and Mestl, 1999), can also be attacked by carbon and silicon, like Ni in the anode. From **Figure 4**, the siloxanes prefer to deposit around the silver/YSZ interface. The degradation of silver current collector/electrode can also be verified by electrochemical characterization analysis from **Figure 11** in which an obvious impedance increase can be noticed after siloxane contamination. The composition map of the pellet after $\text{H}_2+\text{N}_2+\text{H}_2\text{O}+\text{D4}$ exposure support significant silicon and oxygen deposition around the silver. These results all suggest that silver is extremely vulnerable to siloxane contamination. Moreover, for the setup in this study, the failure of the silver current collector not only leads to poor conductivity for electrochemical reactions, but also creates leakage around the anode. This can also cause a significant performance loss for the SOFC. In future work, siloxane deposition on silver and nickel still needs to be addressed.

CONCLUSION

In this study, D4 and L4 are used to represent cyclic and linear structure siloxanes, respectively, to investigate contamination of SOFCs utilizing biogas. SOFC degradation experiments with

H₂+N₂+L4/D4 as the fuel were conducted. According to polarization curves and EIS results, the SOFC in the experiment with D4 as contamination source had higher degradation than with L4.

To reveal the mechanism causing the SOFC degradation difference by cyclic and linear structure siloxanes and also investigate the relationship between the chemical adsorption of siloxane and deposition process on YSZ, pure YSZ pellet experiments with H₂+N₂+H₂O+D4/L4, H₂+N₂+D4/L4 and N₂+D4/L4 as the fuel were conducted. Postmortem analysis including SEM/WDS, XRD and Raman all indicated that the deposition from D4 was more significant than from L4, in general. Among these experiments with different surface hydroxylation extent, H₂+N₂+H₂O+D4/L4 experiment had the most deposition due to more hydroxyl groups. Considering that the siloxane deposition process is highly dependent on the extent of the surface hydroxylation, it can be concluded that the YSZ surface chemical adsorption process is a critical step. Thus, the high adsorption and the low desorption rates of cyclic siloxane compared with linear siloxanes on YSZ may explain the deposition and SOFC degradation.

Besides silicon deposition, carbon deposition including SiC and amorphous carbon was also noted from XRD and Raman results due to siloxane contamination. Electrochemical characterization results from the YSZ pellet experiments also support that silver current collector accelerated siloxane deposition which can cause the SOFC performance degradation.

REFERENCES

- Bouhamed, H. (2017). Improved Structural Stability and Electrochemical Performance of 8YSZ Electrolyte by MxOy Doping for Low Temperature Solid Oxide Fuel Cells (LT-SOFCs). *Mater. Sci. Eng. B* 225, 182–188. doi:10.1016/j.mseb.2017.08.020
- Caliandro, P., Nakajo, A., Diethelm, S., and Van herle, J. (2019). Model-Assisted Identification of Solid Oxide Cell Elementary Processes by Electrochemical Impedance Spectroscopy Measurements. *J. Power Sourc.* 436, 226838. doi:10.1016/j.jpowsour.2019.226838
- Ciucci, F., and Chen, C. (2015). Analysis of Electrochemical Impedance Spectroscopy Data Using the Distribution of Relaxation Times: A Bayesian and Hierarchical Bayesian Approach. *Electrochimica Acta* 167, 439–454. doi:10.1016/j.electacta.2015.03.123
- da Silva, S. W., Pedroza, R. C., Sartoratto, P. P. C., Rezende, D. R., da Silva Neto, A. V., Soler, M. A. G., et al. (2006). Raman Spectroscopy of Cobalt Ferrite Nanocomposite in Silica Matrix Prepared by Sol-Gel Method. *J. Non-Crystalline Sol.* 352, 1602–1606. doi:10.1016/j.jnoncrysol.2006.01.054
- Dewil, R., Appels, L., Baeyens, J., Buczyńska, A., and Van Vaec, L. (2007). The Analysis of Volatile Siloxanes in Waste Activated Sludge. *Talanta* 74, 14–19. doi:10.1016/j.talanta.2007.05.041
- Downs, R. T., and Palmer, D. C. (1994). The Pressure Behavior of a Cristobalite. *Am. Mineral.* 79, 9–14.
- Effat, M. B., and Ciucci, F. (2017). Bayesian and Hierarchical Bayesian Based Regularization for Deconvolving the Distribution of Relaxation Times from Electrochemical Impedance Spectroscopy Data. *Electrochimica Acta* 247, 1117–1129. doi:10.1016/j.electacta.2017.07.050
- Ferrari, A. C. (2007). Raman Spectroscopy of Graphene and Graphite: Disorder, Electron-Phonon Coupling, Doping and Nonadiabatic Effects. *Solid State Commun.* 143, 47–57. doi:10.1016/j.ssc.2007.03.052
- Finocchio, E., Garuti, G., Baldi, M., and Busca, G. (2008). Decomposition of Hexamethylcyclotrisiloxane Over Solid Oxides. *Chemosphere* 72, 1659–1663. doi:10.1016/j.chemosphere.2008.05.032

DATA AVAILABILITY STATEMENT

The original contributions presented in the study are included in the article/Supplementary Material, further inquiries can be directed to the corresponding author.

AUTHOR CONTRIBUTIONS

JT: Conceptualization, Methodology, Validation, Investigation, Writing–Original Draft, Writing–Review and Editing. RM: Conceptualization, Methodology, Validation, Investigation, Writing–Review and Editing, Supervision, Funding acquisition.

FUNDING

This material is based upon work supported by the U.S. Department of Energy under award number DE-EE0007721.

ACKNOWLEDGMENTS

We acknowledge the use of facilities within the Eyring Materials Center at Arizona State University supported in part by NNCI-ECCS-1542160.

- Gandiglio, M., Lanzini, A., Santarelli, M., Acri, M., Hakala, T., and Rautanen, M. (2020). Results from an Industrial Size Biogas-Fed SOFC Plant (The DEMOSOFC Project). *Int. J. Hydrogen Energ.* 45, 5449–5464. doi:10.1016/j.ijhydene.2019.08.022
- Gun'ko, V. M., Borysenko, M. V., Pissis, P., Spanoudaki, A., Shinyashiki, N., Sulim, I. Y., et al. (2007). Polydimethylsiloxane at the Interfaces of Fumed Silica and Zirconia/Fumed Silica. *Appl. Surf. Sci.* 253, 7143–7156. doi:10.1016/j.apsusc.2007.02.185
- Guo, X. (2001). Size Dependent Grain-Boundary Conductivity in Doped Zirconia. *Comput. Mater. Sci.* 20, 168–176. doi:10.1016/S0927-0256(00)00174-9
- Guo, X., and Waser, R. (2006). Electrical Properties of the Grain Boundaries of Oxygen Ion Conductors: Acceptor-Doped Zirconia and Ceria. *Prog. Mater. Sci.* 51, 151–210. doi:10.1016/j.pmatsci.2005.07.001
- Haga, K., Adachi, S., Shiratori, Y., Itoh, K., and Sasaki, K. (2008). Poisoning of SOFC Anodes by Various Fuel Impurities. *Solid State Ionics* 179, 1427–1431. doi:10.1016/j.ssi.2008.02.062
- Hecht, E. S., Gupta, G. K., Zhu, H., Dean, A. M., Kee, R. J., Maier, L., et al. (2005). Methane Reforming Kinetics within a Ni-YSZ SOFC Anode Support. *Appl. Catal. A: Gen.* 295, 40–51. doi:10.1016/j.apcata.2005.08.003
- Hong, J., Bhardwaj, A., Bae, H., Kim, I.-H., and Song, S.-J. (2020). Electrochemical Impedance Analysis of SOFC with Transmission Line Model Using Distribution of Relaxation Times (DRT). *J. Electrochem. Soc.* 167, 114504. doi:10.1149/1945-7111/aba00f
- Jerng, S.-K., Seong Yu, D., Hong Lee, J., Kim, C., Yoon, S., and Chun, S.-H. (2011). Graphitic Carbon Growth on Crystalline and Amorphous Oxide Substrates Using Molecular Beam Epitaxy. *Nanoscale Res. Lett.* 6, 1–6. doi:10.1186/1556-276X-6-565
- Jonsson, O., Erik, P., Jan, K., Rolf, E., Hakan, S., and Staffan, I. (1997). *Sustainable Gas Enters the European Gas Distribution*. Tokio: World gas conference.
- Kikuchi, Y., Matsuda, J., Tachikawa, Y., Shiratori, Y., Taniguchi, S., and Sasaki, K. (2017). Degradation of SOFCs by Various Impurities: Impedance Spectroscopy and Microstructural Analysis. *ECS Trans.* 78, 1253–1260. doi:10.1149/07801.1253ecst

- Kogler, M., Köck, E.-M., Bielz, T., Pfaller, K., Klötzer, B., Schmidmair, D., et al. (2014). Hydrogen Surface Reactions and Adsorption Studied on Y2O3, YSZ, and ZrO2. *J. Phys. Chem. C* 118, 8435–8444. doi:10.1021/jp5008472
- Lanzini, A., Madi, H., Chiodo, V., Papurello, D., Maisano, S., Santarelli, M., et al. (2017). Dealing with Fuel Contaminants in Biogas-Fed Solid Oxide Fuel Cell (SOFC) and Molten Carbonate Fuel Cell (MCFC) Plants: Degradation of Catalytic and Electro-Catalytic Active Surfaces and Related Gas Purification Methods. *Prog. Energ. Combustion Sci.* 61, 150–188. doi:10.1016/j.pecs.2017.04.002
- Lu, Y., Yuan, T., Wang, W., and Kannan, K. (2011). Concentrations and Assessment of Exposure to Siloxanes and Synthetic Musks in Personal Care Products from China. *Environ. Pollut.* 159, 3522–3528. doi:10.1016/j.envpol.2011.08.015
- Macdonald, J. R., and Garber, J. A. (1977). Analysis of Impedance and Admittance Data for Solids and Liquids. *J. Electrochem. Soc.* 124, 1022–1030. doi:10.1149/1.2133473
- Madi, H., Diethelm, S., Poitel, S., Ludwig, C., and Van herle, J. (2015a). Damage of Siloxanes on Ni-YSZ Anode Supported SOFC Operated on Hydrogen and Bio-Syngas. *Fuel Cells* 15, 718–727. doi:10.1002/fuce.201400185
- Madi, H., Lanzini, A., Diethelm, S., Papurello, D., Van herle, J., Lualdi, M., et al. (2015b). Solid Oxide Fuel Cell Anode Degradation by the Effect of Siloxanes. *J. Power Sourc.* 279, 460–471. doi:10.1016/j.jpowsour.2015.01.053
- Mondal, P., Klein, A., Jaegermann, W., and Hahn, H. (1999). Enhanced Specific Grain Boundary Conductivity in Nanocrystalline Y2O3-Stabilized Zirconia. *Solid State Ionics* 118, 331–339. doi:10.1016/s0167-2738(98)00452-4
- Nagy, A., and Mestl, G. (1999). High Temperature Partial Oxidation Reactions Over Silver Catalysts. *Appl. Catal. A: Gen.* 188, 337–353. doi:10.1016/S0926-860X(99)00246-X
- Nielsen, J., and Hjelm, J. (2014). Impedance of SOFC Electrodes: A Review and a Comprehensive Case Study on the Impedance of LSM:YSZ Cathodes. *Electrochimica Acta* 115, 31–45. doi:10.1016/j.electacta.2013.10.053
- Ong, K., Hanna, J., and Ghoniem, A. F. (2016). Investigation of a Combined Hydrogen and Oxygen Spillover Mechanism for Syngas Electro-Oxidation on Ni/YSZ. *J. Electrochem. Soc.* 164, F32–F45. doi:10.1149/2.0161702jes
- Papurello, D., Borchellini, R., Bareschino, P., Chiodo, V., Freni, S., Lanzini, A., et al. (2014). Performance of a Solid Oxide Fuel Cell Short-Stack with Biogas Feeding. *Appl. Energ.* 125, 254–263. doi:10.1016/j.apenergy.2014.03.040
- Papurello, D., Lanzini, A., Drago, D., Leone, P., and Santarelli, M. (2016). Limiting Factors for Planar Solid Oxide Fuel Cells under Different Trace Compound Concentrations. *Energy* 95, 67–78. doi:10.1016/j.energy.2015.11.070
- Papurello, D., and Lanzini, A. (2018). SOFC Single Cells Fed by Biogas: Experimental Tests with Trace Contaminants. *Waste Manage.* 72, 306–312. doi:10.1016/j.wasman.2017.11.030
- Park, J.-W., and Shin, H.-C. (2001). Surface Emission of Landfill Gas from Solid Waste Landfill. *Atmos. Environ.* 35, 3445–3451. doi:10.1016/S1352-2310(01)00118-2
- Rasmussen, J. F. B., and Hagen, A. (2009). The Effect of H2S on the Performance of Ni-YSZ Anodes in Solid Oxide Fuel Cells. *J. Power Sourc.* 191, 534–541. doi:10.1016/j.jpowsour.2009.02.001
- Riley, D. M., Tian, J., Güngör-Demirci, G., Phelan, P., Villalobos, J. R., and Milcarek, R. J. (2020). Techno-Economic Assessment of CHP Systems in Wastewater Treatment Plants. *Environments* 7, 74. doi:10.3390/environments7100074
- Rillo, E., Gandiglio, M., Lanzini, A., Bobba, S., Santarelli, M., and Blengini, G. (2017). Life Cycle Assessment (LCA) of Biogas-Fed Solid Oxide Fuel Cell (SOFC) Plant. *Energy* 126, 585–602. doi:10.1016/j.energy.2017.03.041
- Rücker, C., and Kümmerer, K. (2015). Environmental Chemistry of Organosiloxanes. *Chem. Rev.* 115, 466–524. doi:10.1021/cr500319v
- Ryckebosch, E., Drouillon, M., and Vervaeren, H. (2011). Techniques for Transformation of Biogas to Biomethane. *Biomass and Bioenergy* 35, 1633–1645. doi:10.1016/j.biombioe.2011.02.033
- Scarlat, N., Dallemand, J.-F., and Fahl, F. (2018). Biogas: Developments and Perspectives in Europe. *Renew. Energ.* 129, 457–472. doi:10.1016/j.renene.2018.03.006
- Schwejkofler, M., and Niessner, R. (2001). Removal of Siloxanes in Biogases. *J. Hazard. Mater.* 83, 183–196. doi:10.1016/S0304-3894(00)00318-6
- Skinner, B., and Appleman, D. (1963). Melanophlogite, a Cubic Polymorph of Silica. *Am. Mineral.* 48, 854–867.
- Soreanu, G., Béland, M., Falletta, P., Edmonson, K., Svoboda, L., Al-Jamal, M., et al. (2011). Approaches Concerning Siloxane Removal from Biogas - A Review. *Can. Biosyst. Eng./Le Genie Des Biosyst. Au Can.* 53, 8.1–8.18.
- Sumi, H., Shimada, H., Yamaguchi, Y., Yamaguchi, T., and Fujishiro, Y. (2020). Degradation Evaluation by Distribution of Relaxation Times Analysis for Microtubular Solid Oxide Fuel Cells. *Electrochimica Acta* 339, 135913. doi:10.1016/j.electacta.2020.135913
- Tian, J., and Milcarek, R. J. (2020). Investigating the Degradation Mechanism of the Solid Oxide Fuel Cell Nickel-Yttria Stabilized Zirconia Anode Under Siloxane Contamination. *J. Power Sourc.* 480, 229122. doi:10.1016/j.jpowsour.2020.229122
- Tian, J., and Milcarek, R. J. (2021). Siloxane Deposition on the Ni-YSZ Solid Oxide Fuel Cell Anode Exposed to Bio-Syngas. *J. Electrochem. Soc.* 168, 044503. doi:10.1149/1945-7111/abf21a
- Trendewicz, A. A., and Braun, R. J. (2013). Techno-Economic Analysis of Solid Oxide Fuel Cell-Based Combined Heat and Power Systems for Biogas Utilization at Wastewater Treatment Facilities. *J. Power Sourc.* 233, 380–393. doi:10.1016/j.jpowsour.2013.01.017
- Vaiss, V. S., Fonseca, C. G., Antunes, F. P. N., Chinelatto Jr., L. S., Jr., Chiaro, S. S. X., Souza, W. F., et al. (2020). Experimental and Theoretical Study of Deactivated HDT Catalysts by Si Species Deposited on Their Surfaces: Models Proposition, Structural and Thermodynamic Analysis. *J. Catal.* 389, 578–591. doi:10.1016/j.jcat.2020.06.007
- Van Herle, J., and McEvoy, A. J. (1994). Oxygen Diffusion through Silver Cathodes for Solid Oxide Fuel Cells. *J. Phys. Chem. Sol.* 55, 339–347. doi:10.1016/0022-3697(94)90230-5
- Wan, T. H., Saccoccio, M., Chen, C., and Ciucci, F. (2015). Influence of the Discretization Methods on the Distribution of Relaxation Times Deconvolution: Implementing Radial Basis Functions with DRTtools. *Electrochimica Acta* 184, 483–499. doi:10.1016/j.electacta.2015.09.097
- Wang, N., Tan, L., Xie, L., Wang, Y., and Ellis, T. (2020). Investigation of Volatile Methyl Siloxanes in Biogas and the Ambient Environment in a Landfill. *J. Environ. Sci.* 91, 54–61. doi:10.1016/j.jes.2020.01.005
- Yan, P., Mineshige, A., Mori, T., Wu, Y., Auchterlonie, G. J., Zou, J., et al. (2013). Microanalysis of a Grain Boundary's Blocking Effect in Lanthanum Silicate Electrolyte for Intermediate-Temperature Solid Oxide Fuel Cells. *ACS Appl. Mater. Inter.* 5, 5307–5313. doi:10.1021/am401195e
- Yu, Y., Wang, Y., Lin, K., Hu, N., Zhou, X., and Liu, S. (2013). Complete Raman Spectral Assignment of Methanol in the C-H Stretching Region. *J. Phys. Chem. A* 117, 4377–4384. doi:10.1021/jp400886y
- Yuan, M., Dong, W., Wei, L., Liu, Q., Meng, Y., Wang, X., et al. (2020). Stability Study of SOFC Using Layered Perovskite Oxide La1-85Sr0.15CuO4 Mixed with Ionic Conductor as Membrane. *Electrochimica Acta* 332, 135487. doi:10.1016/j.electacta.2019.135487
- Zhao, G. L., and Bagayoko, D. (2000). Electronic Structure and Charge Transfer in 3C- and 4H-SiC. *New J. Phys.* 2, 16. doi:10.1088/1367-2630/2/1/316

Conflict of Interest: The authors declare that the research was conducted in the absence of any commercial or financial relationships that could be construed as a potential conflict of interest.

Publisher's Note: All claims expressed in this article are solely those of the authors and do not necessarily represent those of their affiliated organizations, or those of the publisher, the editors and the reviewers. Any product that may be evaluated in this article, or claim that may be made by its manufacturer, is not guaranteed or endorsed by the publisher.

Copyright © 2021 Tian and Milcarek. This is an open-access article distributed under the terms of the Creative Commons Attribution License (CC BY). The use, distribution or reproduction in other forums is permitted, provided the original author(s) and the copyright owner(s) are credited and that the original publication in this journal is cited, in accordance with accepted academic practice. No use, distribution or reproduction is permitted which does not comply with these terms.



Biogas Upgradation Through CO₂ Conversion Into Acetic Acid via Microbial Electrosynthesis

Moumita Roy, Sukrampal Yadav and Sunil A. Patil*

Department of Earth and Environmental Sciences, Indian Institute of Science Education and Research Mohali (IISER Mohali), Manauli, India

OPEN ACCESS

Edited by:

Uwe Schröder,
University of Greifswald, Germany

Reviewed by:

Falk Hamisch,
Helmholtz Centre for Environmental
Research (UFZ), Germany
Mohammad Zain Khan,
Aligarh Muslim University, India

*Correspondence:

Sunil A. Patil
sunil@iisermohali.ac.in
sunilmicro12@gmail.com

Specialty section:

This article was submitted to
Bioenergy and Biofuels,
a section of the journal
Frontiers in Energy Research

Received: 16 August 2021

Accepted: 20 October 2021

Published: 03 November 2021

Citation:

Roy M, Yadav S and Patil SA (2021)
Biogas Upgradation Through CO₂
Conversion Into Acetic Acid via
Microbial Electrosynthesis.
Front. Energy Res. 9:759678.
doi: 10.3389/fenrg.2021.759678

Biogas is one of the promising futuristic renewable energy sources with enormous market potential. However, the presence of CO₂ lowers down the calorific value of biogas. Hence, various biogas upgradation technologies are under intense investigation to increase the methane content to the desired level. This study reports on enhancing methane content in biogas through CO₂ sequestration into acetic acid via microbial electrosynthesis (MES) process. The previously enriched mixed chemolithoautotrophic microbial culture dominated by *Acetobacterium* spp. used CO₂ present in the biogas as the sole carbon source. After establishing a stable performing biocathode at a fixed cathodic potential of −1 V (vs. Ag/AgCl) through batch mode operation, biogas was fed continuously at different feed rates, viz., 0.5, 0.3, and 0.2 ml/min to the cathode chamber. The highest feed rate of 0.5 ml/min was least effective both for methane content increment (from 61 ± 3% to 86 ± 2%) and acetic acid titer (1.5 ± 0.5 g/L; 0.107 ± 0.02 g/L/d.). In comparison, the lowest flow rate of 0.2 ml/min was the most effective for the intended process (methane upgradation from 62 ± 7% to 93 ± 3% and acetic acid titer 3.4 ± 0.6 g/L produced at 0.24 ± 0.04 g/L/d rate). Both acetic acid bioproduction and biogas upgradation occurred best at an E_{cell} of 3.3 ± 0.35 V at the low feed rate. A maximum of 84 ± 7%, 57 ± 10% and 29 ± 2% coulombic, carbon and energetic efficiencies, respectively, were achieved in acetic acid. Cyclic voltammograms of biocathodes revealed the decrease in hydrogen evolution potential and increased bioelectrocatalysis, thereby suggesting the contribution of microbes in the process. *Acetobacterium*, which is known for CO₂ fixation, was found to be the dominant microbial genus in biogas fed reactors. The demonstrated approach not only offers the advantage of obtaining two products, one in the bulk phase and the other in the off-gas, it also validates the applicability of the bioelectrochemical biogas upgradation technology.

Keywords: biocathode, *Acetobacterium*, methane, electricity-driven bioproduction, bioelectrochemical systems (BES)

1 INTRODUCTION

According to the World Energy Forum, fossil fuel sources will be exhausted by the next 10 decades due to the unquenchable global energy demand (Weiland, 2010; Sahota et al., 2018). Since energy is the pillar of globalization, its demand is increasing exponentially with time. Under these circumstances and for sustainable growth, immediate measures need to be taken to rapidly

implement renewable energy. Among various sources, biogas is a promising source to meet the world's importunate energy demand. It has a great potential to evolve as an alternative fuel for vehicles or to meet the ever-growing electricity demand and is increasingly gaining preference throughout the globe. For example, CNG fueled buses are already operating in the United States. Over 2,200 digesters are currently operational for biogas production in the United States (Biogas Industry Market Snapshot | American Biogas Council). Due to the price increase of gasoline in Europe and North America, more inclination is visible for biomethane (Engerer and Horn, 2010). About 42 million anaerobic digesters produce around 13 million m³ biogas in China. By the end of 2030, Germany will be producing near about 10 billion m³ biogas. In India, 4.9 million digesters with a two million m³ biogas production capacity are present (Thiruselvi et al., 2021). India has planned to target renewable energy at 275 gigawatts by the end of 2027 (Thiruselvi et al., 2021). Several initiatives have also been taken up by the Indian Government like the Sustainable Alternative toward Affordable Transportation (SATAT) initiative to secure the off-take of compressed biomethane, the National Policy on Biofuels (2018) for financing as well as fiscal incentives, and Motor vehicles rule to promote the usage of BioCNG in motor vehicles. Climate Change Levy of United Kingdom and Finland provide tax exemption for energy from renewable sources. These data suggest the prominence of biogas in renewable energy development programs across the globe.

The key challenge in using biogas as fuel is its low calorific value due to the presence of CO₂. For instance, the upgraded BioCNG (around 52,000 kJ/kg) has around 2.5-fold higher calorific value than untreated biogas containing ~55% methane (around 19,500 kJ/kg) (Dere et al., 2017). Hence, biogas upgradation is essential to make it a high-quality fuel. To this end, several technologies based on absorption, adsorption, and membrane separation approaches have come up over the years (Kadam and Panwar, 2017; Angelidaki et al., 2018; Sahota et al., 2018; Thiruselvi et al., 2021). Water scrubbing is the most feasible, but it is not considered economical and sustainable due to high capital costs and freshwater requirements. Apart from water scrubbing, pressure swing absorption and chemical adsorption are also established techniques, but they are complex processes with high investment costs (Sahota et al., 2018). More sustainable approaches to biogas upgradation are thus constantly explored. Microbial electrosynthesis (MES) is one of the microbial electrochemical technologies (METs) in which electricity-driven CO₂ reduction is enabled with the help of microbial catalysts. Based on the nature and extent of electrochemical interactions between the working electrode and microbial catalysts, METs are broadly categorized into two groups, namely primary and secondary METs (Schröder et al., 2015). In primary METs, a prominent functional connection between the microbial catalysts and working electrode exists via direct or mediated electron transfer. In secondary METs, electrochemistry is indirectly linked to the microbial process, for instance, through the electrochemical control of parameters such as metabolite concentration and pH. In most MES processes, including the present study, microorganisms catalyze the target reactions via

direct and/or mediated electron transfer mechanisms by forming biofilm at the cathode surface and planktonic growth in the bulk phase (Patil et al., 2015a; Labelle et al., 2020). Using this technique, CO₂ from the biogas can be converted to value-added products like methane, acetic acid, butyric acid, propionic acid, and the methane concentration can be enhanced. The most attractive part of the MES process is the CO₂ utilization instead of just removal. In one approach, the microbial electrolysis process is integrated with anaerobic digesters, and CO₂ is microbially reduced to methane. Significant work has been done on coupling MES with anaerobic digestion (AD) with different reactor designs and operational conditions (Sravan et al., 2020; Wang et al., 2021). Biogas is fed to the MES reactors in another approach, and CO₂ is reduced to methane through hydrogenotrophic, acetoclastic, or methylotrophic pathways (Evans et al., 2019).

Limited work has been done on utilizing CO₂ from biogas to produce organic acids or other products via MES (Jourdin et al., 2015b; Das and Ghangrekar, 2018; Kokkoli et al., 2018). The previous MES studies with biogas feedstock mostly focused on value-added product formation, specifically acetic acid, and barely on enhancing methane content. The present study aimed to investigate the MES applicability for biogas upgradation through CO₂ conversion into acetic acid. After establishing a batch mode process, the effect of different biogas feed rates was studied for the upgradation of biogas along with the production of acetic acid. The cyclic voltammetry and the genomic analyses of the biocathode were conducted to shed light on the bioelectrochemical processes and microorganisms involved in the bioproduction process.

2 MATERIALS AND METHODS

2.1 Microbial Inoculum Source and Cultivation Conditions

A previously enriched chemolithoautotrophic mixed microbial culture dominated by *Acetobacterium* spp. was used as the inoculum source (Roy et al., 2021). For the MES experiments, a minimal medium with pH 7 was used. It contained K₂HPO₄ (5.35 g/L), KH₂PO₄ (2.62 g/L), NH₄Cl (0.25 g/L), KCl (0.5 g/L), CaCl₂·2H₂O (0.15 g/L), MgCl₂·2H₂O (0.6 g/L), trace metal solution (1 ml/L), selenium-tungstate solution (1 ml/L), vitamin solution (2.5 ml/L), 2-bromoethanesulfonate (6.4 g/L), Na₂S·9H₂O (0.3 g/L), and resazurin (0.5 ml/L from a 0.1% stock solution) (Roy et al., 2021). It was cultivated and maintained with CO₂ and H₂ (H₂:CO₂ ratio was 4:1) as the sole carbon and energy sources, respectively, under anaerobic conditions at 28 ± 2°C. An active culture was inoculated in the cathode chamber of MES reactors to have 0.25 OD₆₀₀ in suspension during the start-up phase.

2.2 Biogas Sampling and Characterization

The biogas was collected from an operational and well-maintained anaerobic sewage treatment plant (Phase 3, Panchkula, Haryana). A vacuum pump (Model N86 KT.45.18; KNF pump) was used to collect biogas in 6 L passivated SilcoCan

steel canisters (Restek, United States). A Teflon gas tubing was used to collect the biogas as it can withstand high temperature (>180°C) and pressure (>40 psi). A PTFE filter (0.2 µm) was used in the front of the tubing to restrict the particulate matter from the biogas from entering the canister. At the same time, the moisture content was minimized with the help of a moisture trap installed in gas tubing where magnesium perchlorate was used as the moisture-absorbing reagent. The biogas samples were analyzed by GC with TCD (Agilent 490 Micro GC, *Analysis and Calculations*). The major components of biogas were methane (60 ± 2%), CO₂ (28 ± 5%), and N₂ (10 ± 2%). A trace amount of H₂S was also present in the sample. 1 ± 0.1% O₂ was also observed, which was most likely present due to manual sampling error.

2.3 MES Reactor Setup and Experiments

Custom-made double-chambered glass reactors with an empty bed volume of 700 ml (350 ml each chamber) were used for this study. The catholyte was the same as mentioned in *Microbial Inoculum Source and Cultivation Conditions* and the anolyte was 0.5 M Na₂SO₄ with pH 2.5 (adjusted with 1 M H₂SO₄). The experiments were conducted in three-electrode configuration mode under potentiostatically controlled conditions (VSP300, BioLogic Science Instruments, France). The working volume was 250 ml. A graphite plate with 10 cm² and dimensionally stable mixed metal oxide coated titanium plate with 7.5 cm² projected surface area were used as working (cathode) and counter (anode) electrodes, respectively. The anode and cathode chambers were separated by a 117 Nafion proton exchange membrane (Sigma-Aldrich). Water oxidation/oxygen evolution and CO₂ reduction reactions take place in the anode and cathode chambers, respectively. The cathode material and proton exchange membrane were pretreated as described elsewhere (Roy et al., 2021). All MES experiments were performed in duplicate at an incubation temperature of 28 ± 2°C. The performance of the duplicate reactors for reported parameters was reproducible and very close; therefore average data has been presented in all the figures. The electrode potential data are reported against Ag/AgCl (3.5 M KCl) reference electrode (0.205 V vs. SHE). The experimental setup and the reactions in MES reactors are illustrated in **Supplementary Figure S1**. Two types of control experiments were conducted. These include biotic open circuit potential (OCP) experiment (with all media components and carbon source but not electrically connected, i.e., no electron/energy source), and abiotic connected (with all the components and electrically connected but uninoculated) experiment.

Activation polarization was performed at -0.6 V before inoculation or starting the main experiment for electrochemical activation of the electrodes, membrane, and electrolyte. A constant potential of -1.0 V vs. Ag/AgCl was applied at the cathode to facilitate H₂-based bioproduction by using the chronoamperometry (CA) technique. The reduction current response was monitored at a constant time interval (5 min). Cyclic voltammetric analysis was conducted for two cycles within a potential window of -1.4 and -0.2 V at a constant scan rate of 1 mVs⁻¹ at different experimental conditions, i.e., before inoculation, after inoculation, and at the end of

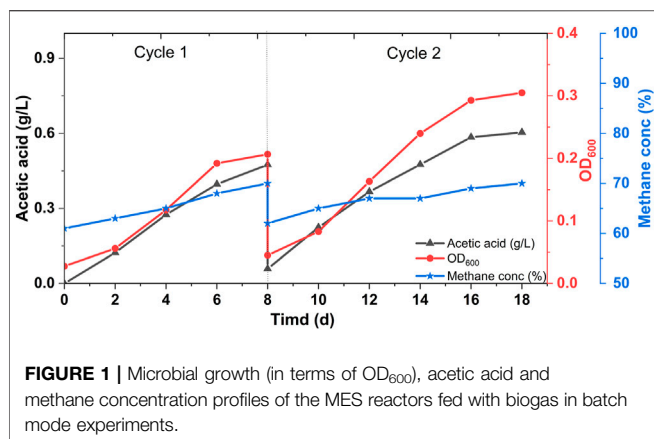
each biogas feed condition. The data of the second cycle was used for analysis.

2.4 Biogas Feeding

In the first phase, 30 ml of CO₂ containing biogas (with the composition stated in *Biogas Sampling and Characterization*) was added to the catholyte daily to establish a stable performing biocathode. The CO₂ present in the biogas got dissolved in the form of bicarbonate at pH 7. This was the sole carbon source for the microbes. A gas displacement assembly was attached to the reactor's outlet to maintain the pressure condition inside the reactors. After the completion of two batch cycles, the biogas was fed in a continuous flow mode at different feed rates, viz., 0.5, 0.3 and 0.2 ml/min using the mass flow controllers (MFCs, Alicat/MCM-100SCCM-D) in the second phase. The MFC calibration was carried out with the air by the manufacturer (Alicat Scientific). The correction factors were applied for different gases depending on their viscosity, density, and compressibility. The standards used for calibrations were NIST (National Institute of Standards and Technology) traceable. The volumetric flow of the off-gas from MFCs was measured to confirm the used flow rates with the help of a water displacement assembly, and it was found to be the same. The volumetric flows of the off-gas from the microbial electrosynthesis reactors were also measured intermittently at each experimental condition and were found to be marginally lower than the applied feed rates. For instance, in the case of 0.5 ml/min biogas feed rate, the off-gas flow was about 0.47 ml/min. Similar trends were observed in other gas feed rates. The effect of different feed rates was evaluated on methane content increase as well as acetic acid production after acclimatization of the reactors for at least 2 days at each feed rate.

2.5 Analysis and Calculations

The bulk phase and gas samples from MES reactors were taken at a regular interval of 2 days. To assess the gas composition in the headspace and to know the methane concentration, the gas analysis was done by GC-TCD (Agilent 490 Micro GC) equipped with three channels for different gases [Channel 1: Column- Molecular sieve for H₂, carrier gas- Ar; Channel 2: Column- Molecular sieve for O₂, N₂, CO and CH₄, carrier gas-He; Channel 3: Column- Pora plot U for CO₂ and H₂S, carrier gas-He]. The bulk phase organics (C1-C4 organic acids and alcohols) analysis by HPLC (Agilent 1260 Infinity II, RID Detector, Hiplux H column, 5 µM H₂SO₄ as mobile phase, flow rate 0.5 ml/min, Temperature 50°C) was performed to evaluate the efficiency of microbes to produce organics from CO₂ in biogas. Additionally, monitoring of microbial growth via OD measurements at 600 nm (Photo-lab 7600 UV-VIS spectrophotometer) and pH (Oakton PC2700) in the bulk phase was done. Different parameters, such as product titer, production rates (normalized by cathode surface area and catholyte volume), coulombic efficiency (electron recovery into organic products), carbon recovery efficiency (Das et al., 2018) and energetic efficiency were calculated as described in **supplementary section S1** (Patil et al., 2015b). Since the methane content increase was not directly related to energy



consumption in this study, we did not consider it in CE and EE calculations.

2.6 Microbial Community Analysis

To understand the microbial communities developed at the biocathode and in the bulk phase, V3-V4 16S amplicon sequencing-based analysis was conducted. For this, the genomic DNA of the inoculum source and from two duplicate MES reactors named R1 and R2 (biocathode and bulk phase) was isolated on the completion of the electrosynthesis experiments using QIAGEN DNeasy PowerSoil Pro Kit. Further DNA quantification was done by Nanodrop (Genova Nano—4359). Agarose gel electrophoresis (1%) was also performed to assess the integrity of the isolated genomic DNA. Since V3-V4 regions of 16S rRNA are the most conserved regions, they were amplified using specific V3 Forward (341F: 5'-GCCTACGGGNGGCWGCAG-3') and V4 Reverse (805R: 5'-ACTACHVGGGTATCTAATCC-3') primers. Again 2% agarose gel electrophoresis was performed to analyze the amplified products. Later, Illumina MiSeq 2,500 platform at Eurofins Genomics India Pvt. Ltd. (Bangalore, India) was used for amplicon sequencing. Trimmomatic v0.38 was used for trimming the adaptor and primers sequences. FLASH v1.2.11 was run for alignment as well as selecting the operational taxonomic unit (OTU). At last, the OTU products were run through the Silva database to find the most similar OTU hits using the Qiime1 pipeline and R packages for visualization. The raw amplicon sequences have been submitted to NCBI short read archive under bio-project PRJNA659908.

3 RESULTS AND DISCUSSION

3.1 Biocathode Development Through Batch Mode Operation

In order to form an efficient biocathode for CO₂ utilization, the biogas was first supplied in a fed-batch mode. Since the enriched mixed culture contained chemolithoautotrophic microbes (Roy et al., 2021), immediate organics production, in particular, acetic acid, was detected from the start of the experiment (Figure 1).

Since the inoculum source contains mainly *Acetobacterium* spp. that follow the Wood-Ljungdahl pathway for CO₂ fixation,

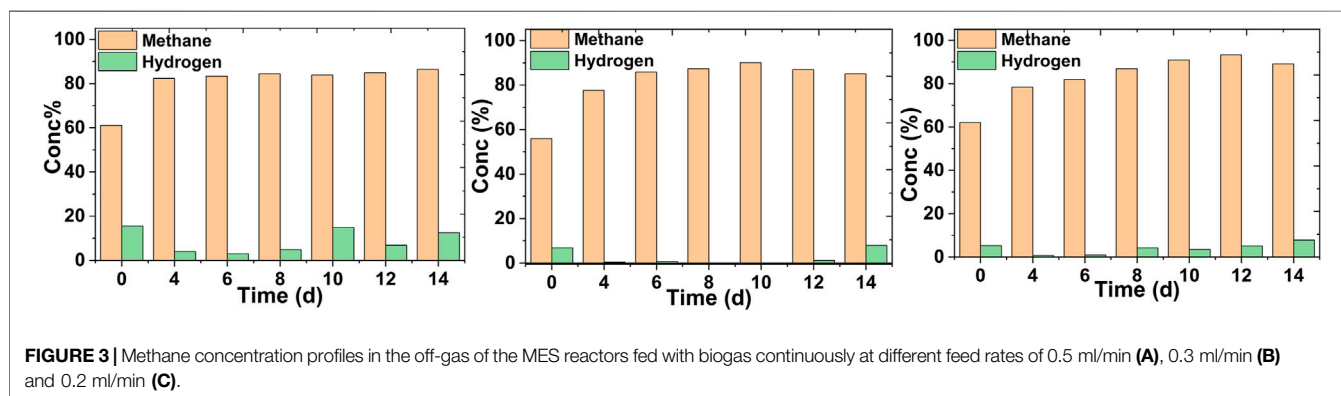
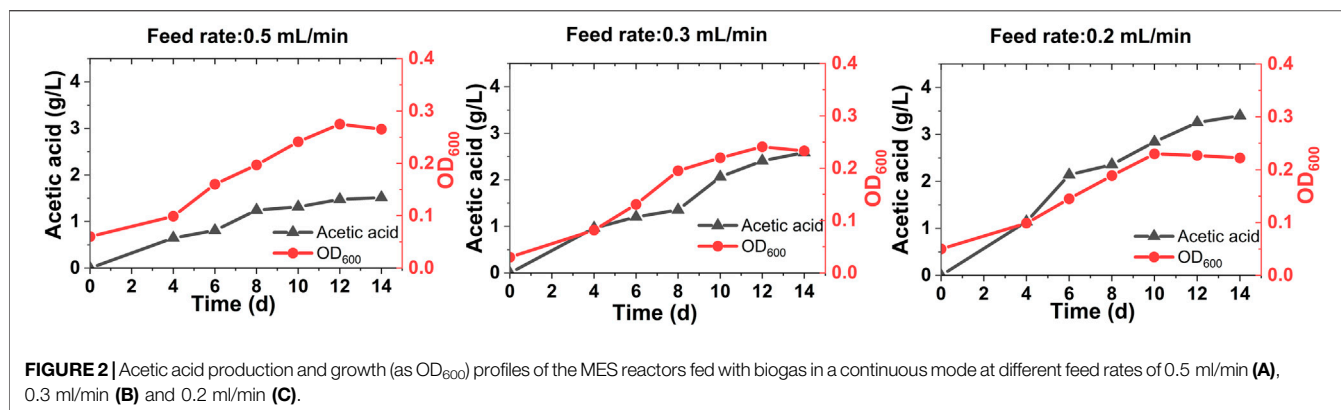
microbial growth and acetic acid concentration are directly correlated. The maximum titer achieved was 0.6 ± 0.1 g/L with a production rate of 0.06 ± 0.001 g/L/d (Figure 1). Along with the acetic acid production increase in the methane content was also evident. As a result of microbial CO₂ utilization from biogas, the methane concentration increased from $61 \pm 3\%$ to $71 \pm 2\%$ (Figure 1). These observations are close to the previously reported data on MES from biogas (Das and Ghangrekar, 2018). The volumetric measurement of the off-gas was not performed regularly in this study. It is important to take into account the changes in the off-gas volume during continuous experiments for the optimization and development of such processes. The batch mode operation and consistent acetic acid production for two consequent cycles suggested biocathode development with biogas feed. No microbial growth and acetic acid production were observed in control MES reactors (Supplementary Figure S2).

3.2 MES Experiments in a Continuous Mode Operation

After developing stable performing biocathodes in a fed-batch mode operation (*Biocathode Development Through Batch Mode Operation*), biogas was fed at different feed rates in a continuous mode. In all cases, instant microbial growth and acetic acid production were observed (Figure 2), implying successful acclimatization of the biocathode (Marshall et al., 2012). A trace amount of formic acid (up to 0.120 g/L) was also detected. As microbial growth is directly linked with organics production, the OD and acetic acid titer data correlated well (Ragsdale, 2008). Compared to the batch mode operation, the acetic acid production was considerably higher in the case of continuous feed operation. It is mainly due to the unlimited and more CO₂ supply to the microbes in the continuous mode than a limited and less CO₂ availability in the batch mode operation. With the highest biogas feed rate of 0.5 ml/min, the maximum acetic acid titer reached to 1.5 ± 0.5 g/L with a volumetric production rate of 0.107 ± 0.02 g/L/d and a cathode surface area-based rate of 27 ± 9 g/m²/d after 14 days (Figure 2A). The acetic acid production was leveled off after 10 days. For 0.3 ml/min feed rate, the maximum acetic acid titer was 2.5 g/L with a production rate of 0.17 ± 0.3 g/L/d and a cathode surface area-based rate of 46 ± 7 g/m²/d (Figure 2B). The maximum acetic acid titer of 3.4 g/L was achieved with the lowest feed rate of 0.2 ml/min (Figure 2C). It was produced at 0.23 ± 0.04 g/L/d volumetric and 60 ± 11 g/m²/d cathode surface-based rates. The acetic acid titer tends to increase with the decrease in biogas feed rates based on a 2-fold higher titer at 0.2 ml/min feed rate than 0.5 ml/min. This can be attributed to the retention and thereby microbial utilization of both CO₂ and H₂ (produced at the cathode) in reactors for a longer duration at the lower feed rates.

3.3 Biogas Upgradation

The methane concentration in the off-gas was analyzed at a regular time interval in a continuous mode operation. No methane upgradation was observed in the case of control MES reactors (Supplementary Figure S2). Irrespective of the feed rates, an



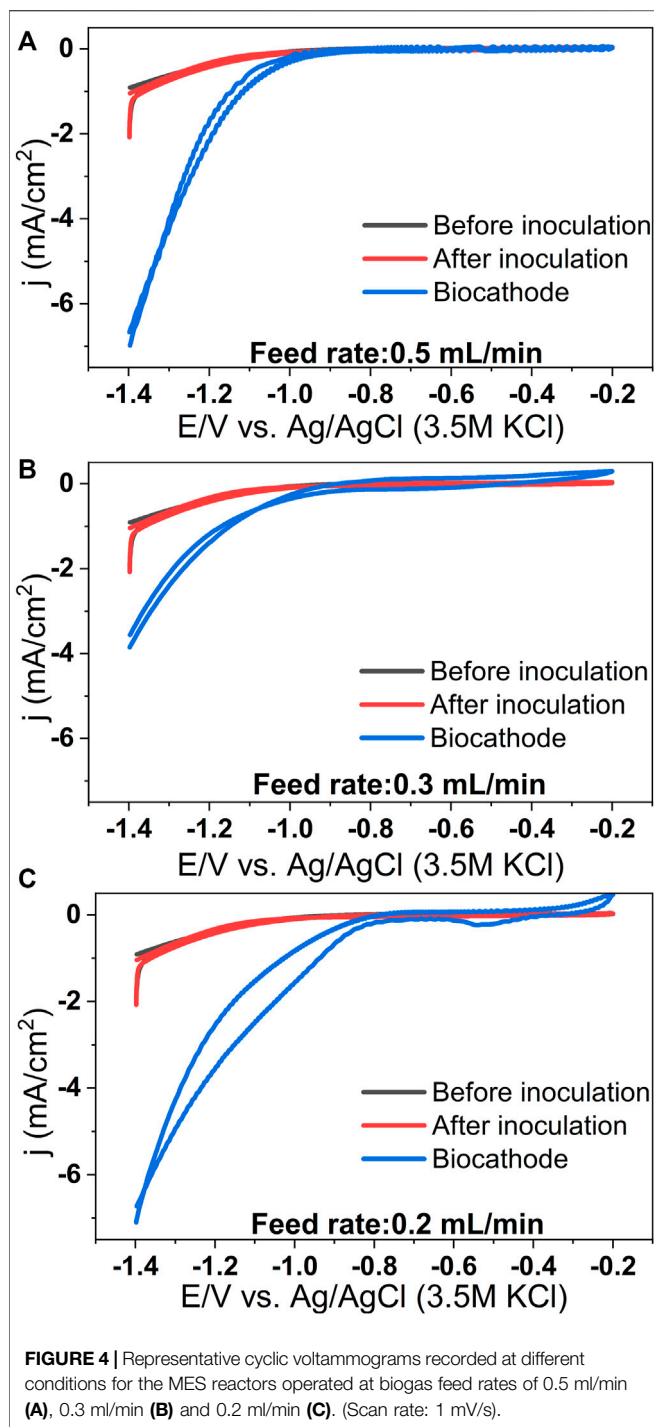
increase in methane content was prominent in all cases (Figure 3). Since microbes utilized CO₂ present in biogas as the sole carbon source, the methane content started to get enriched from the very beginning of the reactor operation at different feed rates.

At the highest feed rate, the methane concentration increased from 62 ± 3 to $82 \pm 2\%$ on the 4th day (Figure 3A) and remained within that range thereafter. A maximum methane concentration of $84 \pm 2\%$ was observed on the 14th day. The hydrogen concentration was mostly about 12% in the off-gas. Most of the hydrogen was getting flushed out in the off-gas due to the higher feed rate. A significant increase in the methane content from 55 ± 6 to $90 \pm 4\%$ was seen at a 0.3 ml/min feed rate after the 10th day (Figure 3B). Hydrogen was mostly utilized in this particular case and was detected when methane concentration was lower. The highest methane concentration was observed with the lowest feed rate after the 12th day (from 62 ± 4 to $93 \pm 3\%$) (Figure 3C). After that, the methane concentration remained almost at the same level. The hydrogen concentration remained at a low level (<7%) in this case. The methane concentration enhancement was pronounced in the case of both 0.3 and 0.2 ml/min feed rates. This can be justified by the fact that at lower feed rates, microbes are able to utilize most of the carbon source for growth and acetic acid production (*MES Experiments in a Continuous Mode Operation*). With the goal of futuristic green fuel, a combination of hydrogen and methane can be more promising (Nanthagopal et al., 2011).

3.4 Electrochemical Analysis of the Biocathodes

In the case of control MES reactors, the reduction current was almost negligible (Supplementary Figure S3). A significant increase in reduction current was observed with all feed rates, and it was maximum for the lowest feed rate. These observations align well with the acetic acid production data (Supplementary Section S4, Supplementary Figure S4). Cyclic voltammograms (CVs) were recorded at different experimental conditions. The blank CV was performed before inoculation, and the inoculated and biocathode CVs were performed just after microbial source inoculation and at the end of the cycle, respectively. No redox peaks in the blank CV indicate the absence of any redox-active moieties at the cathode surface or in the catholyte in the uninoculated condition (Figure 4). By comparing blank CV with biocathode CV, it can be seen that the H₂ evolution potential of biocathode is higher than the bare cathode (−0.95 V). For different feed rates of 0.5, 0.3 and 0.2 ml/min, the H₂ evolution potentials are −0.92, −0.77 and −0.76 V. The shift is most prominent (~0.2 V) in case of the lower feed rates (Figure 4C). This observation aligns well with the acetic acid production and methane upgradation data (Figures 2, 3).

The shift in H₂ evolution potential suggests lowering of the H₂ evolution over-potential at the biocathode due to the presence of microbes. Moreover, the reduction current drawn at any cathode potential is higher in the case of biocathode than the abiotic



cathode due to the presence of microbial catalysts. For instance, at -1 V, the current density (in mA/cm^2) of biocathodes are -0.3 (for 0.5 ml/min), -0.4 (for 0.3 ml/min), and -1.2 (for 0.2 ml/min) in comparison to -0.08 mA/cm^2 of the bare cathode. Similar findings have been reported for CO₂ reducing biocathodes earlier (Jiang et al., 2013; Jourdin et al., 2015a; Patil et al., 2015a; Bajracharya et al., 2015). The improved electrocatalytic activity and decreased H₂ evolution overpotential can be attributed to

microbial activity at the cathode of the MES systems (Rozendal et al., 2008; Jourdin et al., 2015a; Patil et al., 2015a).

3.5 Lower Biogas Feed Rate Favors Efficient Bioproduction and Methane Enrichment

3.5.1 Biogas Upgradation and Acetic Acid Bioproduction

Based on the observations of this study, it is evident that the lower biogas feed rate promotes better bioproduction and methane content increase. High feed rates ensure non-limiting carbon supply in the reactor. At the same time, it decreases the retention time of gases in the bulk phase. As a result, the CO₂ (present in the biogas) remains for a short time in the reactor. On the other hand, though carbon supply decreases with the lower feed rate, the retention time of gases is more in the bulk phase. In the case of higher feed rates, the H₂ produced in the cathode also gets removed readily from the system. It can influence the performance of acetogens that use H₂ as the energy source for CO₂ reduction. Hence, an optimum trade-off between the flow rate and key production parameters needs to be established through dedicated process optimization studies for the continuously fed systems. With the lower feed rate, a maximum titer of 3.4 ± 0.6 g/L was achieved along with a methane upgradation to $93 \pm 3\%$. These values are comparable with the previous studies conducted with biogas. For example, 98% methane upgradation was reported via electromethanogenesis by Bo and coworkers in a single chamber reactor which was coupled with an anaerobic digester (Bo et al., 2014). Liu et al. have also reported 96% methane upgradation by coupling electromethanogenesis with anaerobic digester (Liu et al., 2016). Even 97% and higher methane concentrations have been achieved with modified reactor set up (Luo and Angelidaki, 2012; Jin et al., 2017; Kokkoli et al., 2018). In terms of acetic acid titer, this study is at par with previous studies with biogas as a carbon source (Das et al., 2021).

3.5.2 Coulombic Efficiency

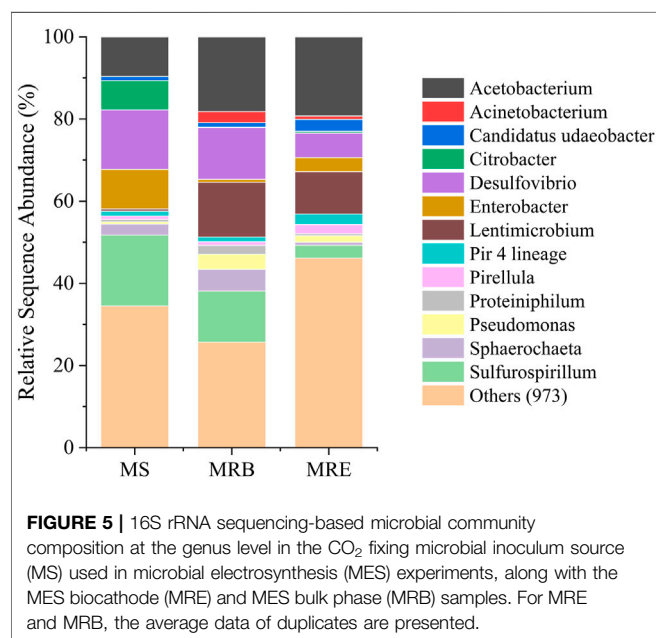
Coulombic efficiency (CE) is the percentage of electrons recovered in the target product (Bajracharya et al., 2015; Patil et al., 2015b). A higher CE portrays an efficient MES system where microbes are able to utilize most of the electrons for product formation. In this study, coulombic efficiencies were quite comparable in all three conditions (Table 1). The highest CE of $90 \pm 1\%$ in acetic acid was achieved at 0.3 ml/min along with $0.7 \pm 0.03\%$ and $3.2 \pm 1.1\%$ electron recovery in H₂ and biomass respectively. With the lowest feed rate, the CE was $84 \pm 7\%$ in acetic acid, $2.7 \pm 0.6\%$ in biomass and $0.5 \pm 0.04\%$ in H₂. At the high feed rate the CE achieved in acetic acid, biomass and H₂ was $82 \pm 1\%$, $3.7 \pm 1.8\%$ and $1.7 \pm 0.03\%$, respectively. These data suggest an efficient electron recovery in acetic acid at all conditions.

3.5.3 Carbon Recovery Efficiency

Carbon recovery efficiency (CRE) is an important parameter to estimate carbon sequestration in the form of the produced organic product. In this study, CO₂ was mainly recovered in

TABLE 1 | Comparison of key production parameters at different biogas feed rates.

Parameter	Biogas feed rate (ml/min)		
	0.5	0.3	0.2
Acetic acid titer (g/L)	1.5 ± 0.5	2.5 ± 0.4	3.4 ± 0.6
Production rate (g/L/d)	0.107 ± 0.02	0.17 ± 0.3	0.23 ± 0.04
Production rate (g/m ² /d)	27 ± 9	46 ± 7	60 ± 11
Methane enrichment (%)	from 62 ± 3 to 84 ± 2	from 55 ± 6 to 90 ± 4	from 62 ± 4 to 93 ± 3
Coulombic efficiency in acetic acid (%)	82 ± 1	90 ± 1	84 ± 7
Carbon recovery efficiency (%) in acetic acid	10 ± 4	30 ± 5	56 ± 10
Energetic efficiency in acetic acid (%)	34 ± 0.6	33 ± 0.04	29 ± 2
E _{cell}	2.7	3.1	3.3



the form of acetic acid. From **Table 1**, it is clear that CRE is reversely proportional to the biogas feed rate. The maximum carbon recovery of 56 ± 10% was obtained with the lowest feed rate followed by 30 ± 5% for 0.3 ml/min and 10 ± 4% at 0.5 ml/min. Similar findings were also reported by Das and coworkers, where 20% CRE was reported with the high biogas feed rates of 3.5 ml/min (Das et al., 2020).

3.5.4 Energetic Efficiency

Energetic efficiency (EE) elucidates the overall energy requirement of the MES system. It helps to determine the overall operational cost of the MES system. EE is one of the critical bottlenecks that limit the effectiveness of the MES process (PrévotEAU et al., 2020). The higher the EE, the better efficient the MES system will be to produce the product of interest. In this study around 34 ± 0.6%, 33 ± 0.04%, and 29 ± 2% energetic efficiency was achieved at 0.5, 0.3 and 0.2 ml/min biogas feed rates, respectively (**Table 1**). A similar range (35–42%) has been observed in previous MES studies but with pure CO₂ feed (Labelle and May, 2017).

When comparing the overall efficiencies, it is clear that though a lower feed rate of 0.2 ml/min leads to better CRE, in terms of CE

and EE, higher feed rates outperformed the lower feed rate. These observations suggest a trade-off among efficiencies at different feed rates, which needs to be understood better and optimized through further research.

3.6 Microbial Community Data

Acetobacterium, *Desulfovibrio*, *Sulfurospirillum*, and *Lentimicrobium* genera dominated the mixed culture (**Figure 5**). The relative sequence abundance of different microbial genera changed according to conditions. For example, the relative abundance of *Acetobacterium* increased in the MES reactors (38 ± 3%) compared to the inoculum source (9%). The relative sequence abundance of *Sulfurospirillum* was prominent in the inoculum source (16%) and bulk phase of reactors (12 ± 1%) but less at the cathodes (3 ± 2%). In the MES reactors, *Acetobacterium* spp. was the most dominant genus with a relative abundance of 18 ± 2% in the bulk phase and 19 ± 2% on the biocathode. This genus is known as acetogens for its H₂ and CO₂ fixing abilities into acetic acid (Ragsdale, 2008). Its primary function is to fix CO₂ through the Wood-Ljungdahl pathway for energy conservation and synthesize acetyl-CoA and biomass (Labelle et al., 2020). This genus played a likely role in acetic acid production in this study (*MES Experiments in a Continuous Mode Operation*). Another dominant genus *Sulfurospirillum* is microaerophilic, which means that they can scavenge small amounts of O₂ that may get transferred from the anode to the cathode chamber. Thus anaerobic conditions in the MES reactors can be maintained (Goris et al., 2014). As they can oxidize acetic acid using O₂ as the electron acceptor, the acetic acid titer may decrease slightly (Labelle et al., 2020). As there are more chances of O₂ presence in the bulk phase, its abundance is higher in the bulk phase compared to the cathode.

Desulfovibrio was one of the dominant genera in this study, with a relative abundance of 14%, 12 ± 1%, and 6 ± 2% at the inoculum source, bulk phase, and biocathode, respectively. These sulfate reducers are capable of direct electron transfer (Aulenta et al., 2012). They can also facilitate H₂ and formate production with the help of cytochromes, hydrogenases, and formate dehydrogenase (Labelle et al., 2020). These can then be utilized as an energy source by the acetogens present in the MES system. *Lentimicrobium* genus was found to be dominant in the MES reactors. In the inoculum source, its relative abundance was only 0.5%. Its relative abundance increased to 13 ± 1% and

10 ± 1% in the MES reactor bulk phase and biocathode, respectively. It is a genus of strict anaerobic bacterium previously reported in biogas upgradation studies (González-Cortés et al., 2021). It has also been reported for acetic acid production under certain conditions (Sun et al., 2016). Apart from these genera, *Pseudomonas* was also present at a low relative abundance of up to ~3.5 ± 0.5% in bulk phase and ~1.5 ± 1% in biocathode. It is known for hydrogen production via electron transfer through redox mediators as well as hydrogenase enzymes and has been reported in bioelectrochemical reactors (Mateos et al., 2019). Some other bacterial genera, namely, *Pirellula*, *Sphaerochaeta* and *Enterobacter*, were also observed in very low abundances, whose role is not very clear in MES systems.

4 CONCLUSION

This study demonstrates that efficient biogas upgradation through CO₂ conversion into acetic acid can be achieved via MES. The lower biogas feed rates performed best in terms of methane upgradation as well as acetic acid production. A considerable decrease in H₂ evolution potential and increase in reduction current suggested the role of microbes in the electrocatalysis process. *Acetobacterium* spp. and *Desulfovibrio* spp. dominated both the bulk phase as well as biocathode. The demonstrated biogas upgradation approach offers the advantage of obtaining two products in different phases: one in the bulk phase (acetic acid) and the other in the off-gas (methane). It puts us one step forward for direct utilization of MES for onsite biogas upgradation.

DATA AVAILABILITY STATEMENT

The datasets presented in this study can be found in online repositories. The names of the repository/repositories and

accession number(s) can be found below: <https://www.ncbi.nlm.nih.gov/>, PRJNA659908.

AUTHOR CONTRIBUTIONS

SAP conceived the study and MR contributed to the design of the study. MR conducted the experiments and wrote the first draft of the manuscript. SY contributed to data analysis and wrote the microbial community section of the manuscript. All authors contributed to manuscript revision, read, and approved the submitted version.

FUNDING

All authors acknowledge the financial support by the Department of Biotechnology (DBT), Government of India, through project no. BT/PR28914/BCE/8/1441/2018.

ACKNOWLEDGMENTS

The authors thank the authorities of the sewage treatment plant (Phase 3, Panchkula, Haryana) for biogas samples. MR and SY are grateful to IISER Mohali for the Ph.D. scholarship. All authors are grateful to Mr. Prathamesh Balasaheb Pol for his experimental assistance. The technical support by Dr. Vinayak Sinha and his research team in collecting the biogas samples is highly appreciated.

SUPPLEMENTARY MATERIAL

The Supplementary Material for this article can be found online at: <https://www.frontiersin.org/articles/10.3389/fenrg.2021.759678/full#supplementary-material>

REFERENCES

- Angelidaki, I., Treu, L., Tsaekos, P., Luo, G., Campanaro, S., Wenzel, H., et al. (2018). Biogas Upgrading and Utilization: Current Status and Perspectives. *Biotechnol. Adv.* 36, 452–466. doi:10.1016/j.biotechadv.2018.01.011
- Aulenta, F., Catapano, L., Snip, L., Villano, M., and Majone, M. (2012). Linking Bacterial Metabolism to Graphite Cathodes: Electrochemical Insights into the H₂-Producing Capability of *Desulfovibrio* Sp. *ChemSusChem* 5, 1080–1085. doi:10.1002/cssc.201100720
- Bajracharya, S., Ter Heijne, A., Dominguez Benetton, X., Vanbroekhoven, K., Buisman, C. J. N., Strik, D. P. B. T. B., et al. (2015). Carbon Dioxide Reduction by Mixed and Pure Cultures in Microbial Electrosynthesis Using an Assembly of Graphite Felt and Stainless Steel as a Cathode. *Bioresour. Tech.* 195, 14–24. doi:10.1016/j.biortech.2015.05.081
- Bo, T., Zhu, X., Zhang, L., Tao, Y., He, X., Li, D., et al. (2014). A New Upgraded Biogas Production Process: Coupling Microbial Electrolysis Cell and Anaerobic Digestion in Single-Chamber, Barrel-Shape Stainless Steel Reactor. *Electrochem. Commun.* 45, 67–70. doi:10.1016/j.elecom.2014.05.026
- Das, S., and Ghangrekar, M. M. (2018). Value Added Product Recovery and Carbon Dioxide Sequestration From Biogas Using Microbial Electrosynthesis. *Indian J. Exp. Biol.* 56, 470–478.
- Das, S., Chatterjee, P., and Ghangrekar, M. M. (2018). Increasing Methane Content in Biogas and Simultaneous Value Added Product Recovery Using Microbial Electrosynthesis. *Water Sci. Technol.* 77, 1293–1302. doi:10.2166/wst.2018.002
- Das, S., Das, I., and Ghangrekar, M. M. (2020). Role of Applied Potential on Microbial Electrosynthesis of Organic Compounds through Carbon Dioxide Sequestration. *J. Environ. Chem. Eng.* 8, 104028. doi:10.1016/j.jece.2020.104028
- Das, S., Das, S., and Ghangrekar, M. M. (2021). Application of TiO₂ and Rh as Cathode Catalyst to Boost the Microbial Electrosynthesis of Organic Compounds through CO₂ Sequestration. *Process Biochem.* 101, 237–246. doi:10.1016/j.procbio.2020.11.017
- Dere, A. J., Kalbande, S. R., and Khambalkar, V. P. (2017). Recent Review on Biogas Production from Different Waste. *Int. J. Curr. Microbiol. App. Sci.* 6, 3452–3457. doi:10.20546/ijcmas.2017.610.407
- Engerer, H., and Horn, M. (2010). Natural Gas Vehicles: An Option for Europe. *Energy Policy* 38, 1017–1029. doi:10.1016/j.enpol.2009.10.054
- Evans, P. N., Boyd, J. A., Leu, A. O., Woodcroft, B. J., Parks, D. H., Hugenholtz, P., et al. (2019). An Evolving View of Methane Metabolism in the Archaea. *Nat. Rev. Microbiol.* 17, 219–232. doi:10.1038/s41579-018-0136-7
- González-Cortés, J. J., Almenglo, F., Ramírez, M., and Cantero, D. (2021). Simultaneous Removal of Ammonium from Landfill Leachate and Hydrogen Sulfide from Biogas Using a Novel Two-Stage Oxidic-Anoxic System. *Sci. Total Environ.* 750, 141664. doi:10.1016/j.scitotenv.2020.141664

- Goris, T., Schubert, T., Gadkari, J., Wubet, T., Tarkka, M., Buscot, F., et al. (2014). Insights into Organohalide Respiration and the Versatile Catabolism of Sulfurospirillum Multivorans Gained from Comparative Genomics and Physiological Studies. *Environ. Microbiol.* 16, 3562–3580. doi:10.1111/1462-2920.12589
- Jiang, Y., Su, M., Zhang, Y., Zhan, G., Tao, Y., and Li, D. (2013). Bioelectrochemical Systems for Simultaneously Production of Methane and Acetate from Carbon Dioxide at Relatively High Rate. *Int. J. Hydrogen Energ.* 38, 3497–3502. doi:10.1016/j.ijhydene.2012.12.107
- Jin, X., Zhang, Y., Li, X., Zhao, N., and Angelidaki, I. (2017). Microbial Electrolytic Capture, Separation and Regeneration of CO₂ for Biogas Upgrading. *Environ. Sci. Technol.* 51, 9371–9378. doi:10.1021/acs.est.7b01574
- Jourdin, L., Freguia, S., Donose, B. C., and Keller, J. (2015a). Autotrophic Hydrogen-Producing Biofilm Growth Sustained by a Cathode as the Sole Electron and Energy Source. *Bioelectrochemistry* 102, 56–63. doi:10.1016/j.bioelechem.2014.12.001
- Jourdin, L., Grieger, T., Monetti, J., Flexer, V., Freguia, S., Lu, Y., et al. (2015b). High Acetic Acid Production Rate Obtained by Microbial Electrosynthesis from Carbon Dioxide. *Environ. Sci. Technol.* 49, 13566–13574. doi:10.1021/acs.est.5b03821
- Kadam, R., and Panwar, N. L. (2017). Recent Advancement in Biogas Enrichment and its Applications. *Renew. Sustain. Energ. Rev.* 73, 892–903. doi:10.1016/j.rser.2017.01.167
- Kokkoli, A., Zhang, Y., and Angelidaki, I. (2018). Microbial Electrochemical Separation of CO₂ for Biogas Upgrading. *Bioresour. Tech.* 247, 380–386. doi:10.1016/j.biortech.2017.09.097
- Labelle, E. V., and May, H. D. (2017). Energy Efficiency and Productivity Enhancement of Microbial Electrosynthesis of Acetate. *Front. Microbiol.* 8, 756. doi:10.3389/fmicb.2017.00756
- Labelle, E. V., Marshall, C. W., and May, H. D. (2020). Microbiome for the Electrosynthesis of Chemicals from Carbon Dioxide. *Acc. Chem. Res.* 53, 62–71. doi:10.1021/acs.accounts.9b00522
- Liu, W., Cai, W., Guo, Z., Wang, L., Yang, C., Varrone, C., et al. (2016). Microbial Electrolysis Contribution to Anaerobic Digestion of Waste Activated Sludge, Leading to Accelerated Methane Production. *Renew. Energ.* 91, 334–339. doi:10.1016/j.renene.2016.01.082
- Luo, G., and Angelidaki, I. (2012). Integrated Biogas Upgrading and Hydrogen Utilization in an Anaerobic Reactor Containing Enriched Hydrogenotrophic Methanogenic Culture. *Biotechnol. Bioeng.* 109, 2729–2736. doi:10.1002/bit.24557
- Marshall, C. W., Ross, D. E., Fichot, E. B., Norman, R. S., and May, H. D. (2012). Electrosynthesis of Commodity Chemicals by an Autotrophic Microbial Community. *Appl. Environ. Microbiol.* 78, 8412–8420. doi:10.1128/AEM.02401-12
- Mateos, R., Sotres, A., Alonso, R. M., Morán, A., and Escapa, A. (2019). Enhanced CO₂ Conversion to Acetate through Microbial Electrosynthesis (MES) by Continuous Headspace Gas Recirculation. *Energies* 12, 3297. doi:10.3390/en12173297
- Nanthagopal, K., Subbarao, R., Elango, T., Baskar, P., and Annamalai, K. (2011). Hydrogen Enriched Compressed Natural Gas (HCNG): A Futuristic Fuel for Internal Combustion Engines. *Therm. Sci.* 15 (4), 1145–1154. doi:10.2298/TSCI100730044N
- Patil, S. A., Arends, J. B. A., Vanwonterghem, I., Van Meerbergen, J., Guo, K., Tyson, G. W., et al. (2015a). Selective Enrichment Establishes a Stable Performing Community for Microbial Electrosynthesis of Acetate from CO₂. *Environ. Sci. Technol.* 49, 8833–8843. doi:10.1021/es506149d
- Patil, S. A., Gildemyn, S., Pant, D., Zengler, K., Logan, B. E., and Rabaey, K. (2015b). A Logical Data Representation Framework for Electricity-Driven Bioproduction Processes. *Biotechnol. Adv.* 33, 736–744. doi:10.1016/j.biotechadv.2015.03.002
- PrévotEAU, A., Carvajal-Arroyo, J. M., Ganigué, R., and Rabaey, K. (2020). Microbial Electrosynthesis from CO₂: Forever a Promise? *Curr. Opin. Biotechnol.* 62, 48–57. doi:10.1016/j.copbio.2019.08.014
- Ragsdale, S. W. (2008). Enzymology of the Wood-Ljungdahl Pathway of Acetogenesis. *Ann. N. Y. Acad. Sci.* 1125, 129–136. doi:10.1196/annals.1419.015
- Roy, M., Yadav, R., Chiranjeevi, P., and Patil, S. A. (2021). Direct Utilization of Industrial Carbon Dioxide with Low Impurities for Acetate Production via Microbial Electrosynthesis. *Bioresour. Tech.* 320, 124289. doi:10.1016/j.biortech.2020.124289
- Rozendal, R. A., Jeremiasse, A. W., Hamelers, H. V. M., and Buisman, C. J. N. (2008). Hydrogen Production with a Microbial Biocathode. *Environ. Sci. Technol.* 42, 629–634. doi:10.1021/es071720+
- Sahota, S., Shah, G., Ghosh, P., Kapoor, R., Sengupta, S., Singh, P., et al. (2018). Review of Trends in Biogas Upgradation Technologies and Future Perspectives. *Bioresour. Tech. Rep.* 1, 79–88. doi:10.1016/j.biteb.2018.01.002
- Schröder, U., Harnisch, F., and Angenent, L. T. (2015). Microbial Electrochemistry and Technology: Terminology and Classification. *Energy Environ. Sci.* 8, 513–519. doi:10.1039/c4ee03359k
- Shravan, J. S., Sarkar, O., and Mohan, S. V. (2020). Electron-regulated Flux towards Biogas Upgradation - Triggering Catabolism for an Augmented Methanogenic Activity. *Sustain. Energ. Fuels* 4, 700–712. doi:10.1039/c9se00604d
- Sun, L., Toyonaga, M., Ohashi, A., Tourlousse, D. M., Matsuura, N., Meng, X.-Y., et al. (2016). Lentimicrobium Saccharophilum Gen. nov., Sp. nov., a Strictly Anaerobic Bacterium Representing a New Family in the Phylum Bacteroidetes, and Proposal of Lentimicrobiaceae Fam. Nov. *Int. J. Syst. Evol. Microbiol.* 66, 2635–2642. doi:10.1099/ijsem.0.001103
- Thiruselvi, D., Kumar, P. S., Kumar, M. A., Lay, C.-H., Aathika, S., Mani, Y., et al. (2021). A Critical Review on Global Trends in Biogas Scenario with its Upgradation Techniques for Fuel Cell and Future Perspectives. *Int. J. Hydrogen Energ.* 46, 16734–16750. doi:10.1016/j.ijhydene.2020.10.023
- Wang, H., Du, H., Zeng, S., Pan, X., Cheng, H., Liu, L., et al. (2021). Explore the Difference between the Single-Chamber and Dual-Chamber Microbial Electrosynthesis for Biogas Production Performance. *Bioelectrochemistry* 138, 107726. doi:10.1016/j.bioelechem.2020.107726
- Weiland, P. (2010). Biogas Production: Current State and Perspectives. *Appl. Microbiol. Biotechnol.* 85, 849–860. doi:10.1007/s00253-009-2246-7

Conflict of Interest: The authors declare that the research was conducted in the absence of any commercial or financial relationships that could be construed as a potential conflict of interest.

Publisher's Note: All claims expressed in this article are solely those of the authors and do not necessarily represent those of their affiliated organizations, or those of the publisher, the editors and the reviewers. Any product that may be evaluated in this article, or claim that may be made by its manufacturer, is not guaranteed or endorsed by the publisher.

Copyright © 2021 Roy, Yadav and Patil. This is an open-access article distributed under the terms of the Creative Commons Attribution License (CC BY). The use, distribution or reproduction in other forums is permitted, provided the original author(s) and the copyright owner(s) are credited and that the original publication in this journal is cited, in accordance with accepted academic practice. No use, distribution or reproduction is permitted which does not comply with these terms.



Temperature-Dependent Crystallization Mechanisms of Methylammonium Lead Iodide Perovskite From Different Solvents

Oleksandra Shargaieva¹, Hampus Näsström^{1,2}, Jinzhao Li¹, Daniel M. Többsen² and Eva L. Unger^{1,3*}

¹Group of Hybrid Materials Formation and Scaling, Helmholtz-Zentrum Berlin für Materialien und Energie GmbH, Berlin, Germany, ²Department of Structure and Dynamics of Energy Materials, Helmholtz-Zentrum Berlin für Materialien und Energie GmbH, Berlin, Germany, ³Department of Chemical Physics and Nano Lund, Lund University, Lund, Sweden

OPEN ACCESS

Edited by:

Michael Folsom Toney,
University of Colorado Boulder,
United States

Reviewed by:

Maged Abdelsamie,
Lawrence Berkeley National
Laboratory, United States
Chris McNeill,
Monash University, Australia

*Correspondence:

Eva L. Unger
eva.unger@helmholtz-berlin.de

Specialty section:

This article was submitted to
Solar Energy,
a section of the journal
Frontiers in Energy Research

Received: 29 July 2021

Accepted: 25 October 2021

Published: 23 November 2021

Citation:

Shargaieva O, Näsström H, Li J,
Többsen DM and Unger EL (2021)
Temperature-Dependent
Crystallization Mechanisms of
Methylammonium Lead Iodide
Perovskite From Different Solvents.
Front. Energy Res. 9:749604.
doi: 10.3389/fenrg.2021.749604

Hybrid perovskites are a novel type of semiconductors that show great potential for solution-processed optoelectronic devices. For all applications, the device performance is determined by the quality of the solution-processed perovskite thin films. During solution processing, the interaction of solvent with precursor molecules often leads to the formation of solvate intermediate phases that may diverge the crystallization pathway from simple solvent evaporation to a multi-step formation process. We here investigate the crystallization of methylammonium lead iodide (MAPbI₃) from a range of commonly utilized solvents, namely dimethyl sulfoxide (DMSO), N,N-dimethylformamide (DMF), N-methylpyrrolidone (NMP), and gamma-butyrolactone (GBL) at different temperatures ranging from 40°C to >100°C by *in-situ* grazing-incidence wide-angle X-ray scattering (GIWAXS) measurements. For all solvents but GBL, we clearly observe the formation of solvate-intermediate phases at moderate processing temperatures. With increasing temperatures, an increasing fraction of the MAPbI₃ perovskite phase is observed to form directly. From the temperature-dependence of the phase-formation and phase-decomposition rates, the activation energy to form the MAPbI₃ perovskite phase from the solvate-phases are determined as a quantitative metric for the binding strength of the solvent within the solvate-intermediate phases and we observe a trend of DMSO > DMF > NMP > GBL. These results enable prediction of processing temperatures at which solvent molecules can be effectively removed.

Keywords: hybrid perovskites, *in-situ* GIWAXS, temperature-dependent crystallization, solvate intermediate phase, activation energy

INTRODUCTION

Hybrid perovskites have recently become a promising choice of semiconductor material for a variety of optoelectronic applications. Hybrid perovskites offer excellent optoelectronic properties such as high absorption coefficient, long diffusion length, and bandgaps in the visible range of the solar spectrum (Wolf et al., 2014; Dong et al., 2015; Rehman et al., 2017). High-quality thin films of hybrid perovskites can be deposited from precursor solutions followed by annealing at temperatures as low as 50°C (Fu et al., 2015; Xu et al., 2015; Arain et al., 2019). The improvement of the crystalline

properties of the materials and, as a result, their optoelectronic quality is often achieved by optimization of precursor solution composition and deposition procedures (Jeon et al., 2017; Haque et al., 2020).

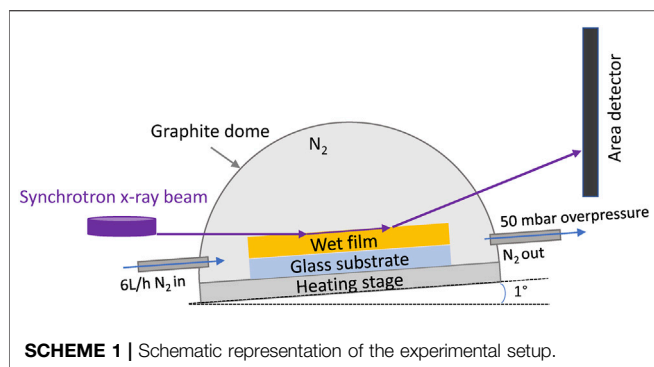
Optimization of precursor solution is often realized by employing solvent mixtures that allow to manipulate nucleation kinetics and chemical pathways leading to the perovskite formation (Singh et al., 2017; Arain et al., 2019). To date, however, the choice of solvents is often based on empirical evidence of quality enhancement of obtained thin films or devices. Early research on precursor solutions of these materials showed that the crystallization of thin films is affected by an interaction between lead halide perovskite precursors and solvent molecules in a precursor solution (Hamill et al., 2018). In solution, this interaction leads to the formation of complexes that may act as “building blocks” for the formation of amorphous and crystalline solvate phases upon drying (Guo et al., 2016; Li et al., 2019; Valencia et al., 2020). In recent years, the application of different crystallization monitoring techniques revealed that not all solvents form intermediate phases with the perovskite precursors (Ortoll-Bloch et al., 2020). In fact, the usage of weakly coordinating solvents has been employed to avoid the formation of solvate-intermediate phases completely. In particular, layers deposited from gamma-butyrolactone (GBL), 2-methoxy ethanol (2-ME), acetonitrile (ACN), and tetrahydrofuran (THF) as solvents and co-solvents showed the direct formation of perovskite phase with enhanced optoelectronic quality (Deng et al., 2019). In contrast, it has been demonstrated that the formation of certain crystalline intermediate phases or the presence of strongly coordinating solvents is beneficial for the formation of the perovskite phase as it acts as a template or induces nucleation (Seo et al., 2017; Li et al., 2021). Interestingly, precursor solutions containing strongly coordinating solvents such as dimethyl sulfoxide (DMSO) and dimethylformamide (DMF) are still among the most commonly used. This indicates that the correlation between solvent coordination strength and quality of resulting materials is not apparent. Moreover, the choice of the solvent mixture is often dictated by the choice of the deposition technique and availability of methods for controlling nucleation and crystallization of materials.

Different strategies have been employed to ensure an efficient solvent removal and transformation of the precursor-solvent complexes or intermediate phases into semiconducting perovskite material. To date, vacuum, gas quenching, anti-solvent quenching, and annealing are the most commonly used methods for inducing crystallization and aiding solvent removal (Jeon et al., 2014; Li et al., 2016; Zhang et al., 2017). Among those, annealing is one of the most versatile methods for material crystallization as it is simple in use and allows easy scaling. Several reports have indicated that applying an annealing procedure, that is optimized for the material and processing conditions, allows to control not only material nucleation but also the transformation from solvate phase into perovskite. This is of particular importance when strongly coordinating solvents are used. In this case, removal of solvent molecules from intermediate phases determines the transformation of the intermediate phase

into perovskite and, as a result, the quality of materials (Tan et al., 2019; Lin et al., 2021). It has been suggested previously that prolonged annealing of >60 min at 100°C is required for complete solvent removal for high-quality materials (Saliba et al., 2018). However, similarly to solution optimization, optimization of annealing procedures is mostly done by assessment of the optoelectronic quality of the resulting materials. Therefore, an in-depth understanding of interactions of solvent and precursor in solution, as well as in solvate intermediate phases, is required for multiparameter optimization of material deposition from various solvents.

It is important to note that the exact mechanism of the perovskite formation from the various different solvate-intermediate phases is not yet understood, however, it is plausible that the ease of the transformation depends on the strength of the chemical interaction between solvent and precursor, stability of the intermediate phase, and evaporation rate of the solvent. Therefore, identifying the parameters influencing the material's transformation from solvate intermediate phase to perovskite phase is an important step for rationalizing this process and developing strategies for the preparation of high-quality materials.

In this work, we investigate the crystallization of methylammonium lead iodide (MAPbI₃) hybrid perovskites from commonly-used solvents with different physical and chemical properties as a function of temperature. The MAPbI₃ hybrid perovskite was chosen as a test material because 1) the coordination of solvents mostly occurs via an interaction with Pb²⁺ and 2) PbI₂ as the main component of other more complex perovskite compositions is responsible for the formation of solvate intermediate phases. The evolution of crystalline solvate intermediate and perovskite phases during drying of blade-coated MAPbI₃ hybrid perovskite films was monitored by synchrotron-based grazing-incidence wide-angle x-ray scattering technique. The crystallization process was studied in a range of processing temperatures between 40 and 100°C. Our findings indicate that at processing temperatures below 75°C, the formation of the MAPbI₃ phase from strongly coordinating solvents (dimethyl sulfoxide, dimethylformamide, n-methyl pyrrolidone) occurs dominantly via decomposition of the solvate intermediate phases. At temperatures above 75°C, the formation of perovskite and decomposition of intermediate phases can occur simultaneously. From Arrhenius plots of the formation and decomposition rate of the solvate intermediate phases as well as the formation of the MAPbI₃ perovskite phase, we determined the respective activation energies for the formation and transformation of MAPbI₃ from the different solvent systems. We observe that the activation energy for solvent removal from the solvate-intermediate phase correlates with the predicted coordination strength of solvent molecules to Pb in solution complexes. Our findings present the fundamental understanding of processes occurring during the formation of MAPbI₃ hybrid perovskites. However, the correlations found in this work can be applied to the other more complex perovskite compositions and solvents. These results indicate an important aspect for the optimization of processing conditions for temperature-controlled hybrid perovskites deposition methods.



MATERIALS AND METHODS

For the temperature-dependent study of perovskite phase formation, 1 mol/L precursor solutions of MAPbI₃ were used.

The solutions contained equimolar amounts of CH₃NH₃I and PbI₂ dissolved in anhydrous dimethyl sulfoxide (DMSO), dimethylformamide (DMF), N-methyl pyrrolidone (NMP), and gamma-butyrolactone (GBL). As-purchased GBL was kept over molecular sieves for 48 h before use. The solutions were prepared in an N₂-filled glovebox, heated for 12 h at 60°C, and cooled down to room temperature before use. Grazing-incidence wide-angle x-ray scattering (GIWAXS) technique was chosen for *in-situ* monitoring of the formation of the intermediate phase and its transformation into the perovskite phase. The synchrotron-based GIWAXS technique allows a simple differentiation between different crystalline phases and fast acquisition times. For *in-situ* grazing-incidence wide-angle x-ray scattering (GIWAXS), 5 μl of the precursor solutions were deposited using manual blade-coating onto a 25 × 25 mm soda-lime glass substrate placed on an Anton Paar heating stage at *T* = 28°C in 6 L/h N₂ flow. The wet film thickness amounted to about 8 μm for all samples resulting in about 1 μm thin films.

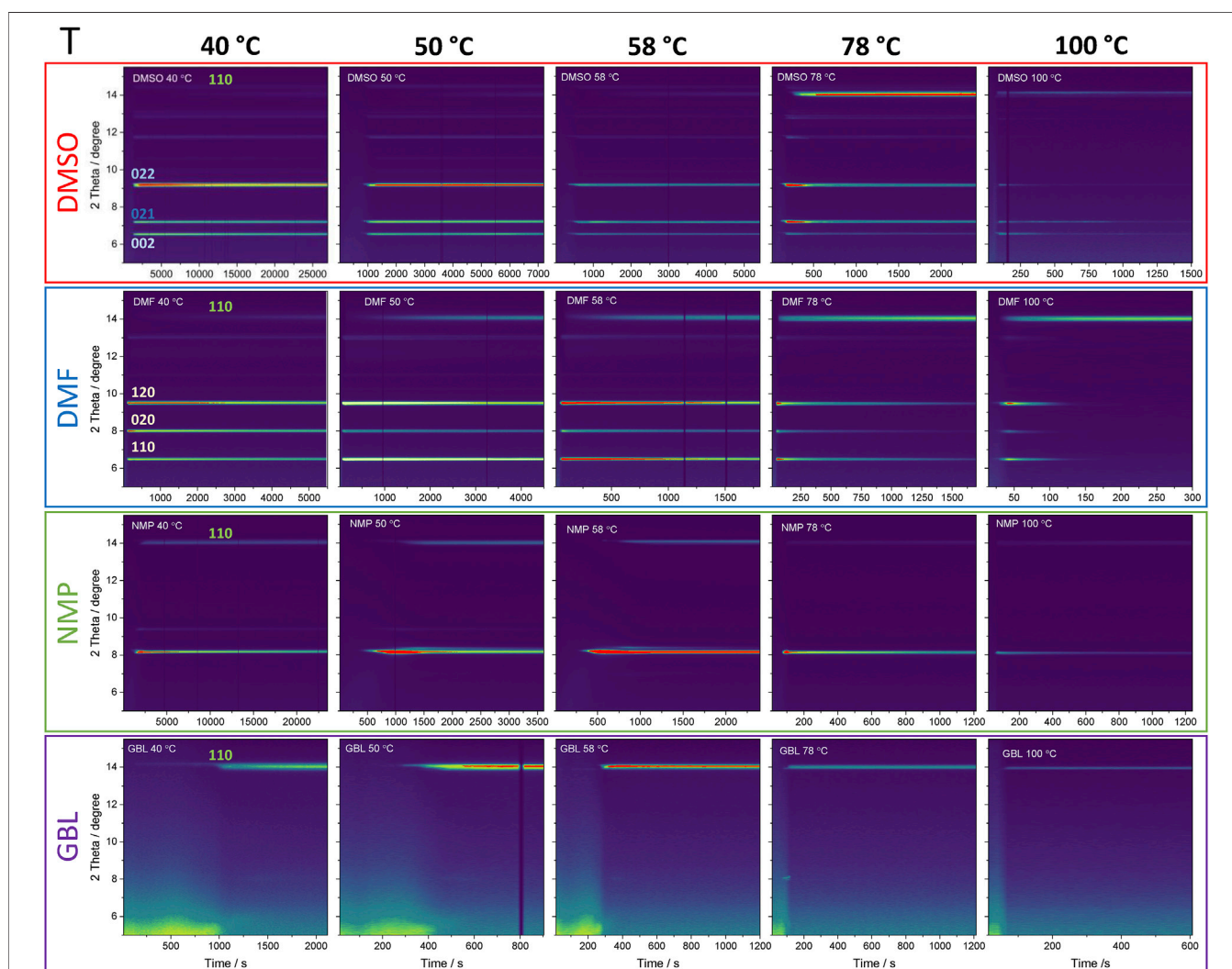


FIGURE 1 | 2D contour plots of the azimuthally integrated GIWAXS detector frames obtained as a function of time during crystallization of MAPbI₃ from DMSO, DMF, NMP, GBL at 40, 50, 58, 78, and 100°C. Wavelength 1.5406 Å is equivalent to Cu K_{α1}.

Next, a graphite dome was attached to the heating stage over the sample. The stage was connected to a dry nitrogen bottle with 6 L/h flow of N_2 and a 50 mbar overpressure valve on the outlet of the stage as shown in **Scheme 1**.

Data collection was done at the KMC-2 DIFFRACTION beamline at the BESSY II synchrotron (Többsen and Zander, 2016), using radiation energy of 8,048 eV ($\lambda = 1.5406 \text{ \AA}$, equivalent to Cu $K\alpha_1$) with flux, $f = 10^{11}$ photon/s/mm². GIWAXS geometry with incidence angle at the sample of 1° and a Valencia et al., 2000 area detector in fixed position covering an angular range from 4.8 to $15.7^\circ 2\theta$ was used for collecting diffraction frame every 14.2 s. The first frame was acquired 60 s after the liquid was dispensed at room temperature. The wet films were heated to the set processing temperature with a 50 K/min rate. The detector image acquisition started prior to the heating of the stage. The data obtained in the isothermal regime was used for the analysis. A new sample was used for each processing temperature regime. To obtain diffraction patterns, the 2D detector images were azimuthally integrated using in-house developed software.

RESULTS AND DISCUSSION

In-situ GIWAXS on MAPbI₃ Precursor Solutions at Different Annealing Temperatures

Figure 1 shows 2D contour plots of the evolution of azimuthally integrated GIWAXS patterns of MAPbI₃ thin-films processed at 40, 50, 58, 78, and 100°C as a function of time. The wet films deposited from solutions of MAPbI₃ in commonly-used organic solvents (DMSO, DMF, NMP, GBL) were investigated. These four solvents exhibit different coordination strengths to lead (DMSO > DMF > NMP > GBL) and evaporation rates (DMF > GBL > NMP > DMSO) (Stevenson et al., 2017; Hamill et al., 2018; Shargaieva et al., 2020).

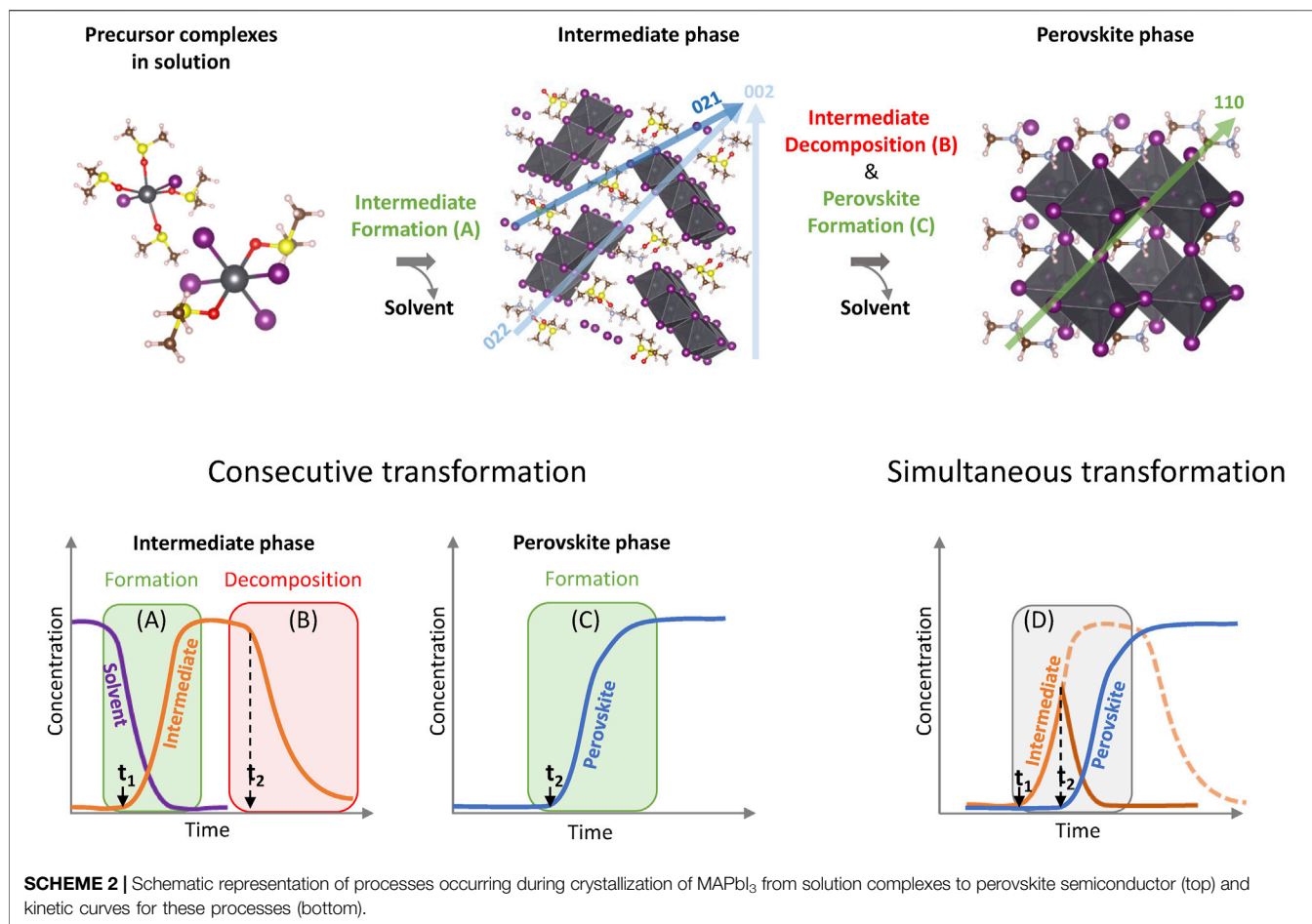
In all solvents, significant differences were observed in terms of the structure of solvate intermediate phases as well as the onset of crystallization and transformation kinetics to MAPbI₃. The crystallization of MAPbI₃ from DMSO occurred via the solvate intermediate phase with diffraction peaks at 6.59 , 7.22 , $9.16^\circ 2\theta$ that have been previously assigned to a phase often referred to as MAPbI₃-DMSO with the stoichiometric formula $MA_2Pb_3I_8(DMSO)_2$ adopting orthorhombic crystal structure with the *Pbc21* space group previously reported by Cao et al. (2016). The individual diffraction pattern of the intermediate phase is shown in **Supplementary Figure S2B** and corresponding 2D detector images are shown in **Supplementary Figure S11**. The onset of crystallization of the solvate intermediate phase showed a strong dependence on the process temperature. At 40°C the onset of crystallization of $MA_2Pb_3I_8(DMSO)_2$ is observed after about 1,300 s, while a low-intensity perovskite phase, indicated by the peak at $14.1^\circ 2\theta$ is observed only after about 7,000 s. An increase of the temperature of annealing to 50°C dramatically accelerated the formation of the solvate-intermediate phase as well as transformation to the perovskite

phase with onsets at 800 s and 3,000 s, respectively. Further increase of annealing temperature decreased the time difference between the crystallization of solvate intermediate phase and its transformation to perovskite phase. Annealing at 100°C led to the simultaneous evolution of both solvate-intermediate and perovskite diffraction peaks indicating the competitive formation of both phases.

The crystallization of MAPbI₃ from DMF also occurred via a solvate-intermediate phase, exhibiting diffraction peaks at 6.5 , 8.0 , and $9.5^\circ 2\theta$ that were previously attributed to a solvate intermediate phase with the stoichiometric formula $MA_2Pb_3I_8(DMF)_2$ adopting orthorhombic crystal structure with the *Pnmm* space group first reported by Petrov et al. (2017). The individual diffraction pattern is shown in **Supplementary Figure S2A**, the corresponding 2D detector images are shown in **Supplementary Figure S11**. Similarly to the crystallization from DMSO solutions, an increase in the processing temperature accelerated the crystallization and formation of both the solvate-intermediate and perovskite phases. At temperatures $T \geq 78^\circ\text{C}$, the simultaneous formation of the perovskite phase and the solvate-intermediate phase is apparent. Compared to the DMSO precursor solution, the formation of MAPbI₃ from DMF solutions via the DMF-solvate phase follows faster kinetics.

Crystallization of MAPbI₃ from NMP-based solutions also occurs via an intermediate phase with diffraction peaks at 8.2 and $9.4^\circ 2\theta$. The position of the individual peaks is indicated in **Supplementary Figure S2C** and corresponding 2D detector images are shown in **Supplementary Figure S12**. The diffraction peaks were previously associated with PbI₂-NMP intermediate but its structure and stoichiometry have not yet been identified (Jo et al., 2016; Li et al., 2019; Ortoll-Bloch et al., 2020). Interestingly, the film crystallized from NMP at a processing temperature of 100°C still exhibited the presence of intermediate phase even after 1,200 s and only processing at 120°C allowed the formation of the perovskite phase without the formation of intermediate phase (see **Supplementary Figure S1**).

Processing of MAPbI₃ from GBL solutions exhibits the presence of an amorphous sol-gel solvate phase with a characteristic broad signal at low diffraction angles ($2\theta < 6$) during the early stages of drying (Lee et al., 2020). Further solvent removal led to the crystallization of wet film directly to the perovskite phase with only a small amount of a crystalline solvate-intermediate phase indicated by a low-intensity diffraction peak at $8.1^\circ 2\theta$. The position of the individual peaks is indicated in **Supplementary Figure S2D**. The corresponding 2D detector images are shown in **Supplementary Figure S12**. In a previous report, we show that an intermediate phase with similar lattice spacings as the DMF solvate phase ($MA_2Pb_3I_8(DMF)_2$) is formed also in GBL (Shargaieva et al., 2020). It was found that the GBL solvate-intermediate phase is highly sensitive to the presence of water in the precursor solution (Shargaieva et al., 2020). Therefore, the low-intensity peak of the intermediate phase from GBL might indicate the suppression of the solvate phase formation due to the presence of water. This behavior is consistent with other reports



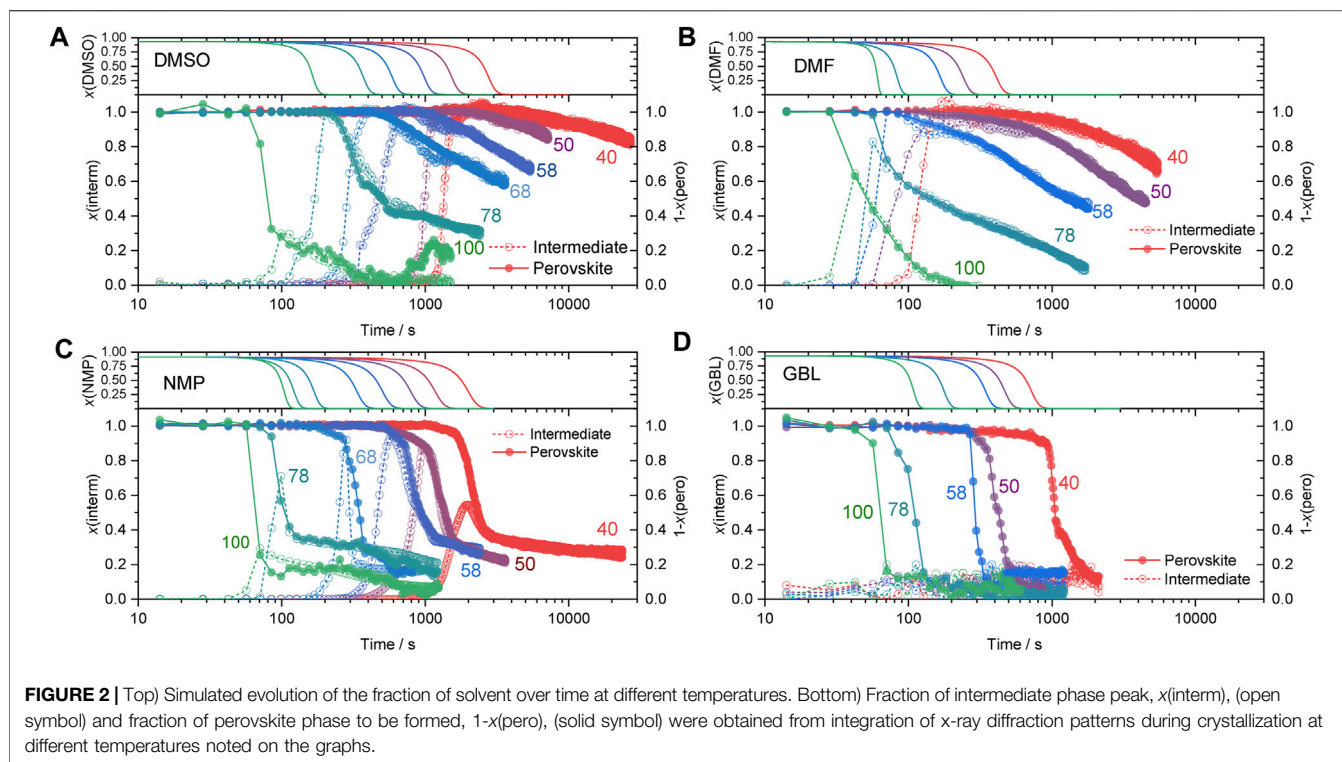
where crystallization of MAPbI₃ from GBL has been observed only through the direct formation of the perovskite phase (Ma et al., 2019).

For all precursor solutions studied, the increase of temperature facilitates the removal of solvent molecules. Solvent evaporation leads, for most cases, to the crystallization of solvate-intermediate phases indicating that these are thermodynamically more favored compared to the MAPbI₃ phase. Therefore, it is plausible that the decomposition of the intermediate phase through solvent removal is required for the formation of the perovskite phase. At higher processing temperatures, however, the formation of solvate-intermediate phases can be suppressed and the crystallization occurs through the perovskite phase likely as the kinetics of solvent removal outcompetes the formation of the solvate-intermediate phases.

Schematic Model of Competitive Formation Processes and Phase Formation Kinetics

In order to analyze the evolution of the intermediate and MAPbI₃ perovskite phases as a function of time, we distinguish the different processes occurring during perovskite crystallization

as schematically shown in **Scheme 2** with structures of complexes and intermediate phases of MAPbI₃ in DMSO used as an example. The crystallization from other solvents occurs via different intermediate phases, however, the generalized approach for the description of processes should be applicable for most solvent systems. The first process corresponds to the increase of concentration of complexes in the solution due to solvent evaporation. This results in the precipitation of the intermediate phase from the solution at a moment of time t_1 as shown in **Scheme 2A**. In our experiments, only a product of the reaction—crystalline intermediate phase—can be detected due to the nature of the measurement technique. During the second process, the formed intermediate phase undergoes decomposition due to further solvent removal which can be observed as a decrease of the peak intensity at the moment of time t_2 indicating a decrease of the amount of the phase as depicted in **Scheme 2B**. At the same time, the intermediate phase acts as a reagent for the formation of the perovskite phase as shown in **Scheme 2C**. In this case, the removal of the solvent from the intermediate phase should occur at the same rate as the formation of the perovskite phase assuming that process 1 has completely finished. However, it is possible that reconstruction of the intermediate phase into perovskite may involve a multistep



process or the formation of a transition phase that due to its distorted or amorphous nature cannot be detected by diffraction-based methods. Additionally, it is plausible that the evolution of the signal intensities of the intermediate phase is affected by simultaneous processes a, b, and c. In the case of simultaneous processes, when t_2 is approaching t_1 (Scheme 2D), the intermediate phase concentration does not reach its maximum value as it is consumed at the same time as it forms. At higher processing temperatures, the perovskite phase may also form directly from the solution-precursor due to fast solvent removal. Therefore, the experimental kinetic traces discussed below may deviate from idealized representation as shown in Scheme 2.

Kinetics of Crystallization at Different Temperatures

To assess the relationship between intermediate and perovskite phases, the rate of the intermediate phase decomposition and MAPbI₃ phase formation need to be compared. In Figure 2, we compare the evolution of intermediate and MAPbI₃ perovskite phases from different solvents as a function of time and processing temperature. The kinetic traces were derived by integration of the characteristic diffraction peaks of the intermediate ($A(\text{interm})$) and perovskite ($A(\text{pero})$) phases as a function of time. The full data sets are shown in Supplementary Figures S3–6. We chose to perform the analysis only on one diffraction peak for each intermediate phase. These were the peaks at 7.22, 6.5, 8.2, and 8.1° for the films deposited from DMSO, DMF, NMP, and GBL, respectively. Additionally, the

analysis on three different crystallographic directions (110, 020, and 120) of the (MA)₂Pb₃I₈ (DMF)₂ phase at 6.5, 8.0, 9.5° 2θ was performed for comparison indicating similar kinetics as shown in Supplementary Figure S7.

Important to note is that the diffraction peak intensity depends on a variety of parameters such as the grain size, shape, orientation, and scattering factors, which are not directly related to the amount of a crystalline phase. To define an analytical expression for the degree of transformation, the peak area was normalized by a predicted peak area corresponding to its maximum value (A_{max}). This way, the normalized peak intensity corresponds to a fraction of the converted material (x) and, therefore, can be compared across different processing temperatures. To obtain the maximum value of the peak area, A_{max} , the experimental curves in the data range corresponding to the formation of intermediate and perovskite phases were fitted with Johnson–Mehl–Avrami–Kolmogorov (JMAK) model (Avrami, 1939; Fanfoni and Tomellini, 1998) expressed as the following equation:

$$A = A_{\text{max}} (1 - \exp(-(k(t - t_0)^n))), \quad (1)$$

where A is peak area, A_{max} is maximum peak area corresponding to full conversion, t -time, t_0 -the onset of the process similar to t_1 and t_2 in Scheme 2, k -reaction rate constant, n -reaction order. The JMAK model (Eq. 1) is largely applied for the calculation of solid phase transformations, however, in recent reports, it has been successfully applied for the investigation of perovskite crystallization kinetics from *in-situ* XRD patterns (Moore et al., 2015; Pool et al., 2017; Suchan et al., 2020). The

obtained values of A_{max} are summarized in **Supplementary Table S1**. The normalized peak areas (A/A_{max}) of the intermediate phases ($x(\text{interm})$) of different solvents at different processing temperatures are shown in **Figure 2** as open symbols.

To allow direct visual comparison of the decomposition of the solvate-intermediate phase and formation of the MAPbI₃ perovskite phase, the normalized peak intensity of the MAPbI₃ phase formation was plotted as $1-x(\text{pero})$ corresponding to the amount of perovskite phase to be formed (**Figure 2** solid symbols). If the perovskite phase is mainly formed via decomposition of the intermediate phase, the relation between the respective amount of these crystalline phases can be expressed as $x(\text{interm}) = 1-x(\text{pero})$.

The kinetic traces in **Figure 2** clearly show a strong dependence of the onset of crystallization of the solvate-intermediate phases on the processing temperature across all studied solvents. To estimate the correlation between the onset of solvate phase crystallization and the concentration of the precursor solution, the evaporation rate of solvents was estimated based on the previously described evaporation model (Shargaieva et al., 2020). The model describes the evaporation of non-coordinated solvent molecules and, therefore, accounts solely for the physical properties of solvents. The onset of crystallization was determined as the moment of the appearance of diffraction peaks of crystalline phases.

The onset of crystallization at different temperatures often correlates with the range of a dramatic change of solvent fraction. The fraction of solvent at the moment of crystallization is increasing with the increase of the processing temperature as shown in **Supplementary Figure S10**. This indicates that at lower processing temperatures (e.g., RT - 50°C) solutions can reach supersaturation due to slow solvent evaporation leading to a higher concentration than the solubility limit. The estimated amount of solvent at the onset of crystallization is summarized in **Supplementary Table S5**. At higher processing temperatures (e.g., 100°C), when the evaporation rate of solvent is higher than solvent diffusion, spontaneous nucleation can occur locally even when large total amounts of solvent are still present. In addition, we observe that at higher processing temperatures the formation of the MAPbI₃ perovskite phase competes with the formation of solvate-intermediate phases. This is likely because, at higher solvent evaporation rates, the concentration of solvent molecules decreases dramatically preventing their incorporation into the intermediate crystal structure and, thus, leading to the direct formation of the perovskite phase.

In the solvate-intermediate phase, solvent molecules are incorporated into the crystal lattice. Hence, their removal depends on the binding strength of the solvent within the crystalline matrix rather than the evaporation rate of non-bound solvent molecules. The strength of solvent coordination within the crystalline intermediate phases can be estimated from the transformation kinetics of the solvate to the MAPbI₃ phase. At low temperatures (40, 50°C) the kinetic curves of the DMSO and DMF intermediate phases (**Figures 2A,B**) reached a plateau indicating that the majority of deposited material formed the crystalline intermediate phase. At higher temperatures, the curves

never reach the plateau and quickly transition into the decomposition regime indicating simultaneous formation and decomposition, as well as the direct formation of MAPbI₃, as illustrated in **Scheme 2D**. For the DMF and DMSO precursor solutions crystallizing at low temperature, the decomposition of the solvate phase and formation of the perovskite phase correlate, as clearly visible from the comparison of $x(\text{interm})$ and $(1-x(\text{pero}))$ in **Figure 2**. This correlation indicates a direct transformation from the solvate to the perovskite phase. Small deviations observed in the $x(\text{interm})$ in the early stages of decomposition likely occur due to a rapid decrease of crystalline size upon removal of solvent.

Crystallization of MAPbI₃ from the NMP precursor solutions exhibits two different regimes of crystallization. In the first regime, a rapid decrease in the amount of the intermediate phase is observed. In the second regime, a much slower transformation rate of the intermediate phase into the perovskite phase is observed. This behavior can be interpreted as a fast nucleation step preceding a second crystal growth or ripening step. This observation suggests that perovskite formation from NMP occurs via a different mechanism than from DMSO, DMF, and GBL. This difference in the transformation behavior is probably related to the differences in the nature of the solvate intermediate phases. While DMSO and DMF have been suggested to form solvate phases incorporating both solvent and MA molecules, NMP has been suggested to form a solvate phase only incorporating the lead iodide precursors, PbI₂-NMP, as previously suggested by Jo et al. (2016). In this case, the MA cation would likely be bound in another, secondary, phase and becomes incorporated only during the transformation step.

Interestingly, different behavior can be observed during the formation of GBL-based wet thin films. Solvent removal led to the crystallization of the materials directly to the perovskite phase following fast formation kinetics. The intermediate phase was formed after the majority of the material has crystallized.

Activation Energy of Phase Transformations

From the temperature dependence of the transformation from solvate intermediate to MAPbI₃ perovskite phase, the activation energies for the formation of the solvate phases as well as solvent removal from the solvate phase can be estimated. The reaction rate constants, k , can be obtained from the JMAK fits of the experimental data similarly as it was done for the determination of A_{max} . In addition to the reaction rate constant, the kinetic curve is also defined by the n parameter. The parameter n , according to JMAK theory, describes the mechanism of the crystallization process in terms of dimensionality of the formed nuclei. Therefore, to compare values of k of different experiments, first, we estimate a common value of n for the kinetic curves obtained for the same solvent within the same process. Estimation of n values was done by plotting the kinetic curves in Sharp-Hancock coordinates $\ln(\ln(1-x))$ vs. $\ln(t-t_0)$. The values of n were determined from the slope of a linear fit of the data in Sharp-Hancock coordinates and rounded to the nearest integer. The Sharp-Hancock fits of the data are shown in **Supplementary Figure S8**. The detailed methodology, as well as the summary of

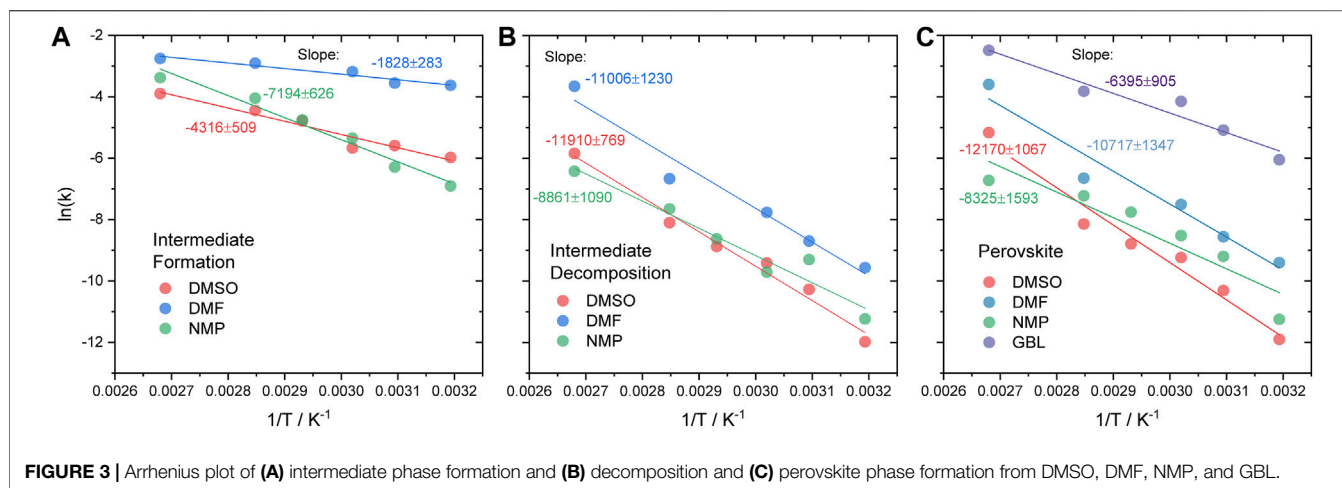


TABLE 1 | Calculated activation energies for the formation ($E_{a(\text{interm. form})}$) and decomposition ($E_{a(\text{interm. decomp})}$) of intermediate phases and formation of perovskite phases ($E_{a(\text{perov. form})}$).

Solvent	$E_{a(\text{interm. form})}/\text{kJ/mol}$	$E_{a(\text{interm. decomp})}/\text{kJ/mol}$	$E_{a(\text{perov. form})}/\text{kJ/mol}$
DMSO	35.9 ± 4	99.1 ± 6	101.2 ± 1
DMF	15.2 ± 2	91.5 ± 10	89.1 ± 1
NMP	59.8 ± 5	73.7 ± 9	69.2 ± 1
GBL	n/a	n/a	53.2 ± 1

the fitting parameters, are shown in Supplementary Information and Supplementary Table S2.

Using the Sharp-Hancock method, analysis was conducted for the intermediate phase formation range of the data. Estimated values of n were $n = 3$ for DMSO, $n = 2$ for DMF, and $n = 3$ for NMP. According to the JMAK model, the values of n of the intermediate phase formation indicate that crystallization in DMSO and NMP occurs via formation and growth of 2D platelets, while in DMF—1D rods assuming sporadic nucleation. The values of $n = 1$ obtained for the perovskite formation from DMF, DMSO, and NMP indicate that the process of the intermediate phase decomposition and perovskite phase formation is limited by the diffusion of the species. In GBL, the formation of the perovskite phase precedes the formation of the intermediate phase and, thus, corresponds to the nucleating species. Therefore, the process in GBL can be described by 1D crystallization of rods assuming sporadic nucleation. Using obtained n values, the experimental data was fitted with the JMAK model described in Eq. 1. The data range corresponding to the decomposition of the intermediate phase was fitted with a modified JMAK-equation for the description of the decomposition process:

$$A = A_{\max}(\exp((-k(t - t_2)^n))), \quad (2)$$

Fitting the intermediate phase decomposition and perovskite phase formation was done in the overlapping range of the data corresponding to the formation of perovskite from the solvate intermediate phase. The fitted curves and the summary of fitting

parameters are shown in Supplementary Figure S9 and Supplementary Table S3. The obtained values of the reaction rate constant, k , were used for calculation of the activation energy required for the formation of perovskite phase from intermediate phase using the Arrhenius equation:

$$k = Ie^{-E_a/RT}, \quad (3)$$

where k is the reaction rate constant, I is the interaction factor, E_a is the activation energy, R is gas constant, and T is temperature. Important to note that the prediction of the reaction rates with the JMAK model assumes homogeneous nucleation and is sensitive to the number of growing nuclei and their volume fraction. Thus, the model will likely deviate from the experiment when nucleation occurs via only a few growing nuclei (Todinov, 2000).

From the Arrhenius equation, activation energy can be obtained from the slope, $-E_a/R$, of the linear fit of the dependencies of the reaction rate constant on the temperature in Arrhenius coordinates. The fits obtained for the decomposition of the intermediate phase and formation of the perovskite phase from DMF, DMSO, NMP, and GBL are shown in Figures 3B,C. The obtained values of the activation energy are noted in Table 1, fitting parameters are shown in Supplementary Table S4. The same approach was applied for the calculation of the activation energy of the intermediate phase formation in DMSO, DMF, and NMP. The fitted values of k are shown in Figure 3A. The activation energies of the formation of the intermediate phase, $E_{a(\text{interm. form})}$, decomposition of the solvate intermediate phase,

$E_{a(\text{interm. decomp})}$ and formation of the MAPbI₃ perovskite phase, $E_{a(\text{pero form})}$ are summarized in **Table 1**.

As the solvate phase formation is dependent on reaching the respective critical concentration, the activation energy should reflect the thermal energy needed to facilitate solvent evaporation. As evident from **Table 1**, $E_{a(\text{interm form})}(\text{DMF}) < E_{a(\text{interm form})}(\text{DMSO}) < E_{a(\text{interm form})}(\text{NMP})$. This trend indicates that both the physical properties of the solvent and their coordination ability influence the activation energy of intermediate phase crystallization. In particular, the high evaporation rate of DMF likely aids its removal from the film and promotes nucleation. Additionally, the high coordination ability of DMF likely stimulates the formation of the intermediate phase through coordination to precursor, thus, lowering the activation energy required for the formation of the intermediate phase. Similarly, DMSO exhibits low activation energy for the formation of the intermediate phase compared to NMP. This lower $E_{a(\text{interm form})}$ can be rationalized with the stronger coordination of DMSO molecules to the precursor in solution. However, despite higher coordination strength $E_{a(\text{interm form})}$ of DMSO is higher than that of DMF possibly due to substantially lower solvent evaporation rate. This trend is in good agreement with the calculated enthalpy of formation of the intermediate phase with DMSO and DMF reported by A. Petrov et al. (2017).

Crystallization from NMP shows a higher $E_{a(\text{interm form})}$ probably due to a combination of weak coordination strength of the solvent to precursor solution complexes and a low evaporation rate. During crystallization from GBL, only a weak peak of the intermediate phase was observed which did not allow to obtain good fitting of the data.

The activation energy of decomposition of intermediate phase $E_{a(\text{interm decomp})}$ and perovskite phase formation $E_{a(\text{pero form})}$ show similar values across different precursor solutions studied. This finding confirms our hypothesis that the MAPbI₃ phase forms by decomposition of the solvate-intermediate phase. Interestingly, the activation energy of the intermediate phase decomposition shows a strong correlation with the coordination strength of the solvent molecules to lead-halide solution complexes shown to be DMSO >> DMF > NMP > GBL (Hamill et al., 2018; Shargaieva et al., 2020). This indicates that the perovskite phase is forming much more readily from solutions containing weakly coordinating solvents.

For DMF and DMSO, the activation energy for the formation of the solvate intermediate phase is clearly much lower than the activation energy for the transformation of the solvate to the perovskite phase: $E_{a(\text{pero form})} > E_{a(\text{interm form})}$. This energetic difference experimentally manifests itself as a long delay between the appearance of the diffraction peaks from the intermediate phases and the MAPbI₃ perovskite phase in **Figures 1, 2**. This proves that for both these solvents, the solvate intermediate phase presents a thermodynamically favored state that can only be avoided upon kinetically controlled process conditions. The formation of a solvate phase can be avoided when the solvent evaporation rate is high enough that the precursor solution is rapidly depleted of solvent molecules. The value of the activation energy for the formation of the perovskite phase from DMF, $E_a = 89.1$ kJ/mol, is

in good agreement with previously reported values of $E_a = 97.3$ and 94 kJ/mol obtained for the formation of MAPbI₃ from DMF with excess of MAI and MAI, respectively, (Moore et al., 2015; Suchan et al., 2020).

In the case of NMP, the activation energies for the formation of the perovskite and solvate intermediate phases are comparable: $E_{a(\text{pero form})} \sim E_{a(\text{interm form})}$. This observation can be interpreted as both the intermediate and MAPbI₃ perovskite phases forming competitively and therefore simultaneously. The delay between the appearance of the diffraction peaks of the intermediate and perovskite phase, as seen in **Figures 1, 2**, is therefore very short.

In the experimental run shown here, only a minor amount of a solvate intermediate phase was found to form for the GBL precursor solution. This is likely due to the fairly low activation energy for the formation of the MAPbI₃ phase determined from the experimental data as summarized in **Table 1**. Additionally, considering the trend in the $E_{a(\text{interm form})}$ as a function of solvent coordination strength, it is plausible to assume that $E_{a(\text{interm form})}$ of GBL would be larger than that of NMP. Thus, $E_{a(\text{pero form})}$ in GBL is likely smaller than $E_{a(\text{interm form})}$ suggesting that the perovskite phase should form much more readily and faster than the intermediate phase. This effect is apparent in the experimental data shown in **Figures 1, 2** where the GBL-intermediate phase is found to appear after the appearance of the diffraction peak associated with the formation of the MAPbI₃ perovskite phase. It is important to note that the formation of the GBL-intermediate phase might be suppressed due to the presence of water.

The obtained data confirms previously reported mechanisms of the formation of hybrid perovskites via crystalline intermediate phases when deposited from strongly coordinating solvents (Qin et al., 2021). When weakly-coordinating solvents are utilized, the direct formation of the perovskite crystalline phase can be observed (Deng et al., 2019). Our findings indicate that the perovskite phase can be formed even at low temperatures from solvent systems in cases where $E_{a(\text{interm decomp})} < E_{a(\text{interm form})}$. The formation from solvent systems with $E_{a(\text{interm decomp})} > E_{a(\text{interm form})}$ will require a larger amount of energy supplied during annealing or usage of quenching techniques to manipulate the values of the energy barrier for the formation of the perovskite phase. This means that the formation of the intermediate phase can be suppressed in favor of the direct formation of the perovskite phase, if process conditions enable fast solvent removal. This is for instance the case, when an anti-solvent is utilized during the perovskite thin-film deposition, as demonstrated in recent reports (Dou et al., 2017; Pratap et al., 2021). The antisolvent may lower the energetic barrier for the formation of the perovskite phase by aiding solvent extraction as shown by A. Taylor et al. (2021)."

It is important to note that only crystalline phases were monitored during the crystallization process. Based on the postulated stoichiometry of the reported crystalline intermediate phases in DMSO and DMF namely (MA)₂Pb₃I₈(Solvent)₂ we conclude that only 2/3 of the materials can be formed directly through decomposition of the intermediate phase and 1/3 of the material require an additional step of incorporation of methylammonium iodide.



We were not able to observe any secondary phases corresponding to the process of incorporation of MAI. Moreover, the kinetic curves of the perovskite formation follow the kinetics of the intermediate phase decomposition during most of the crystallization process indicating that the majority of the material is transformed according to the proposed ratio $x(\text{interm}) = 1 - x(\text{pero})$. Since no PbI_2 formation was observed during the process, we conclude that the incorporation process occurs either via the non-crystalline phase or on the time scale faster than what is achievable within our experimental conditions. Therefore, more insight into mechanistic processes occurring during the transformation of the solvate intermediate phases into the perovskite phase is needed in order to understand the influence of solvents on the processing of hybrid perovskite materials. This is of particular importance for understanding the crystallization process from other intermediate phases that do not include MAI in the crystal structure.

CONCLUSION

To summarize, we were able to rationalize the temperature-dependent crystallization process of the hybrid perovskite material MAPbI_3 from different commonly-used solvents. The nucleation of the solvate intermediate phase showed a strong dependence on both the coordination strength of solvent to lead-halide solution complexes as well as its evaporation rate. Strongly-coordinating solvents such as DMSO are found to readily form solvate-intermediate phases while for weakly coordinating solvents like GBL the MAPbI_3 phase may crystallize directly. From the temperature dependence of the intermediate phase decomposition and perovskite phase formation, the activation energy for solvent removal from the solvate-phase was estimated. We found the activation energy to correlate with the solvent coordination strength to lead iodide with a relative trend of $\text{DMSO} > \text{DMF} > \text{NMP} > \text{GBL}$. At higher processing temperatures, the MAPbI_3 perovskite phase can be formed directly without the intermittent formation of the intermediate phases when processing conditions enable the fast removal of solvents. Our findings contribute to a more detailed understanding of the different roles solvents play in the formation process of halide perovskite semiconductors and enable predicting processing conditions, at which the formation of solvate-intermediate phases can be circumvented.

REFERENCES

- Araïn, Z., Liu, C., Ren, Y., Yang, Y., Mateen, M., Liu, X., et al. (2019). Low-Temperature Annealed Perovskite Films: A Trade-Off between Fast and Retarded Crystallization via Solvent Engineering. *ACS Appl. Mater. Inter.* 11, 16704–16712. doi:10.1021/acami.9b02297
- Avrami, M. (1939). Kinetics of Phase Change. I General Theory. *J. Chem. Phys.* 7, 1103–1112. doi:10.1063/1.1750380
- Cao, J., Jing, X., Yan, J., Hu, C., Chen, R., Yin, J., et al. (2016). Identifying the Molecular Structures of Intermediates for Optimizing the Fabrication of High-Quality Perovskite Films. *J. Am. Chem. Soc.* 138, 9919–9926. doi:10.1021/jacs.6b04924
- De Wolf, S., Holovsky, J., Moon, S.-J., Löper, P., Niesen, B., Ledinsky, M., et al. (2014). Organometallic Halide Perovskites: Sharp Optical Absorption Edge and

DATA AVAILABILITY STATEMENT

The original contributions presented in the study are included in the article/**Supplementary Material**, further inquiries can be directed to the corresponding author.

AUTHOR CONTRIBUTIONS

OS, EU—conceptualization and methodology; OS, HN—data acquisition and analysis; DT, JL—experimental setup and data acquisition. All co-authors have contributed to writing and editing the article.

FUNDING

OS and EU acknowledge funding from the German Science Foundation (DFG) provided in the framework of the priority program SPP 2196, “Perovskite semiconductors: From fundamental properties to devices” Project number 424394788. HN and EU acknowledge funding from the German Ministry of Education and Research (BMBF) for the Young Investigator Group Hybrid Materials Formation and Scaling (HyPerFORME) within the program “NanoMatFutur” (grant no. 03XP0091). JL acknowledges funding from the Chinese Scholarship Council (CSC, grant No. CSC201908120116).

ACKNOWLEDGMENTS

HN and JL acknowledge the support from the HyPerCells graduate school and HI-SCORE research school. OS thanks Rahim Munir for organizing the beamtime and allocating time for the experiments. The authors thank BESSY II synchrotron in Berlin for use of beamtime at KMC-2 DIFFRACTION beamline.

SUPPLEMENTARY MATERIAL

The Supplementary Material for this article can be found online at: <https://www.frontiersin.org/articles/10.3389/fenrg.2021.749604/full#supplementary-material>

its Relation to Photovoltaic Performance. *J. Phys. Chem. Lett.* 5, 1035–1039. doi:10.1021/jz500279b

- Deng, Y., van Brackle, C. H., Dai, X., Zhao, J., Chen, B., and Huang, J. (2019). Tailoring Solvent Coordination for High-Speed, Room-Temperature Blading of Perovskite Photovoltaic Films. *Sci. Adv.* 5, eaax7537. doi:10.1126/sciadv.aax7537
- Dong, Q., Fang, Y., Shao, Y., Mulligan, P., Qiu, J., Cao, L., et al. (2015). Electron-hole Diffusion Lengths > 175 μm in Solution-Grown $\text{CH}_3\text{NH}_3\text{PbI}_3$ Single Crystals. *Science* 347, 967–970. doi:10.1126/science.aaa5760
- Dou, B., Pool, V. L., Toney, M. F., and van Hest, M. F. A. M. (2017). Radiative Thermal Annealing/*In Situ* X-ray Diffraction Study of Methylammonium Lead Triiodide: Effect of Antisolvent, Humidity, Annealing Temperature Profile, and Film Substrates. *Chem. Mater.* 29, 5931–5941. doi:10.1021/ACS.CHEMMATER.7B01467

- Fanfon, M., and Tomellini, M. (1998). The Johnson-Mehl- Avrami-Kohnogorov Model: A Brief Review. *Nouv. Cim. D* 20, 1171–1182. doi:10.1007/BF03185527
- Fu, F., Feurer, T., Jäger, T., Avancini, E., Bissig, B., Yoon, S., et al. (2015). Low-temperature-processed Efficient Semi-transparent Planar Perovskite Solar Cells for Bifacial and Tandem Applications. *Nat. Commun.* 6, 1–9. doi:10.1038/ncomms9932
- Guo, X., McCleese, C., Kolodziej, C., Samia, A. C. S., Zhao, Y., and Burda, C. (2016). Identification and Characterization of the Intermediate Phase in Hybrid Organic-Inorganic MAPbI₃perovskite. *Dalton Trans.* 45, 3806–3813. doi:10.1039/c5dt04420k
- Hamill, J. C., Schwartz, J., and Loo, Y.-L. (2018). Influence of Solvent Coordination on Hybrid Organic-Inorganic Perovskite Formation. *ACS Energy Lett.* 3, 92–97. doi:10.1021/acsenerylett.7b01057
- Haque, M. A., Troughton, J., and Baran, D. (2020). Processing-Performance Evolution of Perovskite Solar Cells: From Large Grain Polycrystalline Films to Single Crystals. *Adv. Energy Mater.* 10, 1902762. doi:10.1002/aenm.201902762
- Jeon, N. J., Noh, J. H., Kim, Y. C., Yang, W. S., Ryu, S., and Seok, S. I. (2014). Solvent Engineering for High-Performance Inorganic-Organic Hybrid Perovskite Solar Cells. *Nat. Mater.* 13, 897–903. doi:10.1038/nmat4014
- Jeon, T., Kim, S. J., Yoon, J., Byun, J., Hong, H. R., Lee, T.-W., et al. (2017). Hybrid Perovskites: Effective Crystal Growth for Optoelectronic Applications. *Adv. Energy Mater.* 7, 1602596. doi:10.1002/aenm.201602596
- Jo, Y., Oh, K. S., Kim, M., Kim, K.-H., Lee, H., Lee, C.-W., et al. (2016). High Performance of Planar Perovskite Solar Cells Produced from PbI₂(DMSO) and PbI₂(NMP) Complexes by Intramolecular Exchange. *Adv. Mater. Inter.* 3, 1500768. doi:10.1002/admi.201500768
- Lee, S., Tang, M.-C., Munir, R., Barrit, D., Kim, Y.-J., Kang, R., et al. (2020). *In Situ* study of the Film Formation Mechanism of Organic-Inorganic Hybrid Perovskite Solar Cells: Controlling the Solvate Phase Using an Additive System. *J. Mater. Chem. A* 8, 7695–7703. doi:10.1039/d0ta00048e
- Li, J., Dagar, J., Shargaieva, O., Flatken, M. A., Köbler, H., Fenske, M., et al. (202120034). 20.8% Slot-Die Coated MAPbI₃ Perovskite Solar Cells by Optimal DMSO-Concentration and Age of 2-ME Based Precursor Inks. *Adv. Energy Mater.* doi:10.1002/aenm.202003460
- Li, X., Bi, D., Yi, C., Décoppet, J.-D., Luo, J., Zakeeruddin, S. M., et al. (2016). A Vacuum Flash-Assisted Solution Process for High-Efficiency Large-Area Perovskite Solar Cells. *Science* 353, 58–62. doi:10.1126/science.aaf8060
- Li, Y., Zhi, L., Ge, G., Zhao, Z., Cao, X., Chen, F., et al. (2019). Investigation on Crystallization of CH₃NH₃PbI₃ Perovskite and its Intermediate Phase from Polar Aprotic Solvents. *Cryst. Growth Des.* 19, 959–965. doi:10.1021/acs.cgd.8b01516
- Lin, P., Zhang, W., Tian, L., Zhang, F., Zhou, S., Liu, R., et al. (2021). Remanent Solvent Management Engineering of Perovskite Films for PEDOT: PSS-Based Inverted Solar Cells. *Solar Energy* 216, 530–536. doi:10.1016/j.solener.2021.01.044
- Ma, Y., Hangoma, P. M., Park, W. I., Lim, J.-H., Jung, Y. K., Jeong, J. H., et al. (2019). Controlled crystal Facet of MAPbI₃ Perovskite for Highly Efficient and Stable Solar Cell via Nucleation Modulation. *Nanoscale* 11, 170–177. doi:10.1039/c8nr08344d
- Moore, D. T., Sai, H., Tan, K. W., Smilgies, D.-M., Zhang, W., Snaith, H. J., et al. (2015). Crystallization Kinetics of Organic-Inorganic Trihalide Perovskites and the Role of the lead Anion in crystal Growth. *J. Am. Chem. Soc.* 137, 2350–2358. doi:10.1021/ja512117e
- Ortoll-Bloch, A. G., Herbol, H. C., Sorenson, B. A., Poloczek, M., Estroff, L. A., and Clancy, P. (2020). Bypassing Solid-State Intermediates by Solvent Engineering the Crystallization Pathway in Hybrid Organic-Inorganic Perovskites. *Cryst. Growth Des.* 20, 1162–1171. doi:10.1021/acs.cgd.9b01461
- Petrov, A. A., Sokolova, I. P., Belich, N. A., Peters, G. S., Dorovatovskii, P. V., Zubavichus, Y. V., et al. (2017). Crystal Structure of DMF-Intermediate Phases Uncovers the Link between CH₃NH₃PbI₃ Morphology and Precursor Stoichiometry. *J. Phys. Chem. C* 121, 20739–20743. doi:10.1021/acs.jpcc.7b08468
- Pool, V. L., Dou, B., Van Campen, D. G., Klein-Stockert, T. R., Barnes, F. S., Shaheen, S. E., et al. (2017). Thermal Engineering of FAPbI₃ Perovskite Material via Radiative thermal Annealing and *In Situ* XRD. *Nat. Commun.* 8, 1–8. doi:10.1038/ncomms14075
- Pratap, S., Babbe, F., Barchi, N. S., Yuan, Z., Luong, T., Haber, Z., et al. (20212021). Out-of-equilibrium Processes in Crystallization of Organic-Inorganic Perovskites during Spin Coating. *Nat. Commun.* 12, 1–9. doi:10.1038/s41467-021-25898-5
- Qin, M., Chan, P. F., and Lu, X. (2021). A Systematic Review of Metal Halide Perovskite Crystallization and Film Formation Mechanism Unveiled by *In Situ* GIWAXS. *Adv. Mater.* 2105290. doi:10.1002/ADMA.202105290
- Rehman, W., McMeekin, D. P., Patel, J. B., Milot, R. L., Johnston, M. B., Snaith, H. J., et al. (2017). Photovoltaic Mixed-Cation lead Mixed-Halide Perovskites: Links between Crystallinity, Photo-Stability and Electronic Properties. *Energy Environ. Sci.* 10, 361–369. doi:10.1039/C6EE03014A
- Saliba, M., Correa-Baena, J. P., Wolff, C. M., Stollerfoht, M., Phung, N., Albrecht, S., et al. (2018). How to Make over 20% Efficient Perovskite Solar Cells in Regular (N-i-p) and Inverted (P-i-n) Architectures. *Chem. Mater.* 30, 4193–4201. doi:10.1021/acs.chemmater.8b00136
- Seo, Y.-H., Kim, E.-C., Cho, S.-P., Kim, S.-S., and Na, S.-I. (2017). High-performance Planar Perovskite Solar Cells: Influence of Solvent upon Performance. *Appl. Mater. Today* 9, 598–604. doi:10.1016/J.APMT.2017.11.003
- Shargaieva, O., Näsström, H., Smith, J. A., Többsen, D., Munir, R., and Unger, E. (2020). Hybrid Perovskite Crystallization from Binary Solvent Mixtures: Interplay of Evaporation Rate and Binding Strength of Solvents. *Mater. Adv.* 1, 3314–3321. doi:10.1039/d0ma00815j
- Singh, R., Suranagi, S. R., Kumar, M., and Shukla, V. K. (2017). Investigations on the Role of Mixed-Solvent for Improved Efficiency in Perovskite Solar Cell. *J. Appl. Phys.* 122, 235302. doi:10.1063/1.4998630
- Stevenson, J., Sorenson, B., Subramaniam, V. H., Raiford, J., Khlyabich, P. P., Loo, Y.-L., et al. (2017). Mayer Bond Order as a Metric of Complexation Effectiveness in Lead Halide Perovskite Solutions. *Chem. Mater.* 29, 2435–2444. doi:10.1021/acs.chemmater.6b04327
- Suchan, K., Just, J., Becker, P., Unger, E. L., and Unold, T. (2020). Optical *In Situ* Monitoring during the Synthesis of Halide Perovskite Solar Cells Reveals Formation Kinetics and Evolution of Optoelectronic Properties. *J. Mater. Chem. A* 8, 10439–10449. doi:10.1039/d0ta01237h
- Tan, Q., Hinrichs, K., Mao-Dong, H., Fengler, S., Rappich, J., Prajontat, P., et al. (2019). Temperature Dependent Diffusion of DMSO in CH₃NH₃PbI₃ Precursor Films during Layer Formation and Impact on Solar Cells. *ACS Appl. Energy Mater.* 2, 5116–5123. doi:10.1021/acsaem.9b00769
- Taylor, A. D., Sun, Q., Goetz, K. P., An, Q., Schramm, T., Hofstetter, Y., et al. (2021). A General Approach to High-Efficiency Perovskite Solar Cells by Any Antisolvent. *Nat. Commun.* 12, doi:10.1038/S41467-021-22049-8
- Többsen, D. M., and Zander, S. (2016). KMC-2: an X-ray Beamline with Dedicated Diffraction and XAS Endstations at BESSY II. *Jlsrf* 2, 49. doi:10.17815/jlsrf-2-65
- Todinov, M. T. (2000). On Some Limitations of the Johnson-Mehl-Avrami-Kolmogorov Equation. *Acta Materialia* 48, 4217–4224. doi:10.1016/S1359-6454(00)00280-9
- Valencia, A. M., Shargaieva, O., Schier, R., Unger, E., and Cocchi, C. (2020). Fingerprints of Iodoplumbate Chains in the Optical Absorption of lead-halide Perovskite Solution Precursors. arXiv.
- Xu, M.-F., Zhang, H., Zhang, S., Zhu, H. L., Su, H.-M., Liu, J., et al. (2015). A Low Temperature Gradual Annealing Scheme for Achieving High Performance Perovskite Solar Cells with No Hysteresis. *J. Mater. Chem. A* 3, 14424–14430. doi:10.1039/c5ta02730f
- Zhang, M., Yun, J. S., Ma, Q., Zheng, J., Lau, C. F. J., Deng, X., et al. (2017). High-Efficiency Rubidium-Incorporated Perovskite Solar Cells by Gas Quenching. *ACS Energy Lett.* 2, 438–444. doi:10.1021/acsenerylett.6b00697

Conflict of Interest: The authors declare that the research was conducted in the absence of any commercial or financial relationships that could be construed as a potential conflict of interest.

Publisher's Note: All claims expressed in this article are solely those of the authors and do not necessarily represent those of their affiliated organizations, or those of the publisher, the editors and the reviewers. Any product that may be evaluated in this article, or claim that may be made by its manufacturer, is not guaranteed or endorsed by the publisher.

Copyright © 2021 Shargaieva, Näsström, Li, Többsen and Unger. This is an open-access article distributed under the terms of the Creative Commons Attribution License (CC BY). The use, distribution or reproduction in other forums is permitted, provided the original author(s) and the copyright owner(s) are credited and that the original publication in this journal is cited, in accordance with accepted academic practice. No use, distribution or reproduction is permitted which does not comply with these terms.



Modeling and Simulation of Large-Scale Wind Power Base Output Considering the Clustering Characteristics and Correlation of Wind Farms

Mingzhe Zhao¹, Yimin Wang^{1*}, Xuebin Wang^{1*}, Jianxia Chang¹, Yong Zhou² and Tao Liu^{1,3}

¹State Key Laboratory of Eco-hydraulics in Northwest Arid Region of China (Xi'an University of Technology), Xi'an, China, ²Yalong River Hydropower Development Company, Ltd, Chengdu, China, ³Northwest Engineering Corporation Limited, Xi'an, China

OPEN ACCESS

Edited by:

ZhaoYang Dong,
University of New South Wales,
Australia

Reviewed by:

Davide Astolfi,
University of Perugia, Italy
Meysam Majidi Nezhad,
Sapienza University of Rome, Italy

*Correspondence:

Yimin Wang
wangyimin@xaut.edu.cn
Xuebin Wang
xuebin1990@163.com

Specialty section:

This article was submitted to
Wind Energy,
a section of the journal
Frontiers in Energy Research

Received: 06 November 2021

Accepted: 17 February 2022

Published: 22 March 2022

Citation:

Zhao M, Wang Y, Wang X, Chang J, Zhou Y and Liu T (2022) Modeling and Simulation of Large-Scale Wind Power Base Output Considering the Clustering Characteristics and Correlation of Wind Farms. *Front. Energy Res.* 10:810082. doi: 10.3389/fenrg.2022.810082

The rapid development of renewable energy improves the requirements of renewable energy output simulation. The clustering characteristics and correlation of renewable energy would improve the accuracy of power output simulation. To clarify the typical power output process of a large-scale wind power base, a novel method is proposed for wind power output scene simulation in this paper. Firstly, the genetic algorithm (GA) Kmeans is used to divide the wind farm clusters. The wind power output of each cluster is calculated by the wind turbine model. Then, the Copula principle is used to describe the correlation characteristic of wind farm clusters. Finally, the power output scenes are simulated by the Markov chain Monte Carlo (MCMC) method. To verify the effectiveness of proposed method, the wind power base in the downstream Yalong River basin is taken as the case study. The results show that the 65 wind farms should be divided into 6 clusters. The five typical power output scenes in winter–spring and summer–autumn seasons are simulated respectively based on the clustering characteristics and correlation of wind farms. This study provides a valuable reference for other large-scale renewable power bases all over the world.

Keywords: output scene simulation, GA-Kmeans method, Copula principle, large-scale wind power base, renewable energy

INTRODUCTION

An energy structure with fossil energy as its main source brings many problems, such as environmental pollution, climate change, and energy depletion crisis, which seriously restrict the development of the social economy (Zhang et al., 2018; Wang et al., 2018). Since the 21st century, energy structure transformation has become the focus of countries worldwide (Hou et al., 2019). Under the guidance of the concept of energy structure transformation, the development of the global renewable energy industry has been accelerating, and the installed capacity of renewable energy has increased from 812 GW in 2004 to about 3,089 GW in 2021. However, the high randomness, intermittency, and uncontrollability of renewable energy result in large-scale wind and photovoltaic (PV) power generation presenting large challenges for integration into a power grid (Wang et al., 2019; Wang et al., 2019; Liu et al., 2020). Therefore, clarifying the characteristics of large-scale renewable energy and simulating the power output

scene is of great significance for renewable energy development (Kim et al., 2020; Zhang et al., 2020).

Currently, numerous studies focus on the analysis of the spatial and temporal distribution of renewable energy, as well as the evaluation of complementary characteristics of various clean energy power stations. De Blasis et al. (2021) applied a high-order multivariate Markov model to clarify the cross- and auto-correlation characteristics between wind speed and direction. Almeida et al. (2021) proposed a Monte Carlo-based multi-area reliability assessment method to represent the relevant features and intermittency of variable renewable energy resources. Xu et al. (2017) constructed the relation function of the marginal cumulative distribution function of the intensity of wind speed and light irradiance through the Copula function and used the Kendall rank correlation coefficient to describe the spatial and temporal characteristics of wind and PV indirectly. Huang et al. (2021) used the Copula method to analyze the uncertainties of wind and solar power for quantifying the risk of wind-solar-hydro complementary system. Cantao et al. (2017) used hydro-wind correlation maps to analyze the wind and hydropower complementarity, which are quantitative and more intuitive. Based on the variable-structure Copula function, Wang et al. (2020) proposed a novel method to describe the correlation and complementarity of distributed wind power and load for optimizing the planning capacity of distributed wind power. Antunes Campos et al. (2020) assessed the complementary nature between wind with the Pearson's correlation coefficient and PV power and optimized energy storage capacity in the utility-scale hybrid power plants. However, the research on the combination of temporal-spatial distribution characteristics of renewable energy and output simulation or prediction is still insufficient.

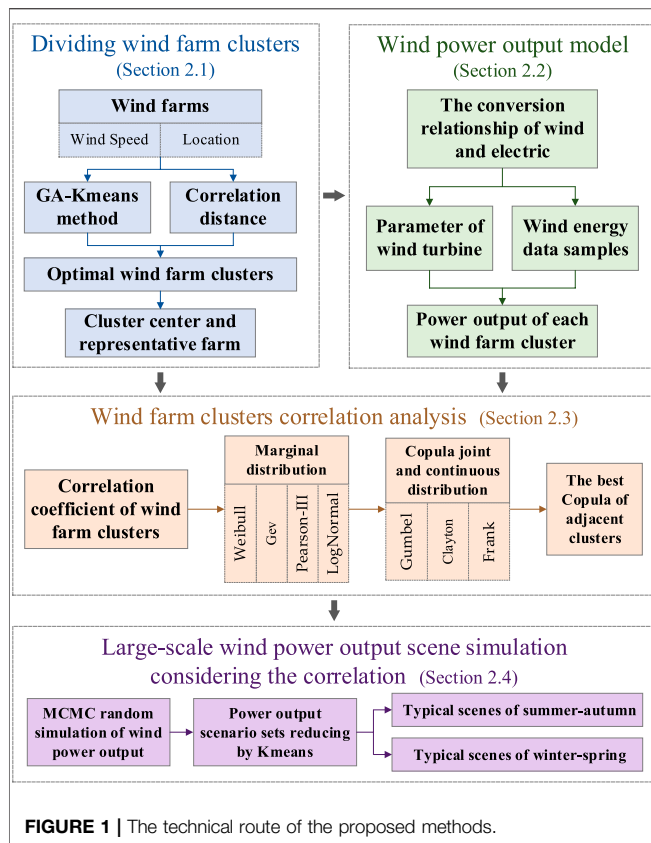
Based on the complementary characteristics of new energy such as wind energy and solar energy, there have been many scholars who have studied the clustering characteristics of new energy in different regions. Dai et al., 2017 proposed an evaluation method of cluster output smoothness and quantified the contribution of wind power clustering to reduce the fluctuation of wind power output. Yesilbudak (2016) adopted the Kmeans clustering method with Squared Euclidean, City-Block, Cosine, and Pearson Correlation distance measures to analyze the clustering characteristics of 75 provinces' wind speed in Turkey. According to the aggregate effect of wind and solar power plants, Liu et al. (2020) aggregated all the power plants of study area into a virtual wind power plant and a virtual solar power plant. Chidean et al. (2018) presented the Second-Order Data-Coupled Clustering (SODCC) algorithm to analyze the wind power resource in the Iberian Peninsula. Yan et al. (2020) proposed a scenario generation method and established the planning model of renewable energy based on cluster partition. Nevertheless, there is less research focused on the correlation of multiple renewable energy clusters.

To develop and utilize large-scale renewable energy and reduce the adverse impact of renewable energy uncertainty, many scholars have conducted research on renewable energy scene simulation and power forecasting. Renewable power output scene simulation aims to fully tap the overall characteristics and

statistical laws of renewable energy, generate typical power output scenes, and provide basis for renewable power system planning (Densing and Wan, 2022). In the previous literature, Deng et al. (2018) used a typical scenario simulation method of renewable power output calculating the renewable energy accommodation capability. Ding et al. (2016) proposed a short-term stochastic simulation method based on the renewable power output error and used the method for a real power grid in Northwest China. Compared with renewable power output scene simulation, renewable energy prediction provides a basis for making power system generation plan and power grid dispatching operation (Zhang et al., 2020). Renewable energy forecast generally uses the statistical regression methods and machine learning technologies to estimate the future power output process. Wang et al. (2020) proposed a hybrid wind power forecasting approach based on Bayesian model averaging and Ensemble learning. Neshat et al. (2021) proposed a novel three stages' composite deep learning-based evolutionary approach to forecast the power output in wind-turbine farms with the chaotic characteristics of wind speed series. Singh et al. (2021) represented the short-term wind power forecasting accuracy of five machine learning methods, such as k-nearest neighbor (kNN), decision-tree, extra tree regression, random forest, and gradient boosting machine (GBM). However, most of the existing research ignores the characteristic differences between different wind farms, and there are only a few studies on wind power simulating or forecasting of large-scale wind power bases based on the clustering method.

At present, research on the characteristics of new energy resources, cluster division, and renewable power output forecasting and simulating has achieved phased results, but there are still some deficiencies. In the planning and designing stage of the renewable energy system, the simulation scenes of renewable power output would be frequently used. However, the unreasonable wind power output scenes would seriously affect the development and management of the renewable energy system. In particular, previous research on renewable energy simulation assumes that the power output should be consistent in the whole area. The power output scenes of a representative wind farm would be usually used to describe all wind farms in the region. However, for large-scale wind power bases, there are certain differences in wind power output characteristics in the region. Ignoring the correlation and complementarity of wind farm clusters will lead to a large deviation in the simulation results of the wind power output. Consequently, researching on power output scene simulation of large-scale wind power base considering the power station cluster division and power output correlation of adjacent clusters is very necessary and urgent.

In order to fill this gap and obtain the accurate power output scenes of large-scale wind power bases, this paper proposed a power output scene simulation method considering power station clustering and cluster correlation. Firstly, the wind farm clusters are divided by the genetic algorithm (GA)-Kmeans method with similar distances. Secondly, based on the conversion relationship of wind speed and electric power, the wind power output physical model is used to calculate the wind power output of each wind



farm cluster. Then, using the joint and conditional distribution functions of Copula, the correlation between different clusters is analyzed. Finally, the Markov chain Monte Carlo (MCMC) method is used to simulate the power output scenes of large-scale wind bases. The wind power base of the downstream Yalong River basin is taken as an example to verify the validity and rationality of the new method.

METHODOLOGY

The methods to be used for simulating the power output scene of large-scale wind power mainly consists of four parts. The technical route of the large-scale wind power base output simulating method with the correlation is shown in **Figure 1**. The nomenclature table of abbreviations, variables, and constants is shown in **Table 1**.

Wind Farm Cluster Division With the GA-Kmeans Method

The GA-Kmeans method was performed to divide the wind farm clusters. The uncertainty caused by the clustering number K and clustering center $\{c_1, c_2, \dots, c_k\}$ is difficult to solve using the conventional Kmeans method. The GA, which has a fast computing speed, a stable operation, and a strong global searching ability, was combined with the Kmeans method in

this article. The GA-Kmeans method can reduce the influence of the initial cluster number and the selection of cluster center on the resulting cluster effectively. Besides, the GA-Kmeans method can improve the accuracy of clustering results and avoid Kmeans clustering into a local optimum (Yesilbudak, 2016).

Furthermore, the correlation distance was selected as the distance evaluation index in the Kmeans clustering process. The fitness function optimized by the GA algorithm was constructed by counting the intra-class distance and inter-class distance of each cluster.

The correlation distance between $X = (x_1, x_2, \dots, x_n)$ and $C = (c_1, c_2, \dots, c_n)$ can be expressed as:

$$d(X, C) = 1 - \frac{(x - \bar{x})(c - \bar{c})'}{\sqrt{(x - \bar{x})(x - \bar{x})'}\sqrt{(c - \bar{c})(c - \bar{c})'}} \quad (1)$$

$$\bar{x} = \frac{1}{p} \left(\sum_{j=1}^p x_j \right) \bar{1}_p \quad (2)$$

$$\bar{c} = \frac{1}{p} \left(\sum_{j=1}^p c_j \right) \bar{1}_p \quad (3)$$

where $\bar{1}_p$ is the row vector of $[1, 1, 1, \dots, 1]_p$.

The similarity of objects in the Kmeans cluster can be expressed by the average class inner distance as follows:

$$ICS = \sum_{i=1}^k \sum_{j=1}^{N_i} \frac{d(x_{ij}, c_i)}{N_i} \quad (4)$$

where x_{ij} is the j th object of class i , N_i is the sample size of class i , c_i is the cluster center of class i , and $d(x, y)$ is the relative distance between two samples.

The object difference between clusters of Kmeans clustering can be expressed by class spacing as:

$$ICD = \sum_{i=1}^{k-1} \sum_{j=i+1}^k d(c_i, c_j) \quad (5)$$

The fitness function was defined as:

$$F = ICD/ICS \quad (6)$$

The fitness function value was determined by the quality of clustering results. The fitness function value is larger when the average in-class distance is smaller and class distance is larger. Currently, the clustering effect is better.

Calculation Method of Wind Power Output

The wind speed and electric power conversion model is adopted to calculate the output power of a single wind turbine. The total output process of the wind farm can be obtained by the ratio of the unit capacity to the installed machine. The power conversion relation of a wind turbine is shown as:

$$P_{W,t} = \begin{cases} 0 & 0 \leq v_t \leq v_{ci} \\ C_p S \rho v^3 / 2 & v_{ci} \leq v_t \leq v_r \\ P_r & v_r \leq v_t \leq v_{co} \\ 0 & v_t \geq v_{co} \end{cases} \quad (7)$$

TABLE 1 | The nomenclature table of abbreviations, constants, and variables.

A. Abbreviations			
AIC	Akaike Information Criterion	GA	Genetic algorithm
GBM	Gradient boosting machine	GEV	Generalized extreme value
kNN	k-nearest neighbor	Ln	Lognormal distribution
MCMC	Markov chain Monte Carlo	P-III	Pearson type III distribution
PV	Photovoltaic	RMSE	Root Mean Square Error
SODCC	Second-Order Data-Coupled Clustering	WMCB	The watershed-type multi-energy complementary bases
B. Constants			
C_p	Energy utilization coefficient of wind turbine	ρ_0	Dry-air density at normal pressure and temperature
P_r	Rated power	P_w	The water pressure
v_{ci}	Cut in wind speed	v_{co}	Cut out wind speed
v_r	Rated wind speed	$\vec{1}_p$	The unit row vector
C. Variables			
β_1	Probability of occurrence of minimum value	β_2	Probability of occurrence of maximum value
$C(\cdot)$	Copula joint distribution	$c(\cdot)$	Copula joint probability density
c_i	The cluster center of class i	$\{c_1, c_2, \dots, c_k\}$	Clustering center
$d(X, C)$	Correlation distance between two samples X and C	$F(v u)$	Copula conditional probability distribution function
$F(x)$	Cumulative distribution function	$f(x)$	Probability density function
$F_X(x)$	Marginal distribution of random variables X	$F_Y(y)$	Marginal distribution of random variables Y
$F(X, Y)$	Joint distribution function	$f_c(x; R)$	Continuous function
ICS	The average class inner distance	lcd	Class spacing distance
K	Clustering number	N_i	The sample size of class i
Pe_i	Empirical frequency	P_i	Theoretical frequency
P	The air pressure at the hub height of wind turbine	$P_{W,t}$	The power output of unit wind turbine at time t
S	The swept leaf area	T	Temperature
u	Random variables of Copula	v	Random variables of Copula
v_t	The real wind speed at time t	x_{ji}	The j_{th} object of class i
\vec{C}	Row vector of $C = (c_1, c_2, \dots, c_n)$	\vec{X}	Row vector of $X = (x_1, x_2, \dots, x_n)$
∂	Partial derivative	θ	Parameter of Copula function
ρ	Moist-air density	$\delta(\cdot)$	Dirac delta function
r_n	Pearson linear correlation coefficient	τ_n	Kendall rank correlation coefficient
ρ_n	Spearman correlation coefficient		

$$\rho = \rho_0 \cdot \frac{273.15}{273.15 + T} \times \frac{P - 0.378P_w}{1013.25} \quad (8)$$

where $P_{W,t}$ is the power output of unit wind turbine at time t , kW; P_r is rated power, kW; C_p represents the wind energy utilization coefficient of the wind power; S is the swept leaf area; v is the real wind speed at time t , m/s; v_{ci} , v_{co} , and v_r are cut in, cut out, and rated wind speed, respectively, m/s; ρ is the moist-air density, kg/m³; ρ_0 is the dry-air density at normal pressure and temperature, $\rho_0 = 1.293 \text{ m}^3/\text{kg}$; T is temperature, °C; P is the air pressure at the hub height of wind turbine, hPa; P_w is the water pressure, hPa.

Wind Farm Clusters Correlation Analysis With the Copula Principle

The correlation analysis method of adjacent wind farm clusters based on the Copula principle includes the marginal distribution model of wind farm cluster power output, the Copula function type and conditional distribution of adjacent wind power cluster output, and the goodness-of-fit test method of the distribution model.

The Marginal Distribution of Wind Power Output

The main distribution marginal functions widely used in statistical analysis are Pearson type III distribution (P-III), lognormal distribution (Ln), Generalized extreme value

distribution (Gev), and Weibull distribution. In this paper, four distributions are used to fit the marginal distribution of each wind power cluster's output.

It is worth noting that if the wind power output is taken as the random variable, there are multiple repeated minimum and maximum values in the sample sequence. Moreover, the probabilities of minimum and maximum values are not equal to 0, which leads to the discontinuity of probability density function and cumulative distribution function of wind power output. Therefore, the probability distribution of wind power output needs to be described by the interception distribution model, and the probability density and cumulative distribution function can be expressed as:

$$f(x) = \beta_1 \delta(x - X_{\min}) + f_c(x; R) + \beta_2 \delta(x - X_{\max}) \quad (9)$$

$$F(x) = \begin{cases} \beta_1 & x = X_{\min} \\ \int_{X_{\min}}^x f_c(x; R) dx & X_{\min} < x < X_{\max} \\ 1 & x = X_{\max} \end{cases} \quad (10)$$

where, β_1 and β_2 represent the probability of occurrence of minimum and maximum events, respectively; $\delta(\cdot)$ is the Dirac delta function; $f_c(x; R)$ is a continuous function and satisfies $\int_{X_{\min}}^{X_{\max}} f_c(x; R) dx = 1 - \beta_1 - \beta_2$; R is a vector parameter.

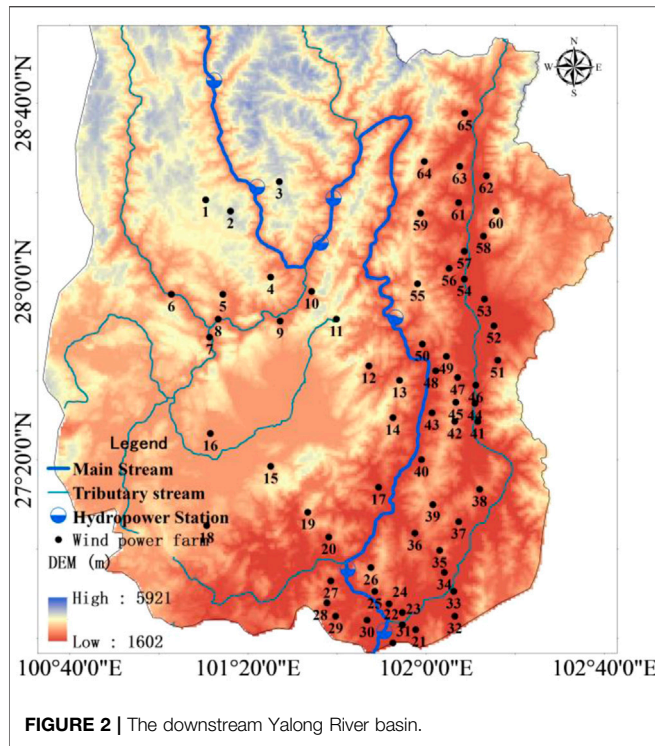


FIGURE 2 | The downstream Yalong River basin.

The Copula Function Type and the Conditional Distribution

Sklar (1959) introduced the theory of Copula into statistics, providing an effective method for multivariate analysis. For 2-dimensional random variables, random variables X and Y obey the marginal distribution $F_X(x)$ and $F_Y(y)$, respectively. $F(X, Y)$ represent their joint distribution function. There is a Copula:

$$F(x, y) = C(F_X(x), F_Y(y)) \quad (11)$$

where $x \in [0, 1]$ and $y \in [0, 1]$.

If F_X and F_Y are continuous functions, then the $C(\cdot)$ is unique, and the joint distribution density function can be expressed as:

$$\begin{aligned} c(x, y) &= \frac{\partial^2 C(u, v)}{\partial x \partial y} = f(x, y) \\ &= c(F_X(x), F_Y(y)) \cdot f_X(x) \cdot f_Y(y) \end{aligned} \quad (12)$$

where u and v are random variables.

Analyzing the correlation between variables is the basis of constructing Copula joint distribution. Pearson linear correlation coefficient (r_n), Spearman correlation coefficient (ρ_n), and Kendall rank correlation coefficient (τ_n) were used to describe the correlation of wind energy in wind power cluster.

Nelson (1999) gave a detailed introduction to the Copula function and its properties. Generally, Copula functions can be divided into three types: Elliptic, Archimedean, and Quadratic. The Archimedean Copula with one parameter is the most widely used.

In this paper, three Archimedean Copula (Gumbel Copula, Clayton Copula, and Frank Copula) are used to construct the

joint distribution of wind power of each wind farm cluster. The joint distribution functions and conditional distribution functions of three Copula type are provided as follows:

- 1) The joint distribution function and conditional distribution function of Gumbel Copula are shown as:

$$C(u, v) = \exp\left\{-\left[(-\ln u)^\theta + (-\ln v)^\theta\right]^{1/\theta}\right\} \quad (13)$$

$$\begin{aligned} F(v|u) &= \partial C(u, v) / \partial u \\ &= \frac{(-\ln u)^{\theta-1} \left[(-\ln u)^\theta + (-\ln v)^\theta\right]^{(1-\theta)/\theta}}{ue \left[(-\ln u)^\theta + (-\ln v)^\theta\right]^{1/\theta}} \end{aligned} \quad (14)$$

where θ is the parameter of the Gumbel Copula function, and $\theta \in [1, \infty)$.

- 2) The joint distribution function and conditional distribution function of Clayton Copula are shown as:

$$C(u, v) = (u^{-\theta} + v^{-\theta} - 1)^{-1/\theta} \quad (15)$$

$$F(v|u) = \partial C(u, v) / \partial u = \left[1 + u^\theta (v^{-\theta} - 1)\right]^{-(1+\theta)/\theta} \quad (16)$$

where θ is the parameter of the Clayton Copula function, and $\theta \in (0, \infty)$.

- 3) The joint distribution function and conditional distribution function of Frank Copula are shown as:

$$C(u, v) = -\frac{1}{\theta} \ln \left[1 + \frac{(e^{-v\theta} - 1)(e^{-u\theta} - 1)}{e^{-\theta} - 1}\right] \quad (17)$$

$$\begin{aligned} F(v|u) &= \partial C(u, v) / \partial u \\ &= e^{-u\theta} (e^{-v\theta} - 1) / \left[(e^{-v\theta} - 1)(e^{-u\theta} - 1) + e^{-\theta} - 1\right] \end{aligned} \quad (18)$$

where θ is the parameter of the Frank Copula function, and $\theta \in R$.

The Goodness-of-Fit Test Index

Root Mean Square Error (RMSE) and Akaike Information Criterion (AIC) were used to evaluate the goodness of fit of the Copula joint distribution function.

- 1) RMSE is the most commonly used index for the goodness-of-fit test.

$$RMSE = \sqrt{\frac{1}{n} \sum_{i=1}^n (Pe_i - P_i)^2} \quad (19)$$

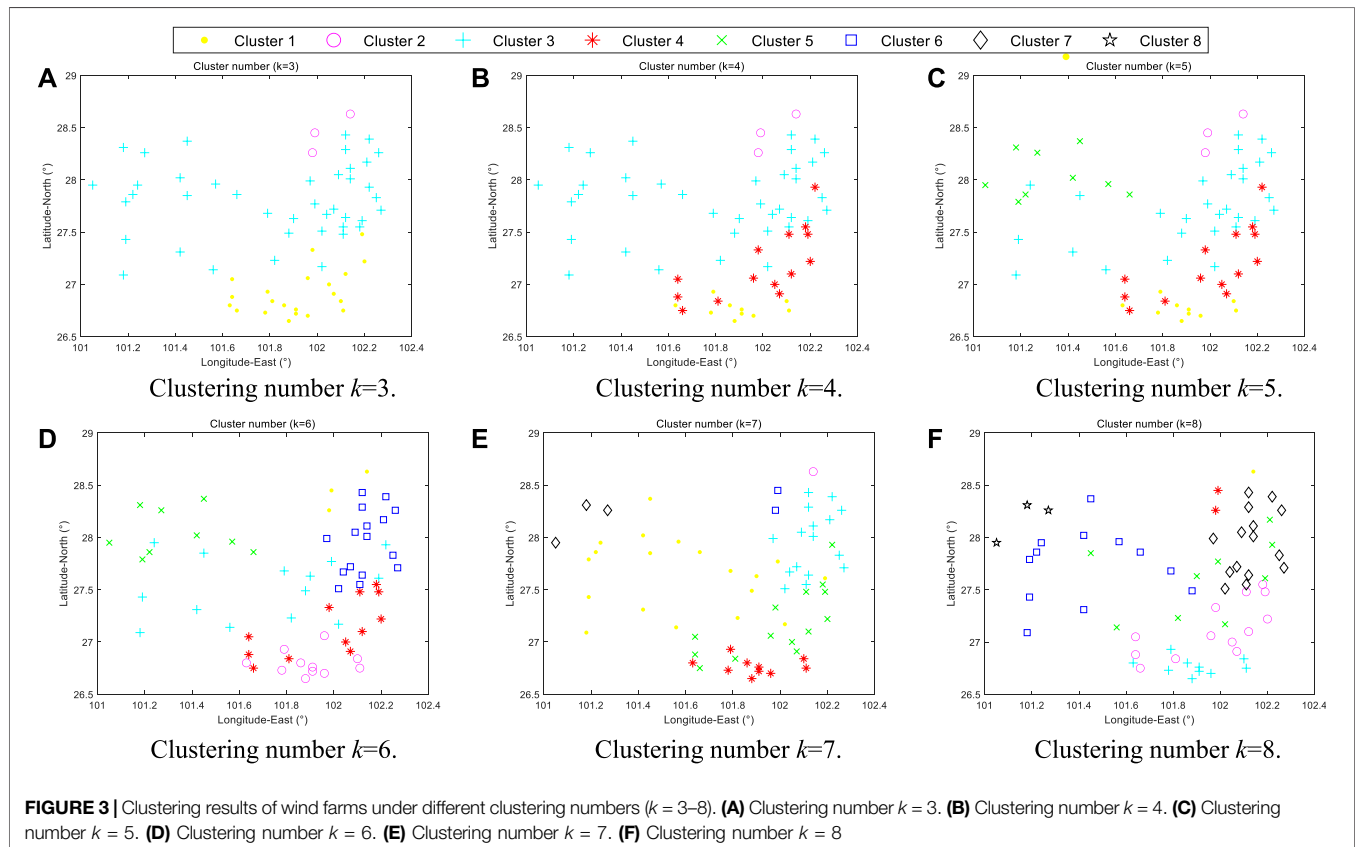
where Pe_i and P_i are the empirical frequency and theoretical frequency, respectively.

- 2) AIC considers the deviation of Copula function fitting and the uncertainty caused by the number of parameters of Copula function.

$$AIC = n \ln \left(\frac{1}{n} \sqrt{\sum_{i=1}^n (Pe_i - P_i)^2} \right) + 2m \quad (20)$$

TABLE 2 | The main technical parameters of the GW121-2.5MW wind turbine.

Operating parameters	Rated power	Design wind zone level	Design service life	Unit operating temperature
	2.5 MW	IEC II A	≥20 years	−30°C~+40°C
Specifications	Cut in wind speed	Rated wind speed	Cut out wind speed	Unit survival temperature
	3 m/s	9.7 m/s	22 m/s	−40°C~+50°C
	Impeller diameter	Tower type	Hub height	
	120 m	Steel tower	90 m	



where m is the number of model parameters. The smaller value of the AIC and RMSE, the better fitting degree of the Copula function.

Large-Scale Wind Power Output Scene Simulation Considering the Correlation

According to the correlation characteristics among wind power clusters, the MCMC method is used in this study to randomly sample from the conditional distribution of each variable and its related variables in a fixed order to form the output scenario set of large-scale wind power bases, and the sampled output scenarios are reduced based on the synchronous backstepping method to extract representative typical output scenarios. The steps of output scenario simulation of large-scale wind power are as follows:

- 1) Generate N random numbers $a_N \in (0, 1)$; let it be the marginal probability of wind power output of the first cluster, that is, $P(X_1 \leq x_1) = a_1$; bring a_1 into the inverse

function of marginal distribution $F_1^{-1}(a_1) = x_1$, and solve for x_1 , which is the first cluster power output.

- 2) Let a_i $i \in [2, N]$ be the conditional transition probabilities from the second cluster to the last cluster $P(X_i \leq x_i | X_{i-1} = x_{i-1}) = a_i$; bring a_i into the conditional distribution among each cluster one by one, $F(v|u) = P(X_i \leq x_i | X_{i-1} = x_{i-1})$, and calculate the marginal probability v_i ; according to the inverse function of marginal distribution $F_i^{-1}(v_i) = x_i$, solve for x_i , which is the power output of i cluster.
- 3) Calculate the output of all wind farm clusters (x_1, x_2, \dots, x_N) and accumulate the wind farm clusters' power output to obtain the output scenario of a large-scale wind power base.
- 4) Repeat steps (1) to (3) M times to obtain the output scenario set of a large-scale wind power base.
- 5) Based on the Kmeans scenario reduction method, the representative typical output scenarios are extracted in the output scenario set of a large-scale wind power base.

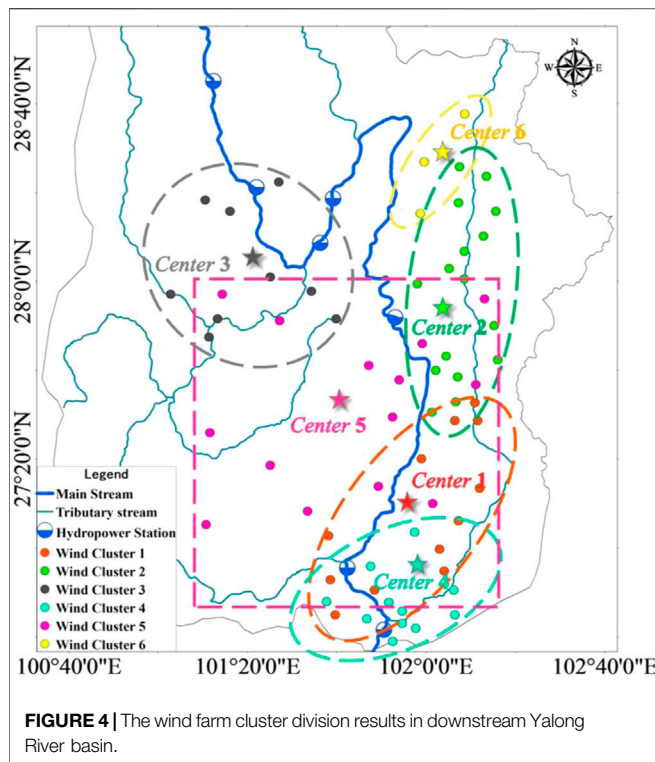


FIGURE 4 | The wind farm cluster division results in downstream Yalong River basin.

CASE STUDY

This study focuses on the Yalong River (the longest tributary of the Jinsha River), which is located in Southwest China. Its geographical location is 96°52'E to 102°48'E and 26°32'N to 33°58'N. The Yalong River basin is an area that is rich in wind energy and solar energy resources. There are abundant wind and PV power resources on both sides of the river basin, and it has great development potential (Wang et al., 2016; Liu et al., 2019). The complementary characteristics of wind, PV, and hydropower resources within the year are fully used to improve the comprehensive benefits. According to the preliminary plan of the watershed-type multi-energy complementary bases (WMCB) in the downstream Yalong River basin, there are more than 65 wind power farms with a total capacity of 7 GW; there are nearly 19 PV power stations with a total capacity of about 5.6 GW; the hydropower installed capacity of the downstream Yalong River basin is 14.7 GW (Zhang et al., 2020).

According to the planned location of the wind farms in the lower reaches of the Yalong River (as shown in **Figure 2**), the wind energy reanalysis data at each station location are extracted, and the wind speed power conversion model is used to calculate the long-series output process of each wind farm. The advanced GW121-2.5MW wind turbine is selected as the reference unit in the research process. The main technical parameters of the GW121-2.5MW wind turbine are shown in **Table 2**.

RESULTS AND DISCUSSION

In order to numerically verify the effectiveness of the research model and method, the results and discussion of the wind farms cluster in the downstream Yalong River basin are performed.

Dividing the Wind Farm Clusters

Kmeans method should determine the clustering number k firstly. Generally, the optimal clustering number is between $[2, \sqrt{N}]$, where N represents the number of clustering wind farms. In this study, 65 wind farms in the downstream Yalong River basin are clustered. Considering the geographical location, scale, wind energy, and other specific conditions of the wind farms, the maximum clustering number is 8 and the minimum clustering number is 3. Then, the clustering results of wind farms in the downstream Yalong River basin under different clustering numbers are shown in **Figure 2**. As can be seen from **Figure 3**, with the increase of the clustering number, the concentration of each wind farm cluster increases. However, when the clustering number is too large, the number of wind farms in individual clusters is too less.

Therefore, comparing the clustering results under different cluster numbers, the optimal clustering number is $k = 6$. The cluster division results and cluster centers of wind farms in downstream Yalong River basin are shown in **Figure 4**. The cluster center, representative wind farm, and capacity of each wind farm cluster are shown in **Table 3**. From **Figure 4**, the clustering results calculated by GA-Kmeans show obviously regional characteristics, and the characteristics are consistent with the actual situation of the Yalong River basin.

Power Output Characteristic of Wind Farm Clusters

According to the wind power cluster division results, the power output of each cluster is calculated by the wind power output

TABLE 3 | The cluster center and representative wind farm of dividing wind farm clusters.

Cluster num	Cluster center	Representative wind farm	Represents farm coordinates	Cluster capacity (MW)
Cluster1	101.9708°E, 27.1325°N	36	101.9572°E, 27.0597°N	1,294.9
Cluster2	102.1344°E, 27.9581°N	54	102.1428°E, 28.0091°N	1,726.5
Cluster3	101.3344°E, 28.0422°N	04	101.4182°E, 28.0162°N	971.2
Cluster4	101.8991°E, 26.7945°N	23	101.9108°E, 26.7634°N	1,187.0
Cluster5	101.6885°E, 27.5115°N	12	101.7859°E, 27.6843°N	1,510.7
Cluster6	102.0386°E, 28.4440°N	64	101.9929°E, 28.4481°N	323.7

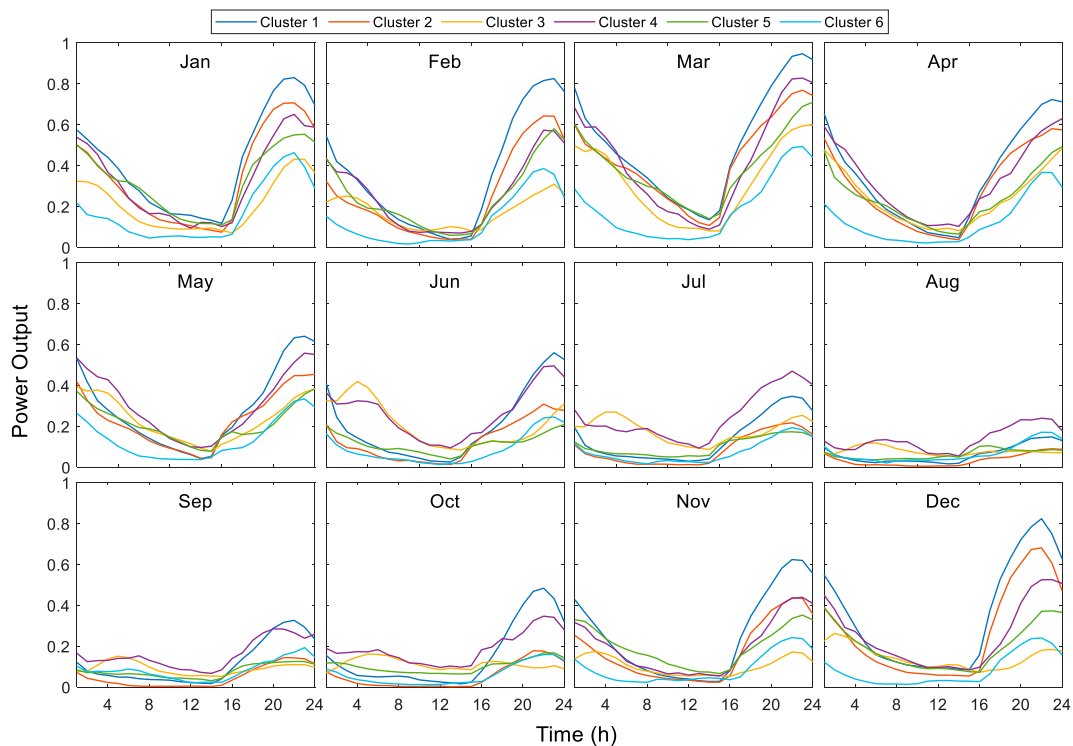


FIGURE 5 | Daily power output variation curve of six wind farm clusters in each month.

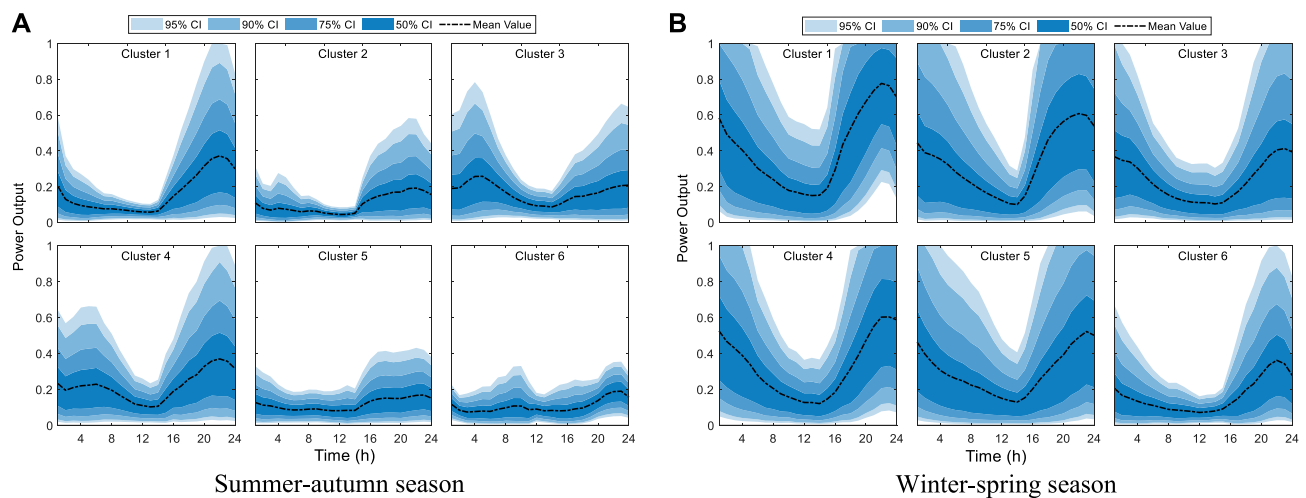


FIGURE 6 | Daily power output interval of six wind farm clusters in summer-autumn and winter-spring seasons. **(A)** Summer-autumn season. **(B)** Winter-spring season.

physical model, and the typical daily power output of 6 clusters in each month is shown in **Figure 5**. It can be seen from **Figure 5** that the wind power output has obvious daily and annual variation rules. In the short term, the wind power output is low from 10:00 to 15:00, and the wind power output usually reaches the peak at about 20:00, which is the same time as the peak load. In the long term, the output of wind power clusters

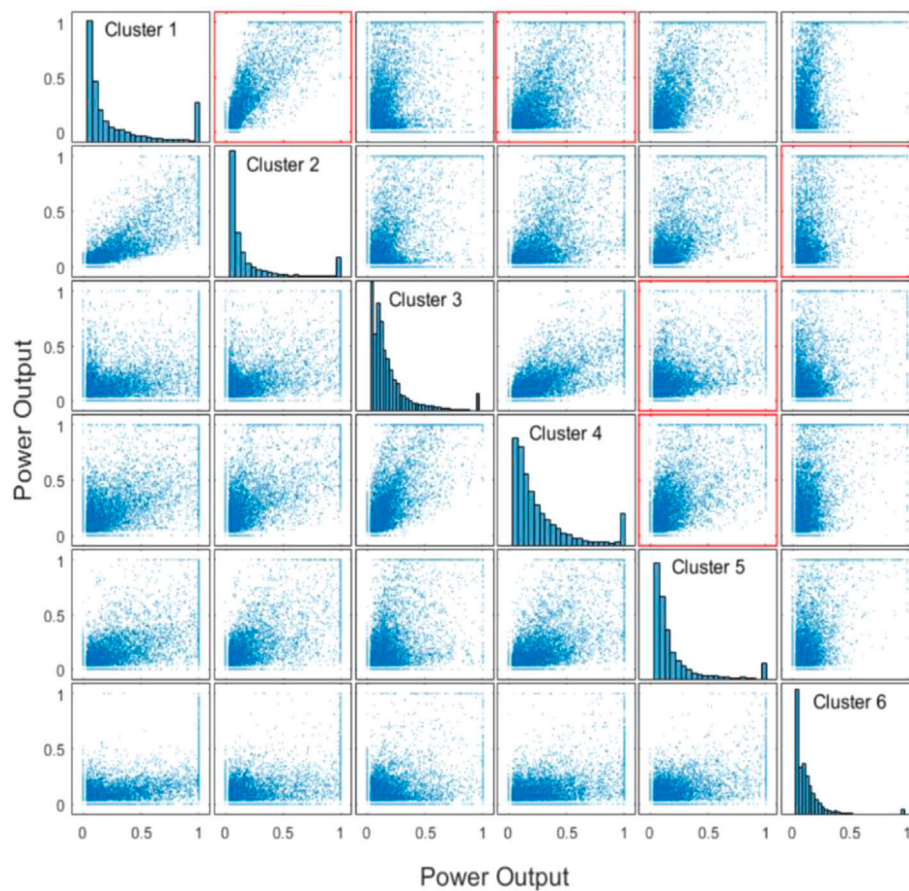
shows obvious seasonal law. From June to October, the power output of each cluster is significantly lower than that in other months. Therefore, it can be divided into two characteristic periods: summer-autumn and spring-winter.

The daily power output intervals of 6 wind farm clusters in the winter-spring and summer-autumn seasons are shown in **Figure 6**. From **Figure 6**, there are significant differences in

TABLE 4 | The correlation coefficients of wind farm clusters in the downstream Yalong River basin.

Cluster num	Correlation coefficient	Cluster1	Cluster2	Cluster3	Cluster4	Cluster5	Cluster6
Cluster 1	Pearson	-	0.906	0.563	0.800	0.774	0.625
	Spearman		0.897	0.473	0.776	0.729	0.557
	Kendall		0.755	0.344	0.595	0.566	0.425
Cluster 2	Pearson	0.906	-	0.664	0.772	0.666	0.628
	Spearman	0.897		0.491	0.684	0.606	0.567
	Kendall	0.755		0.362	0.518	0.443	0.425
Cluster 3	Pearson	0.563	0.664	-	0.748	0.806	0.482
	Spearman	0.473	0.491		0.695	0.730	0.256
	Kendall	0.344	0.362		0.525	0.567	0.180
Cluster 4	Pearson	0.800	0.772	0.748	-	0.806	0.577
	Spearman	0.776	0.684	0.695		0.734	0.481
	Kendall	0.595	0.518	0.525		0.542	0.347
Cluster 5	Pearson	0.774	0.666	0.806	0.806	-	0.676
	Spearman	0.729	0.606	0.730	0.734		0.505
	Kendall	0.566	0.443	0.567	0.542		0.370
Cluster 6	Pearson	0.625	0.628	0.482	0.577	0.676	-
	Spearman	0.557	0.567	0.256	0.481	0.505	
	Kendall	0.425	0.425	0.180	0.347	0.370	

The bold values represent the adjacent wind clusters with the best correlation.

**FIGURE 7 |** The correlation scatter diagram matrix of wind farm cluster.

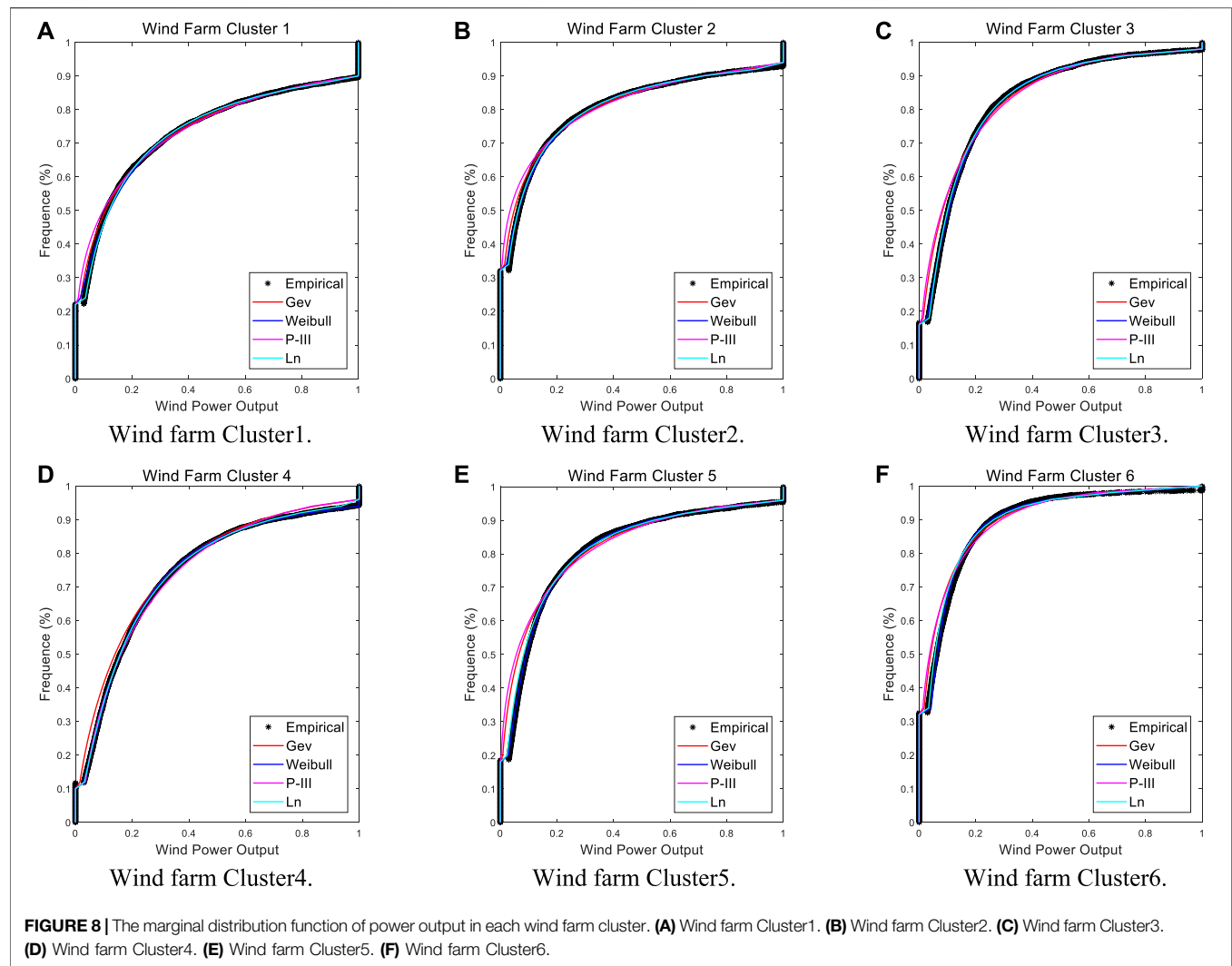


FIGURE 8 | The marginal distribution function of power output in each wind farm cluster. **(A)** Wind farm Cluster1. **(B)** Wind farm Cluster2. **(C)** Wind farm Cluster3. **(D)** Wind farm Cluster4. **(E)** Wind farm Cluster5. **(F)** Wind farm Cluster6.

TABLE 5 | Parameter estimation and the goodness-of-fit test index of the joint distribution function.

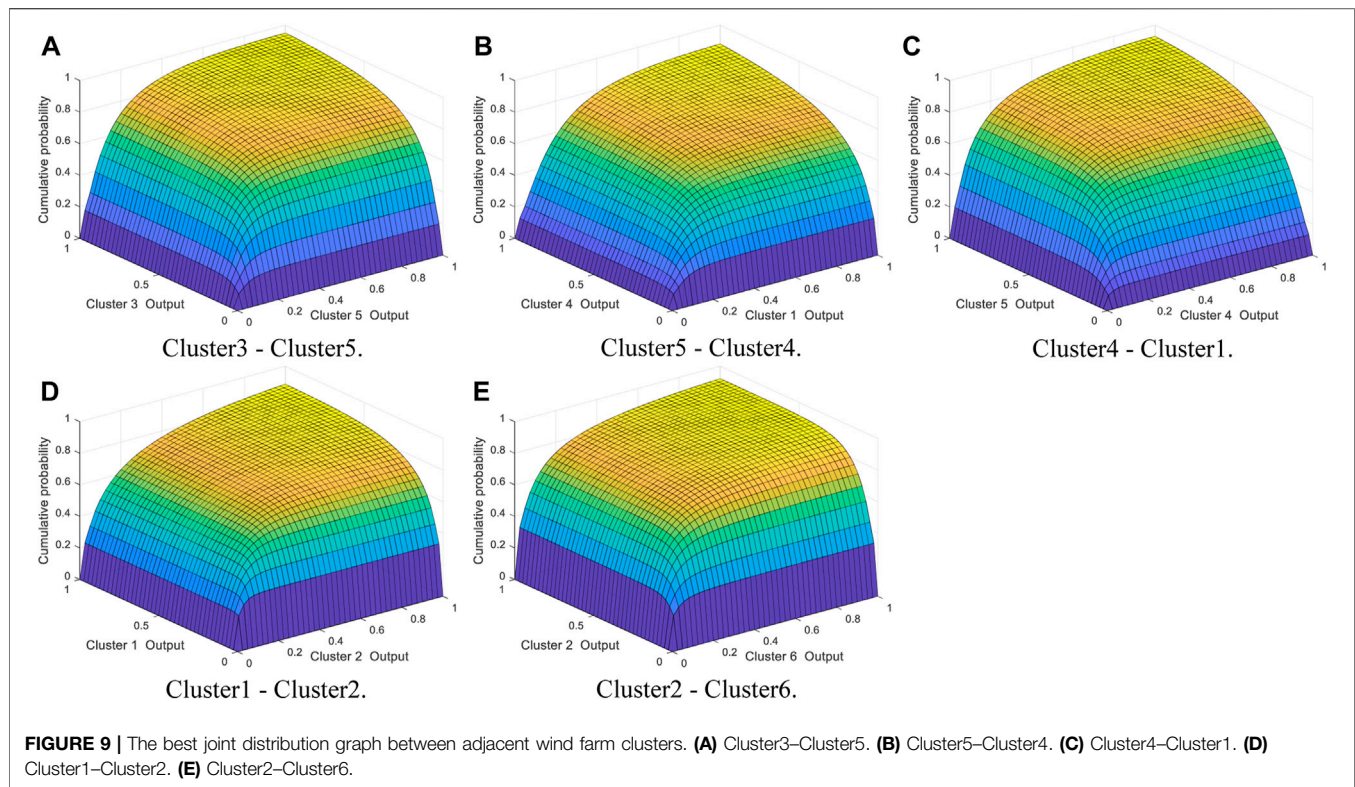
Type	Index	Cluster3 –Cluster5	Cluster5 –Cluster4	Cluster4 –Cluster1	Cluster1 –Cluster2	Cluster2 –Cluster6
Gumbel Copula	Parameter θ	1.736	7.214	2.180	4.569	2.121
	RMSE	0.111	0.185	0.135	0.031	0.025
	AIC	-38,486	-29,543	-35,048	-60,773	-64,542
Clayton Copula	Parameter θ	2.083	11.064	2.858	5.335	3.548
	RMSE	0.119	0.192	0.149	0.047	0.055
	AIC	-37,283	-28,953	-33,310	-53,695	-50,783
Frank Copula	Parameter θ	5.625	22.945	6.969	15.551	7.215
	RMSE	0.111	0.187	0.140	0.038	0.041
	AIC	-38,489	-29,344	-34,426	-57,455	-56,142

The bold values indicate the best copula type.

the daily power output intervals of different seasons and different clusters. In the spring–winter season, the mean value and variation range of daily power output are relatively large, while in the summer–autumn season, the mean value and variation range of daily power output are both small.

Correlation Analysis of Wind Farm Clusters Based on Copula

According to wind farm cluster division results in downstream Yalong River basin and power output sequence and characteristic of each wind cluster, analyze the correlation



of adjacent wind farm clusters with three types of Copula function.

The Correlation Coefficient of Adjacent Wind Farm Clusters

In this study, the Pearson, Spearman, and Kendall correlation coefficients are used to evaluate the correlation among six wind farm clusters in downstream Yalong River basin, as shown in **Table 4**. The scatter matrix of wind farm clusters is drawn in **Figure 7**.

Because it is hard to analyze the correlation of multiple wind farm clusters directly, this study uses a set of correlations of adjacent wind farm clusters to represent the correlation of multiple wind farm clusters. According to the three correlation coefficients and scatter matrix of each wind power cluster, the adjacent wind farm clusters with strong correlation are selected to form the adjacent wind farm clusters connected head to tail: Cluster3–Cluster5, Cluster5–Cluster4, Cluster4–Cluster1, Cluster1–Cluster2, and Cluster2–Cluster6. **Figure 7** and **Figure 4** indicate that the selected adjacent wind power clusters are consistent with the spatial distribution law of wind farm clusters in downstream Yalong River basin.

The Marginal Distribution of Each Wind Farm Cluster

In this paper, the generalized extreme value distribution, Weibull distribution, Pearson type III distribution, and lognormal distribution are selected as the marginal distribution function to fit the power output of each wind farm cluster, and the marginal distribution parameters are estimated by the

maximum likelihood method. The cumulative distribution curves of the power output of six wind power clusters in downstream Yalong River basin are shown in **Figure 8**.

From **Figure 8**, comparing the empirical frequency with the cumulative frequency of each marginal distribution, it can be found that the goodness-of-fitting of the four distribution curves is roughly the same, and four type distributions could fit the data samples well. After screening, the optimal marginal distributions of Cluster1, Cluster3, Cluster5, and Cluster6 are lognormal distribution, the optimal marginal distributions of Cluster2 and Cluster4 are Weibull distribution, and the optimal marginal distribution of each wind farm cluster is used to construct Copula joint distribution. Moreover, the interception distribution model used in this study can effectively fit the samples with the power output of 0 and 1 in the data series.

The Copula Joint Function of Adjacent Wind Farm Clusters

According to the adjacent wind farm clusters and the marginal distribution of each wind power cluster, the Gumbel Copula, Clayton Copula, and Frank Copula are used to construct the joint distribution of adjacent wind farm clusters. The Copula joint distribution parameters are estimated by the maximum likelihood method. The AIC and RMSE criteria are used to test the goodness-of-fitting of Copula functions, as shown in **Table 4**. As can be seen from **Table 5**, the best joint distribution in Cluster3–Cluster5 is Frank Copula function. The best joint distribution in Cluster5–Cluster4, Cluster4–Cluster1, Cluster1–Cluster2, and Cluster2–Cluster6 is the Gumbel

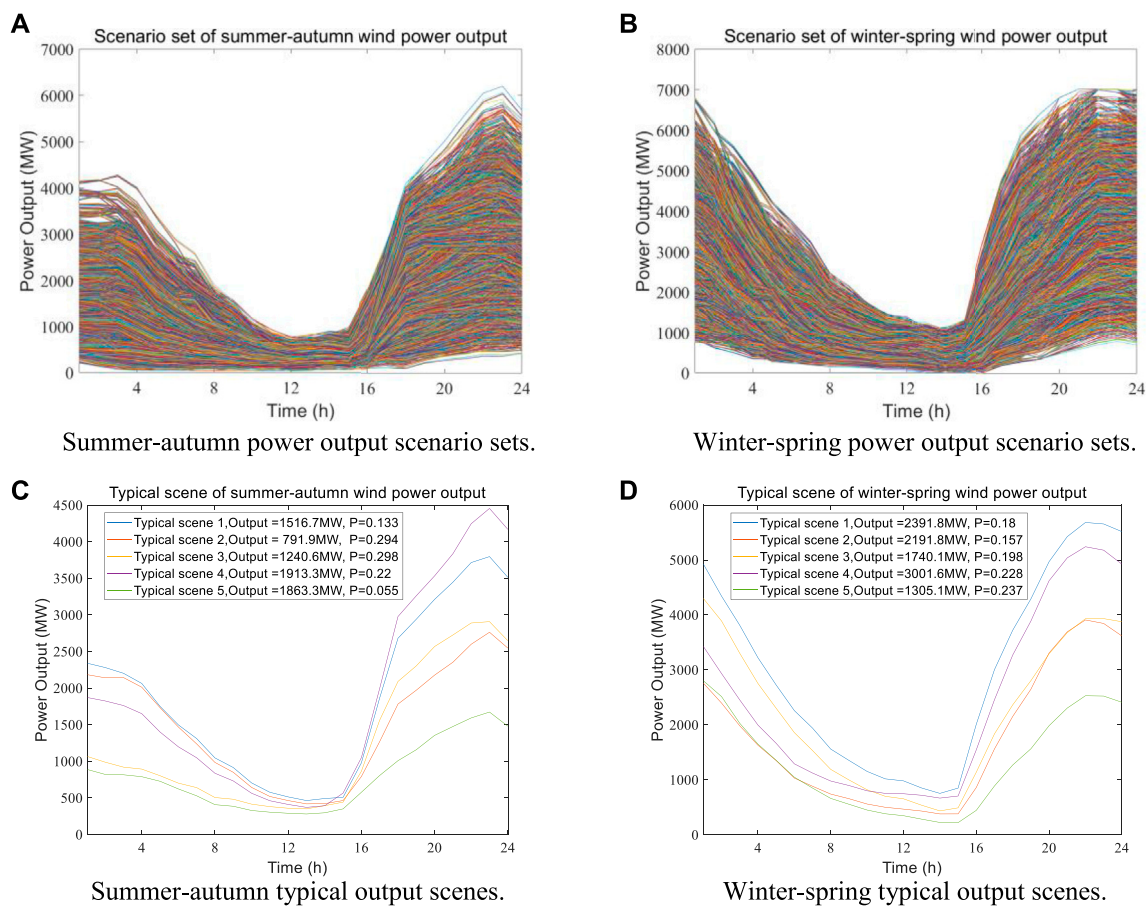


FIGURE 10 | The power output scenario sets and the typical output scenes of the Yalong River wind power base in the summer–autumn and winter–spring seasons. **(A)** Summer–autumn power output scenario sets. **(B)** Winter–spring power output scenario sets. **(C)** Summer–autumn typical output scenes. **(D)** Winter–spring typical output scenes.

Copula function. The best Copula joint distribution of adjacent wind farm clusters is shown in **Figure 9**.

Figure 9 indicates that the Copula joint distribution diagram can intuitively reflect the joint probability of adjacent wind farm clusters. According to the joint distribution of wind farm clusters, when the power output of a wind farm cluster is certain, the conditional probability of power output of its adjacent cluster can be determined. On the contrary, given the joint probability of adjacent wind farm clusters and one of the cluster power output, the corresponding power output of the other cluster can be deduced.

Output Scenario Combination of Large-Scale Wind Power

Based on the Copula joint distribution, the 10,000 sets of power output scenarios of downstream Yalong River wind power base in summer–autumn and winter–spring are simulated by the MCMC method and shown in **Figures 10A, B**. From **Figure 6** and **Figures 10A, B**, the simulated power output scenario sets of

wind power base in summer–autumn and winter–spring have the same law as the daily power output interval.

However, the power output scenario sets of wind power base in summer–autumn and winter–spring are too complex, so the power output scenario sets need to be reasonably reduced. The Kmeans scenario reduction model is used to reduce 10,000 sets of scenarios into five typical scenarios. The representative typical wind power output scenarios and the corresponding scenario probabilities in the winter–spring and summer–autumn seasons are shown in **Figures 10C, D**. From **Figure 10**, the typical power output scenes can basically cover the original scenario set, and each typical power output scenario is highly representative. Otherwise, comparing the typical power output scenes of wind power base in summer–autumn and winter–spring seasons, the probability of each scene in winter–spring season is relatively similar, and the scene probability is about 0.2. In the summer–autumn season, the probability of each scene is quite different. The probability of Scene2 and Scene3 is close to 0.3, while the probability of Scene5 is only 0.055. In general, the power output simulation method of large-scale wind power base can

realize the rapid modeling and solution of the integrated output of abundant wind farms.

CONCLUSION

The continuous expansion of new energy such as wind power directly leads to the increase of power system uncertainty and the difficult grid integration of new energy. It is beneficial to divide the large-scale wind power base into wind power clusters and quantify the correlation of wind power clusters. Therefore, this paper proposed a power output scene simulation method of large-scale wind power bases considering power station clustering and cluster correlation characteristics. The method is applied in the Yalong River downstream, and the main conclusions of this paper can be summarized:

- 1) GA-Kmeans clustering method with a similar distance to the evaluation standard can quickly and accurately divide the clusters of renewable energy power stations and effectively solve the influence of cluster number and initial cluster center on Kmeans clustering results. In the case study, this method is applied to divide the 65 wind farms in the downstream Yalong River basin into 6 clusters, and the cluster division results are consistent with the spatial distribution characteristics of wind energy resources in the basin.
- 2) Copula function can effectively reflect the output correlation of multi-dimensional wind farm clusters and significantly improve the simulation or prediction effect of the power output in large-scale wind power bases. In the case study, the Copula function is constructed to determine the best joint distribution of 6 adjacent wind farm clusters in the downstream Yalong River basin. Then, based on the correlation characteristic, the MCMC sampling method is used to simulate the typical power output of the Yalong River downstream wind power base in winter–spring and summer–autumn seasons, respectively.

REFERENCES

- Almeida, D. B., Borges, C. L. T., Oliveira, G. C., and Pereira, M. V. (2021). Multi-area Reliability Assessment Based on Importance Sampling, MCMC and Stratification to Incorporate Variable Renewable Sources. *Electric Power Syst. Res.* 193, 107001. doi:10.1016/j.epr.2020.107001
- Antunes Campos, R., Rafael Do Nascimento, L., and Rüther, R. (2020). The Complementary Nature between Wind and Photovoltaic Generation in Brazil and the Role of Energy Storage in Utility-Scale Hybrid Power Plants. *Energy Convers. Manag.* 221, 113160. doi:10.1016/j.enconman.2020.113160
- Cantão, M. P., Bessa, M. R., Bettega, R., Detzel, D. H. M., and Lima, J. M. (2017). Evaluation of Hydro-Wind Complementarity in the Brazilian Territory by Means of Correlation Maps. *Renew. Energy* 101, 1215–1225. doi:10.1016/j.renene.2016.10.012
- Chidean, M. I., Caamaño, A. J., Ramiro-Bargueño, J., Casanova-Mateo, C., and Salcedo-Sanz, S. (2018). Spatio-temporal Analysis of Wind Resource in the Iberian Peninsula with Data-Coupled Clustering. *Renew. Sust. Energy Rev.* 81 (2), 2684–2694. doi:10.1016/j.rser.2017.06.075
- De Blasis, R., Masala, G. B., and Petroni, F. (2021). A Multivariate High-Order Markov Model for the Income Estimation of a Wind Farm. *Energies* 14 (2), 388. doi:10.3390/en14020388

- 3) Compared with the power output scenario sets, the typical power output scenes can effectively remove the redundant information in many scenario sets and highlight the representative situation of the integrated output of a large-scale wind power base. Furthermore, the typical power output scenes could be conducive to the application of scenes in practical work such as planning, design, scheduling, and operation of large-scale wind power base.

DATA AVAILABILITY STATEMENT

The raw data supporting the conclusion of this article will be made available by the authors, without undue reservation.

AUTHOR CONTRIBUTIONS

MZ designed the framework and analyzed the data of this study; YW and XW provided significant suggestions on the methodology and structure of the manuscript; YZ, JC, and TL collected the data; MZ wrote the paper.

FUNDING

This research was funded by the Natural Science Foundation of China (grant numbers U1965202, 52009101, and 51909207).

ACKNOWLEDGMENTS

The authors gratefully thank the Yalong River Hydropower Development Co., Ltd. and Southwest Branch of State Grid Corporation of China for providing the data.

- Deng, J., Wang, A., Hu, Y., Ren, A., and Wang, K. (2018). Analysis of Renewable Energy Accommodation Capability of Shanxi Power Grid Based on Operation Simulation Method. *2018 2ND IEEE CONFERENCE ENERGY INTERNET ENERGY SYSTEM INTEGRATION (Ei2)*, 1–9. doi:10.1109/EI2.2018.8582094
- Densing, M., and Wan, Y. (2022). Low-dimensional Scenario Generation Method of Solar and Wind Availability for Representative Days in Energy Modeling. *Appl. Energy* 306, 118075. doi:10.1016/j.apenergy.2021.118075
- Ding, K., Wang, N., Xie, H., and Bie, Z. (2016). Production Simulation of Power Systems Considering the Forecast Error of Renewable Energy. *2016 IEEE PES ASIA-PACIFIC POWER ENERGY ENGINEERING CONFERENCE (Appec)*, 2091–2095. doi:10.1109/APPEEC.2016.7779855
- Hou, Q., Zhang, N., Du, E., Miao, M., Peng, F., and Kang, C. (2019). Probabilistic Duck Curve in High PV Penetration Power System: Concept, Modeling, and Empirical Analysis in China. *Appl. Energy* 242, 205–215. doi:10.1016/j.apenergy.2019.03.067
- Huang, K., Liu, P., Ming, B., Kim, J.-S., and Gong, Y. (2021). Economic Operation of a Wind-Solar-Hydro Complementary System Considering Risks of Output Shortage, Power Curtailment and Spilled Water. *Appl. Energy* 290, 116805. doi:10.1016/j.apenergy.2021.116805
- Kim, H., Lee, J., Yoon, M., Lee, M., Cho, N., and Choi, S. (2020). Continuation Power Flow Based Distributed Energy Resource Hosting Capacity Estimation Considering Renewable Energy Uncertainty and Stability in Distribution Systems. *Energies* 13 (17). doi:10.3390/en13174367

- Liu, B., Lund, J. R., Liao, S., Jin, X., Liu, L., and Cheng, C. (2020). Optimal Power Peak Shaving Using Hydropower to Complement Wind and Solar Power Uncertainty. *Energy Convers. Manag.* 209, 112628. doi:10.1016/j.enconman.2020.112628
- Dai, J., Cao, J., Liu, D., Wen, L., and Long, X. (2017). Power Fluctuation Evaluation of Large Scale Wind Turbines Based on SCADA Data. *IET Renew. Power Gen.* 11, 395–402. doi:10.1049/iet-rpg.2016.0124
- Liu, Y., Jiang, Z., Feng, Z., Chen, Y., Zhang, H., and Chen, P. (2019). Optimization of Energy Storage Operation Chart of Cascade Reservoirs with Multi-Year Regulating Reservoir. *Energies* 12 (20), 3814. doi:10.3390/en12203814
- Nelsen, R. B. (1999). *An Introduction to Copulas*. Springer. New York, p 216.
- Neshat, M., Nezhad, M. M., Abbasnejad, E., Mirjalili, S., Groppi, D., Heydari, A., et al. (2021). Wind Turbine Power Output Prediction Using a New Hybrid Neuro-Evolutionary Method. *Energy* 229, 120617. doi:10.1016/j.energy.2021.120617
- Singh, U., Rizwan, M., Alaraj, M., and Alsaidan, I. (2021). A Machine Learning-Based Gradient Boosting Regression Approach for Wind Power Production Forecasting: A Step towards Smart Grid Environments. *Energies* 14(16). doi:10.3390/en14165196
- Sklar, A. (1959). Fonctions de Repartition a n Dimensions et Leurs Marges. *Publications de l'Institut de statistique de l'Université de Paris* 8.
- Wang, G., Jia, R., Liu, J., and Zhang, H. (2020). A Hybrid Wind Power Forecasting Approach Based on Bayesian Model Averaging and Ensemble Learning. *Renew. Energy* 145, 2426–2434. doi:10.1016/j.renene.2019.07.166
- Wang, X., Chang, J., Meng, X., and Wang, Y. (2019). Hydro-thermal-wind-photovoltaic Coordinated Operation Considering the Comprehensive Utilization of Reservoirs. *Energy Convers. Manag.* 198, 111824. doi:10.1016/j.enconman.2019.111824
- Wang, X., Chang, J., Meng, X., and Wang, Y. (2018). Short-term hydro-thermal-wind-photovoltaic Complementary Operation of Interconnected Power Systems. *Appl. Energy* 229, 945–962. doi:10.1016/j.apenergy.2018.08.034
- Wang, X., Mei, Y., Cai, H., and Cong, X. (2016). A New Fluctuation Index: Characteristics and Application to Hydro-Wind Systems. *Energies* 9 (2), 114. doi:10.3390/en9020114
- Wang, Y., Yang, R., Xu, S., and Tang, Y. (2020). Capacity Planning of Distributed Wind Power Based on a Variable-Structure Copula Involving Energy Storage Systems. *Energies* 13 (14), 3602. doi:10.3390/en13143602
- Wang, Y., Zhao, M., Chang, J., Wang, X., and Tian, Y. (2019). Study on the Combined Operation of a hydro-thermal-wind Hybrid Power System Based on Hydro-Wind Power Compensating Principles. *Energy Convers. Manag.* 194, 94–111. doi:10.1016/j.enconman.2019.04.040
- Xu, L., Wang, Z., and Liu, Y. (2017). The Spatial and Temporal Variation Features of Wind-Sun Complementarity in China. *Energy Convers. Manag.* 154, 138–148. doi:10.1016/j.enconman.2017.10.031
- Yan, J., Sang, Z., Wang, S., Du, Z., Huang, J., Yang, D., et al. (2020). Analysis of Solar and Wind Power on Access Planning of Multiple Renewable Energy Sources. *2020 5TH INTERNATIONAL CONFERENCE RENEWABLE ENERGY ENVIRONMENTAL PROTECTION* 621. doi:10.1088/1755-1315/621/1/012069
- Yesilbudak, M. (2016). Clustering Analysis of Multidimensional Wind Speed Data Using K-Means Approach. *2016 IEEE INTERNATIONAL CONFERENCE RENEWABLE ENERGY RESEARCH APPLICATIONS (Icrera)*, 961–965. doi:10.1109/ICRERA.2016.7884477
- Zhang, L., Xie, J., Chen, X., Zhan, Y., and Zhou, L. (2020). Cooperative Game-Based Synergistic Gains Allocation Methods for Wind-Solar-Hydro Hybrid Generation System with Cascade Hydropower. *Energies* 13 (15), 3890. doi:10.3390/en13153890
- Zhang, X., Ma, G., Huang, W., Chen, S., and Zhang, S. (2018). Short-Term Optimal Operation of a Wind-PV-Hydro Complementary Installation: Yalong River, Sichuan Province, China. *Energies* 11 (4), 868. doi:10.3390/en11040868
- Zhang, Z., Qin, H., Li, J., Liu, Y., Yao, L., Wang, Y., et al. (2020). Short-term Optimal Operation of Wind-Solar-Hydro Hybrid System Considering Uncertainties. *Energy Convers. Manag.* 205, 112405. doi:10.1016/j.enconman.2019.112405

Conflict of Interest: Author YZ is employed by Yalong River Hydropower Development Company, Ltd. Author TL is employed by Northwest Engineering Corporation Limited.

The remaining authors declare that the research was conducted in the absence of any commercial or financial relationships that could be construed as a potential conflict of interest.

Publisher's Note: All claims expressed in this article are solely those of the authors and do not necessarily represent those of their affiliated organizations, or those of the publisher, the editors, and the reviewers. Any product that may be evaluated in this article, or claim that may be made by its manufacturer, is not guaranteed or endorsed by the publisher.

Copyright © 2022 Zhao, Wang, Wang, Chang, Zhou and Liu. This is an open-access article distributed under the terms of the Creative Commons Attribution License (CC BY). The use, distribution or reproduction in other forums is permitted, provided the original author(s) and the copyright owner(s) are credited and that the original publication in this journal is cited, in accordance with accepted academic practice. No use, distribution or reproduction is permitted which does not comply with these terms.

Advantages of publishing in Frontiers



OPEN ACCESS

Articles are free to read
for greatest visibility
and readership



FAST PUBLICATION

Around 90 days
from submission
to decision



HIGH QUALITY PEER-REVIEW

Rigorous, collaborative,
and constructive
peer-review



TRANSPARENT PEER-REVIEW

Editors and reviewers
acknowledged by name
on published articles

Frontiers

Avenue du Tribunal-Fédéral 34
1005 Lausanne | Switzerland

Visit us: www.frontiersin.org

Contact us: frontiersin.org/about/contact



REPRODUCIBILITY OF RESEARCH

Support open data
and methods to enhance
research reproducibility



DIGITAL PUBLISHING

Articles designed
for optimal readership
across devices



FOLLOW US

@frontiersin



IMPACT METRICS

Advanced article metrics
track visibility across
digital media



EXTENSIVE PROMOTION

Marketing
and promotion
of impactful research



LOOP RESEARCH NETWORK

Our network
increases your
article's readership